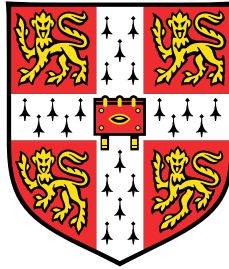


Inlet Recirculation in Radial Compressors



Christoph Schreiber

Department of Engineering
University of Cambridge

This dissertation is submitted for the degree of
Doctor of Philosophy

Darwin College

February 2017

Declaration

I hereby declare that except where specific reference is made to the work of others, the contents of this dissertation are original and have not been submitted in whole or in part for consideration for any other degree or qualification in this, or any other university. This dissertation is my own work and contains nothing which is the outcome of work done in collaboration with others, except as specified in the text and Acknowledgements. This dissertation contains approximately 60,000 words including appendices, bibliography, footnotes, tables and equations and has 94 figures.

Christoph Schreiber
February 2017

Acknowledgements

I would like to thank Mitsubishi Heavy Industries for funding this research project. Furthermore, I would like to express my gratitude to my supervisor Liping Xu for his expertise, guidance and critical review of my work. He gave me the freedom to explore the subject in various ways whilst still keeping me on track. Furthermore I would like to thank my technician Nick Hooper. His skill and knowledge largely contributed to the realisation of the test stand. Special thanks to Ivor Day who's advice and encouragement in some of the most difficult moments of this thesis kept me going. My advisors Mick Casey and Rob Miller helped a lot with their input and clarity of thought. My examiners Andrew Wheeler and Mehrdad Zangeneh gave helpful comments to round up this thesis. The help and intense discussions with my colleague Robert Grewe contributed significantly to finding my way.

A big thanks to all my friends, in particular Sean Dyde, Will Playford, Douwe Kiela, Florian Roessler, Ludovika Vissat, Timo Nussbaum, Rüdiger Heinritz, Kilian Schmidt and Christoph Sirtl. I would like to thank Franziska Diller for the time and all her support.

I would like to thank my mother for always being there for me, for her encouragement and all the patience. Finally, I would not have been able to finish this work without the love, selfless support and motivation of Mathilde Durand.

Abstract

Deficient performances of turbocharger compressors inside turbo-charged engines limit the behaviour of the drive train, particularly during transient conditions such as the drive-away process or acceleration from low engine-speeds. This problem has shifted the design space for compressors towards their performance at part-speed and low-flow conditions. The most dominant feature of these flow conditions is the phenomenon of inlet recirculation, where a large portion of the flow into the rotor of the machine is expelled again through the inlet, creating a blockage ring on the casing. While on the one hand, inlet recirculation is the main loss-source at low-speed and low-flow within centrifugal compressors, on the other hand, it also keeps the compressors functioning, rather than stalling or dropping into a surge hysteresis loop.

This thesis aimed towards increasing the understanding of inlet recirculation, with the scope on improving the part-speed, low-flow performance of automotive turbocharger compressors, more specifically their range and transient behaviour.

The research has been carried out on an automotive turbocharger compressor which was available at the Whittle Laboratory. An experimental set-up was built to obtain insight with measurements, and a numerical model based on the compressor geometry was used to carry out time averaged numerical simulations.

It was shown that inlet recirculation is a phenomenon which takes place in the tip region of the rotor inlet of a radial compressor wheel at part speed. The recirculation bubble can extend far downstream into the rotor and far upstream into the inlet. Furthermore, the flow within the recirculation bubble features a strong positive swirl component. The phenomenon is non-periodic in a time-averaged sense. Furthermore, inlet recirculation can extend into the passage radially up to 20% of the span. Using a control volume analysis approach, the onset of inlet recirculation and established recirculation were discussed separately. The research in this work investigated the rotor flow-field with regard to inlet recirculation for the first time. It was found that the real starting point of inlet recirculation is located far downstream inside the rotor passage close to the splitter blade pressure side. The established recirculation zone

could be characterised based on mass, momentum and energy.

Using a compressor map, inlet recirculation was found in a large region of the compressor at flow-rates lower than design conditions, well before the compressor went into surge. In terms of flow range, inlet recirculation at low rotational speeds was present over 40% of the map width. This value decreased as the rotor speed was increased. It was present beyond the point where the inlet flow became transonic. As soon as shocks were present, the recirculation region diminished significantly. This behaviour was associated with the destabilising effect of the shock.

A study of the mass flow expelled from the rotor into the inlet showed a linear correlation with the global flow coefficient of the machine. Furthermore, the energy that was transported in this flow held around constant levels. This linear energy-flow allowed a low-order model of inlet recirculation to be derived based on simple correlation.

Inlet recirculation required a significant amount of additional work input into the compressor. A “lumped” recirculation-loss parameter was derived to account for the performance penalty due to inlet recirculation. The loss was shown to be up to 35% of the total loss occurring in a compressor at low speed, and thus its largest source. The “lumped” loss came from two sources: around 80% from the additional energy required to sustain the inlet recirculation bubble, and 20% from secondary losses.

The tip clearance flow in a compressor was identified to be one of the major contributors to the low momentum region in the casing, particularly in turbocharger compressors which feature a large relative tip gap size. A tip gap study showed that it had no effect on the onset point of inlet recirculation, although it led to an altered three-dimensional flow structure within the rotor. It was shown that the size and intensity of inlet recirculation was independent of the tip gap size. Furthermore, the “lumped” inlet recirculation loss was unaffected by the tip gap. The efficiency gains due to a reduced tip gap were marginalised as soon as inlet recirculation was present. However, the rotor still benefited from enhanced pressure rise capabilities for reduced tip gap sizes.

Table of contents

List of figures	xiii
List of tables	xix
Nomenclature	xxi
1 Introduction	1
1.1 Scope of work	9
2 Compressor low flow behaviour	13
2.1 Introduction	13
2.2 Compressor instability	14
2.3 Compressor component matching	17
2.4 A definition of compressor low flow phenomena	21
2.4.1 Stall	21
2.4.2 Modal stall inception	21
2.4.3 Spike type stall inception	22
2.4.4 Rotating Stall	22
2.4.5 Surge	23
2.4.6 Inlet recirculation	24
2.5 Low flow behaviour of radial compressor rotors	26
2.5.1 Inlet recirculation	30
2.6 Low flow behaviour of radial compressor diffusers and volutes	47
2.6.1 Vaneless diffusers	47
2.6.2 Vaned diffusers	51
2.6.3 Volute	52
2.7 Summary	55

3	Methods	57
3.1	Introduction	57
3.2	Research compressor	58
3.2.1	Inlet	60
3.2.2	Rotor	61
3.2.3	Diffuser	63
3.2.4	Volute	67
3.3	Experimental setup	68
3.3.1	Sensors and calibration	74
3.3.2	Validation	75
3.4	Numerical setup	77
3.4.1	Inlet boundary condition	81
3.4.2	Exit boundary condition	82
3.4.3	Volute 1-D model	86
3.4.4	Validation	90
3.5	Summary	97
4	Key features of inlet recirculation	101
4.1	Introduction	101
4.2	The onset of inlet recirculation	107
4.3	Established inlet recirculation	111
4.4	Conclusions	122
5	Compressor low flow operation analysis	125
5.1	Introduction	125
5.2	Compressor low flow operation analysis	126
5.3	Conclusions	137
6	The energetic cost of inlet recirculation and accounting for it during preliminary design	139
6.1	Introduction	139
6.2	Compressor performance analysis	140
6.2.1	Intake box and Inlet	144
6.2.2	Rotor	147
6.2.3	Diffuser	152
6.2.4	Volute	153
6.2.5	Loss breakdown	154

6.2.6	Conclusions	160
7	The effect of tip clearance on inlet recirculation and its onset point	163
7.1	Introduction	163
7.2	The effect of tip clearance on inlet recirculation and its onset point	164
7.3	Analysis of the 3D flow field	173
7.4	Conclusions	189
8	Conclusions and future work	193
8.1	Introduction and scope of work	193
8.1.1	Under which conditions does inlet recirculation occur?	194
8.1.2	What are its effects on compressor performance in terms of energetic cost?	195
8.1.3	How can inlet recirculation be accounted for in preliminary design?	195
8.1.4	How can a designer influence the mechanisms sustaining recirculation?	195
8.2	Experimental and numerical methods and validation	196
8.3	Key features of inlet recirculation	197
8.4	When does inlet recirculation occur?	198
8.5	Reduced order modelling of inlet recirculation	199
8.6	The energetic costs of inlet recirculation	200
8.7	The effect of tip clearance on inlet recirculation	201
8.8	Future work	202
	References	205
	Appendix A Measurement equipment specifications	209
A.1	Temperature probes	209

List of figures

1.1	LCV annual market growth 2012 - 2019 [31]	1
1.2	IC engine characteristic and compressor working line [4]	3
1.3	Compressor with casing treatment: casing pressure distribution [4]	6
1.4	Compressor map for a compressor with and without casing treatment	7
1.5	Sequential charging concept: serial turbochargers	8
1.6	Sketch of a compressor wheel with recirculation flow pattern	10
2.1	Classification of surge cycles. Left: Mild Surge ; Right: Deep Surge [18]	14
2.2	Simplified model of a compression system as a mass-spring-damper system [19]	15
2.3	Circumferential variation of static pressure at the inlet and outlet of a vaneless diffuser of a turbocharger compressor operating at minimum, optimum and maximum mass flow [41]	18
2.4	Mach number effect on the component matching	19
2.5	jet wake rotor outlet velocity profile [12]	26
2.6	Combination of secondary flows due to curvature and rotation at the rotor outlet [20]	27
2.7	Schematic of stall inception mechanisms [9]; left: Modal Stall; right: Spike Stall	29
2.8	Power balance over the relative swallowing capacity of a centrifugal pump [43]	30
2.9	Schematic of different flow conditions of an axial blower [11]	32
2.10	Sketch of a closed casing radial vaned rotor with developed recirculation [20]	33
2.11	Schematic of different flow conditions of an axial blower [11]	34
2.12	Relative velocity distribution at the throat of the rotor [20]	35
2.13	Meridional cut through mixed flow pump showing the qualitative circumferentially averaged total pressure distribution. Flow direction from left to right. Without rib: Inlet recirculation; With rib: Suppressed Inlet recirculation	37
2.14	Inlet hot wire traverse upstream of a rotor at different flow coefficients [37]	39

2.15	compressor map with different types of instabilities [30]	40
2.16	Critical area ratio criterion compared to numerical data [23]	43
2.17	Blockage correlation [23]	43
2.18	Location of the compressor instability line: SW=smooth wall; RC=recirculation channel; CS=recirculation channel with counter swirl vanes	44
2.19	Change in instability limit through inlet fins [45]	45
2.20	Change in instability limit and efficiency in a turbocharger compressor [24]	46
2.21	Logarithmic spiral surface streaklines in an industrial compressor diffuser [27]	48
2.22	Experimentally obtained meridional velocity from traverse data in a vaneless diffuser at different radii showing thickening of the boundary layers [40]	48
2.23	Back flow close to the impeller trailing edge in a vaneless diffuser [27]	49
2.24	velocity and pressure fluctuations in a vaneless diffuser under rotating stall; Top: Experiment; Bottom: Numerically obtained results [48]	51
2.25	Circumferential static pressure distribution, and velocity vectors in a volute with resulting separation zones; Top: Design flow rate; Middle: Low flow rate; Bottom: High flow rate [20]	54
3.1	Research Compressor	58
3.2	Research compressor operating map	59
3.3	Sketch: Compressor inlet with Bellmouth	60
3.4	Key geometry features of the rotor	61
3.5	Leading edge span-wise blade angle distribution	62
3.6	Diffuser Geometry	63
3.7	Theoretical correlation for α_{2crit} [49]	65
3.8	Experimental correlation for α_{2crit} with $\frac{b_2}{R_2}$ [49]	66
3.9	Sketch: Volute with key geometry features	67
3.10	Principle sketch of the experiment	68
3.11	Sketch of the compressor test rig: parts of the setup	69
3.12	Sketch of the compressor test rig: mean line measurement planes	70
3.13	Sketch of the compressor measurement arrangement: probing positions	70
3.14	pitot probe and total pressure sensors at the compressor exit	71
3.15	circumferential pressure tappings in the diffuser back plate	72
3.16	pressure tap positions in the housing relative to the volute tongue	72
3.17	casing pressure tap position	73
3.18	Calibration curve of the pressure sensor	74
3.19	Compressor characteristic: comparison measurement and Manufacturer data	75
3.20	Comparison of physical and virtual geometry	77

3.21	Sketch of the overall computational domain	78
3.22	Grid topology around the main and splitter blades	79
3.23	Grid structure in tip gap	79
3.24	Non dimensional wall distance within the model at 50% speed normal flow conditions; Left: Hub surfaces and Rotor blades; Right: Shroud surfaces	80
3.25	Intake total pressure traverse measurements of Traverse 2 at 50% speed	81
3.26	Top: compressor characteristics in form of pressure rise and efficiency; Bottom: Diffuser inlet circumferential pressure distribution	82
3.27	Top: static pressure rise over the rotor; Bottom: Diffuser inlet circumferential pressure variation	83
3.28	Diffuser inlet circumferential pressure distribution close to recirculation	84
3.29	Sketch: Volute with key geometry features	86
3.30	pressure recovery coefficient from experimental data of two volutes	89
3.31	Comparison of the calculated compressor map with manufacturer data	90
3.32	Comparison of the calculated performance characteristics with manufacturer data	91
3.33	Overall compressor Model error as a sum of CFD and Volute model error	92
3.34	Casing pressure distribution from Experiment and Simulation at $Mu_2 = 0.65$: Compressor characteristic	93
3.35	Casing pressure distribution from Experiment and Simulation at $Mu_2 = 0.65$: Medium	94
3.36	Casing pressure distribution from Experiment and Simulation at $Mu_2 = 0.65$: High flow	95
3.37	Casing pressure distribution from Experiment and Simulation at $Mu_2 = 0.65$: Low flow	96
4.1	disk with radial blades rotating in a closed housing [20]	102
4.2	Qualitative pattern of inlet recirculation in a rotor (figure without casing): a: meridional cut b: Cross-sectional cut of the impeller inlet	102
4.3	Pitchwise averaged radial profiles in the inlet plane of the research compressor	103
4.4	Inlet casing flow visualisation: a) Measurement b) CFD	105
4.5	Critical area ratio of the research compressor compared to correlations from literature	108
4.6	Control volume rotor with mass flows going in and out during inlet recirculation	111
4.7	Predicted mass flow into the rotor relative to the mass flow going through the machine over the global flow coefficient at different rotor speeds	112

4.8	Predicted mean momentum fluxes in the recirculation flow coming out of the rotor inlet	114
4.9	Casing pressure distribution from Experiment and Simulation at $Mu_2 = 0.65$: Compressor characteristic	116
4.10	Casing pressure distribution from Experiment and Simulation at $Mu_2 = 0.65$: Clean flow	116
4.11	Casing pressure distribution from Experiment and Simulation at $Mu_2 = 0.65$: Established recirculation	117
4.12	Casing pressure distribution from Experiment and Simulation at $Mu_2 = 0.65$: Strong recirculation	117
4.13	Predicted mean momentum fluxes in the flow going into the rotor inlet . . .	118
4.14	Top: Predicted enthalpy in the recirculated mass flow exiting the rotor for different speeds ; Bottom: Predicted enthalpy in the mass flow entering the rotor for different speeds	121
5.1	Rotor and diffuser stability [$M_{u2}=0.65$]	128
5.2	Numerically obtained diffuser inlet angle for all rotor speeds	130
5.3	Numerically obtained inlet pitchwise averaged axial velocity distribution [$M_{u2}=0.65$]	131
5.4	Numerically obtained inlet pitchwise averaged axial velocity distribution for all rotor speeds	132
5.5	Compressor map with normal flow region in green and recirculation region in red	133
5.6	Measure for the part of the map which is occupied by recirculation in terms of map width W_{rc} over the tip speed Mach number	134
5.7	View into the inducer part of the compressor wheel rotating around the x-axis showing contours of constant absolute Mach number of unity just prior to inlet recirculation for a inlet tip Mach number of 0.87 in green and 0.94 in red	135
6.1	1-D Measurement planes	140
6.2	Comparison of the compressor performance in terms of total to total polytropic efficiency at different speeds from: GT - Manufacturer; SIM - Combined Model; EX - Experiment	143
6.3	Sketch of intake duct	144
6.4	Loss coefficient in the intake duct and inlet bellmouth	146
6.5	work coefficient and pressure rise over the rotor	150
6.6	polytropic total to total efficiency of the rotor	151

6.7	diffuser pressure recovery coefficient derived from the numerical model . . .	152
6.8	Volute pressure recovery coefficient	153
6.9	Meridional cut through the rotor and inlet: Inlet plane with recirculation and normal sub planes, recirculation bubble and streamline	155
6.10	Loss breakdown of the compression system at low speed of $Mu_2=0.65$; Losses stacked in the order of the legend from bottom to top	157
6.11	Loss breakdown of the compression system at low speed of $Mu_2=0.65$; Losses stacked in the order of the legend from bottom to top	158
7.1	Meridional cut through the tip gap of the research compressor with tip gap variations as dashed lines	164
7.2	Absolute size of the tip gap for the case study	165
7.3	Compressor performance	166
7.4	tip leakage mass flow as percentage of overall mass flow for different tip gap heights	168
7.5	Rotor performance and inlet casing pressure over the global flow coefficient	170
7.6	Spanwise axial velocity distributions upstream of the rotor leading edge at a rotor speed of $Mu_2=0.65$	172
7.7	"lumped" inlet recirculation loss for different tip gap heights	174
7.8	Surface stream lines on surface of constant radius 98% passage height; Left: Case B = 98.6% span ; Right: Case C = 97.5% span; Black: Point-X ; Blue: Point-Y; Red: Point-Z	175
7.9	Surface stream lines on ISO surface at 100% span; Left: Case B = 98.73% passage height; Right: Case C = 99.78% passage height; ; Black: Point-X ; Blue: Point-Y; Red: Point-Z	176
7.10	Streamlines of relative velocity for operating points X(top),Y(middle) and Z(bottom). left: Case B; right: Case C	177
7.11	Meridional cut through the machine at the rip radius showing the total to static pressure rise for Operating points: X (top), Y (middle) and Z (bottom). Positive velocity: red; Negative velocity: blue Left: Case B; Right: Case C	181
7.12	Non dimensional tip gap mass flux over non dimensional chord for the main and splitter blade for operating points X(top),Y(middle) and Z(bottom). left: Case B; right: Case C	184
7.13	Blade loading in terms of non dimensional pressure at 98% passage height for Case B (=98.6% span) as full lines and for Case C (=97.5% span) as dashed lines; Left: Main blade Right: Splitter blade; Top: Point-X ; Middle: Point-Y; Bottom: Point-Z	186

-
- 7.14 Blade loading in terms of non dimensional pressure at 96% passage height for Case B (=96.6% span) as full lines and for Case C (=95.5% span) as dashed lines; **Left:** Main blade **Right:** Splitter blade; **Top:** Point-X ; **Middle:** Point-Y; **Bottom:** Point-Z 187
- 7.15 Axial velocity field at the main and splitter passage entries for **Operating points:** X (top), Y (middle) and Z (bottom). **Positive velocity:** red; **Negative velocity:** blue **Left:** Case B; **Right:** Case C 188

List of tables

3.1	GT3776 Key performance parameters	58
3.2	Inlet bellmouth main geometry parameters	60
3.3	GT3776 Diffuser key parameters	64
3.4	Source of experimental data shown in figure 3.8	66
3.5	GT3776 Volute key parameters	67
3.6	Mean measurement planes: measured properties	69
6.1	measured thermodynamic properties	140
6.2	Intake and Inlet bellmouth loss coefficients	146
7.1	Tip gap size in absolute terms and relative to the leading edge span	165
A.1	Cole Parmer Model EW-68848-28	209

Nomenclature

Roman Symbols

0	Intake position
1	Rotor inlet position
2	diffuser inlet position
3	Volute inlet position
4	Volute outlet position
A	Area
a	Speed of sound -or- 2/4 Stroke parameter
B	Greitzer B parameter
b	Width
c	Absolute velocity
L	Length
m	Mass
n	Rotational speed
p	Pressure
R	Gas constant
r	Radius
T	Temperature

u Blade speed

V Volume

w Relative velocity

Greek Symbols

α Absolute flow angle

β Relative flow angle

λ Work coefficient

ϕ Flow coefficient

π Pressure ratio

ζ Loss coefficient

Superscripts

c Compressor

e Engine

Subscripts

a Axial -or- Outer passage location - shroud

corr Corrected

crit Critical

ex Expansion

i Inlet

i inner passage location - hub

m Meridional

o Outlet

q 1D - mean value

r Radial

SW Swept

t Tangential

vol Volumetric

Acronyms / Abbreviations

AIRS Abrupt impeller rotating stall

bf Best fit

Combined model 3D CFD model + 1D model

GT Manufacturer (Garrett)

HCV Heavy commercial vehicle

IC Internal combustion

LCV Light commercial vehicle

Low Order model 1D model

MCV Medium commercial vehicle

Numerical model 3D CFD model

PIV Particle image velocimetry

RMS Root mean square

TEIS Two elements in series

VDRS Vaneless diffuser rotating stall

Chapter 1

Introduction

Due to increasing fuel costs and more restrictive emission regulations, fuel-saving technologies are becoming increasingly important in the automotive industry. Turbocharged internal combustion (IC) engines are an effective technology to achieve higher power-to-weight ratios and efficiencies. This enables manufacturers to build downsized and down-speeded engines while keeping the same power level. The strength of this trend towards turbocharged engines can best be seen when looking at the development of the commercial vehicle market shown in **figure 1.1**. Here, the trends in terms of market size for light (LCV), medium (MCV) and heavy (HCV) commercial vehicles is shown as vehicle type 1,2 and 3. For LCV's the expected average annual market growth between 2012 and 2019 is around 10%.

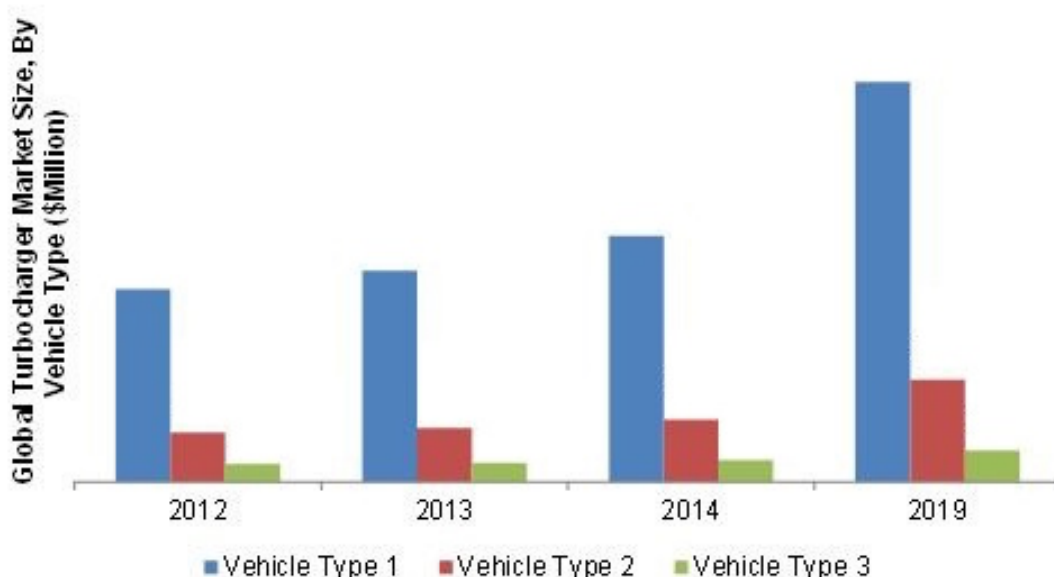


Fig. 1.1 LCV annual market growth 2012 - 2019 [31]

These growth rates are mostly due to the new technical developments in turbocharging petrol engines which, for example in Germany, are present in more than 75% of all cars on the street in 2011 [15]. Whilst turbocharging is well established in diesel engines, it is much more difficult to realise in petrol-powered IC engines. In general, a turbocharger which is well matched to an IC engine needs to satisfy two key requirements:

1. The compressor provides high pressure air over the whole operational range of the IC engine and therefore needs a wide operating range itself.
2. For good acceleration of the IC engine, the compressor has to provide high pressure air ideally from engine startup. This is limited by the compressor transient speed behaviour which is determined by rotor inertia and off-design performance. This is commonly known as the turbo lag.

These requirements can be better explained in **figure 1.2** which shows an IC engine characteristic drawn in compressor map coordinates. For better understanding, a compressor map is shown in thin dashed lines, but will not be explained in detail here. In order to plot the IC engine characteristics in terms of compressor corrected mass flow and pressure rise, it is necessary to convert engine behaviour into the same dimensions. IC engines are positive displacement devices, where air mass flow is proportional to the product of engine speed, swept volume, inlet manifold density and volumetric efficiency. Furthermore, the compressor is mounted to the engine inlet. Compressor and engine inlet mass flow as well as compressor outlet pressure and engine inlet pressure are thus nearly the same. These correlations lead to **equation 1.1** which gives an almost linear relationship between pressure ratio and compressor corrected mass flow for constant IC engine speeds.

$$\pi^c = \frac{p_o^c}{p_i^c} \approx \frac{p_i^e}{p_i^c} = \dot{V}_i^c \frac{T_i^e}{T_i^c} \frac{a}{V_{sw} \eta_{vol} n^e} = \dot{m}_{corr}^c \frac{T_i^e}{\sqrt{T_{ti}^c}} \frac{R^c a}{V_{sw} \eta_{vol} n^e} \quad (1.1)$$

$$2 - \text{strokeengine} : a = 1 \quad (1.2)$$

$$4 - \text{strokeengine} : a = 2 \quad (1.3)$$

Based on equation 1.1, the IC engine characteristic can be plotted into figure 1.2 as an array of constant engine speed lines. Those are displayed in bold blue. In order to obtain a better understanding for in-operation behaviour, a representative working line of a Turbocharger compressor is plotted in the diagram in red. In the low-speed region, the dashed red line represents the ideal working line based on the demands of the IC engine while the full red line represents the working line accessible by the turbocharger. Generally,

the working line can be divided into two sections, a and b, which will be discussed separately.

Section a represents a drive-away process of the vehicle, where engine load is continuously increased at constant engine speed as more fuel is injected. Engine efficiency is assumed to be constant during the process which continuously raises the exhaust temperature and makes more power available to the turbine. The Turbocharger can then speed up, which gives more power to the compressor. The latter can provide higher pressure and thus density to the engine. From an IC engine point of view, high pressure air should be available immediately at its inlet. Section a would then be reduced to the vertical part of the ideal working line shown in dashed red. In reality, the transition speed through the Turbocharger acceleration process strongly depends on rotor inertia and the power balance between turbine and compressor. Consequently, high compressor efficiency in the low speed, low-flow region is a crucial factor for good transient behaviour.

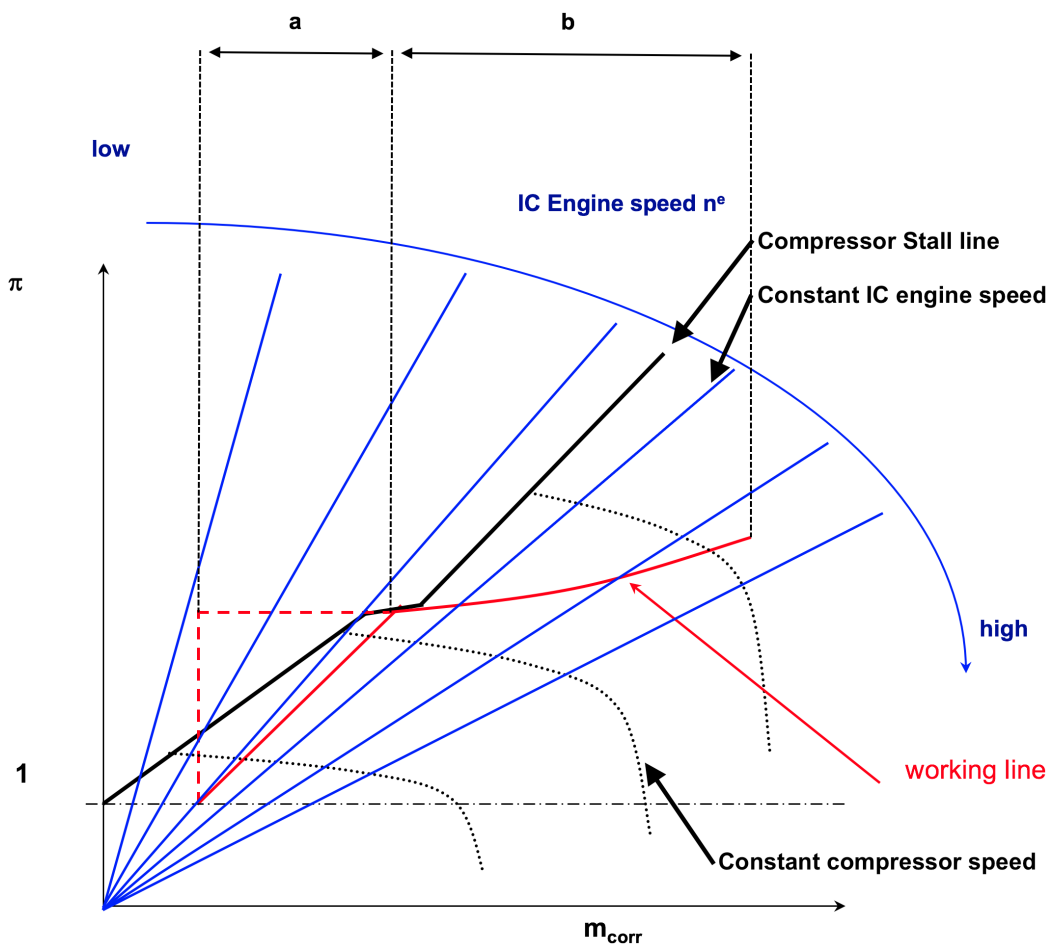


Fig. 1.2 IC engine characteristic and compressor working line [4]

In **section b**, the engine has reached the torque level required to accelerate the car and starts speeding up under constant load conditions. With the assumption of constant volumetric efficiency of the IC engine, mass flow increases almost linearly with increasing engine speed. An increased mass flow leads to more power available on the turbine side. The Turbocharger can speed up and increase compressor delivery pressure. This is represented in section b as a slight positive slope, as the compressor outlet pressure rises with increasing impeller speed.

Figure 1.1 shows that the IC engine and the compressor work well together as long as the operating point does not drop out of the compressor map boundaries. It is thus the compressor that restricts the operational range of the engine. Besides choking, which limits high IC engine speed, in-service behaviour of the drive train is particularly affected by the low-flow, part-speed region, reducing the theoretically available range of the IC engine. From an IC engine point of view, the constant load working line would extend along the horizontal part of the ideal working line in section a and obtain an ideal range of section a and b together. Based on this example, it becomes clear that the compressor is one of the bottlenecks for good vehicle drivetrain performance. In order to overcome the limitations outlined above, different charging techniques for improved matching have been developed.

One approach to reduce the turbo lag is to use a mechanically driven supercharger which is directly connected to the engine crank shaft. The mechanical connection enables it to provide dense air over the whole operational range of the engine. Transient problems in the low-speed region do not occur since power is provided directly by the IC engine. Although the mechanical connection is beneficial for operation, it also means that a significant amount of shaft energy is consumed by the supercharger. In terms of overall efficiency, this technique is thus not beneficial since energy that has already been made accessible is redirected back into the engine. In comparison, turbochargers are driven by the remaining energy in the exhaust gas, the blow down energy. This energy normally is wasted. The presence of the turbocharger turbine in the exhaust increases the IC engine back pressure and consequently leads to a reduction in power. However, this penalty is compensated by the increased IC engine inlet pressure provided by the compressor side of the turbocharger. Due to the ability of making use of wasted energy, turbochargers improve overall efficiency.

Another innovative technique is pressure wave charging (Hyprex) which is based on the principle of pressure wave reflection. A Hyprex consists of a cylindrical engine driven rotor that splits into several passages which are open at both ends. One end is connected to the intake, the other to the outtake of the engine. The oncoming exhaust pressure waves and intake suction waves interact in the rotor. They are timed so that the exhaust pressure wave

compresses the intake air while the intake suction wave expands the exhaust gas. Although this technique has several advantages - it does not suffer from transient problems, and has a wide operating range, for instance - it still has not yet been developed to a maturity phase. The main reason for this is because of the sensitive timing of the intake and outlet waves, which is essential to getting this method to work. Even small changes in thermodynamic conditions, such as pressure variations at the inlet, can cause the system to fail as those parameters affect the pressure wave propagation speed within the Hyprex passages. As a result, the wave propagation is not synchronised with the opening times of the passage inlets and outlets. Failure then means that the Hyprex does not provide compressed fresh air to the IC engine inlet, instead it releases a mix of fresh air and exhaust gas or even pure exhaust gas.

Advancements in bearing technology, electric motor development and electric energy storage allowed the realisation of electrically driven turbo compressors. High power electric motors are used in these machines. Although they have the capability to spin a turbo compressor at sufficiently high speed and power levels to provide the pressure rise needed for IC engine applications, the electric motors suffer from cooling problems. As a consequence, electrically driven turbo compressors cannot be operated continuously at the current state of development. Operation times of less than a minute have been achieved in experiments representative for commercial automotive applications. Whilst not sufficient for continuous operation, the operation time could still be sufficient to bridge the turbo lag in an application where the electric turbo compressor is put in sequence with a turbo charger. Setups in sequence with a turbo charger are used in recent formula one cars. However, this technology has not reached the commercial market yet due to high cost and complexity.

By far the most successful technique to increase inlet air density is turbocharging, where different setups are used to match with the IC engine. Single turbochargers with casing treatment on the compressor side are state of the art and can be found in almost all modern diesel engines. The basic idea behind casing treatment is that reduced incidence at low flow rates stabilises the impeller and prevents it from developing instabilities. Therefore a fraction of the main flow is bled off from the impeller and injected upstream of the leading edge. A meridional cut through such a machine is shown in the upper part of **figure 1.3**. In the casing, a bleed channel connects the inlet and the inducer around the whole radius. One end is located upstream of the main blade leading edge of the impeller. The other is provided downstream of it. The exact position of the slots can vary and influence bleed flow behaviour. The flow direction through the bleed channel is determined by the static pressure difference between its ends. The upstream end is located in the intake of the compressor and

can be assumed to have constant ambient pressure. As a consequence, bleed flow direction is determined by the static wall pressure of the downstream end. Static wall pressure is plotted over the meridional distance through the machine in the lower diagram of figure 1.3. The pressure is plotted for three different operating points.

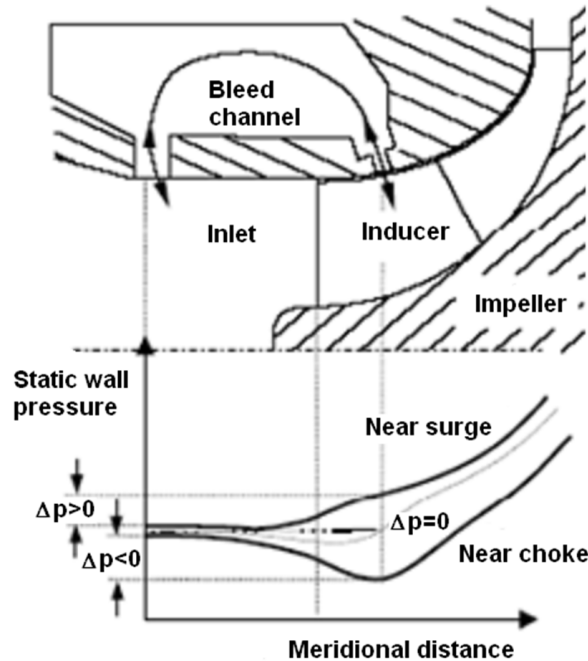


Fig. 1.3 Compressor with casing treatment: casing pressure distribution [4]

The thin grey line in the middle represents pressure at design condition. Here, the pressure difference between the bleed channel ends is close to zero and no flow is bypassed through it. Normally choking at the inlet limits the maximum swallowing capacity of a well designed machine. Near this point, the inducer acts as a nozzle and the static pressure at the downstream slot drops below the inlet value, as can be seen in the lower bold black line of the graph. The pressure difference lets additional flow go through the bleed channel into the impeller. As a result, the bleed system increases the swallowing capacity of the machine as an additional flow portion is diverted around the choked inlet.

For near-stall conditions, blade loading is shifted closer to the front of the impeller. This leads to a change in static pressure distribution as shown in the upper bold line. In the region between the leading edge and the downstream bleed slot, much more pressure rise is generated. This leads to a higher wall pressure at the bleed channel slot than in the region upstream of the impeller. The pressure difference forces flow to recirculate back upstream of the impeller inlet. There, it increases the mass flow seen by the impeller inlet and therefore reduces incidence. Then, the compressor can be operated at overall mass flows that are much

lower than without the bleed channel. In terms of operating range, this means that casing treatment is beneficial at both limiting criterions. It moves choke to higher flow rates and shifts stall towards more reduced mass flows.

The beneficial effects of casing treatment are outlined in **figure 1.4** which provides a scheme of the operating limit of a standard compressor marked as a full black line and the limit with casing treatment indicated as dashed black line. The graph shows that casing treatment largely improves the stall margin in the high-speed region. However, the map width enhancement capabilities of the bleed slot rapidly drop to zero in the low-speed region. This means that casing treatment loses its benefits for wider range exactly in the region which is most important for transient behaviour. A full explanation as to why the low-speed region does not benefit from a bleed system has not yet been found. One of the mechanisms which has been suggested is the too small pressure difference between the ends of the bleed slot which is insufficient to drive the flow through the channel.

Despite its ineffectiveness in the low-speed, low-flow region, which is most important for good transient behaviour, compressors with casing treatment do not produce a sufficiently wide map for petrol engines since the mass flow variation through such an IC engine is about 1.5 times larger than in diesel engines. This means that the operating range of a petrol engine cannot be covered with one single compressor at the moment.

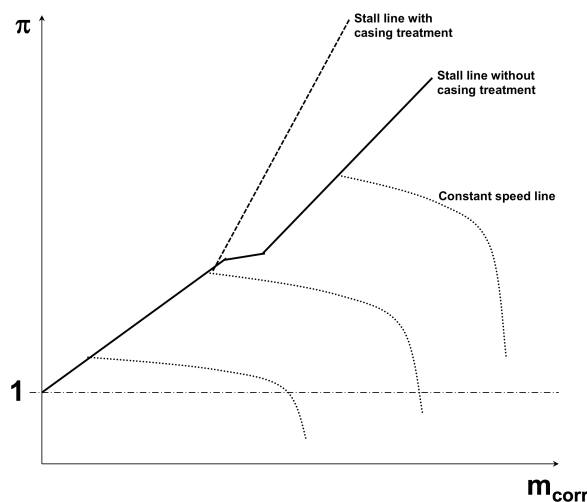


Fig. 1.4 Compressor map for a compressor with and without casing treatment

In order to compensate for the limited operating range of single stage compressors, different multi-stage charging concepts have been developed. An example is shown in **figure 1.5**. A small and a large compressor are combined in series to create a so-called sequential turbocharging concept. The figure here shows two turbochargers combined, but the smaller engine can also be replaced with a supercharger. At low engine speeds, the smaller unit is

operative and provides pressure rise. Because of its small size, the device features low inertia and thus provides good transient behaviour. At high engine speeds, the small compressor's swallowing capacity is reached and the system switches to the bigger unit which covers the rest of the engine characteristic. Sequential turbocharging currently is applied in premium gasoline-driven cars. Due to its complexity, the concept is costly and consequently difficult to apply to cheaper cars with high part numbers.

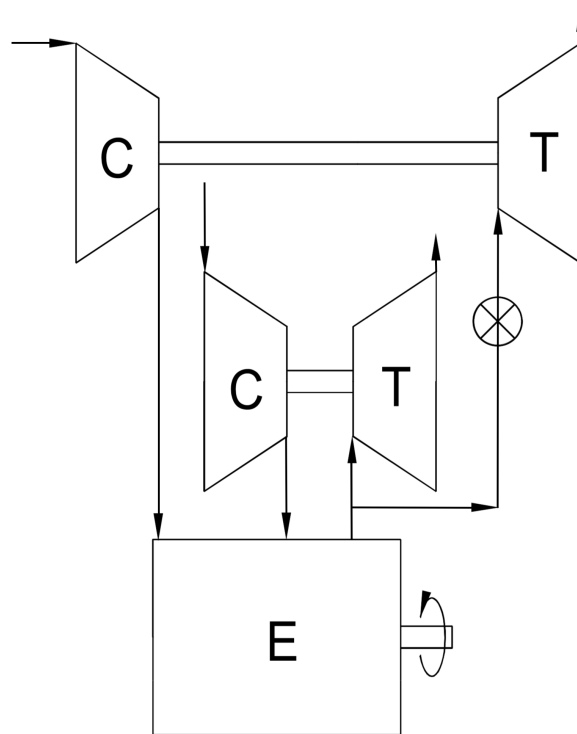


Fig. 1.5 Sequential charging concept: serial turbochargers

1.1 Scope of work

The complexity and cost of state-of-the-art solutions to charge a petrol-fired IC engine raise the question of whether a single turbocharger compressor stage can be further improved. In order to address this question, it is necessary to clarify the requirements for such a machine first. When looking at the design requirements of turbochargers, those changed significantly over time.

Turbochargers were first applied to larger scale diesel engines in shipping, trains and lorries. In all these applications, the engines are designed to operate most efficiently around one single operating point equivalent to cruise conditions during a long distance drive, where it is used most of the time during a load cycle. Looking at the working line of the IC engine shown in figure 1.2, this load cycle translates into one single point centred on the middle of section b. As a result, compressors for these applications are designed to provide good peak efficiency around this operating point.

Later, turbochargers were adapted to small, diesel-driven passenger vehicles. These have a different load cycle, since the machines get used more in inner city traffic. Consequently the engine has to operate in a broader range of operating points corresponding to section b in figure 1.2. Section b of the working line can be approximated to one single compressor speed, its design speed. For such an application, the compressor is thus designed for good performance over the whole map width at design speed at the cost of peak efficiency.

Because of the changed load cycle for passenger cars, the acceleration process, which happens more frequently in inner city operation, becomes more important for passenger cars too. The operating conditions correspond to section a of the working line in figure 1.2. The most recent change in compressor design requirements is thus an increased importance of performance at low speed and low-flow.

From the change in application comes a change in areas of interest for the compressor designer. Most optimisation work used to be done for design conditions and the behaviour there is well understood. As outlined above, modern passenger car turbochargers have to provide good performance over varying flow coefficients and speeds so that the compressor has to function at off-design conditions where the flow behaves differently.

Under low-flow conditions at part speed, the most dominant flow feature is inlet recirculation, a stable flow pattern which occurs at the inlet of the rotor. **Figure 1.6** shows a sketch of a radial compressor rotor at an operating point with inlet recirculation. The sketch on the left shows a meridional cut plane. On this plane, surface streamlines of the recirculating flow are shown in red. These occupy the shroud region of the rotor inlet as well as the shroud region in the inducer part of the impeller blocking off a part of the rotor span. They

cause the oncoming flow, displayed as black surface stream lines, to be diverted towards the hub section of the rotor. In this region the flow path is not blocked so that the fluid can proceed towards the rotor exit and the machine remains functional. The right side of figure 1.6 shows a cut perpendicular to the rotational axis through the inlet of the machine just upstream of the impeller leading edge. Here, the recirculation region is marked in red. The phenomenon is present around the whole annulus and appears to be stable. This makes it possible for the compressor to operate under these flow conditions without being exposed to strong vibrations and material stress due to annular flow non-uniformities. As the flow in the recirculation region is fed from the rotor into the inlet, it carries a strong positive swirl component, indicated by green arrows in the sketch.

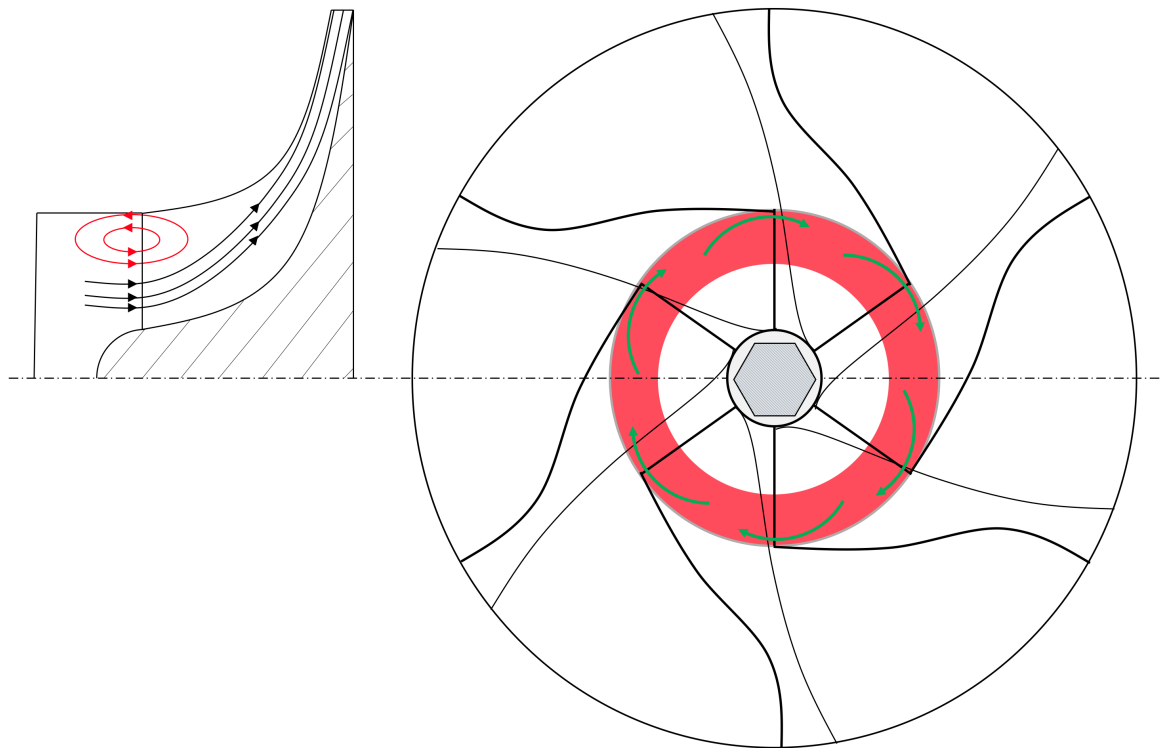


Fig. 1.6 Sketch of a compressor wheel with recirculation flow pattern

Whilst the phenomenon of inlet recirculation has been known for a long time, particularly in hydraulic pumping devices, it is not very well-understood. Prior investigations have revealed the general flow structure of the phenomenon as outlined above [37] and a significant amount of loss has been related to it [43]. Furthermore attempts to depict inlet recirculation in reduced order models have been made but a sufficient method remains undiscovered [23]. Detailed investigations into the three dimensional flow structure of inlet recirculation have not been carried out until now. Studies about design parameters are very scarce and limited

to the use of inlet guide vanes.

This work increases the understanding of inlet recirculation as a dominant feature in the part speed low-flow region of radial compressors with the scope on improving performance of automotive turbocharger compressors, more specifically their range and transient behaviour. Therefore, the following research questions have been raised:

- 1. Under which conditions does inlet recirculation occur?**
- 2. What are its effects on compressor performance in terms of energetic cost?**
- 3. How can inlet recirculation be accounted for in preliminary design?**
- 4. How can a designer influence the mechanisms sustaining recirculation?**

In order to answer these questions, an automotive turbocharger compressor has been investigated alongside experiments and numerical simulations.

Chapter 2

Compressor low flow behaviour

2.1 Introduction

This chapter provides an overview about the state-of-the-art of knowledge regarding compressor low flow behaviour. A description about the instabilities in a compression system is provided. Furthermore, a brief discussion about the change in component matching of a compression system with rotor speed is presented, which shows how this effect can influence the location of origin of compressor instabilities. In order to increase understanding, clear definitions of terms describing low flow phenomena are included. Subsequently, a more detailed discussion about the general low flow behaviour of radial compressor rotors is provided and particular information about the phenomenon of inlet recirculation is outlined. Finally, the state-of-the-art knowledge about the phenomenon of inlet recirculation is presented and put in perspective with other low flow phenomena and a connection back to the general research framework presented in section 1.1 is made.

2.2 Compressor instability

When thinking about operation of a compressor at low flow coefficients, machine behaviour is different from at design conditions due to the presence of different flow phenomena. A clear line can be drawn between conditions where stable operation is possible and those where the machine cannot be operated due to periodic disturbances. These disturbances cause the mass flow through the machine to reverse either locally or reverse fully. Mass flow fluctuations going along with flow reversal are known as the surge cycle. It induces periodic changes in the loading and thus stresses the material. Depending on the intensity of the surge cycle, **Greitzer [18]** distinguished between two types of cycles: mild surge and deep surge. Both phenomena can best be explained based on a pressure rise characteristic with its limiting stability throttle line as shown in **figure 2.1**.

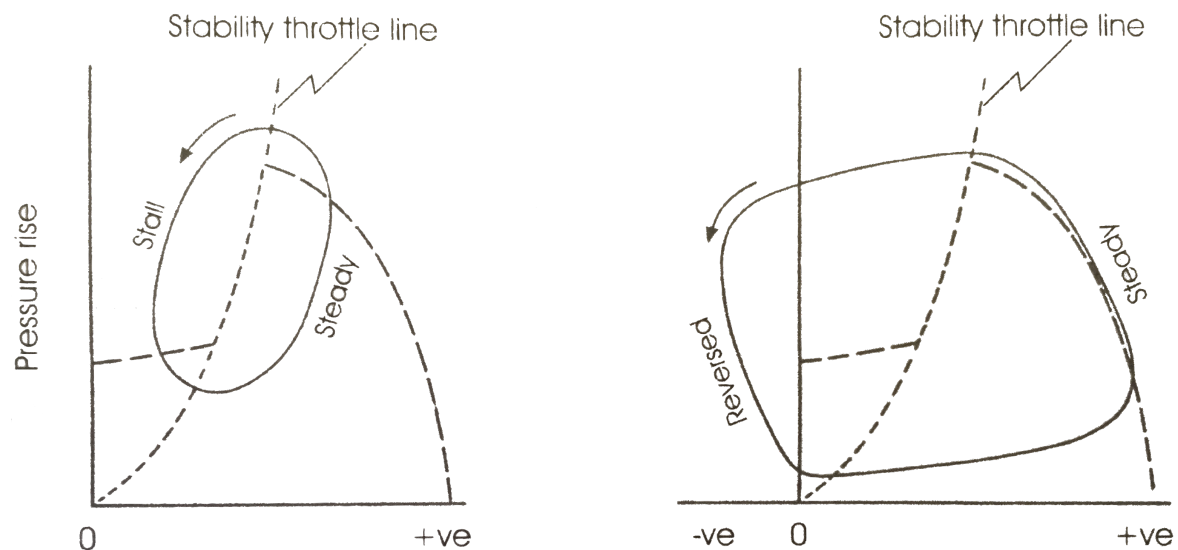


Fig. 2.1 Classification of surge cycles. Left: Mild Surge ; Right: Deep Surge [18]

The left hand graph shows a mild surge cycle. There, a mass flow fluctuation is present, but the magnitude of the resulting hysteresis loop is smaller than the absolute mass flow going through the machine so that there is still flow passing through the machine. This is the case for example in compressors with small attached plenum volumes.

The right hand graph shows a deep surge cycle. Here, the mass flow fluctuation is so big that it results in a complete mass flow reversal. Deep surge occurs for example in compressors which are attached to large plenum volumes.

Greitzer provides a simple model to estimate the type of surge cycle where the compression system is regarded as a simple mass-spring-damper model as shown in **figure 2.2**.

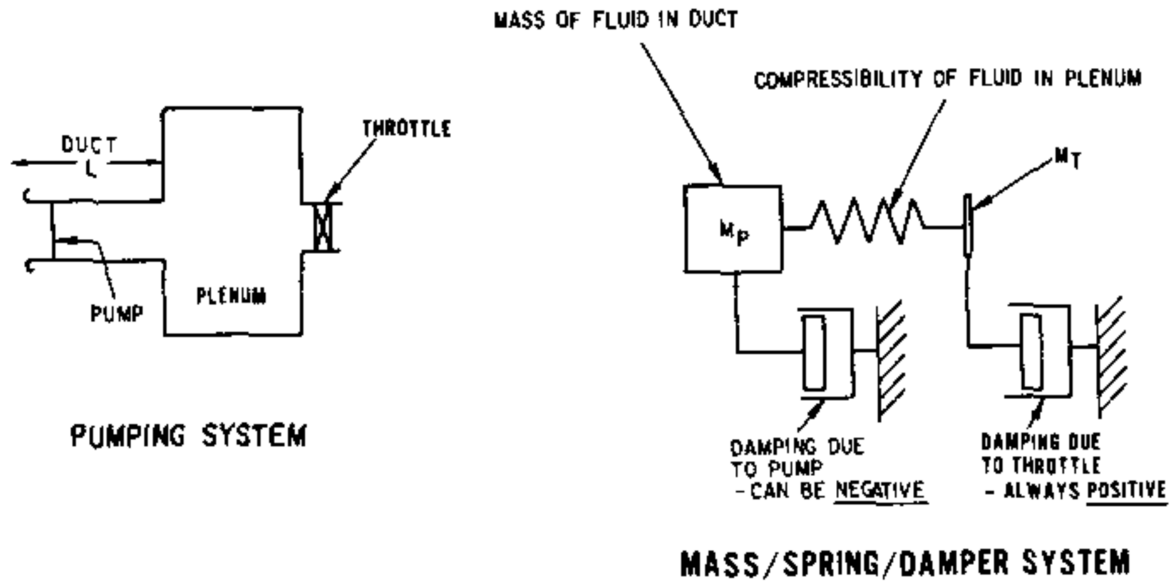


Fig. 2.2 Simplified model of a compression system as a mass-spring-damper system [19]

The left hand side shows a simplified compression system consisting of a pump attached to a duct with a cross-sectional area A and a specific length L , a plenum Volume V and a downstream throttle.

On the right hand side, the corresponding mass-spring-damper model is shown. In this system, the mass represents the fluid in the duct, the spring represents the compressible fluid in the plenum and the downstream throttle is represented by a damper with a positive damping coefficient in series with the spring. The pump itself is represented by a damper which is parallel to the spring. This damper offers the special feature of a negative damping coefficient corresponding to an energy input into the system. Greitzer proposed a parameter B based on this model which is presented in **equation 2.1**. It allows to give an estimate about the type of instability to expect, taking into account the above mentioned geometrical features of the model as well as the speed of sound a and the blade speed u . In the equation, the parameter A_c represents the compressor flow through area and the parameter L_c represents the effective length of the compressor duct.

$$B = \frac{u_{tip}}{2a} \sqrt{\frac{V}{A_c L_c}} = \frac{M_{tip}}{2} \sqrt{\frac{V}{A_c L_c}} \quad (2.1)$$

For high values of B , the compressor is most likely to deep surge. This is the case, when large plenum volumes are connected to compressors with high blade speeds via short, low area ducts.

Low values of B indicate a system where mild surge occurs. Here, small plenum volumes are connected to low blade speed compressors via long large area ducts.

The transient region between both mechanisms has been found for values of B around one but it strongly depends on the individual compression system, particularly its geometry. From equation 2.1, it can be seen that B changes with the rotor tip speed, respectively the tip speed Mach number. A compression system operating at high speeds is thus more likely to go into deep surge directly, whereas the same system tends to experience mild surge at low speeds. It has been observed that pumps and low speed fans do not go into deep surge at all but can be operated down to zero mass flow although they suffer from huge separations and rotating stall [6].

For turbocharger compressors, which are attached to relatively small plenum volumes, the parameter B changes a lot due to the huge variation in impeller speeds. It can thus be inferred that a turbocharger compressor is likely to have a shift in instability mechanism along the surge line.

Casey and Robinson [6] describe that for high speeds, instabilities occur at the point of peak-pressure-rise in the characteristics whereas for low speeds, the compressor operated at mass flows lower than peak-pressure-rise. They assume that at speeds much lower than design speed and very low flow coefficients, the impeller inlet experiences inlet recirculation, which could be a result of part span stall. Examples for the presence of inlet recirculation under these conditions were provided by Harley [22], who conducted a numerical study and by Gancedo [17], who worked experimentally using particle image velocimetry (PIV).

These observations raise the question whether a radial compressor develops a rotating stall flow pattern or whether inlet recirculation occurs instead, leading to deep surge directly when throttled to lower flow rates. One conclusion is that for small values of B , the likelihood of inlet recirculation is highest.

2.3 Compressor component matching

Instabilities can occur in different parts of the compressor. In the case of an automotive turbocharger, the compressor consists of three main components, the rotor, the vane-less diffuser and the volute. Each of these components has a certain characteristics itself and they are matched by the designer to obtain the desired overall characteristics. Each part also has an individual operation limit and can fail. Consequently it has to be discussed how and when these components destabilise and whether the matching changes with operating point.

The most simple part to discuss in this context is the volute which is not known to become unstable itself. However, it features strong variations in performance. The most influence of a volute on compressor performance is the strong circumferential variation in pressure occurring at off design as shown in **figure 2.3** which presents experimental data from Sideris. The figure shows the static pressure distribution around the circumference of an automotive turbocharger diffuser at inlet and outlet for different operating points. The middle graph shows design conditions where only a small pressure variation is present. For flow rates smaller than design like in the top graph, the static pressure around the tongue at 90 degrees shows a 20% lower pressure than the average pressure implying high volute inlet angles and a very tangential flow. At high mass flow rates, as shown in the bottom graph, the tongue region shows a 35% higher pressure which is due to the small volute inlet angle and the blockage caused by the tongue. Sideris furthermore shows that these variations are also present at the diffuser inlet, causing a low static pressure region around the position of the tongue for low flow coefficients and a high pressure region for high flow coefficients. Gancedo [17] investigated an automotive turbocharger compressor with a ported shroud experimentally. He conducted PIV measurements at the rotor inlet and observed that the asymmetry in annular flow distribution caused by the volute can still be present upstream of the impeller. This was particularly the case when recirculation was present, meaning at low flow conditions. As recirculation means that the flow from the downstream parts of the machine reverses back upstream along the shroud, the upstream influence of the volute should be most visible in the region where the recirculation is present. This is exactly what can be seen in Gancedo's results which show that the annular non-uniformity is propagated not only through the impeller eye but even more pronounced through the bypass port in the casing.

The volute induced circumferential asymmetry imposed on the diffuser and the impeller cause those parts to operate at different operating points periodically during a rotation depending on the relative position to the tongue. It is this effect which deteriorates the stability of the diffuser and the impeller, both parts of the machine which can be the source of instabilities.

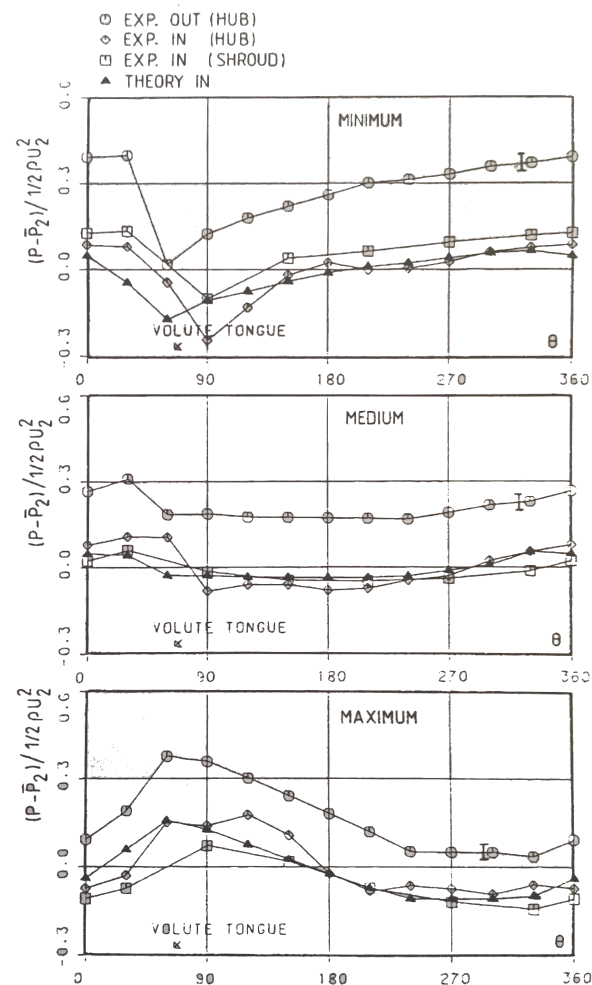


Fig. 2.3 Circumferential variation of static pressure at the inlet and outlet of a vane-less diffuser of a turbocharger compressor operating at minimum, optimum and maximum mass flow [41]

The matching of the rotor and the diffuser changes significantly due to Mach number effects causing a change in density, respectively volume flow at the rotor outlet. Casey and Robinson [5] give a comprehensive explanation for the shift in matching based on the diffuser inlet flow angle α_2 which determines the diffuser operating point. They present **equation 2.2** which expresses this angle as a function of the work coefficient and the rotor outlet flow coefficient.

$$\tan\alpha_2 = \frac{c_{u2}}{c_{m2}} = \frac{c_{u2}}{u_2} \frac{u_2}{c_{m2}} = \frac{\lambda}{\phi_2} \quad (2.2)$$

Casey and Robinson give the following example to understand the Mach number effect on matching. They describe the situation where the Mach number increases at a constant inlet flow coefficient. In this situation, the density change causes an increase in work coefficient and a decrease in rotor outlet flow coefficient resulting in an increase of diffuser inlet angle. As a result, the diffuser operates under conditions with higher swirling flow and closer to its stability limit. When operated at rotational speeds lower than design, the diffuser sees a lower swirling flow and thus operates at conditions higher than its design flow coefficient. In terms of instability, this implies that the location where instabilities initiate can change from the rotor to the diffuser and vice versa due to a change in component matching in the compressor when operated at different speeds.

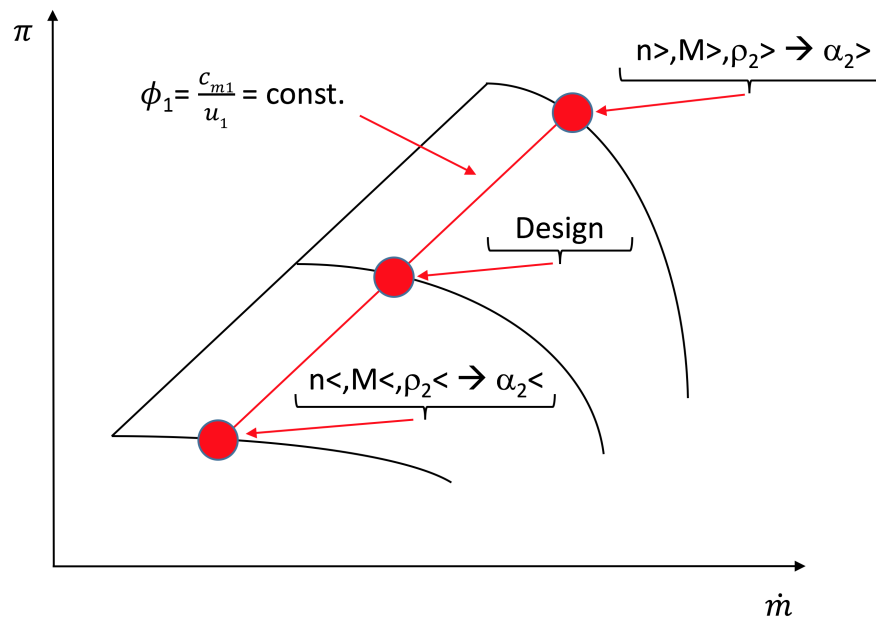


Fig. 2.4 Mach number effect on the component matching

Figure 2.4 shows the sketch of a compressor map with a line of constant inlet flow coefficient drawn into it. The design point is set on the middle speed line and the components are matched.

If the compressor now operates at higher rotational speeds, this means that the diffuser will operate at a larger angle making it more likely to cause instabilities due to longer flow paths, thicker boundary layers and earlier separation.

In the opposite case, the diffuser is pushed towards lower inlet angles and thus operates stably. Consequently it is more likely for the diffuser to fail at high rotational speeds than at low speeds, assuming the components were matched for medium speed.

In terms of instabilities in the diffuser, those originate from local return flow which is most

likely to occur in the boundary layer. However, the dynamic characteristics depend on the inviscid part of the flow [16].

For the low speed and low flow region of a compressor map, the matching behaviour outlined above means that the occurring instabilities most likely originate from the rotor whilst diffuser operation is stable.

2.4 A definition of compressor low flow phenomena

In order to clarify the difference between the terms introduced in the previous section, a brief overview of definitions for what is described by low flow phenomena such as Stall, Spike type stall, Modal Stall, Rotating Stall, Recirculation and Surge is provided in this section.

2.4.1 Stall

Stall is a term which is used in aerodynamics and aviation to describe the loss of performance due to flow separation. On an airfoil, this means the loss of lift due to suction side separation under high angles of attack for example. In a turbomachine rotor or bladed diffuser, stall means the loss in blade loading at high incidence. In case of a vane-less diffuser, stall describes the loss in ability to recover pressure due to for example flow separation on the diffuser walls and the aerodynamic reduction in outlet area.

The different usages show that the term stall is not bound to any geometry. As a result, it can be used to describe the loss of performance on a whole machine, a blade or only a specific region of the airfoil. It also means that for example one blade row or a specific blade can be stalled whilst the rest of the machine still remains functional.

In turbomachinery, specific terms have been established to separate different types of stall, depending on the origin of the separation and on whether only parts of the machine are affected or the whole machine loses its performance. So far, two separate stall inception mechanisms have been identified which both lead to separated regions of flow that propagate around the annulus. The resulting flow pattern is called rotating stall.

2.4.2 Modal stall inception

Moore and Greitzer [32] described how a compressor can fail due to the gradual build up of long length-scale mass flow perturbations in the pumping system which start to occur when the machine is throttled to low flow conditions. Those perturbations are called **modal oscillations** and were found to have different wavelengths. The first order mode corresponds to one circumference of the compressor. Higher order modes can also occur with wavelengths equal to half the circumference or equally smaller portions of it.

Modal oscillations are always present in a compressor. When destabilised, those modal oscillations start to grow first linearly but then exponentially. The perturbations eventually lead to the development of a local stall cell which has been found to originate from either the hub or the tip of a blade. At the tip of the blade, it was found that a spike like stall inception is triggered due to the modal perturbation, see spike type stall below.

The transition from the mass flow perturbations to a stall cell is gradual and not abrupt. This behaviour is generally known as modal stall inception. Because modal stall inception is a phenomenon which involves the whole compressor, its inception is not confined to one single passage but was found to lead to stall cells the size of several passages. Because of their size, the propagation speed of these stall cells around the annulus is comparatively low at less than 50% of the rotor speed for low speed compressors.

In general, the rotational speed of a stall cell depends on the inertia of the flow. As a result, larger stall cells rotate at a lower speed. In case of turbocharger compressors, large stall cells tend to develop which consequently travel at low speeds.

2.4.3 Spike type stall inception

Another stall inception mechanism which can occur in a rotor blade row has been described by Camp and Day [3]. When the compressor is throttled to low flow conditions, a short length-scale disturbance, a spike, occurs on a single blade and quickly evolves into a stall cell which then propagates around the annulus. It has been found that the propagation speed of this kind of stall cell is around 70 to 80% of the rotor speed in a low speed compressor initially. The higher propagation speed, compared to a modal stall cell derives from the smaller size of the spike induced stall cell. As stall cells originating from this inception mechanism quickly develop into cells with a size similar to the ones originating from modal stall inception, their propagation speed eventually decreases and becomes as slow.

2.4.4 Rotating Stall

Both of the inception mechanisms described above lead to separated regions of flow which propagate around the annulus. This behaviour is called rotating stall. The development of these stall cells from the initial disturbance normally takes about five rotor revolutions [10]. As mentioned above, the pattern of these disturbances as well as their propagation speed is different depending on the type of stall inception mechanism. Generally, a distinction between **part span stall** and **full span stall** cells is made. A part span stall cell only occupies a part of the span, usually around the tip, where the lower part of the blade remains functional. This is more likely to happen in high aspect ratio blade rows like in the first stages of a multi stage compressor. Full span stall occupies the whole blade passage.

In terms of the inception mechanism, modal stall is more likely to lead to full span stall as it causes mass flow perturbations in the whole annulus.

Spike type stall is localised to the tip of a blade and consequently is more likely to lead to part span stall.

Corresponding to the amount of blockage induced by the stall cells, part span stall goes along with a much smaller drop in pressure rise capability of the compressor than full span stall which shows a large drop in pressure rise on the characteristic. The same logic applies to the induced flow unsteadiness, making full span stall much more critical for the engine integrity as it induces stronger stresses to the material.

Regarding the number of stall cells present around the annulus of a blade row, part span stall always leads to more than one stall cell. Those stall cells are always equally distributed around the annulus.

Full span stall normally results in one big stall cell but in rare cases, multiple full span stall cells have been reported [9]. Those were not evenly distributed around the annulus.

The size of the stall cell also correlates with their propagation speed around the annulus. As mentioned above, part span stall cells were found to propagate at around 70 to 80% of the rotor speed whereas full span stall cells are travelling at lower speeds of around 30 to 50% rotor speed.

This means that the smaller the stall cell and thus the fewer blade passages involved, the quicker it propagates around the annulus.

2.4.5 Surge

Surge is the description of compressor instability from a system dynamic point of view. It leads to the characteristic mass flow oscillations in form of a hysteresis loop as shown in figure 2.1 which were described by Greitzer [18]. These oscillations cause strong variations in loading in the mechanical components of a compressor which can quickly lead to failure of the machine.

Depending on the type of compression system and its operating speed, the intensity of the surge cycle is variable, as described by Greitzer [18] and outlined in more detail in the first section of this chapter. Mild surge describes a partial flow reversal which occurs for example when rotating stall has been established. Under rotating stall, parts of the machine lose their pressure rise capabilities and the mass flow can reverse in these regions. Consequently, the expressions rotating stall and mild surge are very closely related. When rotating stall occurs, the compression system will experience mild surge as a consequence. On the other hand, mild surge can occur from other reasons than rotating stall.

A clear connection between stall and surge can be made regarding the intensity of mass flow fluctuations. Part span stall goes along with small stalled regions and as a result causes small mass flow fluctuations. It is described as mild surge from the system dynamics point of view. Full span stall would still be described as mild surge as it would cause higher mass flow oscillations but no full flow reversal. Only when the mass flow oscillations are strong enough

to cause negative mass flows through the machine, see the right side graph in figure 2.1, the expression deep surge is used. This state normally is reached when a compressor is throttled to very low flow conditions. When a compressor with developed rotating stall pattern is throttled to even lower flow conditions, the stalled regions, and consequently the stall cells, grow in size until eventually these regions are so big that the compressor itself cannot maintain its pressure rise capabilities and fails so that full mass flow reversal takes place.

A more clear distinction between rotating stall and surge can be given based on a dimensional comparison. Surge is a one dimensional phenomenon. It occurs in the meridional direction of the flow and does not feature any circumferential variations. Rotating stall on the other hand is a two dimensional phenomenon as it is caused by circumferential variations which lead to mass flow fluctuations [13].

In terms of the frequencies of the fluctuations caused by the phenomena, the surge frequency is orders of magnitude lower than the frequency of rotating stall [18].

On a more general note, surge can be seen as an instability of the overall compression system whereas stall is an instability of the compressor, which itself represents only a component of the compression system.

2.4.6 Inlet recirculation

Another flow pattern which can occur under low flow conditions and thus in the regime of the phenomena described above is inlet recirculation. This flow pattern has been explored only to a limited extent and very little is known about it.

This section intends to put the phenomenon of inlet recirculation into perspective to stall, rotating stall and surge. A detailed summary of what is known about inlet recirculation and its features is given in **section 2.5.1**.

Inlet recirculation is a flow pattern which is mostly axisymmetric as it builds up a ring of blockage around the whole annulus of the rotor inlet, affecting all blade passages. Small fluctuations around the annulus are present due to the potential field of the blades. It can occur in a variety of machines, particularly radial compressors and pumps. It occurs when a machine is throttled to low flow conditions at part speed and as a result happens under similar conditions to rotating stall. Inlet recirculation is located in the tip region of the rotor leading edge. This means that it occurs in the same location as spike type stall.

Nothing is known about the inception mechanisms of inlet recirculation and potential differences to spike type stall inception. However, a clear difference between inlet recirculation and rotating stall can be outlined.

As described above, rotating stall describes a finite number of stall cells which rotate around

the annulus, resulting in a non axisymmetric flow pattern. Inlet recirculation on the other hand is an axisymmetric flow pattern which occupies the whole annulus. As a result, recirculation could also be described with axisymmetric stall. It could furthermore be said that inlet recirculation represents an alternative flow pattern to rotating stall.

Because inlet recirculation is axisymmetric, the mass flow fluctuations which occur when the phenomenon is present are much smaller and the compressor can continue to operate.

This is a significant difference to rotating stall which is potentially fatal for the mechanical integrity of the machine due to strong mass flow fluctuations and the resulting additional stresses in the material.

When a compressor with inlet recirculation is throttled to even lower flow rates, it eventually surges just like a compressor which shows rotating stall.

2.5 Low flow behaviour of radial compressor rotors

In the first two sections of this chapter, a general estimate about the type and location of instabilities within an automotive turbocharger compressor has been given. It has been shown that the compressor is prone to stall type instabilities for low speeds and that those most likely originate from the rotor. The flow structure in the rotor itself is more complex than for example in an axial machine due to the meridional curvature of the passage, particularly in the exducer. One example is the jet wake structure of the rotor outlet flow, shown by Eckart's [12] experimental results of a backswept impeller in **figure 2.5** which features a strong velocity deficit in the suction side corner of the shroud.

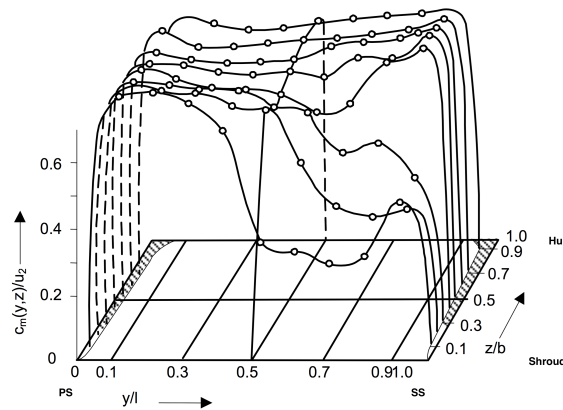


Fig. 2.5 jet wake rotor outlet velocity profile [12]

This velocity structure results from the secondary flows induced by the meridional curvature of the passage and the rotation, as described by Guelich [20]. Their effects on the passage flow are shown separately in the schematic in **figure 2.6**. The secondary flow due to curvature is similar to the exit flow structure of a rotating bend. The bend itself induces a velocity profile with a maximum towards the inside wall due to the conservation of angular momentum. In a rotating bend, this effect gets countered by the centrifugal force, shifting the velocity maximum towards the hub of the rotor, respectively the outside wall of the bend resulting in the shown secondary flow structure. The secondary flow due to rotation, more specifically at part load, causes the flow to shift towards the pressure side of the passage. The combination of both effects results in the flow pattern shown on the right of figure 2.6. The flow gets shifted away from the suction side shroud corner and thus causes a velocity deficit. A sketch of the resulting secondary flow structure is given on the bottom of figure 2.6 which also includes the effect of the tip leakage. The low meridional momentum flow from the tip leakage contributes to the velocity deficit and amplifies the jet wake effect [20].

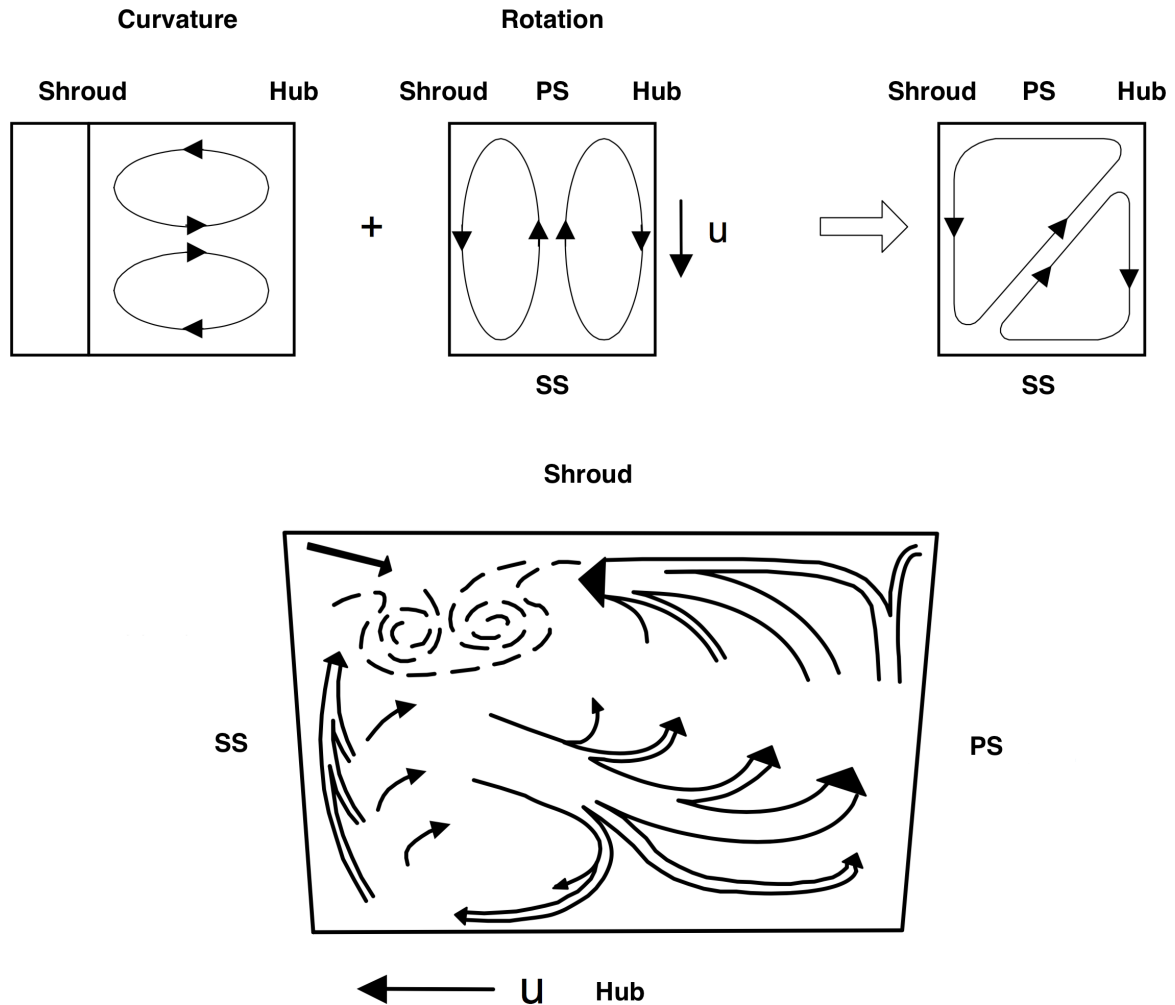


Fig. 2.6 Combination of secondary flows due to curvature and rotation at the rotor outlet [20]

The inducer part of a turbocharger compressor wheel behaves similarly to an axial machine. General subsonic flow features of an unshrouded rotor passage such as profile boundary layers, end-wall boundary layers, the horse shoe vortex and the tip leakage vortex are present. Shocks do occur at transonic flow conditions. When throttled to low mass flows, however, a radial machine behaves differently and can cope with much stronger distortions like local separations, circumferential non-uniformities or the ingestion of a nonuniform flow field due to the centrifugal effect which is present in machines where the rotor outlet radius is larger than the inlet radius [28].

The robustness to disturbances is due to the radial exducer part of the rotor which continues to produce pressure rise and stabilises the system. As a result, the machine can develop large recirculation zones at the inlet and the outlet of the rotor whilst operating stably [6], [35]. In comparison, axial machines would develop rotating stall cells or surge directly

at similar flow coefficients. **Van den Braembussche [49]** describes this increased ability to cope with stalled flow in a centrifugal compressor as progressive impeller rotating stall. He observed that centrifugal rotors, despite having developed stall cells which propagate at sub synchronous speed, remained functional with small disturbances present due to rotating stall. When throttled to lower mass flows, these disturbances grow progressively in terms of magnitude until they become so severe that they can potentially damage the machine. A distinction between stall and surge has been given already in the previous section. Rotating stall has been well characterised by **Day [10]** who describes rotating stall as a circumferentially asymmetric disturbance of through flow velocity around the annulus. Due to the disturbances, the compressor pressure rise capability drops and the flow field around the leading edge of the rotor separates into a clean and a disturbed region (stall cell). The disturbance rotates at speeds lower than rotor frequency and shows pressure fluctuations of a few percent dynamic head defined by blade speed. Although rotating stall increases pressure fluctuations, vibrations and noise, as it leads to a highly distorted flow field, the compressor can still remain functional. This is because only a part of the annulus is blocked while the rest stays intact so that the mean average mass flow remains steady. The stall cell can be of different size, affecting only parts (part span stall) or the full height (full span stall) of the annulus. It has been found that aspect ratio and compressor design loading can have an effect on which type of cell develops.

Two types of stall inception mechanism are known. The first one, modal stall, is described by **Moore and Greitzer [32]** based on a two dimensional model which assumes the flow and perturbations to be uniform in the radial direction. It furthermore assumes that the initial disturbance is of a long length scale ($2\pi R$). A first order mode would be equivalent to the circumference of the compressor. The second mechanism is known as spike type inception. In this case, the perturbation starts from a flow separation on a single blade passage near the rotor tips. The approaching flow then is diverted by this separation and starts propagating around the annulus. A schematic of the two mechanisms is given in **figure 2.7**.

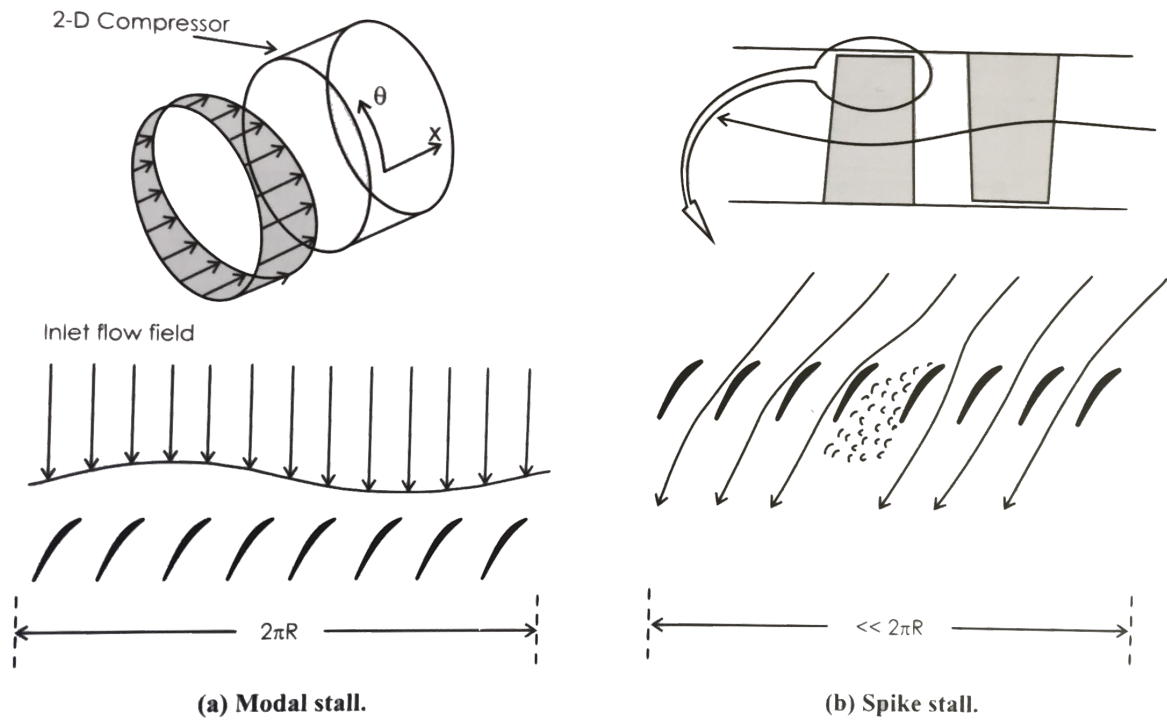


Fig. 2.7 Schematic of stall inception mechanisms [9]; left: Modal Stall; right: Spike Stall

2.5.1 Inlet recirculation

Knowledge about inlet recirculation is much more scarce and the inception mechanisms remain unknown up to now. Most knowledge about the phenomenon comes from incompressible turbomachines such as hydraulic pumps and blowers. Inlet recirculation was first identified in centrifugal pumps by Daugherty [8], who referred to it as churning loss. Pfleiderer [34] also mentioned inlet recirculation but no description in terms of formulas or models had been given. A first quantification about the loss associated with the phenomenon of inlet recirculation was presented by Stepanoff [43] who conducted a power analysis of a centrifugal pump. His results are shown in **figure 2.8** and show the magnitude of recirculation loss relative to other loss sources in a pump. In the power balance, Stepanoff found that a significant amount of power was lost at low flows. This behaviour could not be explained with conventional losses, i.e hydraulic losses as the resulting efficiency would have been too low. From these observations, he inferred that recirculation could be an explanation.

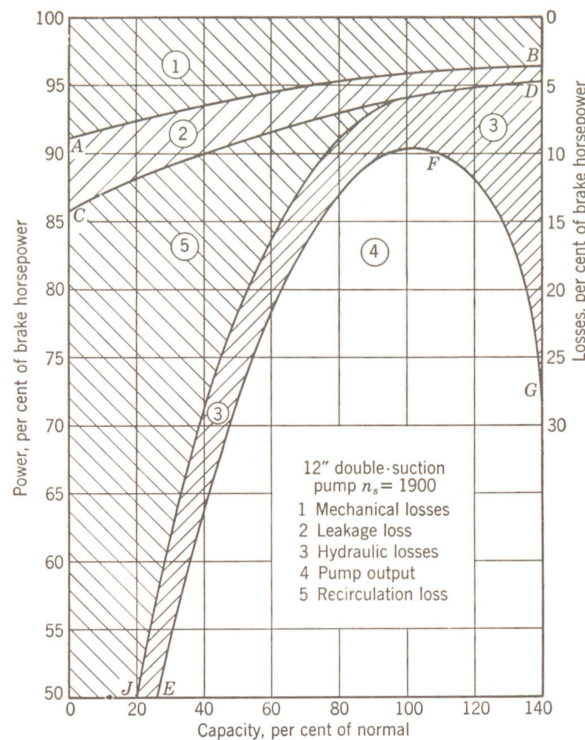


Fig. 2.8 Power balance over the relative swallowing capacity of a centrifugal pump [43]

Recirculation was also observed in axial blowers and fans as described by Eck [11] who characterises their off design behaviour based on a head rise characteristic shown in **figure 2.9**. He explains that blowers become unstable for low flow coefficients and that the head rise curve drops and rises again when throttled towards even lower flow rates up to shut off

conditions as can be seen in the figure. Based on characteristic points in this throttle curve, he describes the development of inlet and outlet recirculation. For the peak efficiency point d, a clean through-flow is present. When throttled to higher flow coefficients, a recirculation zone at the blower outlet shroud B''' is formed. When throttled to flow coefficients lower than best efficiency, large disturbances can occur. Close to the peak pressure rise point c, a small recirculation zone B'' is formed at the trailing edge hub caused by blade profile separation. For the lowest point b of the pressure rise curve, the recirculation B'' has increased in size whilst another recirculation at the leading edge shroud A' has formed. The flow does not pass straight through the rotor anymore but passes through diagonally. At shutoff condition a, the vortices A and B have become so large that they fill out the inlet and outlet of the blower completely. This is accompanied by a lot of noise. Despite zero flow, the highest pressure can occur at point A, because under these conditions, the flow passes through the rotor in a radial way so that a centrifugal component contributes to the head rise. The meridional through-flow velocity distribution upstream of the rotor changes at off design conditions as shown in c' to d'.

Despite a characteristic head rise curve and the gradual development of recirculation when throttled to low flows, Eck also gives measures to stabilise axial fans but only provides brief explanations:

- Fans with vane-less stators are more stable but provide poor efficiency.
- Reduced incidence makes the fan more stable. This can be achieved with variable pitch rotor blades.
- A high number of blades and a high hub to tip ratio reduce the power peak at part load of a fan, particularly for zero flow, making it easier to start up the machine.
- Geometrical structures upstream of the rotor to guide the flow such as radial guide vanes or concentric rings have been tested and shown to be effective to reduce the recirculation.

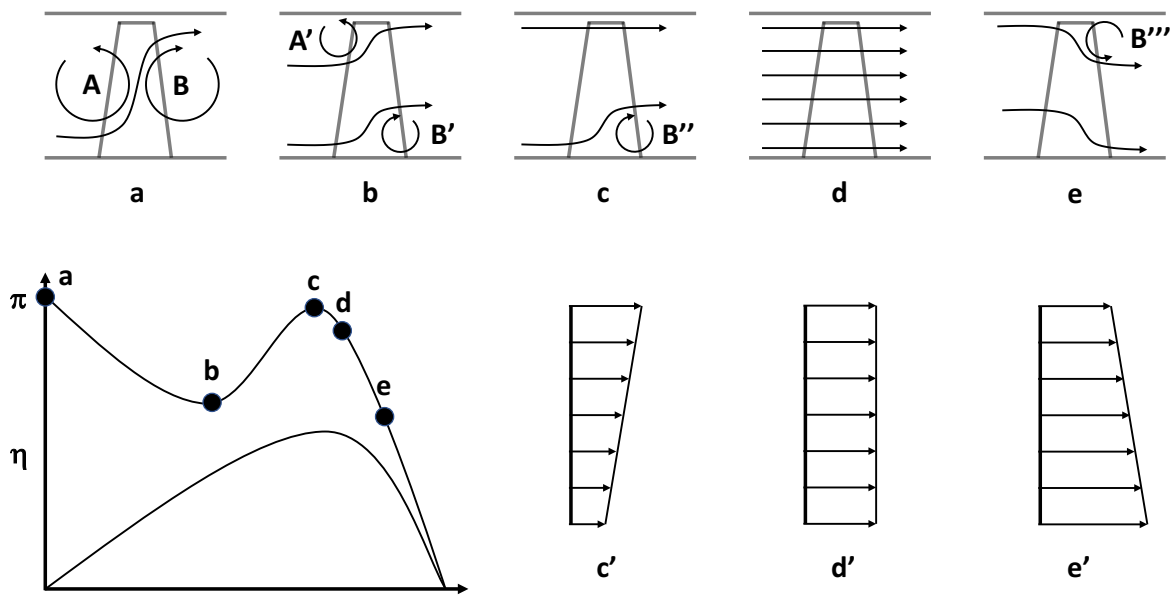


Fig. 2.9 Schematic of different flow conditions of an axial blower [11]

A detailed description of inlet recirculation in hydraulic pumps was given by Guelich [20] who explained that recirculation was to be expected when a pump is operated against a closed valve. He clarified his point by discussing the setup shown in **figure 2.10** which is very similar to Eck's explanation. It shows a closed vessel containing a disk with radial ribs. When the disk rotates, centrifugal forces are acting on the fluid inside the rotor causing a radial pressure gradient with a parabolic distribution to develop as shown in the sketch. Because the pressure is higher at the shroud than at the hub, the fluid will flow out of the rotor at the shroud and into the rotor at the hub forming a recirculation movement to maintain continuity. Because of the rotation, the fluid exiting at the rotor shroud has a high tangential velocity component added. This causes a pre-rotation upstream of the rotor which reduces towards the hub. Guelich mentions that if there are no ribs or guide vanes in the inlet, the recirculation can enter far into the inlet and has been measured at locations more than 10 diameters upstream of the rotor. He adds further that recirculation has been found in radial, axial and semi axial pumps without exception. A general method to predict the onset of recirculation is not given by Guelich and he explains there has not been one found yet. He defines two criteria for recirculation to occur:

1. The flow must separate locally
2. Strong pressure gradients perpendicular to the main flow direction must be present

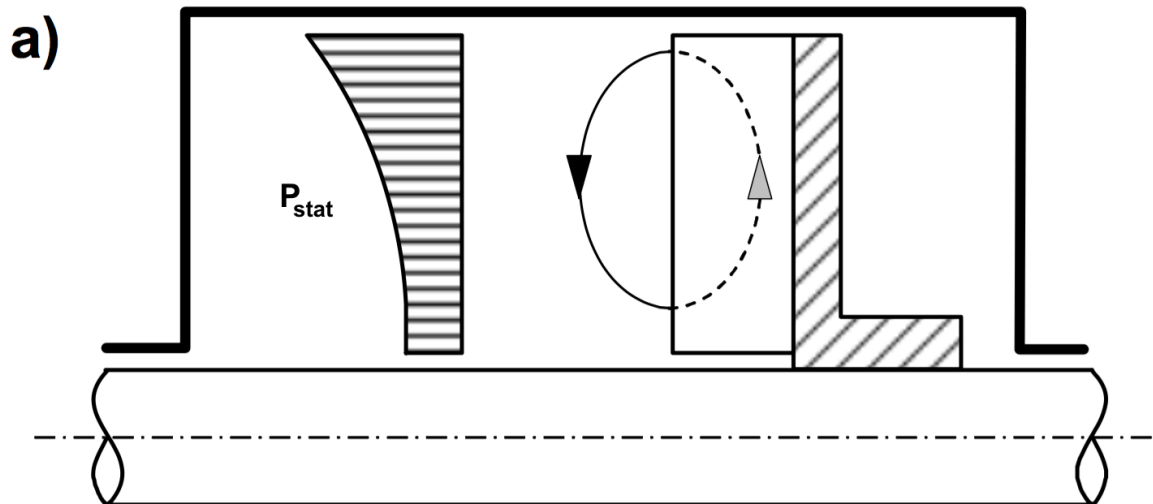


Fig. 2.10 Sketch of a closed casing radial vaned rotor with developed recirculation [20]

According to Guelich, the specific onset and intensity of inlet recirculation depends on boundary layer effects and the force balance in the rotor. It is thus dependant on the geometry and operating point. He mentions that approaches to predict recirculation based on incidence did not succeed because they do not take into account the perpendicular pressure gradients. An explanation for the importance of these pressure gradients can be given based on **figure 2.11a** which shows the inlet relative velocities at the hub, w_{1i} , and at the shroud, w_{1a} , over the flow coefficient. Furthermore the mean relative velocity in the rotor throat derived from continuity, w_{1q} , is given. In the throat, it is assumed that the mean velocity is reached over the whole area. At flow coefficients higher than operating point 1, the flow is accelerated from the leading edge to the throat mean value w_{1q} . At smaller flow coefficients, the flow decelerates at the shroud. As the flow cannot be decelerated to zero velocity for a flow coefficient of zero, it naturally has to separate. This separation is independent of the incidence angle and is caused by the cross-section of the blade. The figure also shows how pressure differences can occur perpendicular to the main flow direction. Deceleration takes place earlier at the shroud than at the hub because relative velocity reduces with radius. Consequently there is more diffusion at the shroud than at the hub which explains the pressure gradient. As soon as separation takes place which reduces diffusion, the separated flow is pushed towards the shroud through centrifugal forces and eventually develops into a recirculation into the inlet once the dead water zone is big enough. This means that the bigger the hub to tip ratio, the bigger the pressure differences perpendicular to the flow direction and the earlier the onset of recirculation and the more intense it will be. Guelich supports his argument with the observation that the onset of recirculation starts at higher flow coefficients relative to best point with increasing specific speed and that radial wheels do have very late recirculation.

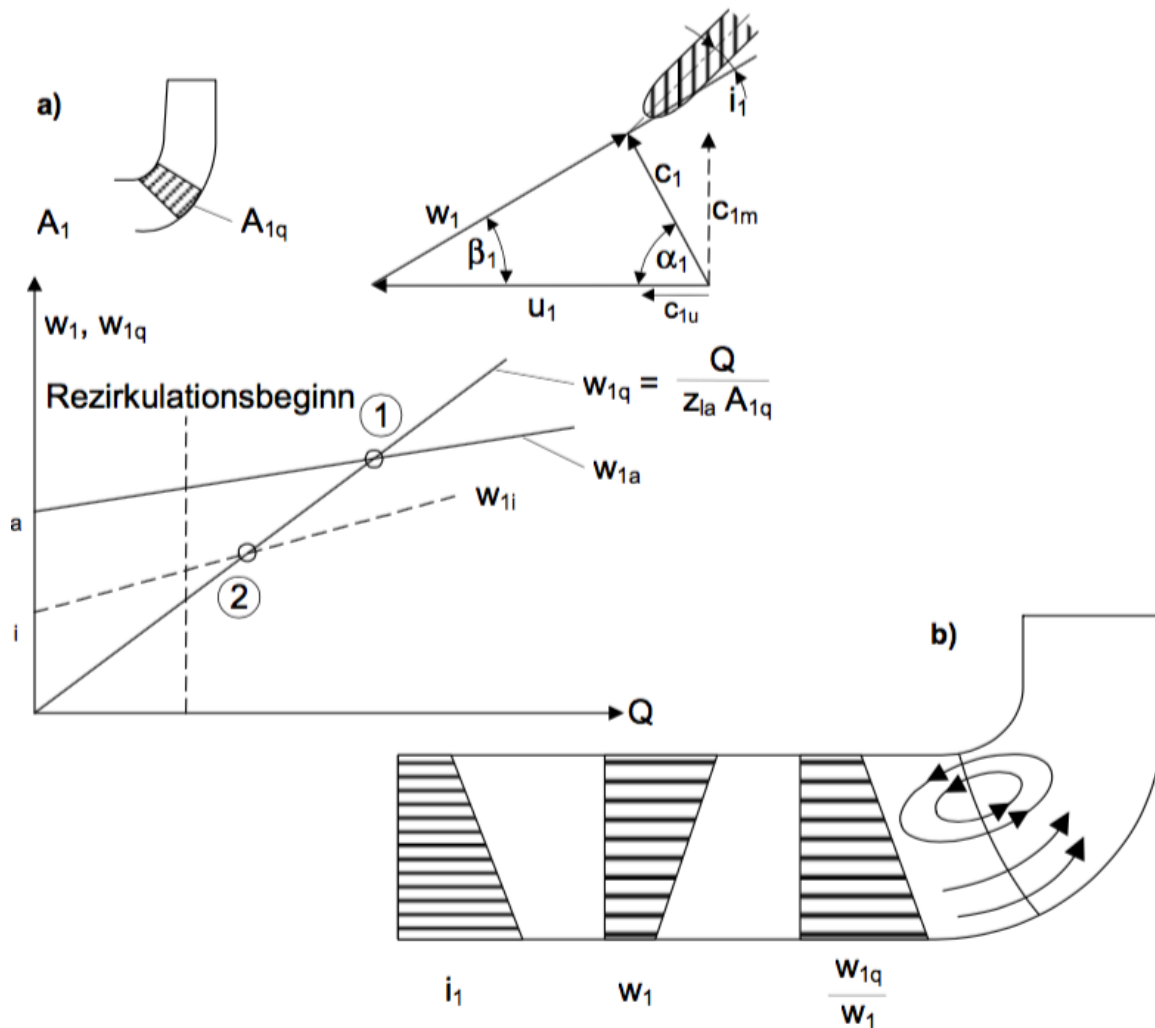


Fig. 2.11 Schematic of different flow conditions of an axial blower [11]

As explained by Guelich, deceleration causes a pressure gradient perpendicular to the main flow direction. More clearly, a strong deceleration of the relative velocity causes a nonuniform velocity distribution at the leading edge and in the throat of the passage as shown qualitatively in **figure 2.12**. Recirculation develops from a velocity deficit on the pressure side which can already be seen at nominal flow $q=1$. The relative velocity gets decelerated on the pressure side compared to the suction side which is induced by the exchange of work between rotor and fluid.

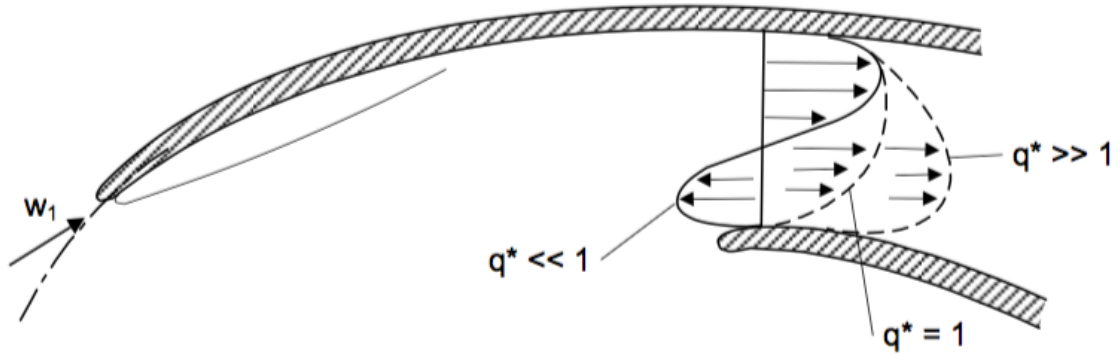


Fig. 2.12 Relative velocity distribution at the throat of the rotor [20]

Guelich quantifies the onset of recirculation to values between 40 to 75% optimum flow rate and deceleration values $\frac{w_{1q}}{w_{1a}}$ between 0.4 and 0.65. He suggested that a correlation with geometrical features was not possible. Despite that, he gives **equation 2.3**, which describes the diffusion in correlation to the flow coefficient and the area ratio between the rotor inlet and the rotor throat.

$$\frac{w_{1q}}{w_1} \approx \frac{Q}{f_q A_{1q} z L a u_1} = \frac{\phi_1 A_1}{z L a A_{1q}} \quad (2.3)$$

He then uses measurement data to correlate **equation 2.4** which estimates the flow coefficient where recirculation starts. The correlation estimates the onset of recirculation with an accuracy of +/- 10% when applied to axial and radial cases. However, the general application remains unclear. The correlation contains components taking into account the deceleration of the radial velocity, the radius ratio as well as the meridional curvature of the passage.

$$\phi_{1, RB} = 0.03 + 0.16 \left(1 + \frac{b_1}{R_{RSW}} \right) \left(\frac{d_{1a}}{d_{1i}} \right) \left(\frac{z L a A_{1q}}{A_1} \right) \quad (2.4)$$

Regarding the pressure gradient perpendicular to the flow direction, Guelich points out several influence parameters. He describes the diameter ratio between hub and tip at the inlet of the rotor as the most important parameter. The rotor throat size is another influence factor. The smaller the throat, the smaller the tendency to develop recirculation because of less diffusion. Guelich sees incidence and the camber as of secondary importance. Further influence factors are sweep, meridional shroud curvature, number of blades, inlet flow velocity distribution and the boundary layer thickness at the shroud as well as the effect of tip

leakage. Guelich also gives a general characterisation of inlet recirculation in pumps. Inlet recirculation occurs at the shroud first in all rotors. More specifically when the deceleration of the relative velocity from the leading edge to the rotor throat exceeds a certain limit which cannot be generally quantified. Pumps with a stable characteristic which do not show any problems at off design also have recirculation. Inlet recirculation does not originate from the leading edge but from the rotor throat or from a location with high blade curvature where radial pressure gradients are present. The force balance between stream lines is key for recirculation. Boundary layer effects may have an effect on initial separation but the onset and intensity of recirculation are practically independent of the Reynolds number. Prior to recirculation, there is a separation on the pressure side of the blade shroud. Pressure gradients perpendicular to the main flow direction are a result of centrifugal effects and different relative velocity decelerations from the leading edge to the passage throat. Separation and recirculation depend on the three dimensional velocity distribution in the rotor and the intake flow structure. These effects cannot easily be described in a general manner and prediction is hard. A correlation between incidence and the onset of recirculation could not be found. Several separation zones are present in the passage which has been shown via tuft probe measurements. A stator which imposes a much more uniform flow field on the exit of the rotor had no effect on inlet recirculation. Volute causes a circumferential pressure variation at off design. As a result, the rotor operates at different points in the characteristic depending on its circumferential position relative to the tongue which can have an effect on inlet recirculation. When the span of the rotor is shortened, inlet recirculation does only change behaviour if the blades are shortened significantly.

As described above, Guelich identifies locations of strong diffusion within the passage as those which trigger inlet recirculation. However, this theory is not supported with experimental or simulation data. Furthermore it cannot be aligned with other theories which identify other mechanisms and locations as the triggering mechanisms of inlet recirculation. One example is Schleer's [38] experimental work, where he identifies the tip leakage vortex as the triggering mechanism for inlet recirculation. He proposes that inlet recirculation is triggered when the machine is throttled to an operating point where the tip leakage vortex hits the leading edge of the adjacent blade. Another theory proposed by Ribi [37] is that inlet recirculation has a similar inception mechanism as spike type stall which would mean that a leading edge separation on the suction side of the blade would cause a disturbance. Instead of a pitch-wise propagating stall cell, a full recirculation ring could be the result of this mechanism as well. Overall, several theories about the inception of inlet recirculation have been published, but clear proof about which of them correctly describes the inception of recirculation is not available.

More applied examples for inlet recirculation in incompressible machines can be found in Tanaka's [46] research who experimentally investigated semi axial pumps. An example for inlet recirculation and its suppression via an inlet rib can be found in work by Muggli [33] who investigated a vertical semi axial mixed flow pump via full annulus simulations. He calculated steady state and unsteady results and validated those with casing pressure measurements. An example of his results is presented in **figure 2.13** which shows a meridional cut through the geometry and compares the circumferentially averaged static pressure field in the pump with and without rib. He found that inlet recirculation and concurrent pre-rotation only exists if there is no rib in the inlet, whereas it is suppressed by the rib.

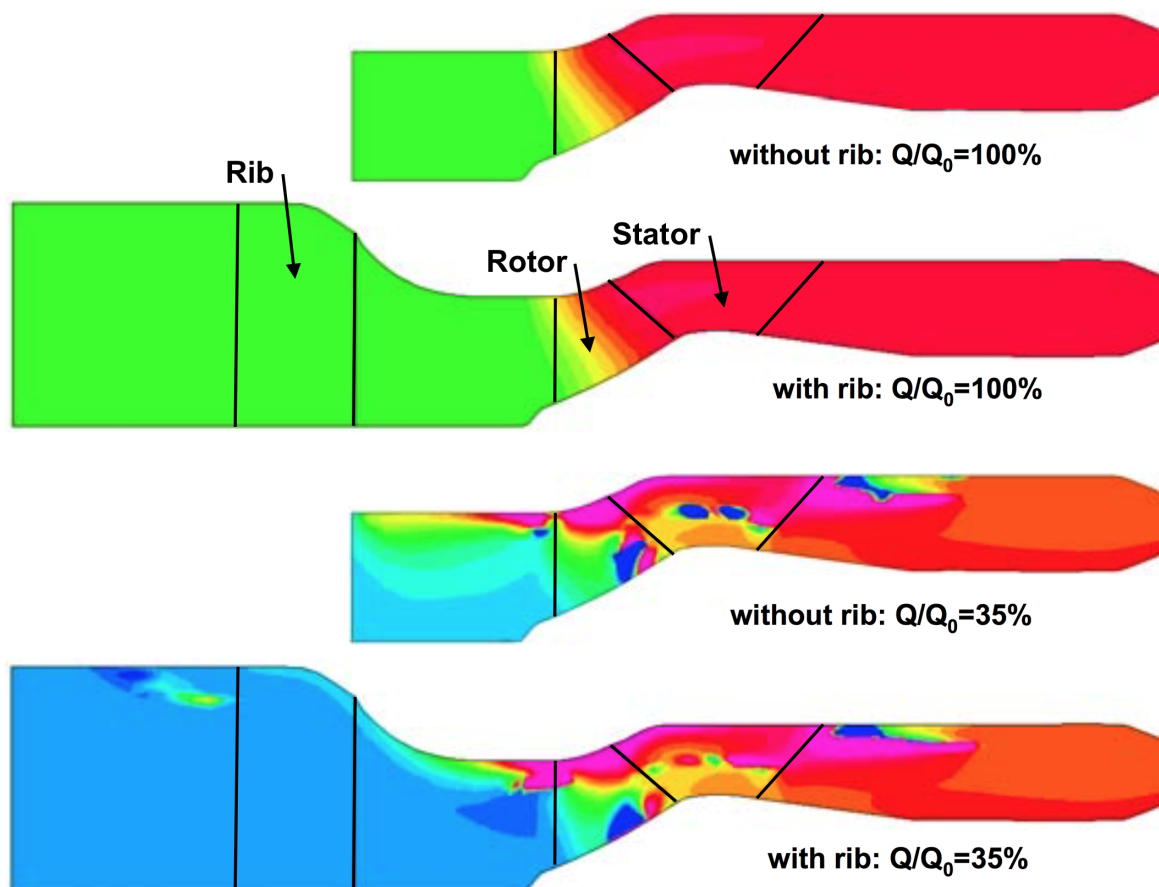


Fig. 2.13 Meridional cut through mixed flow pump showing the qualitative circumferentially averaged total pressure distribution. Flow direction from left to right. Without rib: Inlet recirculation; With rib: Suppressed Inlet recirculation

Inlet recirculation was also found in compressible flow compressors. **Ribi [37]** distinguished two types of instabilities in machines with volutes, inlet recirculation and stationary non axisymmetric stall. He described inlet recirculation as an axisymmetric, non periodic phenomenon occurring near the inducer tips. Non axisymmetric stall was described by

him as a non axisymmetric phenomenon produced by downstream asymmetry from the volute. Furthermore he pointed out that these different patterns can develop in centrifugal machines because of their tolerance to stalled regions since a significant amount of pressure rise is produced by centrifugal effects. In contrast to Guelich, Ribi sees inlet recirculation as triggered by high incidence and the resulting separation at the tip of the blade close to the leading edge which then evolves into a zone of reverse flow. Ribi also notes that inlet recirculation, despite being axisymmetric, corresponds with a certain level of unsteadiness because of the pressure difference between the pressure and suction side of the blades. He further observes a significant reduction of work input due to the locally increased tangential component at the impeller inlet, which results in a depression of the impeller characteristic. Ribi conducted measurements at the LSM air test rig at ETH Zurich and investigated the velocity distribution upstream of the impeller. The results are shown in **figure 2.14**. He compares an operation point where inlet recirculation is not present (highest flow coefficient) with operating points at lower flow rates where inlet recirculation is present. It can be seen that the axial velocity is almost constant for the high flow condition and there is no swirl component present. At lower flow rates, a reverse flow region can clearly be seen in the axial velocity plot. Ribi describes that reverse flow blocks the tip region and forces the flow outside the stall zone to accelerate. The figure also shows the induction of a strong positive swirl component into the inlet. As the machine gets throttled towards lower flow coefficients, the axial velocity becomes more distorted and the positive pre-swirl affects more of the flow outside the recirculation zone. At the lowest flow rate, the axial velocity in the core is about three times higher than the mean value.

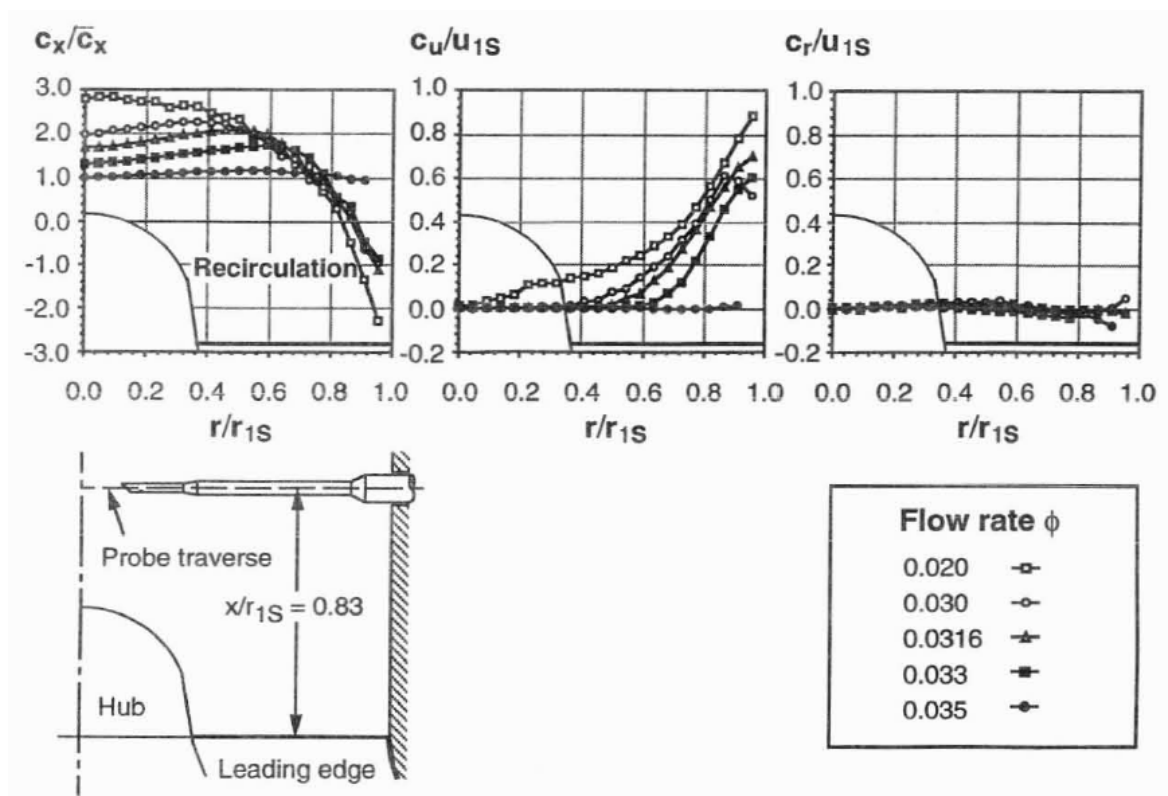


Fig. 2.14 Inlet hot wire traverse upstream of a rotor at different flow coefficients [37]

A clearer distinction between different types of instabilities in centrifugal compressors was given by **Ribaud** [36]. He experimentally investigated three high pressure ratio centrifugal compressors and identified three different operating zones for the rotor. For low inlet flow coefficients, he identified two recirculation, one at the inlet and one at the outlet of the rotor. For moderate flow coefficients, the outlet recirculation disappeared. He postulated that inlet recirculation can stabilise the flow if 2D blade stall occurs which is the case if the inlet flow coefficient is below a certain critical value. Unfortunately, no definition of 2D blade stall is given. Ribaud based the separation of these three zones on two discontinuities which he found in the surge line of the compressors. For low flow coefficients, reverse flow regions were found in the inducer inlet and near the rotor exit. For moderate inlet flow coefficients, the outlet recirculation disappeared.

Ribaud also presents a simple model to estimate the radial extent and the tangential velocity of the inlet recirculation zone based on the area ratio between the relative flow area at the inducer inlet and the rotor throat. However, he uses measurement values of the inlet total pressure and the static pressure at the hub upstream of the rotor to estimate the inlet Mach number of the machine so that prediction is not possible. In the inlet, Ribaud defines an active flow zone and a blocked recirculation zone with positive swirl which gets transferred

into the active flow zone via viscous effects. To estimate pre-whirl, he assumes uniform inflow at the hub and solid body tangential flow at the shroud. From continuity and the radial equilibrium equation he then determines the radial extent of the reverse flow region and its angular velocity. His results show a linear correlation between the radial extent of the recirculation zone and the inlet flow coefficient.

Kaemmerer and Rautenberg [30] investigated the flow conditions at different speeds along the stall line of a centrifugal compressor with vane-less diffuser. They distinguished three kinds of stall phenomena. One type of stall with recirculation of fluid at the impeller inlet was of a non-periodic character and two different types of periodic stall appeared at higher speeds. These periodic stall phenomena showed different behaviour. One was low frequency stall which exhibited features of diffuser generated stall and measured a lobe number of three. The other one was a high frequency type rotating stall which is generated in the impeller by a periodic breakdown of energy transfer from the rotor to the flow. Their different results become clearer when looking at the compressor map they investigated as shown in **figure 2.15**.

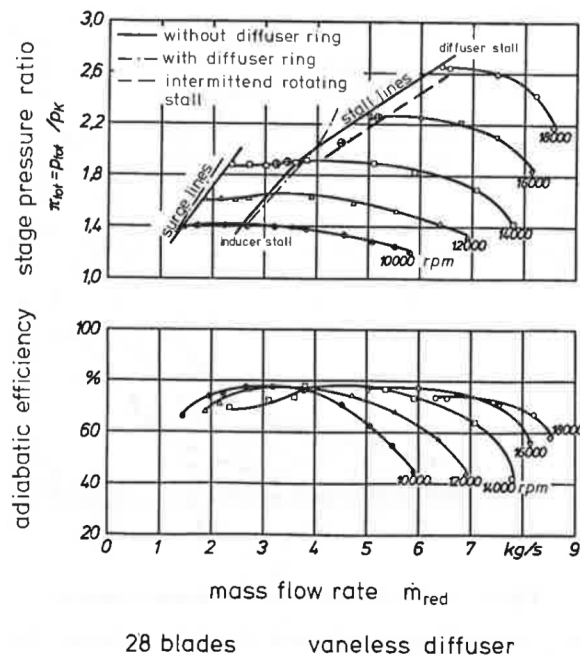


Fig. 2.15 compressor map with different types of instabilities [30]

At low speed, inducer stall determines the stall line of the stage. It goes along with a stationary, non-periodic reverse flow zone in the impeller eye which features a strong rotor induced swirl component. Further throttling increases the extent and magnitude of this reverse flow and reduces the energy transfer into the impeller so that it eventually triggers

compressor surge. At higher shaft speeds, rotating stall is triggered which is of fast rotating type at low rotor speeds and of slowly rotating type at higher speeds. The latter was identified as diffuser rotating stall based on the lobe number and the rotation frequency. The insertion of a ring into the diffuser shifted the stall line and suppressed it to a high degree, giving further evidence for the generation of rotating stall in the diffuser. The fast rotating stall was associated with a periodic breakdown of energy transfer in the impeller. Simple numerical rotor flow calculations confirmed that with increasing speed, the load is shifted away from the inducer into the diffuser and thus at lower rotor speeds, the impeller is likely to cause the stage to stall while at higher speeds it is the unvaned diffuser. This observation agrees with the described shift in location of instability source due to a shift in component matching given in section 2.2.

Schleer [38] performed time resolved measurements along the casing of a scaled up version of a highly loaded splitter bladed subsonic radial compressor and investigated the effect of large relative tip clearances on the onset of instability. He defined that normally tip clearances are in a range of one to five percent of the span. In small scale impellers, a good clearance value is considered 4.5% of span. Schleer investigated two different clearances at a number of different operating points. He found that larger clearances led to a more deteriorated flow field with a stronger tip leakage vortex. As a consequence, stall was reached at higher flow rates. Furthermore he investigated the direction of the tip leakage vortex by monitoring its trajectory via casing pressure probes. At design incidence, the trajectory was in the direction of the splitter blade leading edge. When the mass flow was lowered, the trajectory moved forward in the passage. For a sufficiently low mass flow, the trajectory became perpendicular to the impeller rotational axis. According to his findings, the leakage vortex interacted with the adjacent blade and he judged this flow pattern as the triggering point for inlet recirculation. An indicator for inlet recirculation was the vanished tip leakage vortex. Along with the occurrence of inlet recirculation, also a sudden increase in random pressure fluctuations in the inducer, as well as a change in loading distribution, namely an unloading of the inducer part of the rotor, was observed. For a further decrease in mass flow, Schleer noted that the inlet recovered and rotating stall was initiated in the diffuser.

In order to account for inlet recirculation during preliminary design, **Qiu et. al. [35]** developed a mean line recirculation model and supported it with CFD simulations and measurement data. They modelled recirculation as area blockage and divided the inlet into an active flow zone and a blocked recirculation zone. They found that inlet recirculation reduced incidence in the active flow zone. In their mean line model they set a linear velocity profile in the recirculation zone. The active flow zone was modelled with a constant velocity profile.

The inlet recirculation zone was modelled by assuming constant inlet pressure recovery after having passed a critical incidence, respectively a critical area ratio, following Japinske's two elements in series approach [28]. This was realised by increasing the recirculation area with lowering mass flow. The model offered the possibility to estimate the additional power consumption during recirculation, as well as the head rise. They found that recirculation rose power consumption to up to 150% of the maximum value without recirculation. The mechanism reduced incidence in the active flow region so that head rise could increase continuously with lowered flow rate. Qui et. al. showed that their model was applicable to axial, mixed flow and radial impellers. In axial impellers, inlet recirculation dominated. According to their model, recirculation was triggered by leading edge separation close to the tip. It then developed in this region and was held in the casing region by a strong radial pressure gradient. They also inferred that purely radial machines could not experience inlet recirculation, which was confirmed with CFD and measurements. In radial machines, their calculations showed that strong outlet recirculation occurred instead. For turbocharger impellers, which are axial at the inlet and radial at the outlet, this means that both forms of recirculation can occur. Based on Qiu et al.'s work, inlet recirculation should occur more predominantly in impellers with a low hub to tip radius ratio and thus long blades due to a higher radial pressure gradient.

Harley [23] improved Qiu's model and investigated inlet recirculation in three different automotive turbocharger compressors using steady state time averaged simulations. The calculations were compared to experimental data. Harley showed that the critical area ratio during recirculation does not stay constant as assumed by Qiu. His results show a parabolic correlation between the critical area ratio and the flow coefficient as shown in **figure 2.16** which shows the area ratios of Qiu and Harley over the inlet flow coefficient. Harley's approach allows to give a more accurate estimate of the occurring blockage in the rotor inlet as can be seen in **figure 2.17**, where the inlet blockage predicted by Qiu's model and Harley's model is compared to experimental data.

Harley further developed a model which describes the increased inlet temperature due to inlet recirculation as well as the altered inlet velocity triangle so that the effect can be taken into account during preliminary design [22].

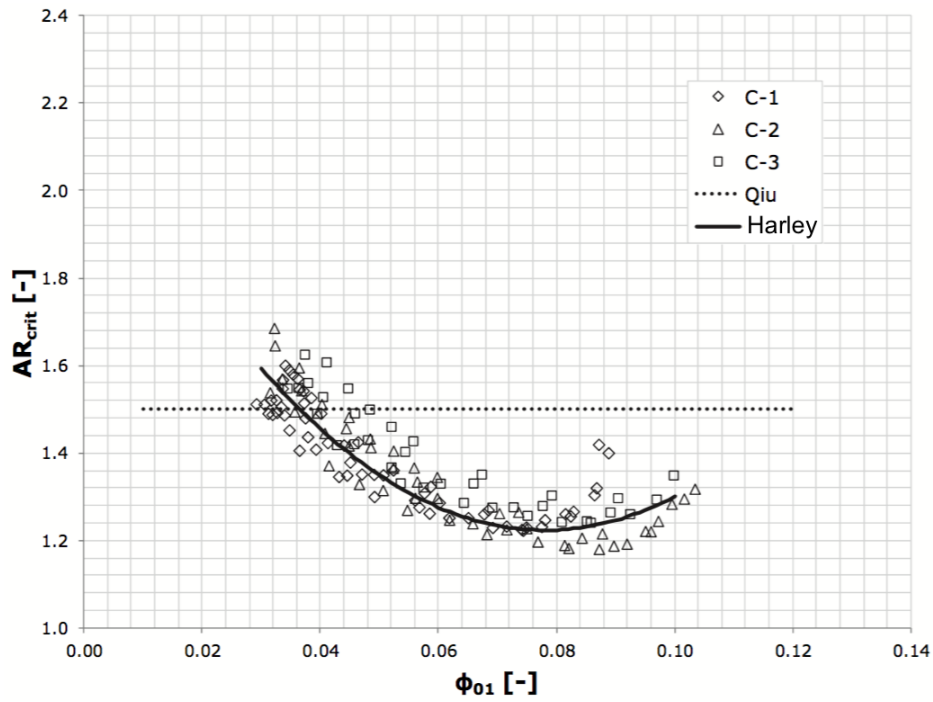


Fig. 2.16 Critical area ratio criterion compared to numerical data [23]

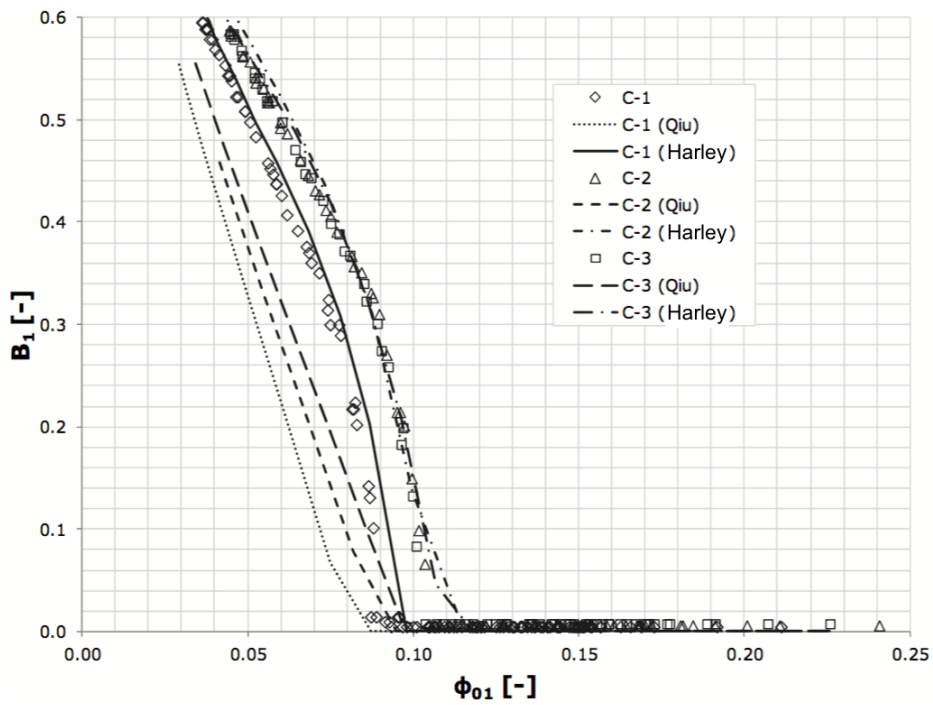


Fig. 2.17 Blockage correlation [23]

Several approaches to alter the inlet flow structure and recirculation have been documented. Tamaki [44],[45] used a high pressure ratio (5.7) marine turbocharger compressor as a base for his investigations in this field. He compared three different intake setups. One with a smooth wall, one with a ported shroud channel and one with a ported shroud channel and integrated vanes which induced a counter swirl into the intake flow. He found that counter swirl shifted the surge line to lower flow rates, as can be seen in the characteristics shown in figure 2.18.

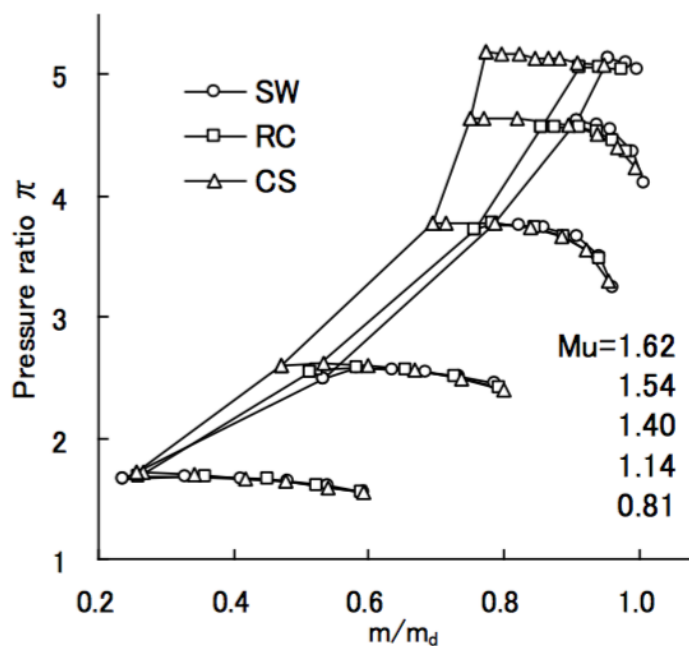


Fig. 2.18 Location of the compressor instability line: SW=smooth wall; RC=recirculation channel; CS=recirculation channel with counter swirl vanes

Tamaki's explanation for the improvement is that additional work input leads to higher load and an increased relative Mach number at the inlet. This results in a downstream relocation of the shock and thus a decreased interaction with the tip leakage vortex. The argument is similar to Hah's [21] numerical studies on an axial compressor with variable tip gap which showed that a reduction in low momentum fluid at the shroud is beneficial for low flow stability. In Tamaki's study, the bleed slot also resulted in reduced blade loading at the tip and a reduced tip leakage vortex as well as the removal of end-wall separation. Altogether, the effects suppressed the stagnation and reverse flow region behind the shock. Although incidence was increased with the approach, no clear leading edge separation was found. In a subsequent study [45], Tamaki investigated the effect of inlet fins directly mounted into the inlet channel to achieve a shift in stability limit as shown in figure 2.19. The fins prevented the inlet recirculation to extend upstream by breaking down the swirling

structure of the phenomenon. He also found that the inlet fins increased the compressor work coefficient and reduced compressor efficiency. As a result, a trade off between operating range, turbocharger response and efficiency would need to be found in an application. Similar results from an investigation with inlet fins were obtained by **Harley [24]**, who experimentally compared a compressor with no casing treatment, a recirculation channel and axial grooves at the shroud. His results are shown in **figure 2.20** which depicts the normalised isentropic efficiency over the normalised mass flow rate in the top graph and the corresponding compressor map with normalised pressure rise coefficients in the bottom graph. In agreement with Tamaki, he found that the axial grooves had a positive effect on the surge margin, particularly at low speed when recirculation occurs. The behaviour can be seen when comparing the low speed surge limits of Harley's baseline case, marked with squares, and the axial groove case, marked with triangles, in the bottom graph of figure 2.20. The improvement in surge margin went along with a decrease in efficiency over the whole operating range, as can be seen in the top graph of figure 2.20.

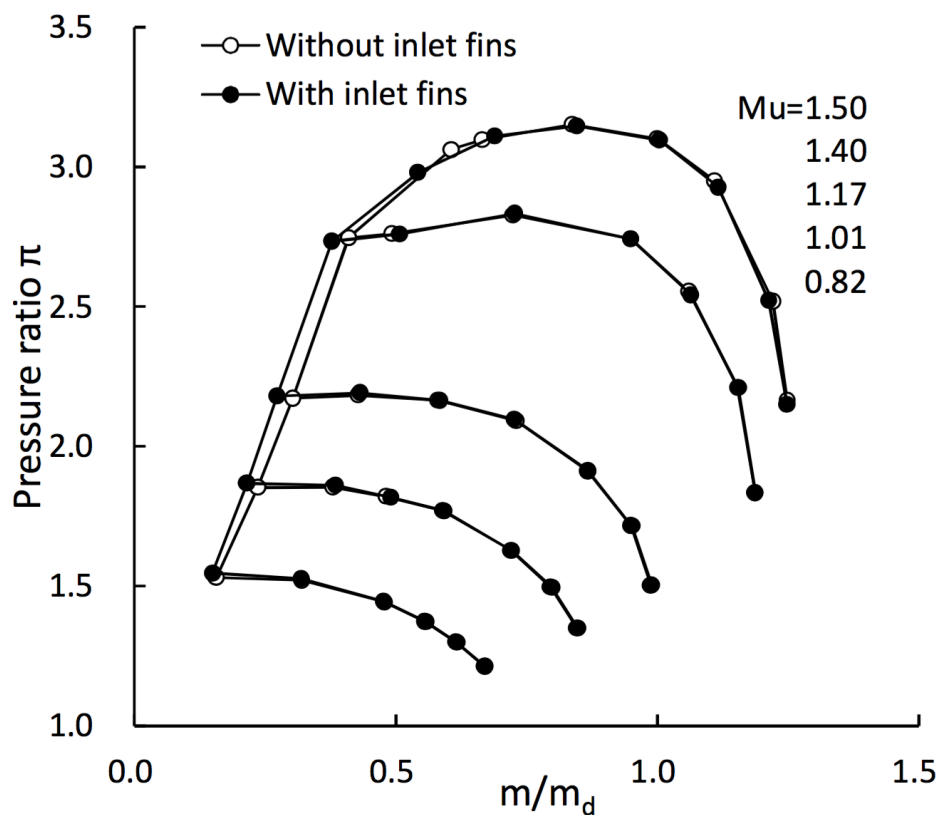


Fig. 2.19 Change in instability limit through inlet fins [45]

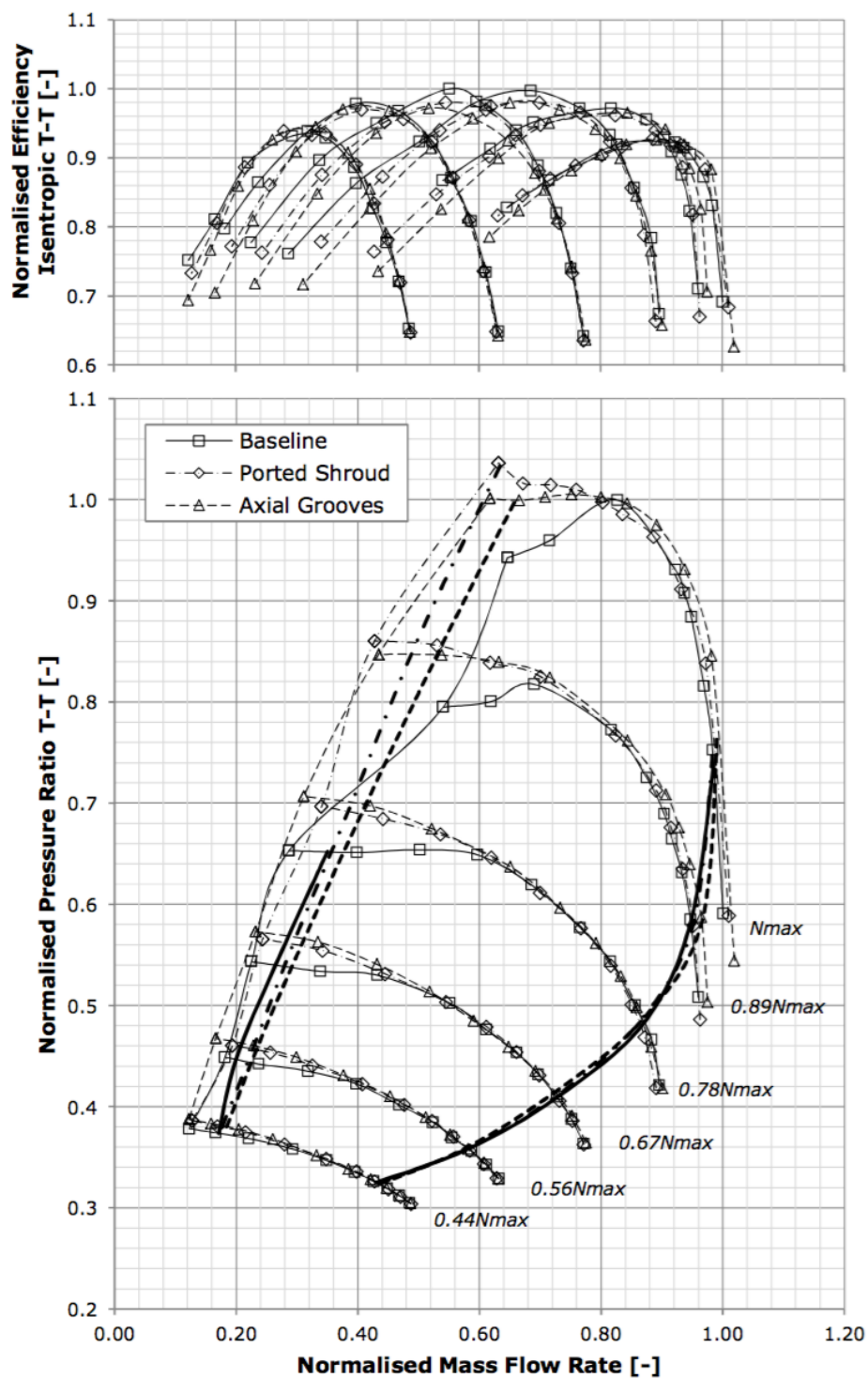


Fig. 2.20 Change in instability limit and efficiency in a turbocharger compressor [24]

2.6 Low flow behaviour of radial compressor diffusers and volutes

In radial compressors, the downstream components face a particularly difficult situation due to the highly non uniform flow field exiting the rotor. This becomes obvious when looking at the results of **Bammert and Rautenberg [1]** as well as **Eckart [12]** who investigated the flow structure at the outlet of the impeller experimentally. They found that the exit velocity flow angle varies strongly over the channel. In the region of the hub and shroud end walls, deviations from the mean passage vector of 10 degrees and more were found. Despite these unfavourable conditions, diffusers in radial compressors can still provide good performance according to **Traupel [47]**.

In order to give a full overview of the instabilities which can potentially occur in a radial compressor, this section provides a brief summary of instability phenomena which occur in those parts of a radial compressor exposed to this highly nonuniform flow, namely diffusers and volutes.

2.6.1 Vaneless diffusers

Vaneless diffusers offer good performance over a wide range of flow coefficients as no blades are present in this type of geometry. Consequently no blade end wall separations as a source of instability can occur. Pressure rise in a vaneless diffuser is achieved in two ways.

Firstly, due to diffusion which is dependent on the area ratio of the diffuser.

Secondly by conservation of angular momentum, as shown in **equation 2.5**, which naturally leads to a conversion of kinetic energy into pressure with an increase in radius.

$$rc_u = \text{const.} \quad (2.5)$$

As a result of the conservation of angular momentum, the flow path within vaneless diffusers under normal flow conditions follows the pattern of a logarithmic spiral. An example of such a flow pattern in an industrial vaneless diffuser was documented by **Japikse [27]** and is provided in **figure 2.21**.

A combination of both of the mechanisms described above can potentially lead to instabilities in a vaneless diffuser. If the diffuser is operated at low flow conditions, the radial velocity component becomes very small and consequently only a small amount of radial momentum to overcome the adverse pressure gradient is available.

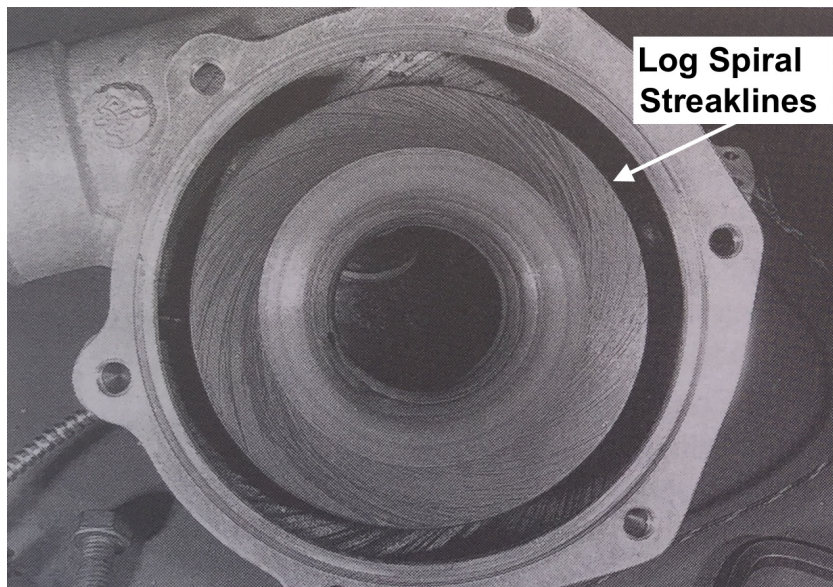


Fig. 2.21 Logarithmic spiral surface streaklines in an industrial compressor diffuser [27]

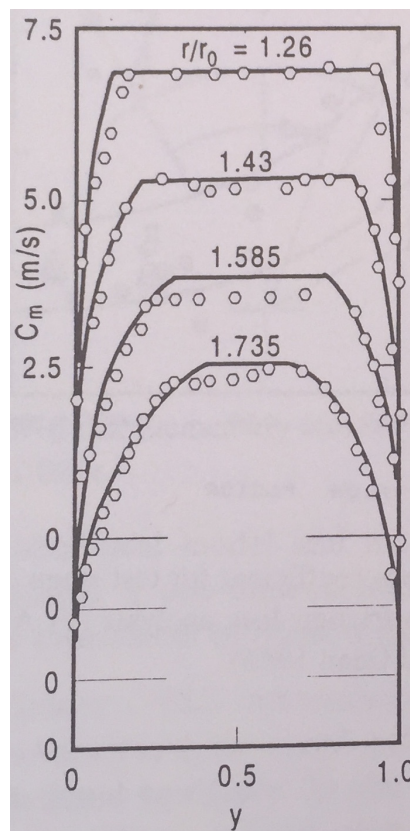


Fig. 2.22 Experimentally obtained meridional velocity from traverse data in a vaneless diffuser at different radii showing thickening of the boundary layers [40]

This can be particularly problematic in the boundary layers of the vaneless diffuser which thicken up significantly under such flow conditions [27].

Examples of the thickening of the boundary layer have been documented by **Senoo [40]** who investigated the flow in a vaneless diffuser experimentally. He conducted traverse measurements at different radial positions of the vaneless diffuser to obtain velocity data. An extract of his work is provided in **figure 2.22** which shows the thickening of the boundary layer with increasing radius ratio based on the meridional velocity component. Furthermore, the decrease in meridional free stream velocity can be observed.

If the diffuser is operated at low flow coefficients, the meridional momentum is not sufficient any more to overcome the adverse pressure gradient in the vaneless diffuser. This leads to a stagnation of the flow in radial direction and the flow can even be forced to return back to the rotor outlet. This flow regime is described as the onset of reverse flow, which has been connected to the onset of rotating stall [27]. An example of return flow to the rotor outlet has been given by Japikse [27] and is shown in **figure 2.23**. The figure shows surface streak lines in a vaneless diffuser with the dividing streakline marking the stagnation point of the flow in the radial direction. It can be seen that a part of the flow at higher radii still propagates downstream as shown by the streakline marked "Outflow", whereas the flow at lower radii aims back to the rotor trailing edge radius, as indicated by the "Inflow" streakline.

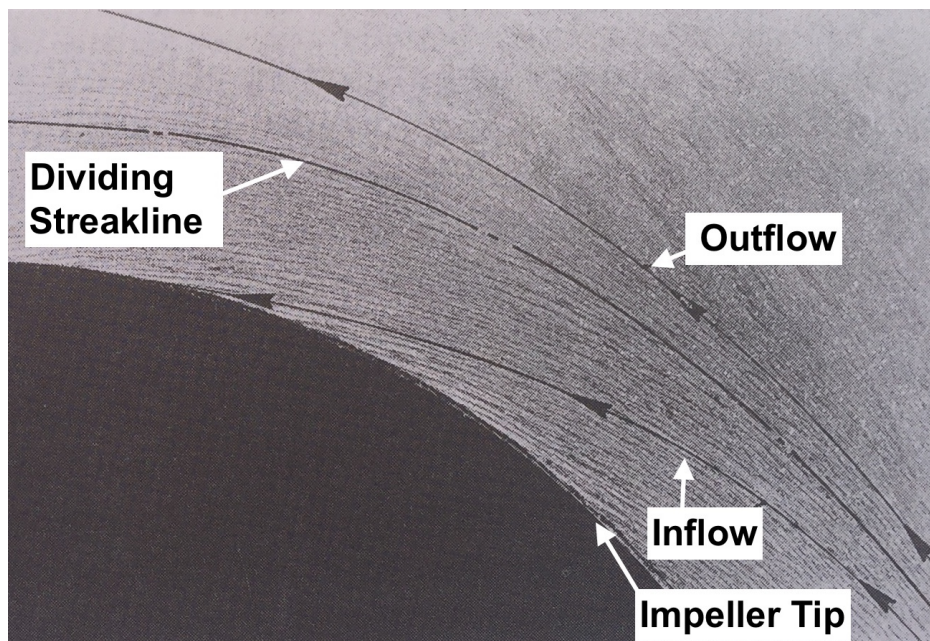


Fig. 2.23 Back flow close to the impeller trailing edge in a vaneless diffuser [27]

It has to be pointed out that this flow pattern is different from a separation as the flow remains attached and only changes its direction back inwards. It has been reported by Traupel

[47] that vaneless diffusers can provide good performance despite local separations being present. This implies that flow separations in the vaneless diffuser do not necessarily lead to instability.

Jansen [25] was the first to demonstrate that vaneless diffuser rotating stall could be triggered by local reversal of the flow as described above and described the phenomenon on a theoretical basis using the continuity and momentum equations for an unsteady, inviscid and incompressible case. **Tsujimoto [48]** showed patterns of vaneless diffuser rotating stall in terms of fluctuations of pressure and velocity from experiments and numerical analysis. His results are shown in **figure 2.24** with the experimentally obtained results on the top and the numerically obtained results on the bottom of the figure. In his results can be seen what **Van den Braembussche [49]** describes as vaneless diffuser rotating stall whereby zones of different flow characteristics rotate in the diffuser at sub-synchronous rotational speed. This means that the flow is split up into stalled zones and zones of increased radial velocity where out flow is still present. Investigations about the onset point of vaneless diffuser rotating stall and the definition of a critical diffuser inlet angle when vaneless diffuser rotating stall is happening have been carried out by **Jansen [26], [25], Fringe and Van den Braembusche [16]** and **Senoo and Kinoshita [51]**. Those will be explained in more detail in section 3.2.3, where their approaches are used to determine the stability of the vaneless diffuser subject to this investigation.

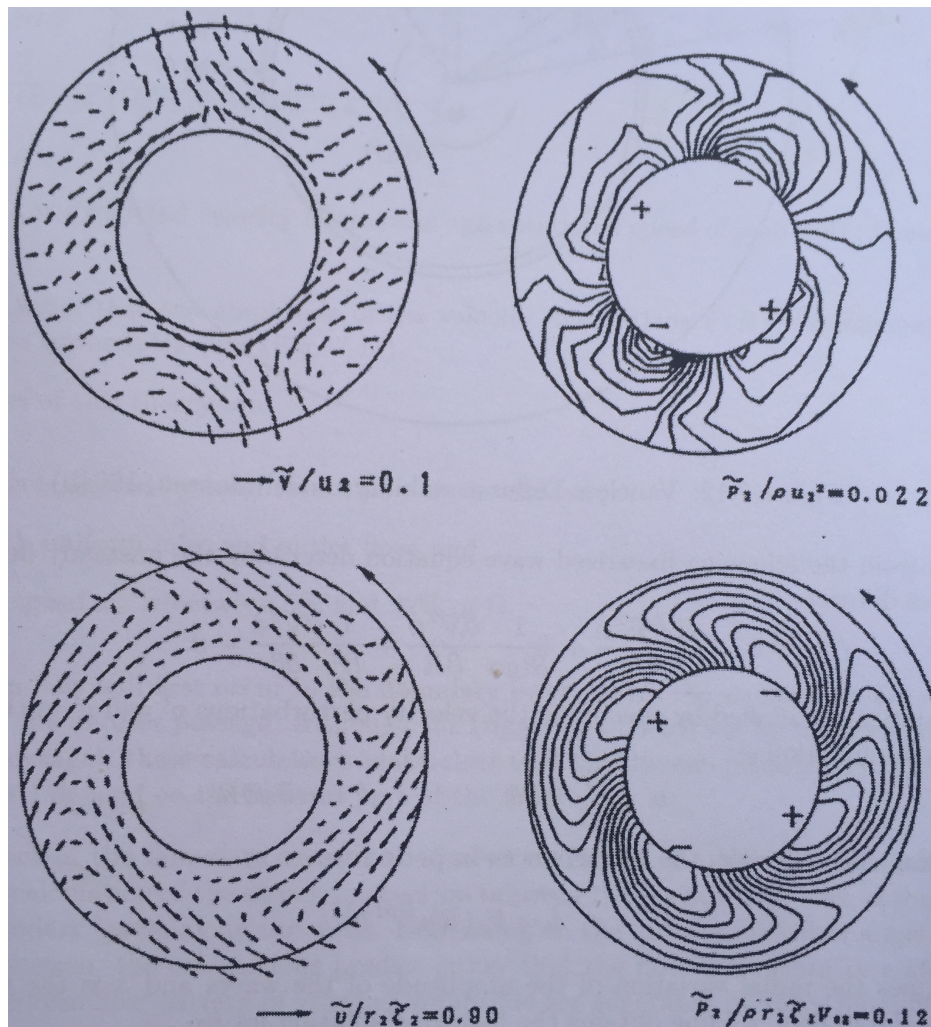


Fig. 2.24 velocity and pressure fluctuations in a vaneless diffuser under rotating stall; **Top:** Experiment; **Bottom:** Numerically obtained results [48]

2.6.2 Vaned diffusers

Only a little amount of information could be found in the public domain which addresses the physics behind the instability behaviour of vaned radial diffusers directly. On a more general note, it can be said that a vaned radial diffuser shares many features with a stator blade row. Consequently, similar flow phenomena such as blade end wall separation or corner separations are to expect at low flow conditions with high levels of incidence. **Sparkovszky** [42] described the instability behaviour of a radial research compressor with a vaned diffuser with respect to system instability. In his study, the vaned diffuser suffered from corner separation at low flow rates. Sparkovszky investigated the development of stall waves in a radial compressor where the inlet, the rotor, the vaneless space, the vaned diffuser and the

downstream volume were modelled separately. He found that at low flow rates, backward travelling stall waves were present in the vaned diffuser. Sparkovszky furthermore pointed out that the vaneless space in radial compressors is much larger compared to axial machines, especially when taking into account the strongly tangential flow path in the absolute frame. Regarding the development of overall system instabilities, his investigation furthermore showed that the vaneless space between the rotor and the stator plays a crucial role because it has a dominant effect on the damping of periodic disturbances such as stall waves in the compression system.

2.6.3 Volutes

The volute is generally not seen as a source of instability compromising the whole system, at least in any of the sources considered in this work. In the compressor, the volute fulfils the task of collecting the fluid which exits radially from the diffuser into the compressor discharge pipe. This function determines the geometrical form of the volute whose meridional wall contour follows a spiral mirabilis. At the beginning of the spiral, the volute features the tongue. The tongue can be considered as the leading edge of an airfoil which has been wrapped around the diffuser in form of the above mentioned spiral mirabilis. Analogue to an airfoil, separations can occur in the tongue region at off design conditions.

Guelich [20] provides a comprehensive sketch comparing volute design and off design operation which is presented in **figure 2.25**. The figure shows the simplified geometry of a volute including the discharge channel and the tongue marked in grey. On the bottom of each of the sketches, the static pressure distribution at the volute inlet is plotted over the circumferential position. The flow direction is shown schematically in form of arrows. In the discharge channel, a velocity profile is provided.

The top part of the figure shows the design conditions where the volute inlet flow is aligned with the geometry, more specifically with the metal angle of the tongue. The inlet pressure distribution is virtually uniform with a small kink around the tongue position due to an increase in blockage from the abrupt change in passage area.

The bottom figure represents the flow conditions in the volute at high flow rates. Here, separations can occur on the "pressure side" of the tongue due to more radial volute inflow. Furthermore, the flow is decelerated around the beginning of the volute due to the blockage of the geometry to the more radial flow entering the volute. Towards the volute exit, the flow then is accelerated as the volume flow is too large for the area available in the volute.

The middle figure shows the flow situation at low flow rates. In this case, the oncoming flow is much more tangential and the volute is "too big" for the amount of oncoming volume flow. Consequently the incidence angle on the tongue is very positive with a flow angle that can

approach zero with respect to the tangential direction. This leads to flow separation on the outside wall of the volute near the tongue, corresponding to a suction side separation in the airfoil analogy. As the volume flow approaching the volute is much too small at low flow rates, a non uniform static pressure distribution is imposed on the volute inlet with a low pressure region around the beginning of the volute and a high pressure region towards its outlet. Under such flow conditions, the volute imposes an unfavourable flow field on the upstream components in two ways. Firstly, the static pressure varies significantly around the circumference forcing the rotor to operate at different conditions periodically with rotor speed. Secondly, the tongue separation induces an additional amount of unsteadiness on the upstream parts. Both of these effects do not result in compressor instability themselves but it has to be assumed that their presence contributes significantly to destabilising the upstream parts, namely the rotor and the diffuser.

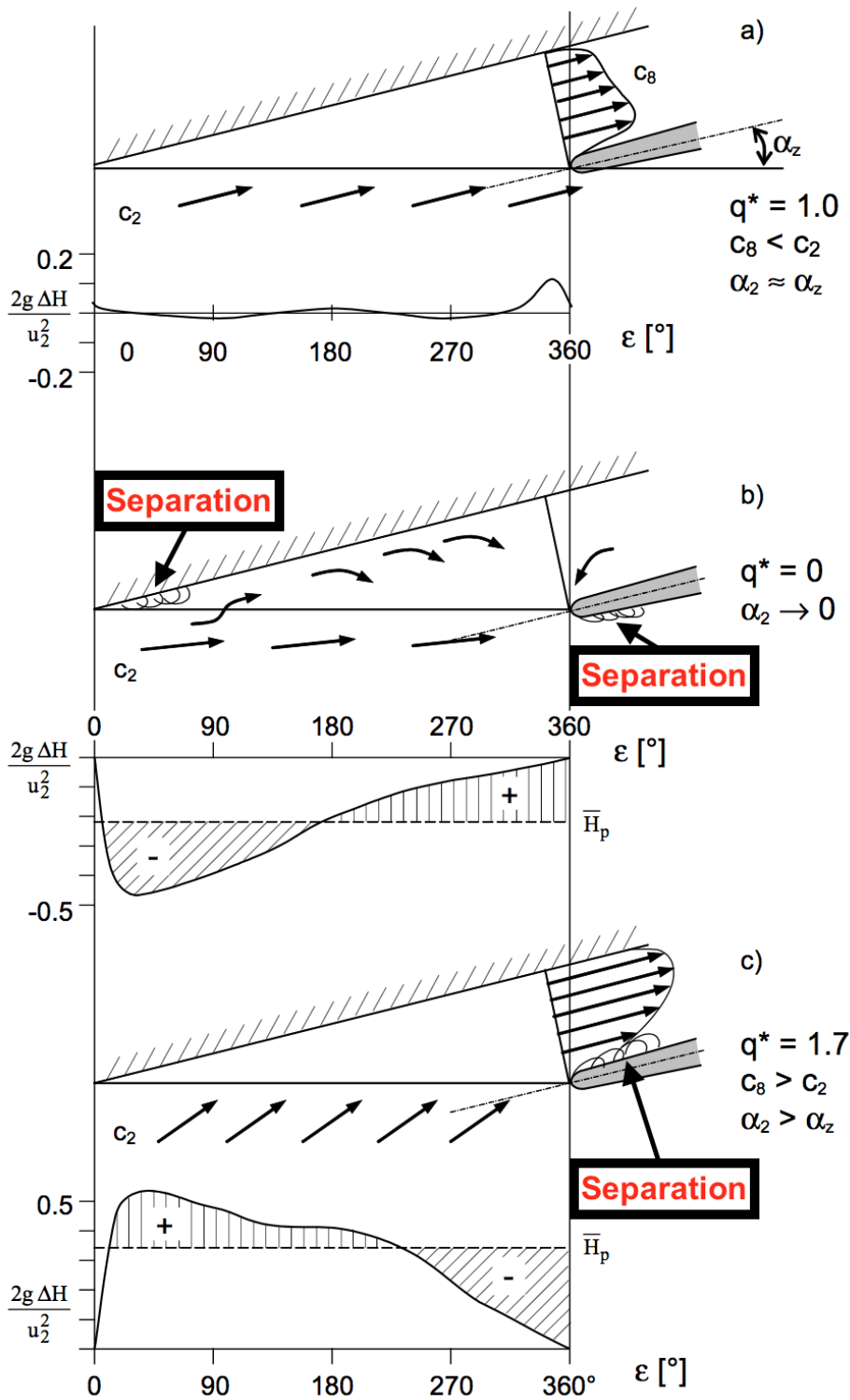


Fig. 2.25 Circumferential static pressure distribution, and velocity vectors in a volute with resulting separation zones; **Top:** Design flow rate; **Middle:** Low flow rate; **Bottom:** High flow rate [20]

2.7 Summary

This chapter gave an overview of the flow phenomena occurring in a compressor under low flow conditions. It was described how the flow structure is much more complex than that at design conditions and eventually leads to periodic fluctuations in the fluid which causes material stresses so high that the machine has to be shut down to avoid destruction. Clear definitions for terms such as Stall, Spike type stall Inception, Modal Stall Inception, Rotating Stall, Surge and Inlet Recirculation have been provided. Furthermore, it has been discussed that at low speed, it is most likely the rotor which causes the instabilities in an automotive turbocharger radial compressor due to the altered amount of compression realised over the rotor which results in a reduced density at the rotor exit. As a consequence, the diffuser operates at higher volume flow rates. Within this context, the phenomenon of inlet recirculation was discussed in further detail. Once it is established, inlet recirculation is a flow pattern which occurs at the rotor inlet and represents an axisymmetric blockage in the shroud region which does not cause intense periodic fluctuations so that the machine can continue operation. It aerodynamically reduces the inlet throat area and consequently reduces incidence in the free part of the rotor inlet due to higher axial velocities. A summary of the scarce knowledge about inlet recirculation was provided and different aspects of the phenomenon were discussed. Despite having been observed in a broad variety of radial, semi axial and axial compressors, very little is known about inlet recirculation and the flow conditions at which it occurs. Furthermore, the information available is partially contradictory.

One example is the inception mechanism which is not yet understood. Although different explanations could be found in the relevant literature, they identify different locations and mechanisms as the origin of inlet recirculation. Examples include the passage throat, the leading edge suction side or generally locations of high diffusion. Although it is not attempted in this thesis to understand the full inception mechanism of inlet recirculation, the question is directly related to the wider research question which aims to clarify the general flow conditions leading to inlet recirculation:

Under which conditions does recirculation occur?

Several studies from the public domain have been introduced, which give limited information about the character of the flow pattern under recirculation and its effects on compressor performance. The altered velocity distribution under recirculation features a negative axial velocity in the recirculation zone that goes along with a positive tangential velocity component has been shown based on experimental results. One of the most important questions regarding the effects of inlet recirculation is its performance penalty. There is only limited

information about this in the relevant literature. In the work presented here, this problem is addressed with the research question:

What are the effects on compressor performance in terms of energetic cost?

Measures to minimise inlet recirculation via struts in the intake have been discussed and their positive effect on map width and performance was shown. Investigations on the relation of inlet recirculation and the rotor geometry have not been found. It is thus also unknown whether inlet recirculation can be altered by modifying the rotor geometry. In order to find out more about the possibilities of altering inlet recirculation, the following research question was raised in this work:

How can a designer influence the mechanisms sustaining recirculation?

Several reduced order models for inlet recirculation available in the public domain were introduced, all of which showed limited accuracy in terms of predicting the onset point of inlet recirculation on the performance map. The models also attempted to depict the intake flow field and the thermodynamic inlet parameters which are getting altered by the phenomenon. Although the alterations have been modelled qualitatively, the accuracy of these models is limited. The problem of reduced order modelling was addressed with the following research question :

How can recirculation be accounted for in preliminary design?

In order to answer these questions, an automotive turbocharger compressor has been investigated complementarily with experiments and numerical simulations. Those methods are presented in detail in the following chapter. .

Chapter 3

Methods

3.1 Introduction

In order to answer the research questions outlined in the previous two chapters, a research turbocharger compressor available at the Whittle Laboratory, which is typical for passenger vehicle applications, has been used. The machine has been investigated experimentally and numerically. The prominent features of the compressor, the experimental setup and the numerical setup are described in this chapter.

3.2 Research compressor

The work for this thesis has been carried out on a (Garrett) Honeywell Turbocharger. The unit is suitable for diesel engines between 2.0 and 4.0 litres. The compressor with the cut open housing is presented in **figure 3.1**.

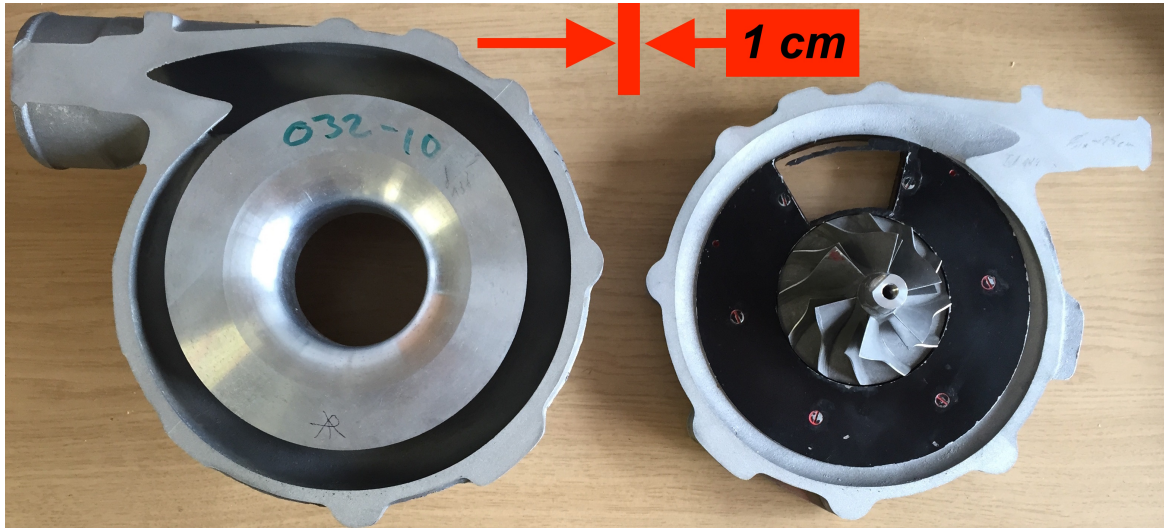


Fig. 3.1 Research Compressor

The machine features oil cooled journal bearings and a simple compressor design without inlet bleed channel as well as a vaneless diffuser and volute. The key performance parameters of the compressor are listed in **table 3.1**.

Table 3.1 GT3776 Key performance parameters

Design speed	105 000	[rpm]
Design blade tip speed Mach number	1.21	[-]
Design mass flow	0.26	[Kgs ⁻¹]
Choking mass flow	0.37	[Kgs ⁻¹]

The lack of a bleed channel leads to a simpler inlet flow structure so that the phenomenon of inlet recirculation can be studied in isolation without the extra complexion of interaction with the bleed channel flow. The lack of the bleed channel also leads to a narrow compressor map at high speeds, as can be seen in the manufacturer operating map shown in **figure 3.2**. More detailed information about the different sections of the compressor is provided in the following sections.

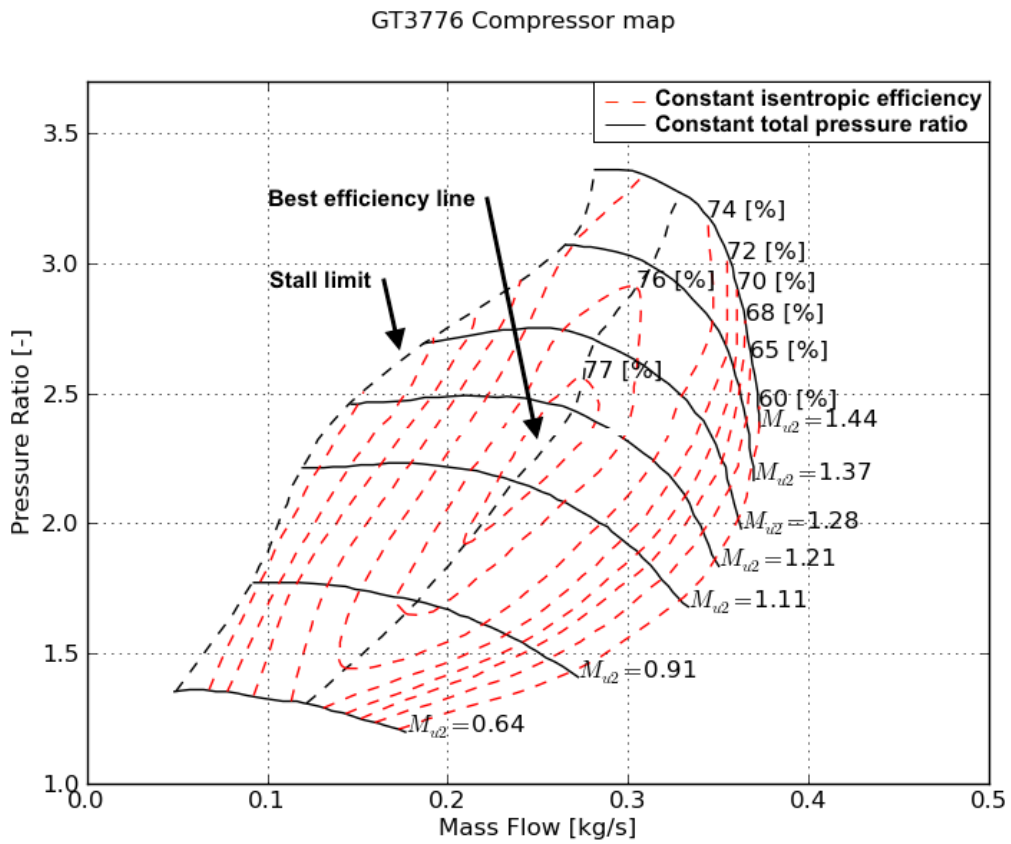


Fig. 3.2 Research compressor operating map

3.2.1 Inlet

The inlet section of the compressor is designed as a straight duct with a bellmouth as inlet. The housing does not have a bleed channel. A sketch of the setup is shown in **figure 3.3** and the key geometrical parameters are listed in **table 3.2**. As the rotor inlet radius r_b is an important geometry feature, non-dimensional geometry lengths have been specified based on it.

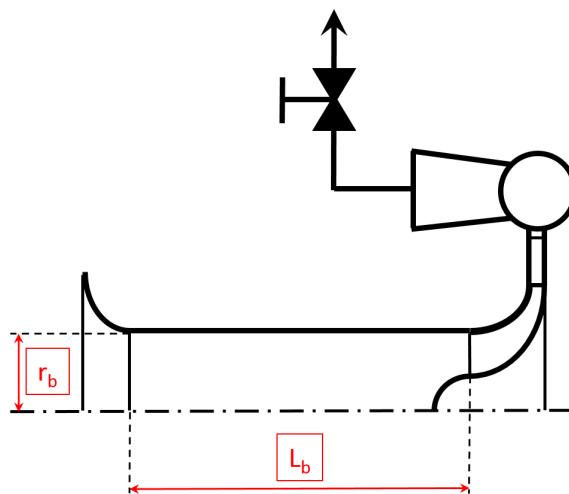


Fig. 3.3 Sketch: Compressor inlet with Bellmouth

Table 3.2 Inlet bellmouth main geometry parameters

Radius	r_b	28.0	[mm]	1.0	$[\frac{1}{r_b}]$
total length	L_b	106.38	[mm]	3.80	$[\frac{1}{r_b}]$

3.2.2 Rotor

The rotor of the research compressor has a diameter ratio $\frac{d_2}{d_1}$ of 1.385 and features six main and six splitter blades. The main blade leading edge is backswept in the meridional plane. The splitter blade has a vertical leading edge. The distributions of the key geometry features of the rotor are presented in non-dimensional form **figure 3.4**, where the main blade features are shown in black and the splitter blade features are shown in blue.

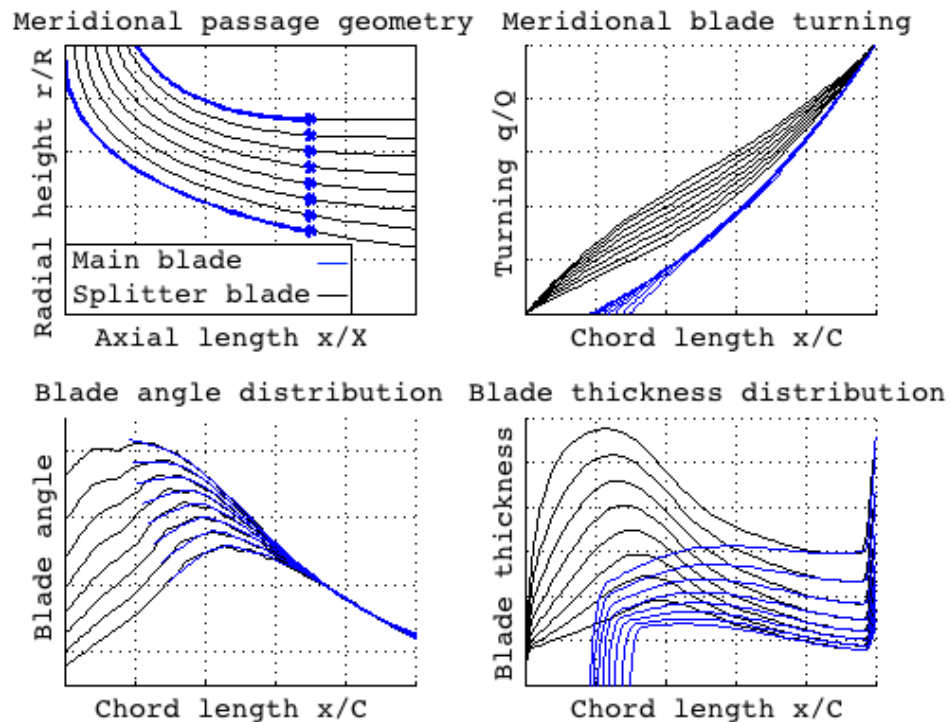


Fig. 3.4 Key geometry features of the rotor

The top left graph shows the meridional passage geometry. It has been non-dimensionalised with the maximum values for X and R . The top right graph shows the meridional blade turning in form of the local turning q non-dimensionalised by the overall turning Q . The turning is calculated as the change in blade angle from the leading edge blade angle. This value is plotted over the chord x which has been non-dimensionalised by the overall chord length C . The bottom left graph shows the absolute blade angle distribution over the non-dimensional chord length. The bottom right graph shows the absolute blade thickness distribution over the non-dimensional chord length. The leading edge angle distribution is shown in more detail in **figure 3.5**. The main blade shows a free vortex design, and the splitter blade a linear blade angle distribution over the span. All geometry parameters have been determined

using a FARO 3D scanner arm with a resolution of 200 microns. An example of a rotor scan is provided in **figure 3.20** where the physical geometry is compared to the numerical geometry used for the CFD calculations. In order to obtain a more approachable description, 8 radial cuts through the rotor blade were evenly distributed over the span and the geometry parameters were extracted in these planes. This data is presented in figure 3.4 above. More detailed information about the rotor performance will be presented in the following result chapters and will not be presented here.

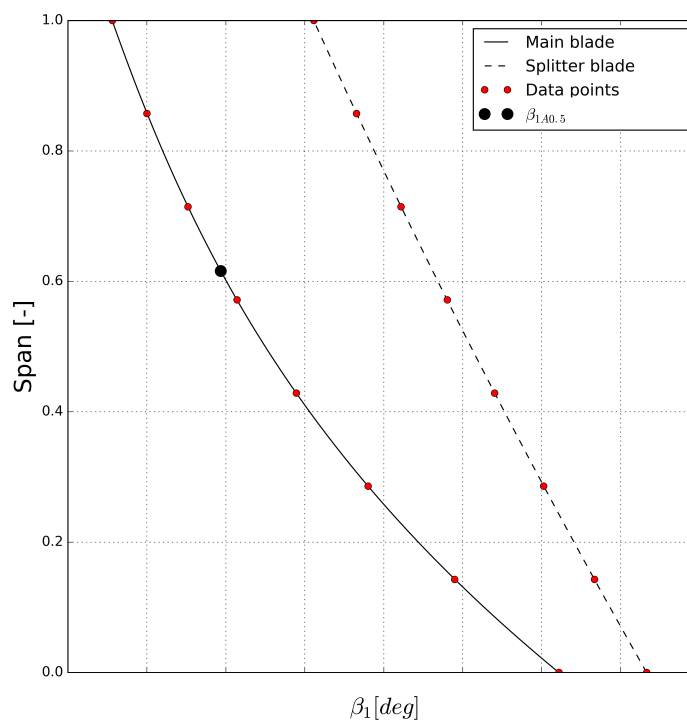


Fig. 3.5 Leading edge span-wise blade angle distribution

3.2.3 Diffuser

This section gives an overview over the diffuser geometry and its performance. In order to achieve wide range at the cost of peak efficiency, the compressor features a vaneless diffuser. Its geometry is shown in **figure 3.6**. It is split into two parts. The pinched section which connects the rotor and the diffuser has a nozzle shape with an area ratio of 0.67 $\left(= \frac{d_2^* b_2^*}{d_2 b_2} \right)$ to accelerate and smoothen the strongly nonuniform flow exiting the rotor. The second part is a parallel walled vaneless diffuser with an area ratio of 1.73. The area ratio from inlet to outlet of the two sections is 1.168. The pinched section alters the rotor outlet flow distribution and affects the performance of both, rotor and diffuser. As suggested by **Traupel [47]**, the effects of the pinched section will not be accounted for separately. Instead, the occurring losses will be included in the following overall diffuser performance estimations.

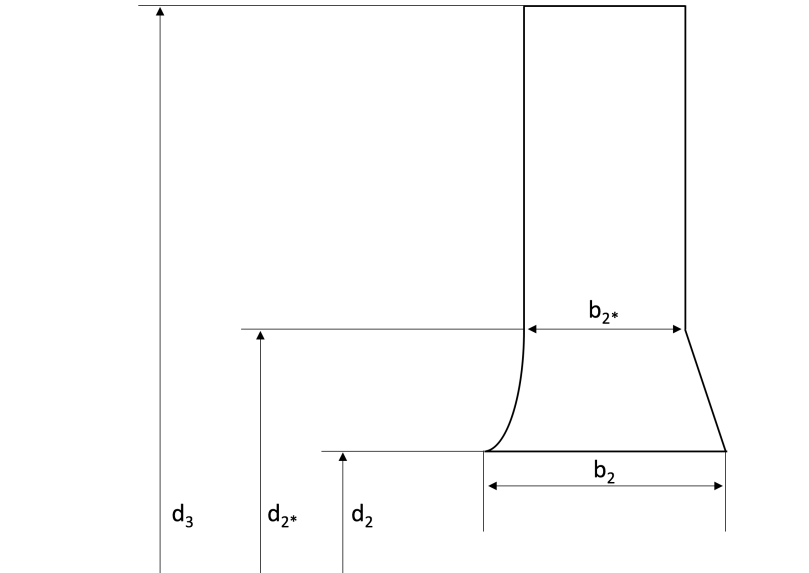


Fig. 3.6 Diffuser Geometry

All key geometry and theoretical performance parameters of the diffuser section are presented in **table 3.3**. An idea about the performance of the diffuser can be gained by looking at the ideal incompressible pressure recovery as defined in **equation 3.1**.

$$cP_{id} = \frac{p_3 - p_2}{\rho c^2 / 2} = 1 - \left[\frac{c_3}{c_2} \right]^2 = 1 - \left[\frac{r_2}{r_3} \right]^2 \quad (3.1)$$

The operating range of the vaneless diffuser is geometrically limited by choking for high flow rates and by **vaneless diffuser rotating stall (VDRS)** towards low flow rates. The

onset of VDRS occurs at a **critical diffuser inlet angle** α_{2crit} and has been investigated theoretically and experimentally.

Table 3.3 GT3776 Diffuser key parameters

Width ratio	$\frac{b_2^*}{r_2}$	0.092	[-]
Radius ratio	$\frac{r_3}{r_2}$	1.78	[-]
Area ratio	$\frac{A_3}{A_2}$	1.168	[-]
ideal pressure recovery	cp_{id}	0.69	[-]
critical inlet angle	α_{2crit}	≤ 78.0	[°]

Jansen [26], [25] provided a theoretical approach to estimate diffuser performance, where he assumed an unsteady, inviscid and incompressible flow. The diffuser behaviour then was modelled via the continuity and momentum equation in the radial and tangential direction. The unsteady flow field was given by steady free vortex flow with a superimposed perturbation. Within this model, Jansen was able to show that rotating stall in the vaneless diffuser was triggered by local reverse flow. He also showed that VDRS occurred even with uniform inlet and outlet flow and thus without interaction of the rotor. The rotational speed of the perturbation he observed was between 5% and 22% of the impeller rotational speed. From his results, Jansen concluded that VDRS was most likely triggered by the boundary layer region as the streamlines there are curved more inwardly but that the dynamics of the instability depend on the inviscid part of the flow.

Fringe and Van den Braembusche [16] were able to confirm the destabilising effect of the boundary layer in their calculations.

Senoo and Kinoshita [51] refined Jansens model. Their studies resulted in the diagram shown in **figure 3.7**. It allows to determine α_{2crit} depending on the ratio of diffuser width to inlet radius $\frac{b_2^*}{R_2}$ and the diffuser inlet to outlet radius ratio $\frac{R_3}{R_2}$.

Van den Braembusche [49] collected experimental results for VDRS from multiple authors and plotted their results into a diagram shown in **figure 3.8** which displays α_{2crit} as a function of the diffuser width ratio. The sources for the experiments shown in the diagram are listed in **table 3.4**. It needs to be taken into account that some of these results are documented to limited details, meaning that it is not always clear if it the machine fails due to VDRS or **abrupt impeller rotating stall (AIRS)**. The distinction is hard to make but it can generally be said that the amplitude of the pressure and velocity variations is smaller for VDRS and the pressure rise curve does not show a discontinuity at the onset of it [49].

For the geometry of the present compressor, a critical diffuser inlet angle α_{2crit} of 80.0 degrees can be determined based on the theoretical approach shown in figure 3.7. The

experimental data shown in figure 3.8 gives an α_{2crit} of 78.0 degrees.

The more conservative experimental value is taken as theoretical critical diffuser inlet angle. In reality, VDRS can occur at even lower diffuser inlet angles due to Mach number, Reynolds number and inlet perturbation effects.

The theoretical value will be compared to the experimental results obtained in the experiments during this research in the following results chapters.

Regarding the coupling between the rotor and the diffuser, **Sparkovszky [42]** reported about the phenomenon of backward travelling rotating stall waves in vaned radial diffusers, which moved against the rotational direction of the flow and described the interaction between the diffuser and the rotor, particularly during the occurrence of instabilities. This behaviour at least partly applies to vaneless diffusers as well.

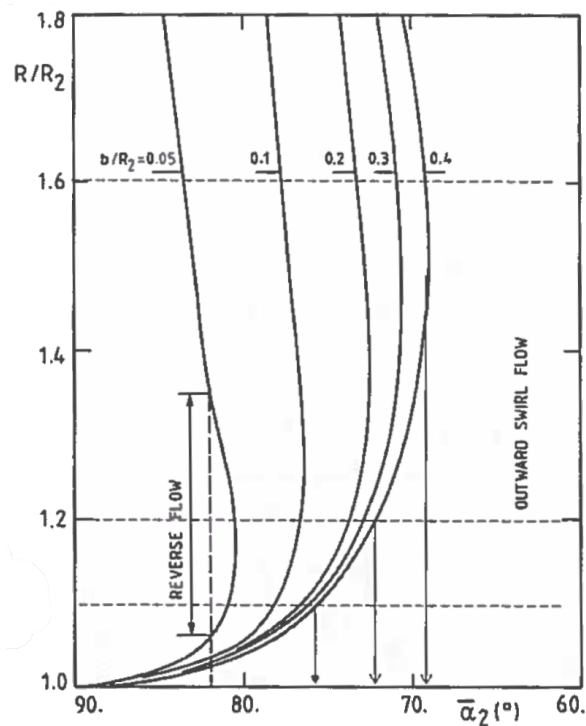


Fig. 3.7 Theoretical correlation for α_{2crit} [49]

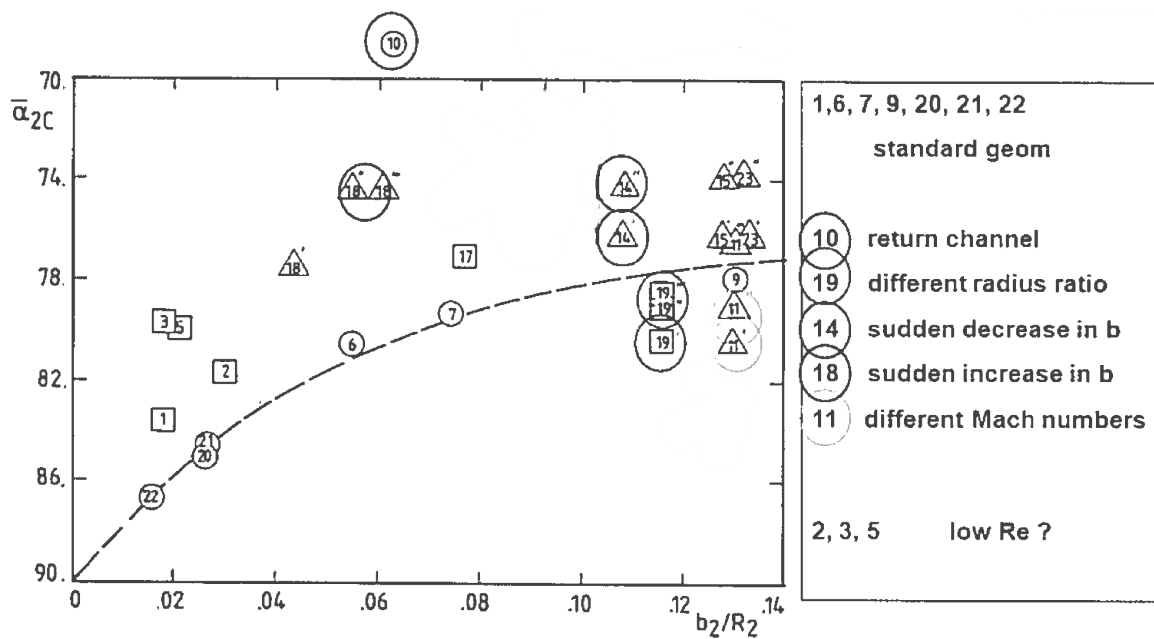


Fig. 3.8 Experimental correlation for α_{2crit} with $\frac{b_2}{R_2}$ [49]

Table 3.4 Source of experimental data shown in figure 3.8

Test point	Reference	Test point	Reference
0	Jansen (1964)	1-2-3-5	V. d. Braembusche et al. (1980)
6-7-9	Senoo and Kinoshita (1978)	10-11	Abdelhamid et al (1979)
14-15	Abdelhamid and Bertrand (1980)	17	Fringe et al (1984)
18	Wachter and Rieder (1985)	19	Abdelhamid (1983)
20-21-22	Kinoshita and Senoo (1985)	23	Kaemmerer and Rautenberg (1986)
24	Imaichi and Tsurusaki (1979)		

3.2.4 Volute

The last section of the research compressor is a volute with an elliptic cross sectional shape and an attached cone diffuser, as displayed in **figure 3.9**. The key non-dimensional performance parameters are listed in **table 3.5**. Regarding the volute performance, a detailed discussion is given in **section 3.4.3**.

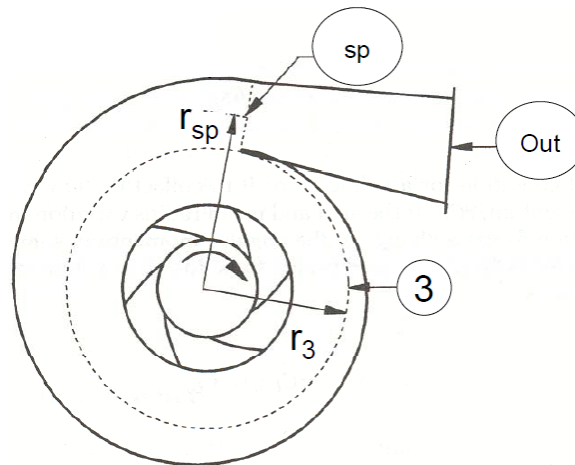


Fig. 3.9 Sketch: Volute with key geometry features

Table 3.5 GT3776 Volute key parameters

Tongue radius ratio	2.042	[-]
Tongue radius ratio (W&K model)	1.579	[-]
Cone diffuser aspect ratio	1.47	[-]
Cone diffuser Area ratio	1.2	[-]

3.3 Experimental setup

In order to investigate the compressor performance under inlet recirculation, the turbocharger has been set up in a simple test rig. A scheme of the experiment is presented in **figure 3.10**. It allows to adjust the compressor operating point via controlling the compressor shaft power and the compressor back pressure. The power input is realised via a vacuum pump which sucks air from ambient conditions through the turbine side of the turbocharger. The power extraction can be controlled by variable inlet guide vanes on the turbine, displayed as valve upstream of the turbine in the sketch. The setup provides about 7 kW to the compressor. This amount of power allows to stably operate over the whole width of the compressor map up to 50% design speed. The test section itself consists of two major parts. The compressor, which sucks air from ambient conditions and a downstream valve which allows to regulate the back pressure.

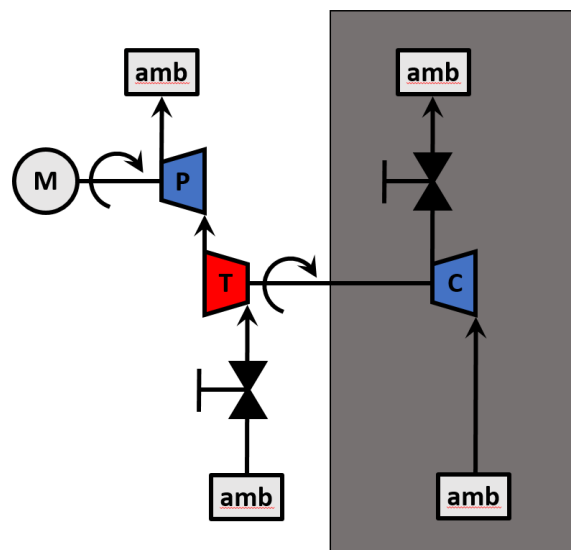


Fig. 3.10 Principle sketch of the experiment

A more detailed layout of the compressor test section is sketched up in **figure 3.11**. It features a separate mass flow measurement unit in form of an inlet bellmouth, which is separated from the compressor inlet by a large diameter airtight settling chamber. This setup is necessary because the flow in the second inlet bellmouth which is connected directly to the compressor is strongly affected by the phenomenon of inlet recirculation. More specifically, the inlet recirculation bubble extends far upstream of the leading edge into the inlet bellmouth causing an alteration in flow field and simultaneously, in casing pressure. A correct mass flow measurement in the bellmouth connected to the compressor is thus impossible under operating conditions where the phenomenon is present. To resolve this problem, the above

mentioned inlet box with an upstream bellmouth was installed. This setup ensures that the mass flow measurement does not deteriorate because of the occurring inlet recirculation and its casing pressure fluctuations. The compressor itself features the inlet bellmouth, as described in **section 3.2.1**. The exit throttle is realised via a simple gate valve.

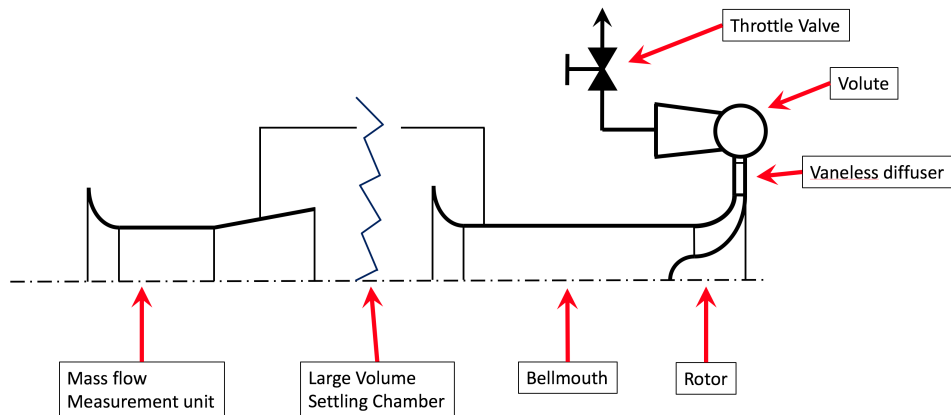


Fig. 3.11 Sketch of the compressor test rig: parts of the setup

The fundamental measurement setup is oriented on the different parts of the machine and four main measurement planes as shown in **figure 3.12** are defined. **Table 3.6** gives an overview of the position of the measurement planes, and the acquired properties at the location. The shaft speed of the turbocharger was measured via an analogue inductive sensor located in the bearing housing of the turbocharger. The analogue signal was passed on to the computer and processed via a Labview routine.

Table 3.6 Mean measurement planes: measured properties

Plane	Location	T_t	p_t	p
Plane 0	ambient	X	X	X
Plane 1	rotor inlet	X	X	X
Plane 2	rotor outlet			X
Plane 3	diffuser outlet			X
Plane 4	volute outlet	X	X	X

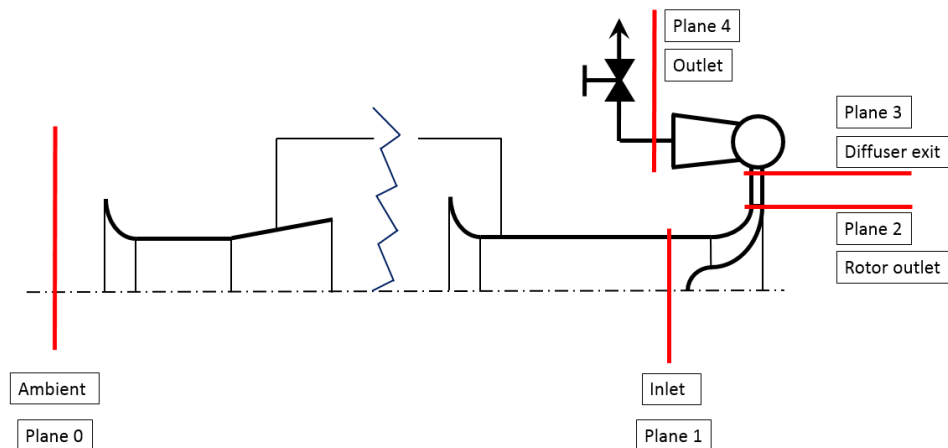


Fig. 3.12 Sketch of the compressor test rig: mean line measurement planes

In order to get more detailed insight into the local flow conditions, several additional measurements were taken. An overview of their location in the test rig is given in **figure 3.13**.

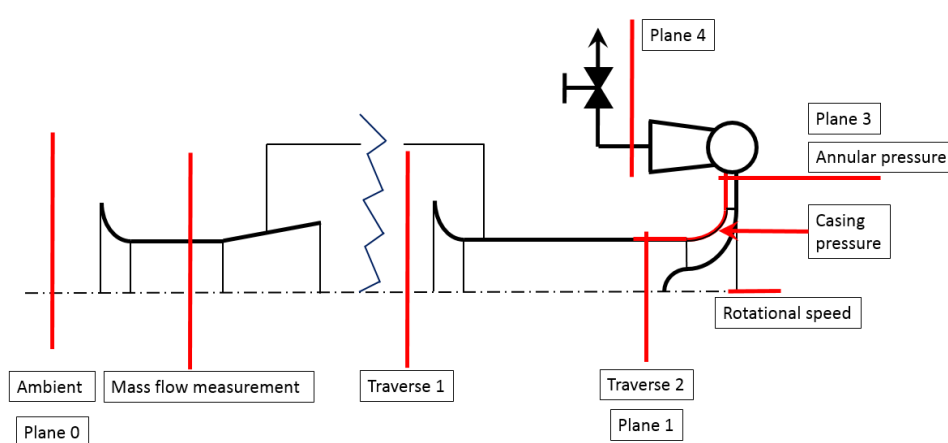


Fig. 3.13 Sketch of the compressor measurement arrangement: probing positions

The compressor mass flow measurement was carried out using a separate mass flow measuring unit that used the Venturi effect. It consisted of a bellmouth, a constant diameter straight measurement tube and a cone diffuser to reduce the exit velocity. The unit was located sufficiently far upstream of the compressor inlet to avoid interference with the recirculation bubble. The bellmouth throat area was designed to produce sufficiently low flow speeds so that thin boundary layers could be assumed. At the same time the throat area was designed to produce a high enough pressure drop for a strong enough signal for the sensor. A total of three static pressure tappings equally distributed around the bellmouth shroud were positioned two inlet diameters downstream of the bellmouth inlet and one inlet

diameter upstream of its outlet to ensure straight flow. The bellmouth at the compressor inlet and the mass flow measurement unit were connected to the compressor using a 310mm diameter settling chamber.

The overall performance was measured using total temperature and total pressure sensors at the measurement planes zero and four. The outlet total pressure probe was adjusted to the outlet flow direction and is shown in **figure 3.14**. In outlet plane four, the total temperature was measured as the average of three equally distributed probes around the annulus. The measurement plane was placed 105mm downstream of the volute exit in a straight pipe which was attached to the volute exit and is shown in **figure 3.14**. The maximum total pressure was found at an angle of 30 degrees counterclockwise from the axial direction at 50% speed design conditions, implying a swirl component at the exit of the volute. This swirl originates from the radial velocity component of the flow entering the volute.

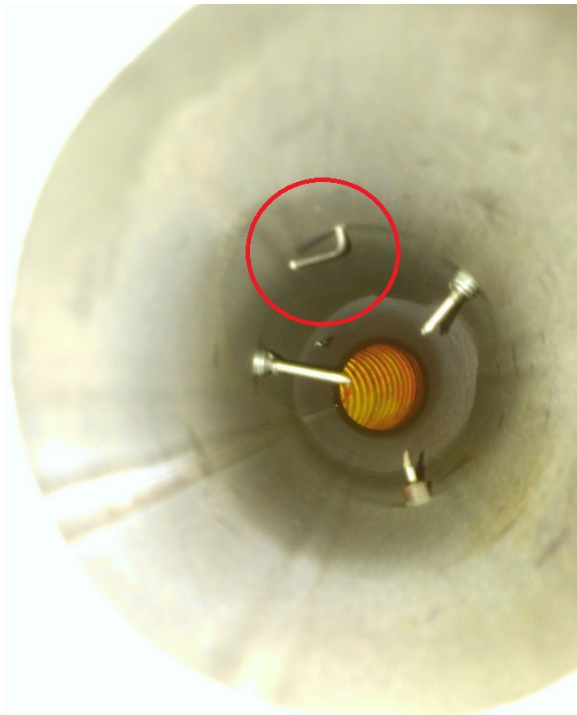


Fig. 3.14 pitot probe and total pressure sensors at the compressor exit

A total pressure traverse measurement was carried out upstream of the compressor bellmouth in order to ensure clean inflow into the test section.

A second total pressure traverse was put 7mm upstream of the rotor leading edge so that the radial total pressure distribution close to the impeller could be studied.

In order to determine the influence of the volute tongue on the diffuser exit pressure field, the annular pressure distribution in the diffuser was measured. For this, 20 casing pressure

tappings with a hole diameter of 1.0 mm were equally distributed around the annulus. The probes were placed at a pitch circle diameter of 97.7 mm and their location is shown in **figure 3.15**.

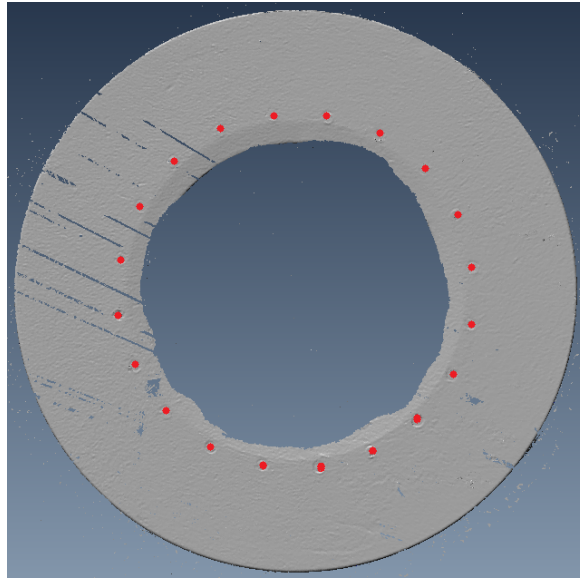


Fig. 3.15 circumferential pressure tapings in the diffuser back plate

The casing was equipped with a set of casing pressure tap holes. Their angular position relative to the volute tongue was 135° in the clockwise direction. A sketch of their position is shown in **figure 3.16**.

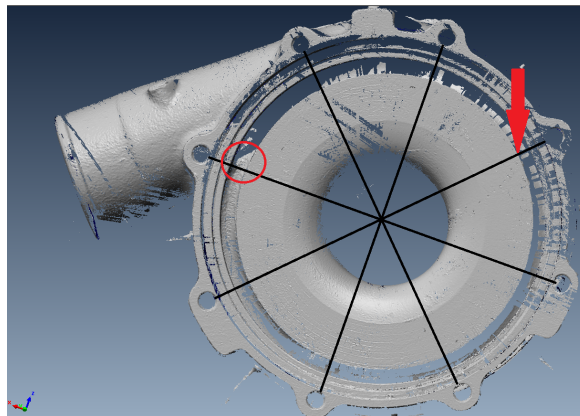


Fig. 3.16 pressure tap positions in the housing relative to the volute tongue

In total, 19 tap positions with a hole diameter of 1.0 mm were distributed between the inlet bellmouth and the diffuser exit of the machine. **Figure 3.17** shows the location of all pressure taps as red dots in a sketch of the compressor casing. The dashed vertical lines mark

the rotor main and splitter leading edges. The dashed horizontal lines mark the rotor trailing edge and the diffuser exit radius.

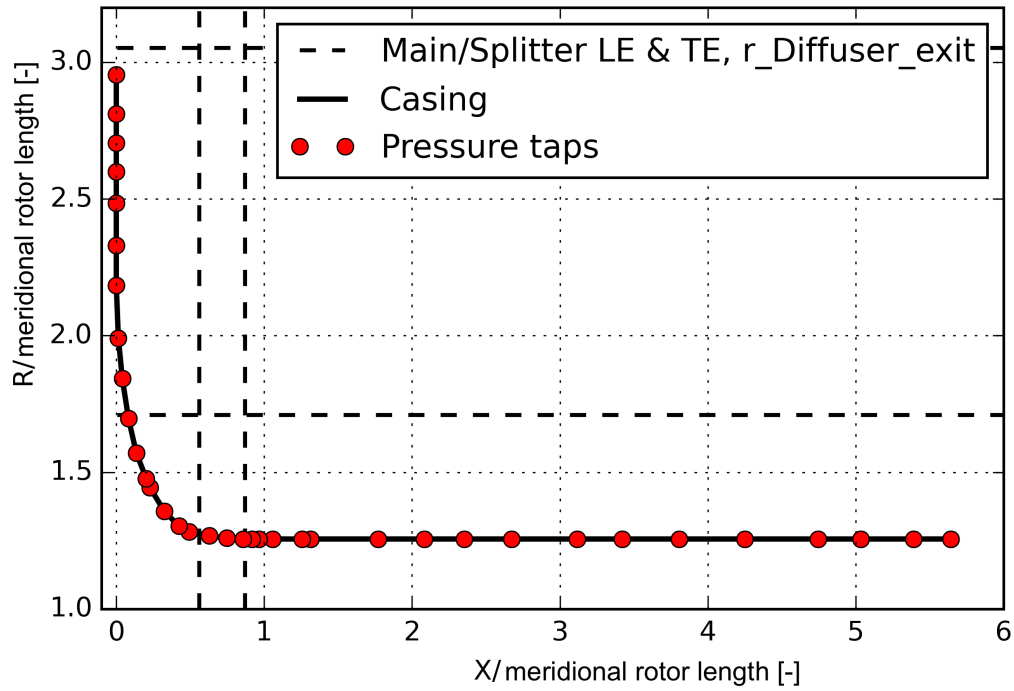


Fig. 3.17 casing pressure tap position

3.3.1 Sensors and calibration

The compressor measurements have been carried out with three types of sensors. An analogue inductive sensor was used to measure the shaft speed by picking up once-per-revolution signals from the shaft. Temperature measurements were carried out using T-Type temperature probes in combination with a Comark Tempscan c8600 thermometer. For the pressure measurements, a Cole Parmer high pressure sensor was used. The calibration curve of the pressure sensor is shown in **figure 3.18**. The sensor was combined with 5 Drallim 6 Channel pressure valves so that a total of 26 separate pressure channels were available. All hardware was connected to a Computer via a NI – Card and fed into a Labview 8.6 virtual measurement environment. More specific details about the measurement sensors can be found in **Appendix A**. All measurements were averaged over a time window of 10 seconds which equaled 9305 revolutions at 50% design speed. In order to assess the accuracy of the pressure transducer, a total of 5 sample measurements were taken. For each measurement, the transducer was exposed to a specific pressure. Those pressures were evenly spread between 88 and 156 kPa. For each measurement, 10 readings were carried out and their average was calculated in order to assess the accuracy. The cumulated accuracy for all 5 measurements was determined to be 0.05% which is equivalent to a deviation of 56.6 Pa.

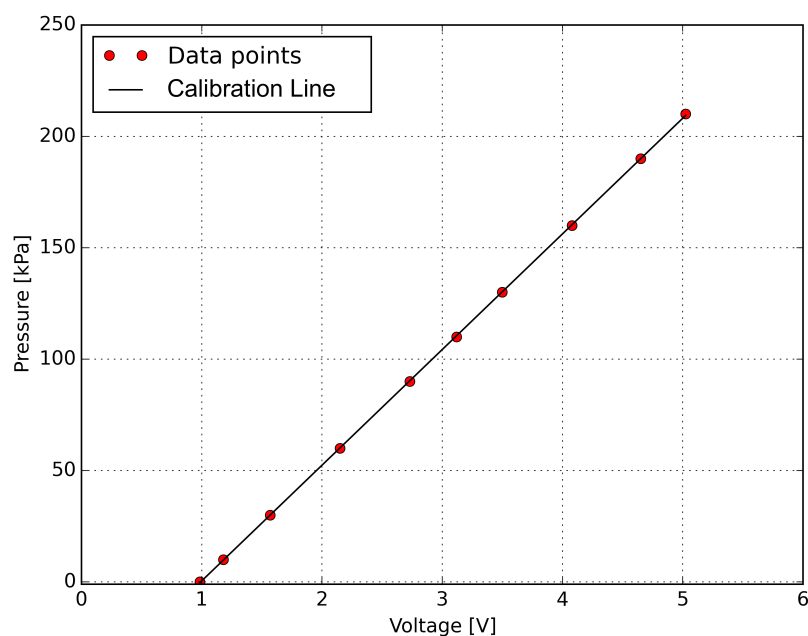


Fig. 3.18 Calibration curve of the pressure sensor

3.3.2 Validation

In a first measurement, the test rig was validated by reproducing the characteristic given by the manufacturer for 50% design speed. **Figure 3.19** shows the total to total pressure rise in the upper part and the isentropic total to total efficiency over the global flow coefficient defined in **equation 3.2**.

$$\phi_{t1} = \frac{\dot{m}}{\rho_{t1} D_2^2 u_2} \quad (3.2)$$

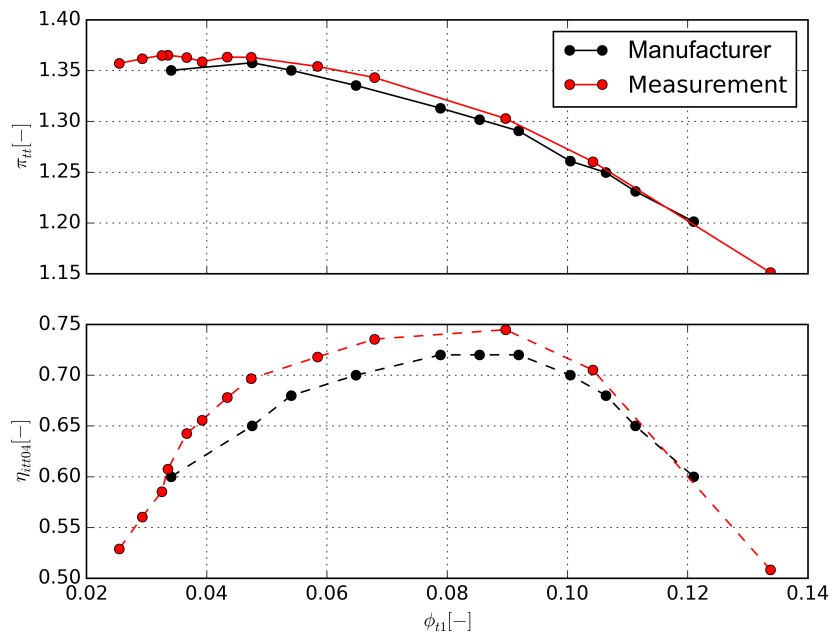


Fig. 3.19 Compressor characteristic: comparison measurement and Manufacturer data

The manufacturer data is plotted as black lines and the measurements are shown in red. Qualitatively, both graphs show a good agreement. In terms of absolute values, the total to total pressure ratio curve is almost identical. However, the efficiency in the measurement is consistently higher than the values provided by the manufacturer. The deviation corresponds to a total temperature difference at the compressor exit of 1.5K. Reasons for this deviation are a different setup of the measurement, particularly the measurement planes. As a result, the probe locations were not setup in the same way as the validation measurement of the manufacturer. Unfortunately, no standard is given here. Furthermore, the test rig has not been insulated towards the surrounding air. As a result, a certain heat loss into the ambient

will occur in the test rig which will contribute to the error in exit total temperature and result in a higher efficiency. Taking into account the differences in terms of setup of the experiment, the data shows reasonable agreement to successfully validate the experimental rig.

3.4 Numerical setup

In the second part of this project, the compressor was modelled numerically to investigate aspects of fluid dynamics associated with inlet recirculation. The calculations for this investigation were carried out with Turbostream 3.1.4 which is an adaption of John Denton's TBLOCK solver to GPU hardware [2]. The calculation scheme is a multi block Reynolds Averaged Navier-Stokes solver. This solver is widely used in turbomachinery research and industry and correspondingly applied to a broad variety of flow problems. The solver is based on the finite volume approach and uses the explicit SCREE algorithm. The calculations were carried out using the Spallart Almaras turbulence model. Depending on the non dimensional wall distance y^+ of the first grid point from the wall, the code uses two different methods to determine the wall shear stress.

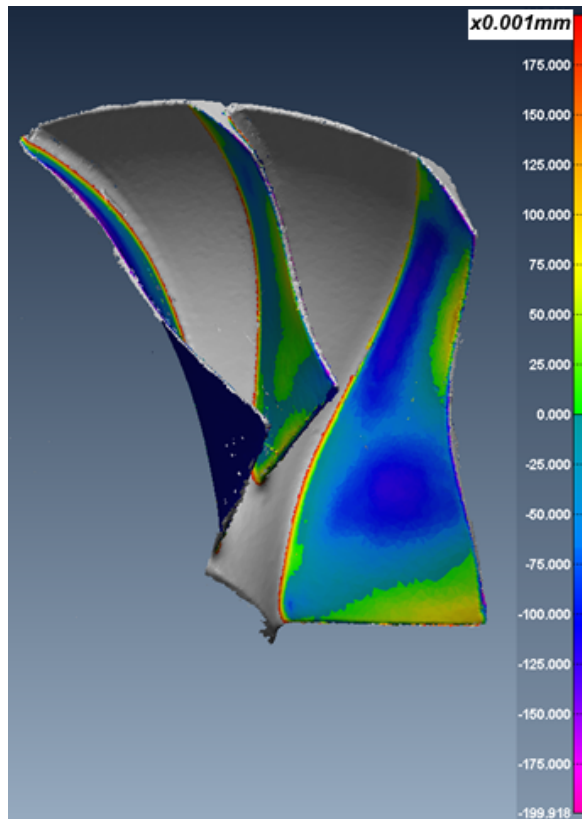


Fig. 3.20 Comparison of physical and virtual geometry

If the non dimensional wall distance of first grid point away from the wall is smaller than ten, which means that it is located within the viscous sublayer, the code calculates the wall shear stress directly from the local velocity. If the first grid point away from the wall lies outside of the viscous sublayer, the code uses wall functions to determine the wall shear

stress. In order to make sure that the virtual geometry exactly matches the real geometry in the experiment, the whole machine was 3d scanned with a FARO 3-D measurement arm. The accuracy of this machine is 200 microns. The comparison is shown in **figure 3.20**, where the deviation of the virtual geometry from the real is shown as a colour-map over the geometry contour.

The maximum measured deviation from the real geometry was 0.1 mm, which means that all geometrical deviations between the real hardware and the virtual model were smaller than the accuracy of the measurement method used. In absolute terms, a mismatch of smaller than 0.1mm is within the manufacturing tolerance, so the virtual model was confirmed to match the real geometry to a sufficient level. It has to be pointed out that the modelled geometry did not feature any real geometry features, such as fillets for example, so that the numerical model still represented a simplification. For the purpose of this study, these simplifications were justifiable as the main interest was on the investigation of a general flow feature rather than a fully accurate reproduction of performance.

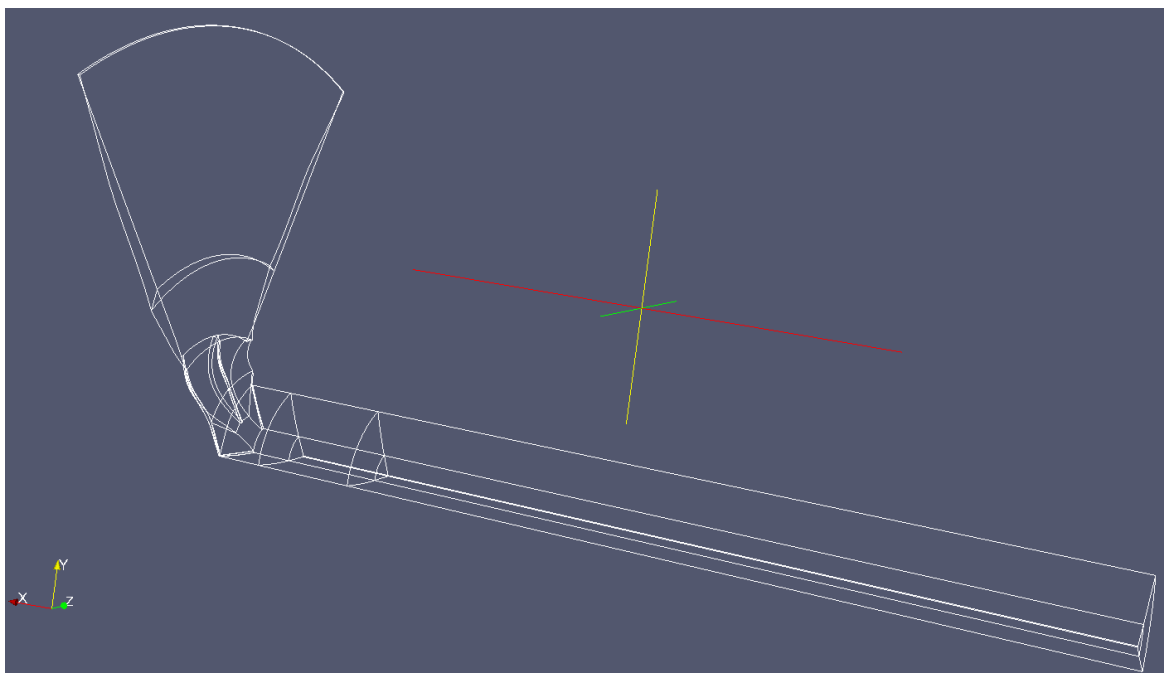


Fig. 3.21 Sketch of the overall computational domain

In order to reduce complexity and mesh size, the volute was not included in the 3D-model. As a result, the numerical domain was simplified to the inlet, the rotor and the vaneless diffuser part of the machine. The inlet was modelled as an angular section of 60 degrees of a cylindrical duct. In order to avoid interference of flow phenomena with the inlet boundary condition, the inlet block was extended to a length of 10 inlet diameters and the mesh was

coarsened towards the inlet boundary condition plane. An exit block in shape of a nozzle was attached to the diffuser end and the mesh was coarsened towards the exit boundary condition plane. The nozzle wall was designed in form of a cosine curve shape with a variable exit area. **Figure 3.21** shows an overview of the numerical model.

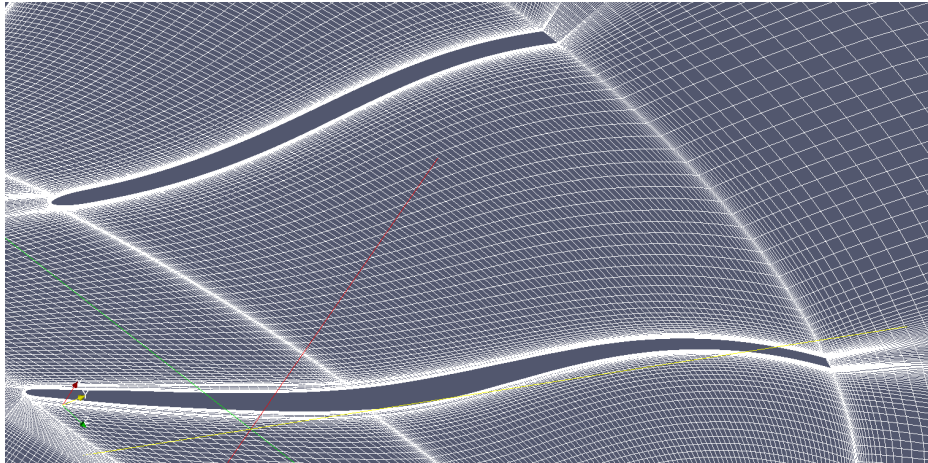


Fig. 3.22 Grid topology around the main and splitter blades

The grid generation was carried out using Ansys - ICEM. Because of the blunt trailing edges of the impeller wheel, a C-mesh topology was chosen. The grid topology around the blades is given in **figure 3.22**. The main blade tip gap was modelled to be uniform over the chord with a clearance of 2.76% relative to the main blade leading edge span. The meridional shape of the tip gap is shown in figure 7.1 and corresponds to the datum case shown there. The splitter blade tip gap has the same shape as the corresponding section of the main blade on the chord. The grid topology in the tip gap is shown in **figure 3.23**. It features 20 mesh points in the radial direction and 38 mesh points in the tangential direction.

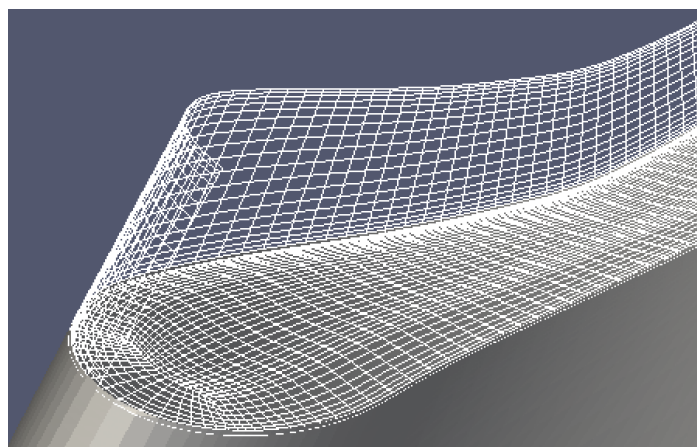


Fig. 3.23 Grid structure in tip gap

In order to determine the mesh quality, the non dimensional wall distance y^+ of the first grid point away from the viscous walls was investigated at a normal flow operating point close to the onset of recirculation at 50% speed. The obtained non dimensional wall distances in the model at this operating point are plotted in **figure 3.24** with the hub and blade surfaces on the left and the shroud surface on the right. The non dimensional wall distance was found to be below five and thus in the viscous sub layer in the regions of interest of the model. However, regions with wall distances above five were present, namely at the rotor trailing edge, in small regions around the blade leading edges as well as on the shroud close to the blade pressure sides. The total mesh size for a single passage was approximately 6 million.

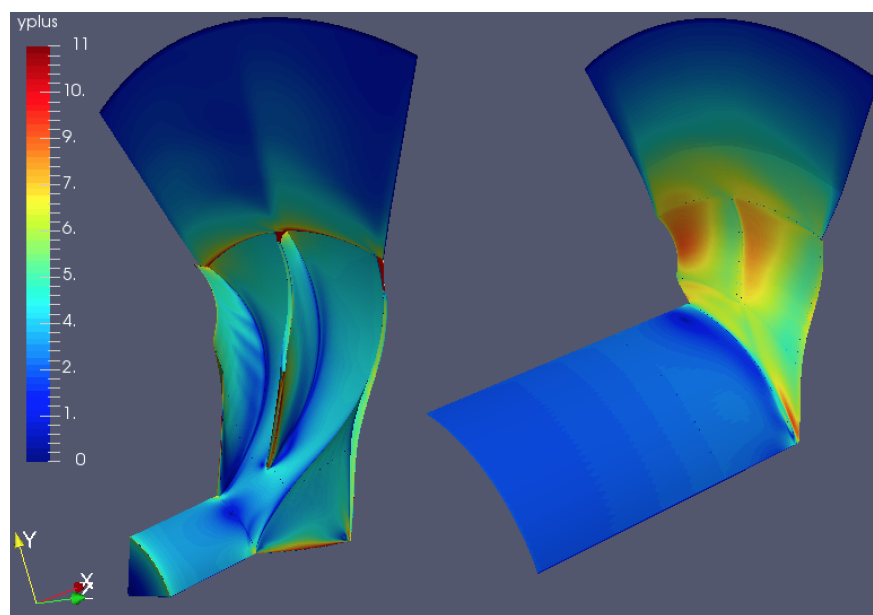


Fig. 3.24 Non dimensional wall distance within the model at 50% speed normal flow conditions; **Left:** Hub surfaces and Rotor blades; **Right:** Shroud surfaces

The calculations were validated with the experimental data obtained during this work as well as the manufacturer compressor map. The inlet and outlet conditions were specified using experimental data described in the following sections.

3.4.1 Inlet boundary condition

In order to achieve an accurate depiction of the experiment in the simulation, total pressure traverse measurements upstream of the compressor bellmouth were taken over the whole range of the characteristic at 50% speed. The results are shown in **figure 3.25**. The upper part of the diagram shows the total to total pressure rise characteristic and the total to total isentropic efficiency of the research compressor at 50% design speed over the global flow coefficient. The bottom diagrams show the radial total pressure distribution upstream of the inlet bellmouth corresponding to each of the operating points in the upper diagrams. The values were non-dimensionalised with the mean total pressure of the traverse so that deviations from it would be detected. From figure 3.25, it can be seen that under all operating conditions at part speed, the inlet boundary conditions remain constant. As a result, the inlet conditions confirm that uniform inflow is given in all operating points at 50% speed so that these conditions can be applied in the numerical simulation as well.

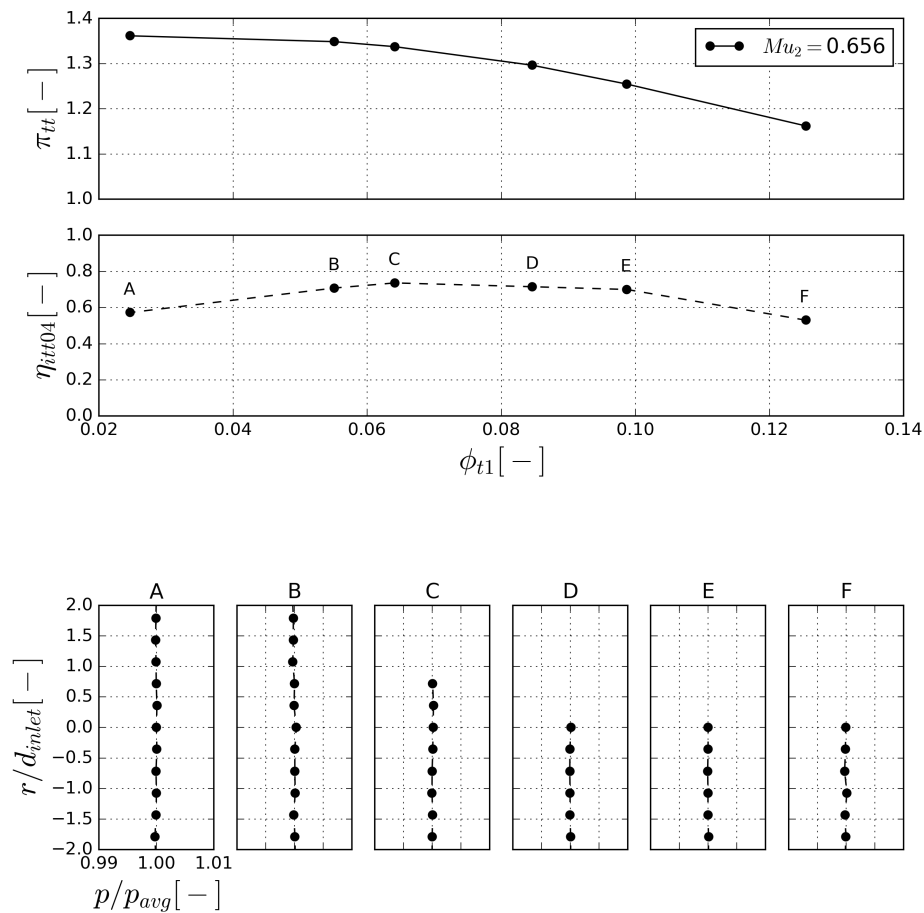


Fig. 3.25 Intake total pressure traverse measurements of Traverse 2 at 50% speed

3.4.2 Exit boundary condition

In order to determine the influence of the volute, which is a non-axisymmetric device, the annular casing pressure variation at the diffuser inlet has been measured. The results are presented in **figure 3.26**, which shows the compressor characteristic at 50% speed in form of the overall total to total pressure rise and the isentropic efficiency over the global flow coefficient in the top two graphs. Furthermore, the onset point of inlet recirculation, which has been determined in **chapter 5** is marked as dashed red line, labelled as RC and the closest measurement point is marked with a red dot. The bottom part of the figure shows graphs of the diffuser annular pressure variation at the operating points given in the above diagrams. The sub-diagrams show the annular position over the local pressure. The local pressure is non-dimensionalised with the RMS value of the annular pressure tapings for the particular operating point.

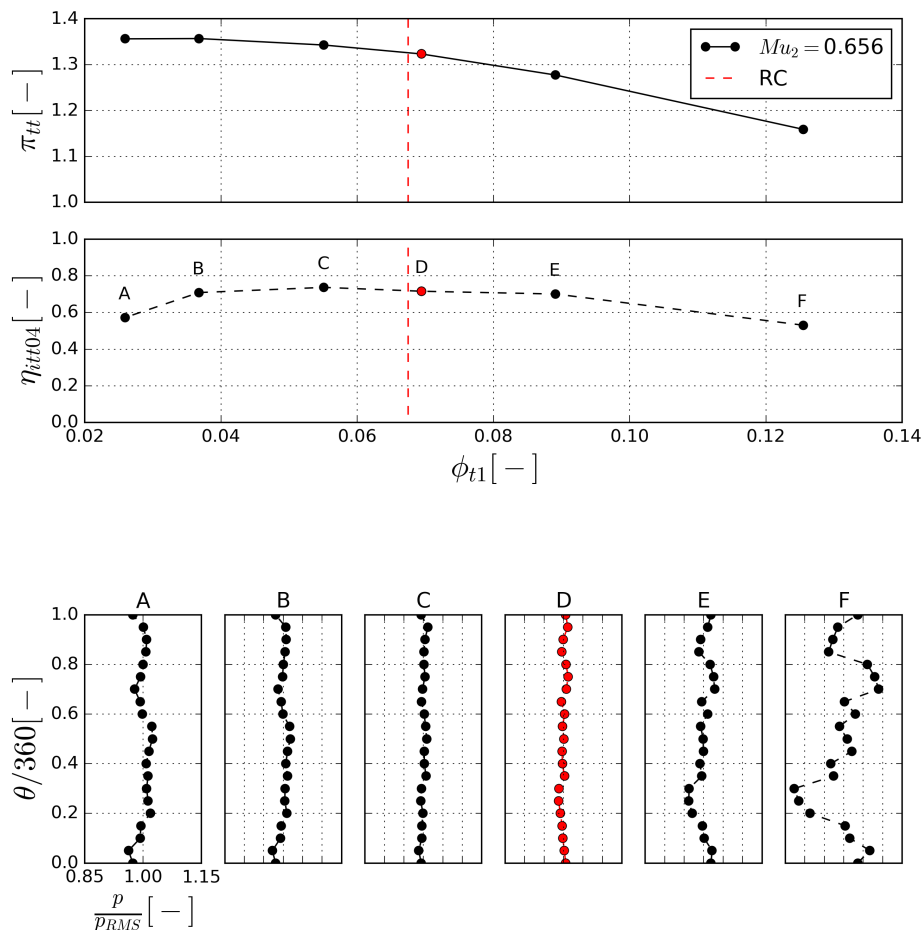


Fig. 3.26 Top: compressor characteristics in form of pressure rise and efficiency; Bottom: Diffuser inlet circumferential pressure distribution

In order to assess the circumferential variation of the static pressure in the diffuser, the measured values have been processed and compared with the static pressure rise over the compressor wheel. Therefore the RMS value from the circumferential pressure tapings has been calculated and the maximum variation from this value has been determined. This deviation value was then divided by the static pressure rise of the corresponding operating point. The results are plotted in **figure 3.27**. The top graph shows the static pressure rise of the wheel over the global flow coefficient, where the static pressure behind the wheel is calculated as RMS value from the circumferential pressure tapings. The bottom graph shows the quotient of the maximum circumferential pressure variation relative to the static pressure rise.

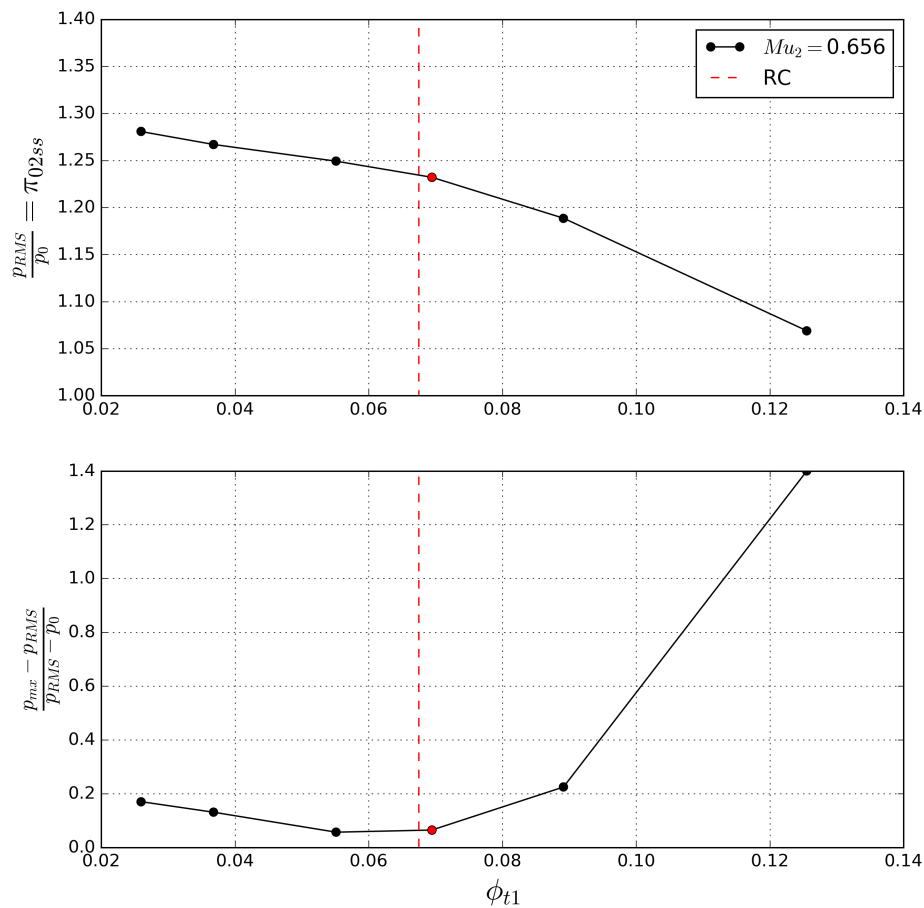


Fig. 3.27 Top: static pressure rise over the rotor; Bottom: Diffuser inlet circumferential pressure variation

Furthermore the onset point of recirculation at a global flow coefficient ϕ_{t1} of 0.0675 has been marked with a red dashed line labelled RC and the closest measurement point has been marked with a red dot. A maximum pressure variation of 140% was measured for the

highest mass flow, where the pressure rise over the compressor wheel is the lowest. For the smallest flow coefficient measured, the pressure variation was 17%. At the onset point of recirculation, the pressure variation of 6.4% was determined. This value is close to the minimum measured circumferential variation of 5.7%, which implies that the volute operates close to its best performance point.

However, the magnitude of the circumferential pressure variation around the onset point of recirculation is too high to be neglected and its effects have to be discussed. Therefore two aspects have to be considered, the origin of the circumferential pressure variation and the effect of the circumferential pressure variation on the rotor performance.

In order to further assess the origin of the circumferential pressure variation, the pressure values which were measured around the annulus in the operating point D, which was closest to the onset point of recirculation, have been investigated. Therefore the measurement values were plotted over the circumferential position of the corresponding tapping in **figure 3.28**. The pressure values are presented as a deviation from the circumferential RMS value, non-dimensionalised by the static pressure rise over the compressor wheel. As can be seen, the presence of the volute at zero degrees results in an increased static pressure in this region. However, there are also other spikes in static pressure around the annulus which cannot be related to the geometry. In the course of this study, the origin of these spikes was not in the focus. One explanation could be the strongly unsteady flow field leaving the rotor which causes these pressure fluctuations. Another influence factor are manufacturing variations. Figure 3.28 shows that the influence of the geometry is of the same order of magnitude as the annular pressure fluctuations which most likely are induced by the unsteadiness of the flow field. Because the volute influence cannot be distinguished from the fluctuations in the flow field, the volute influence will be neglected in these operating points.

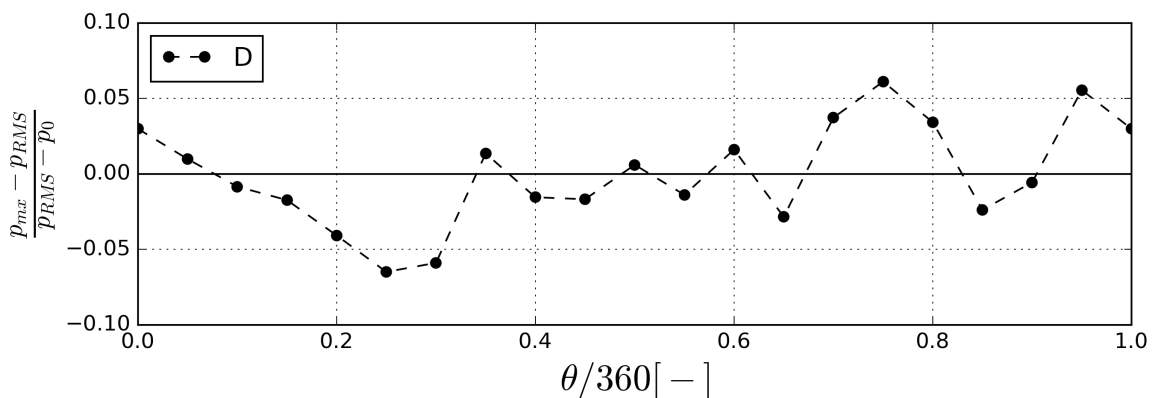


Fig. 3.28 Diffuser inlet circumferential pressure distribution close to recirculation

The presence of a circumferential pressure variation in the diffuser will inevitably have an effect on the rotor performance due to the change in back pressure during one rotation. Scope of this work is the phenomenon of inlet recirculation which is a phenomenon that gradually develops. Furthermore the phenomenon is circumferentially symmetric so that, once the recirculation bubble is established, all passages are occupied equally in a time averaged sense. Assuming that there are no other circumferential non-uniformities, inlet recirculation can be depicted with time averaged single passage simulations. This does not include the inception process or the initial propagation of an emerging disturbance from passage to passage which is inherently unsteady. It is thus important to understand the role of the volute as this is the only influence that avoids using a single passage instead of a full annulus to simulate. As outlined above, the volute disturbance is of the same order of magnitude as the pressure fluctuations which are inherently present at the rotor outlet due to the unsteadiness of the flow. Because the volute influence cannot be separated from other disturbances at the rotor outlet, simplifying the volute influence and assuming a constant pressure distribution around the annulus is justifiable. As the volute influence is so small, it is questionable whether it does have an influence on the location of the triggering point of inlet recirculation in form of a separation in the passage as the effect of a locally higher loading around the circumference is too small. The assumption of a constant back pressure around the annulus allows a simplified model which does not account for all effects present in a real machine but is a good approach to gain further understanding about inlet recirculation in a simplified environment.

3.4.3 Volute 1-D model

In order to reduce the complexity of the numerical model, the volute has been replaced with a one dimensional model based on a simplified volute geometry as shown in **figure 3.29**. The volute can be separated into a spiral part and a cone diffuser part. Those are defined by the radius and area at the inlet plane 3, the spiral outlet plane sp and the cone diffuser outlet area at plane out. The pressure recovery coefficient as defined in **equation 3.3** is used as modelling parameter to represent the volute performance.

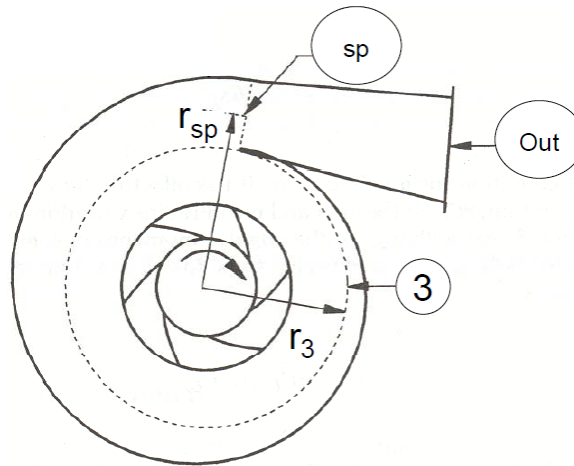


Fig. 3.29 Sketch: Volute with key geometry features

$$cp_{34} = \frac{(p_4 - p_3)}{p_{t3} - p_3} \quad (3.3)$$

In the relevant literature, three models to describe the volute performance can be found. **Weber & Koronowski** [50] modelled the volute performance by taking into account four different loss sources and assuming constant density. The meridional velocity dump loss which assumes that the kinetic energy in the meridional velocity component at the inlet of the spiral is lost. The skin friction loss which is a function of the surface roughness is modelled via standard approaches to pipe friction. The loss occurring in the exit cone of the volute which is modelled as a gradual expansion loss. The tangential velocity dump loss, where the authors took into account that the volute is either too small or too big at off design conditions. As a result, a certain percentage of the tangential velocity is lost. Depending on the condition, the loss either calculates as expansion loss or as a percentage of the difference in kinetic energy at the spiral outlet to the spiral inlet.

Young [29] and **Japinske** [29] based their model on two assumptions. Firstly all kinetic

energy associated with the meridional velocity component at the inlet of the volute is lost. Secondly, in case the volute operates under conditions where it is too large and a pressure rise occurs in the spiral, a stagnation pressure loss occurs which originates from a sudden expansion of the tangential velocity component.

Enyon & Whitfield [14] expanded Young's model and took into account the radius change between the volute inlet and the tongue leading edge.

The model developed in this work is similar to those mentioned above but includes some alterations, namely a cone diffuser. It is further assumed that the volute itself and the cone diffuser are adiabatic and frictionless. In addition the assumption that state change takes place at constant density is made. As mentioned above, the volute can be split into two parts, the spiral and the cone diffuser. In the spiral part, it is assumed that all kinetic energy associated with the meridional velocity component is lost and mixed out. The tangential velocity component experiences a sudden expansion from the inlet to the outlet of the spiral. The cone diffuser is assumed to be loss free. The pressure recovery coefficient can then be rewritten as shown in **equation 3.4**.

$$cp_{34} = \frac{(p_4 - p_3)}{p_{t3} - p_3} = \frac{\frac{\rho}{2}c_3^2 - \frac{\rho}{2}c_{out}^2 - \frac{\rho}{2}c_{r3}^2 - \frac{\rho}{2}(c_{t3} - c_{sp})^2}{\frac{\rho}{2}c_3^2} \quad (3.4)$$

The spiral outlet velocity as well as the volute outlet velocity can be calculated from the continuity equation so that the pressure recovery coefficient can be simplified to **equation 3.5**, where ζ_m represents the meridional kinetic energy loss and ζ_{ex} the expansion loss.

$$cp_{34} = 1 - e_{kinout} - \zeta_m - \zeta_{ex} = 1 - \frac{\cos\alpha_3^2}{A_{r4}} - \cos\alpha_3^2 - \left(\sin\alpha_3 - \frac{\cos\alpha_3}{A_r} \right)^2 \quad (3.5)$$

For validation purposes, all four presented models have been held against measurement data of two volutes. The results are presented in **figure 3.30**, where the pressure recovery coefficient is plotted over the volute inlet angle.

Volute A represents a data set from an automotive turbocharger for HCV's where both geometry and measurement data were accessible to the author. In total, performance data over the whole operating map for six different rotor speeds was available. Due to confidentiality, no further details can be published on the data set.

Volute B represents the geometry of the research compressor in this work introduced in section 3.2.4. Due to the restrictions of the test rig, measurement data were only available at

one constant speed line.

Both volutes are very similar in terms of their geometry. Due to confidentiality, the full specifications cannot be provided. However, a comparison of the main non-dimensional geometry parameters can be given. The radius ratio $\frac{r_{sp}}{r_3}$ of Volute A is around 4% larger than for Volute B so that slightly more diffusion of the tangential velocity component can be realised. The area ratio of the cone diffuser part is 6% smaller so that less diffusion takes place in the cone diffuser of Volute A. Due to their geometrical similarity, the performance of both geometries is very similar as well. This is why Volute A was used as a calibration case for the Author's volute performance model. In a second step, the model was then applied to Volute B as a "blind case". The results for Volute A are shown in the upper part of figure 3.30 and the results of Volute B are presented in the lower part. In order to allow a good comparison with the models, a second order function was fitted to the measurement data. This is appropriate as the losses in the volute are entirely dependent on the kinetic energy. The best fit is shown as full black line in figure 3.30. Weber & Koronowski's model is shown as full cyan line. It shows good agreement for large volute inlet angles but deviates increasingly for low angles. This model will not be included in the further discussion due to its low accuracy for small angles. The models by Young, shown as blue line, Enyon & Whitfield, shown as green line and that by the author, shown as red line, show a good qualitative agreement with the measurement data over the whole operating range.

The measurement data of Volute A reaches a peak pressure recovery of 0.47 at 70 degrees. In this case, the peak pressure recovery angle is estimated very accurately. Young's model gives a 8.5% lower pressure recovery of 0.43 at 69.5 degrees. Enyon & Whitfield estimate the peak pressure recovery 27.6% too high with a value of 0.6 at 71 degrees. The author's model achieves a 2.1% too small pressure recovery at 69.5 degrees. Due to its matching to the rotor and diffuser, Volute A reaches the point where the pressure recovery drops to zero. This point is only previously estimated correctly by Enyon & Whitfield and the Author.

The measurement data of Volute B reaches a peak pressure recovery of 0.42 at a volute inlet angle of 57 degrees. Here, all three models have problems capturing the angle at peak pressure recovery point. Young's model gives a conservative 9% lower value of 0.37 at 63 degrees. Enyon & Whitfield and the author overestimate the peak performance by 16% with a value of 0.5 at 64 degrees.

For both Volutes shown, the author's model delivers the best agreement with the available measurement data. Particularly the "blind case" of Volute B is suitable for evaluation and shows that the authors model is closest to the measurement data. However, the deviation from the measurement data is still significant. It is mainly the peak pressure recovery point which is not predicted correctly.

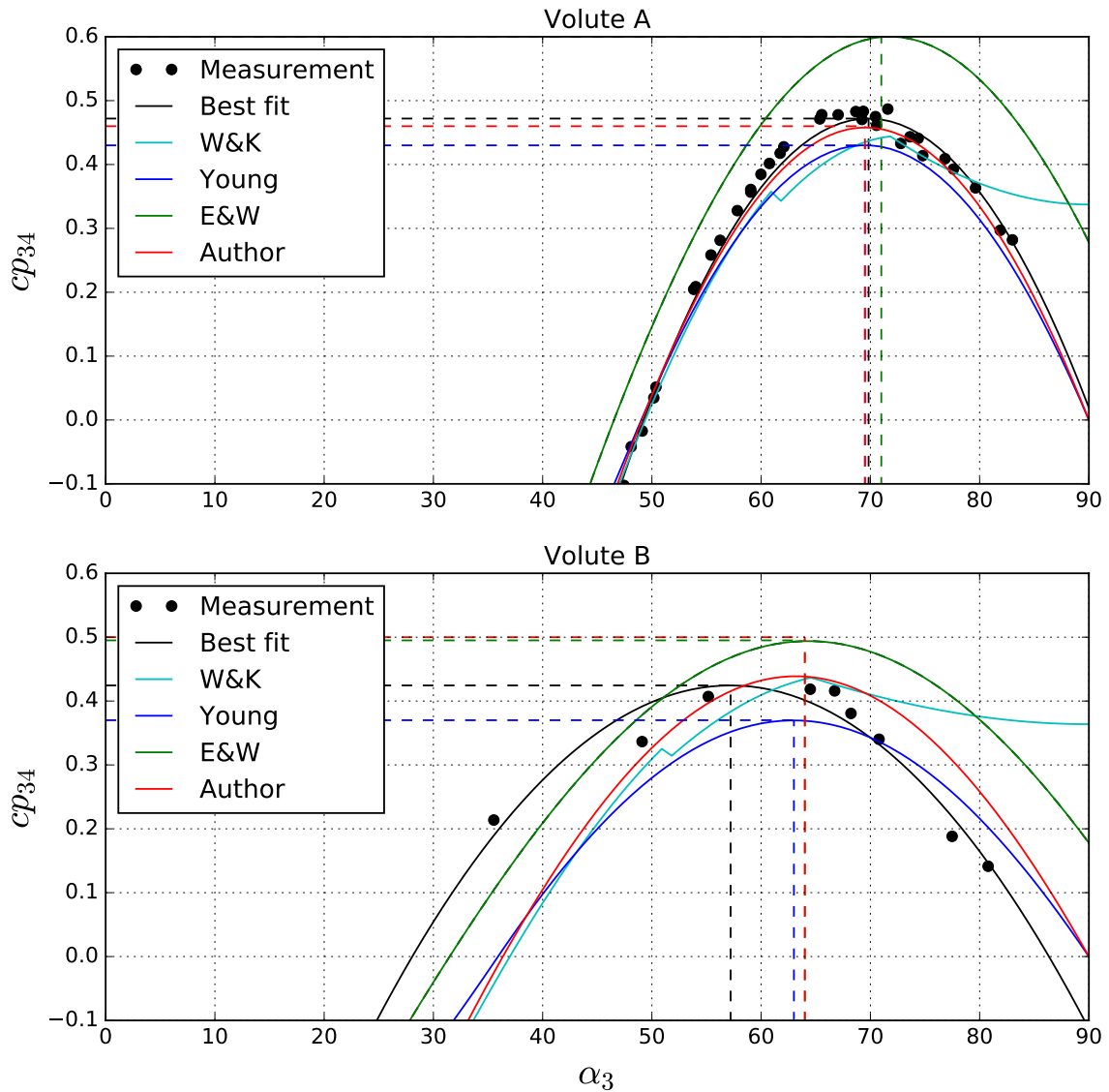


Fig. 3.30 pressure recovery coefficient from experimental data of two volutes

This deviation could result from data recordings for only one constant speed line which could mean that the data is too scarce to depict the volute performance curve. Furthermore a number of initial assumptions are made in the authors prediction model, such as constant density and no friction across the volute. Options to further improve the volute model could be made by an investigation of the friction loss in the volute and an additional term which accounts for it. Furthermore separations can also occur in the volute, particularly at low flow rates. Here, specifically the cone diffuser performance could have deteriorated due to occurring separations.

3.4.4 Validation

The three dimensional model of the rotor and the diffuser, has been validated using the manufacturer compressor map and performance characteristics in terms of total to total polytropic efficiency. In order to do so, the numerical model has been combined with the 1-D volute model introduced in the last section. Furthermore, disk friction was modelled using Daily and Neece's [7] 1-D model. The results of the combined model are superimposed as red dots on the manufacturer compressor map in **figure 3.31** and as red squares with lines on the manufacturer performance characteristics in **figure 3.32**. For both figures, the manufacturer data is shown in black. Furthermore the measurement results, labelled "EX", are shown as black dots with dotted lines for the lowest speed case in the performance characteristics which will not be discussed here but in chapter 6.

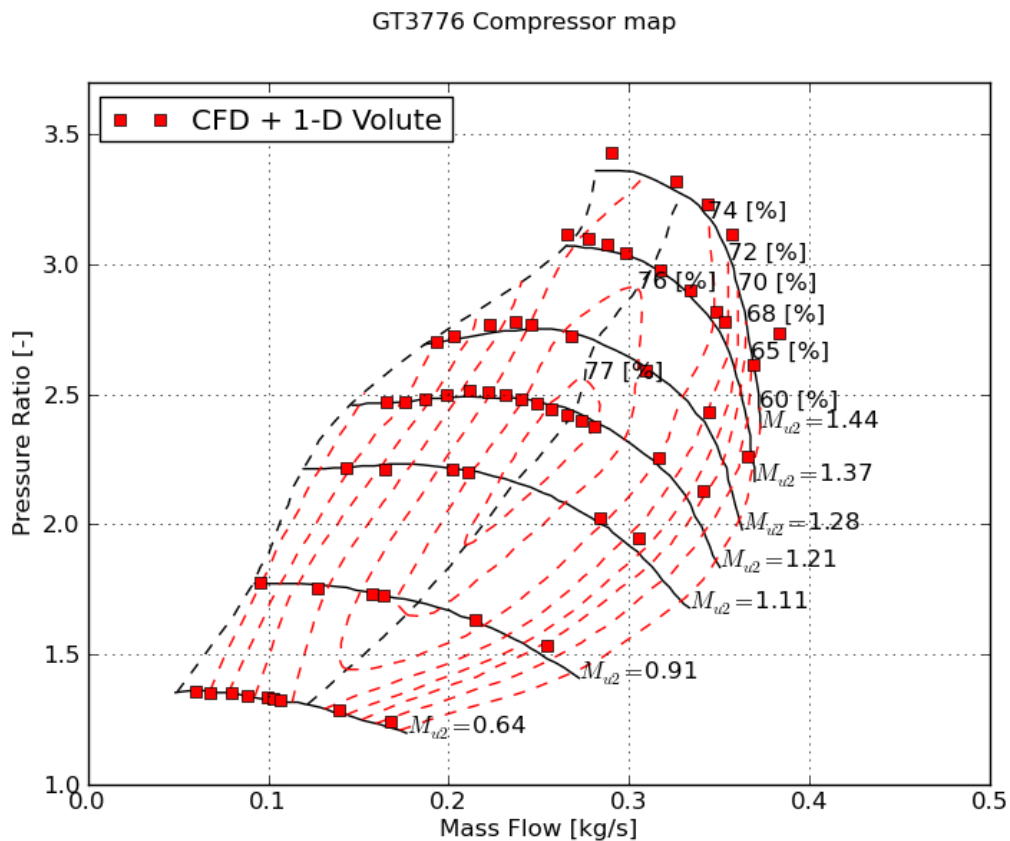


Fig. 3.31 Comparison of the calculated compressor map with manufacturer data

In the compressor map, the data shows good qualitative and quantitative agreement over the whole map and captures the choke and surge limit well. Furthermore, the slopes of the constant speed lines correspond well. In terms of absolute pressure rise, the model deviates

marginally from the manufacturer data, and only shows noticeable deviation for high speeds in the high and low flow range. Particularly, at the highest speed, the predicted pressure rise is above the manufacturer data close to the surge limit at low flows as well as for high mass flows close to the choking limit.

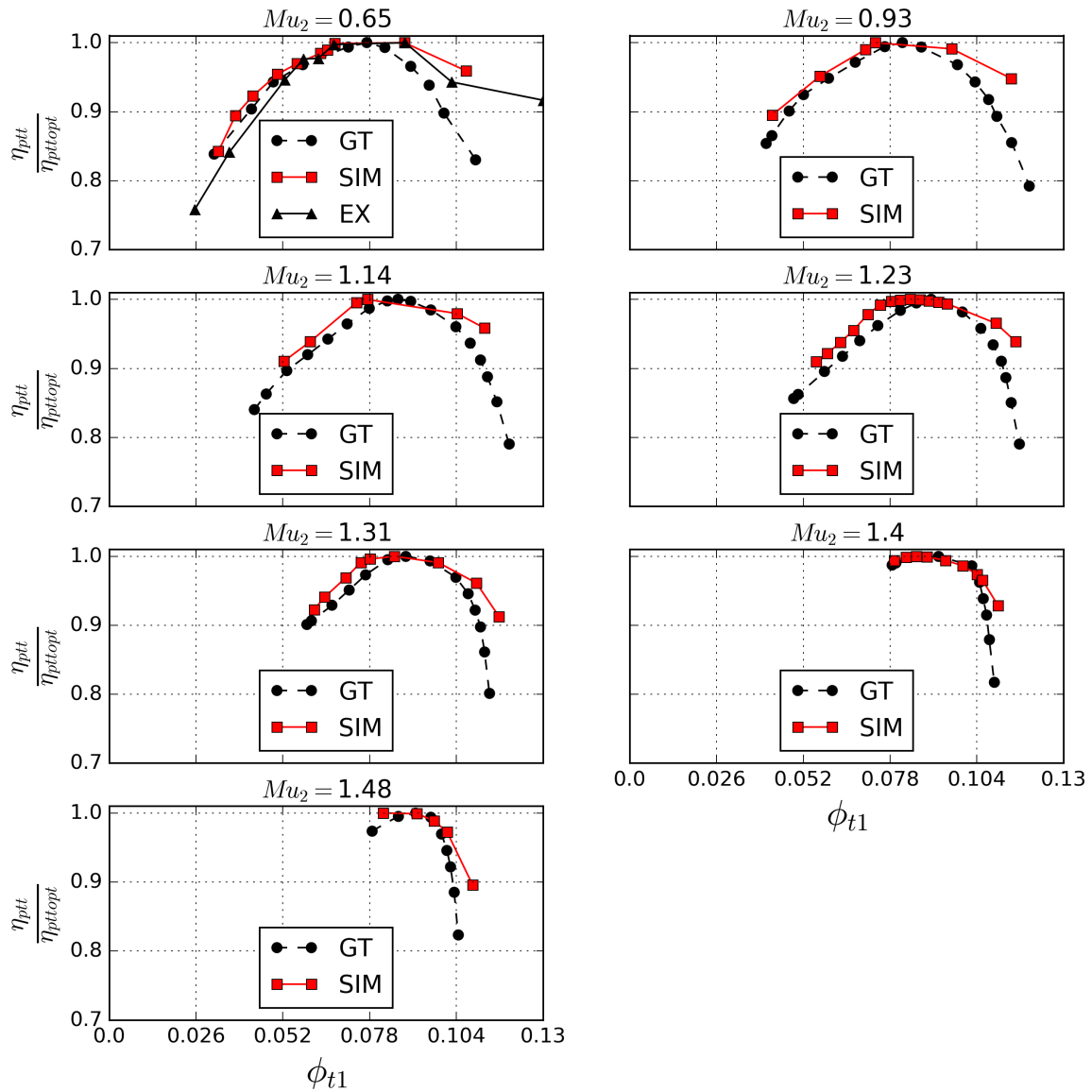


Fig. 3.32 Comparison of the calculated performance characteristics with manufacturer data

The performance characteristics obtained from the combined model show a good qualitative agreement with the manufacturer data around the best efficiency points and for low flow rates for all constant speed lines. Towards choke, the combined model under predicts the losses. Two sources of error can be identified to explain this deviation. Firstly, the numerical

model contributes to the error due to problems in quantitatively predicting the more complex flow field at high incidence. Secondly, it has been shown in the previous section that a certain amount of error sources from the low order volute model for high flow rates.

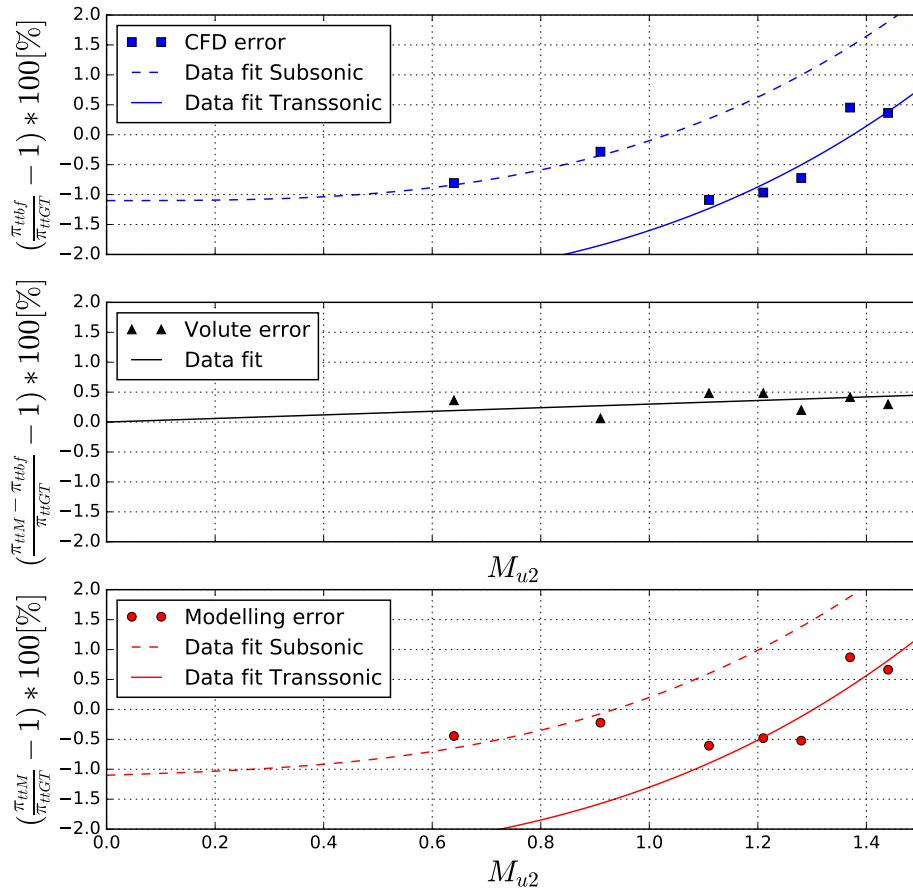


Fig. 3.33 Overall compressor Model error as a sum of CFD and Volute model error

In order to assess the deviation in the region of interest, namely close to the surge line, an error analysis has been carried out. Therefore the last calculated points prior to stall of every constant speed line were chosen. The pressure rise was then compared to the manufacturer data.

In a first step, the volute model was replaced with the best fit curve to the measurement data presented in the previous section. Assuming that the best fit curve perfectly represents the Mach number independent volute pressure recovery, this curve corresponds to the error in the CFD part of the model. The results are presented as blue squares in the top graph of **figure 3.33**. A clear decrease of the modelling error with the rotor speed can be seen, which roughly scales with the rotor speed cubed. Furthermore a jump in error is visible around a tip speed mach number of unity which is close to the region where the rotor flow becomes

transonic. In order to make the cubic correlation in both the subsonic and the transonic case more clear, two cubic functions have been fitted to the data points.

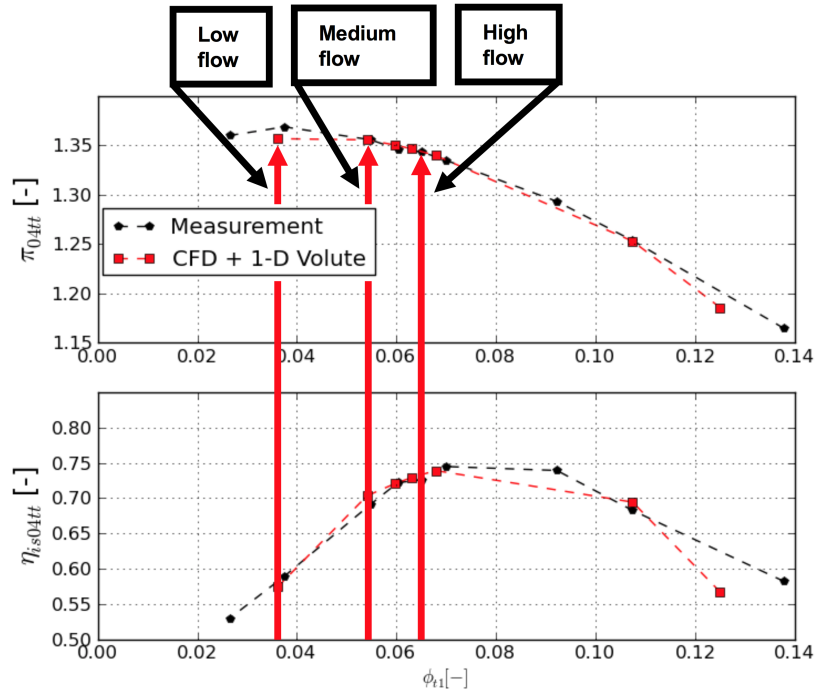


Fig. 3.34 Casing pressure distribution from Experiment and Simulation at $Mu_2 = 0.65$: Compressor characteristic

In a second step, the pressure rise values obtained from the combination of CFD and the author's volute model were taken and subtracted from the best fit results. Compared to the manufacturer data, this value represents the error originating from the volute model and is shown in the middle graph of figure 3.33. As an estimate, this error scales linearly with the rotor speed, as indicated by the added data fit curve.

In a final step, the combined error has been calculated from comparing the CFD model together with the author's Volute model to the manufacturer data. The results are shown in the bottom graph of figure 3.33.

The maximum deviation from the manufacturer data close to the surge limit is -0.4% for the lowest tip speed. Here, the errors occurring in the CFD model and in the Volute model cancel out so that the combined error is lower than the individual errors. For this operating point, the CFD model under-predicts the pressure rise by 0.7% and the volute over-predicts it by 0.3%, resulting in the overall error of -0.4%.

The maximum deviation from the manufacturer data close to the surge limit is around 0.9% for the second highest tip speed. Here, the error in the CFD part of the model is around 0.5% and the modelling error from the 1-D Volute model is around 0.4%.

Within its capabilities, the comparison shows that, the model agrees very well with the validation data available. Furthermore, the given values can only give an estimate of the agreement and it cannot be clarified further whether measurement errors in the test setup or calculation errors in the model are responsible for it.

One way of determining whether the virtual model accuracy is sufficient is a comparison with the deviation of the measurements from the manufacturer data. In order to do so, the data presented in figure 3.19 has been taken and the operating point close to the surge limit which corresponds to the flow coefficient in the simulation has been processed. For this operating point, the deviation of the measurement from the manufacturer data was 0.75% which is in the same order of magnitude as the simulation errors for the CFD model and the 1-D model. Consequently, the virtual model accuracy is taken to be sufficient for the following investigations.

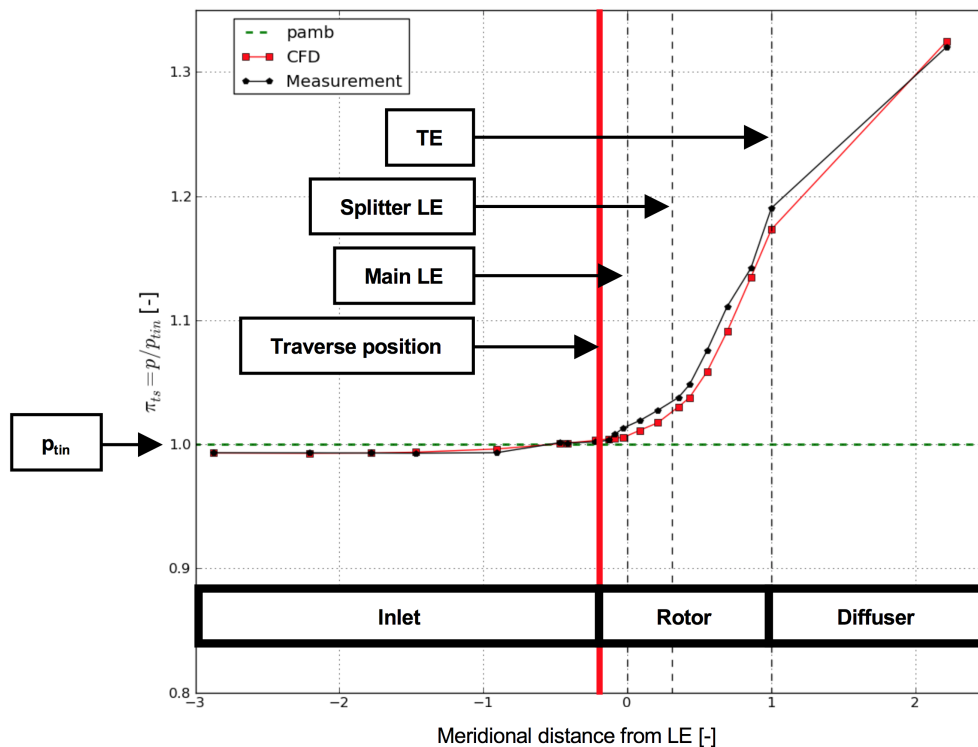


Fig. 3.35 Casing pressure distribution from Experiment and Simulation at $Mu_2 = 0.65$: Medium

Further validation of the numerical model has been carried out using the casing pressure data obtained from the experiment at 50% speed. the results are shown in **figure 3.34 to 3.37**. All graphs show the measured data as black and numerically obtained data in red. Figure 3.34 shows the total to total pressure rise curve over the whole compressor on the top and the isentropic total to total efficiency at the bottom. A total of three operating

points was chosen and marked with red arrows in the graphs. The point at the highest flow coefficient is characteristic for a normal flow pattern. The point at medium flow rate is located around the onset point of inlet recirculation. The point at the lowest flow rate features inlet recirculation. The experimentally and numerically obtained casing pressure distributions, nondimensionalised with the inlet total pressure, for these points are plotted over the non dimensional meridional distance through the machine. In figure 3.36, the highest flow case is shown. In figure 3.35, the medium flow case is shown. In figure 3.37, the low flow case is shown. The figures furthermore contain a description of the different lines in the graph which point out the location of the blade leading edges, trailing edges and the corresponding part of the compressor which has been split up into inlet, rotor and diffuser. Furthermore, the unity value is marked on the y axis as it represents the pressure level corresponding to inlet total pressure. A more detailed explanation of the figures can be found in chapter 4.

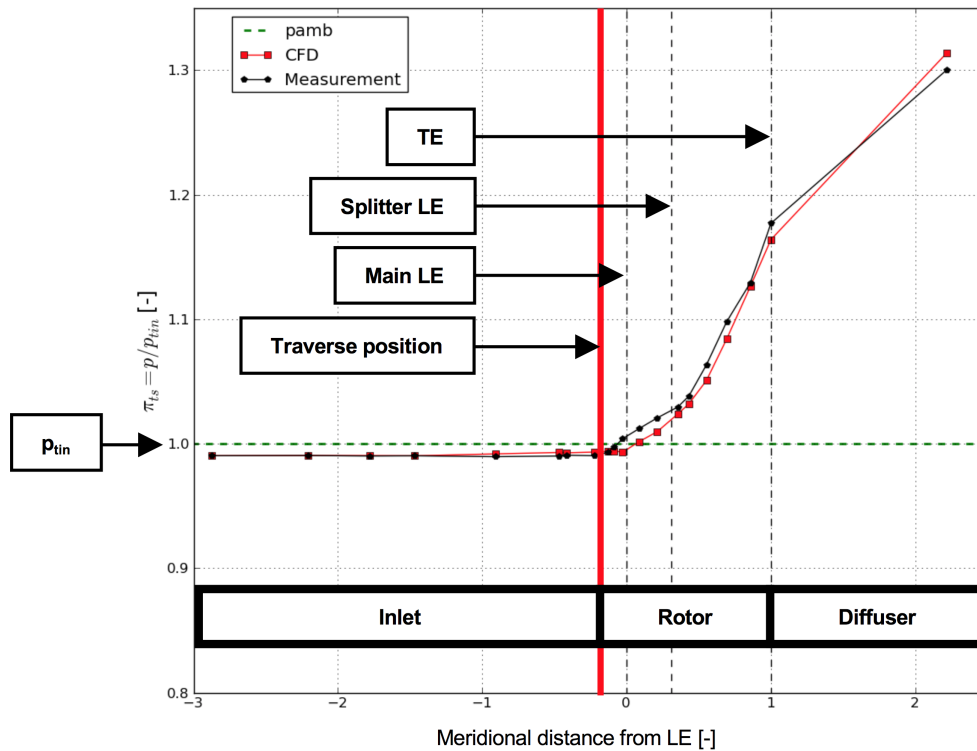


Fig. 3.36 Casing pressure distribution from Experiment and Simulation at $Mu_2 = 0.65$: High flow

Regarding the comparison between experimental and numerical data, the following observations can be made:

For the highest flow rate, the measurement data and the numerically obtained casing pressure values show good qualitative and quantitative agreement throughout the whole compressor.

For the medium flow case, small deviations in terms of pressure increase are present within the rotor so that still good qualitative and sufficient quantitative agreement is given.

For the low flow case, the casing pressure in the rotor is under predicted in the numerically obtained results, yet the qualitative trend is captured. This operating point features strong inlet recirculation in the shroud region which leads to a highly complex flow field in this area. Although the numerical model has difficulties in reproducing the measurement data quantitatively, it still shows good qualitative agreement and captures the overall trend well. Particularly the agreement in the inlet part allowing to track the axial extend of the recirculation bubble is well included in the numerical result.

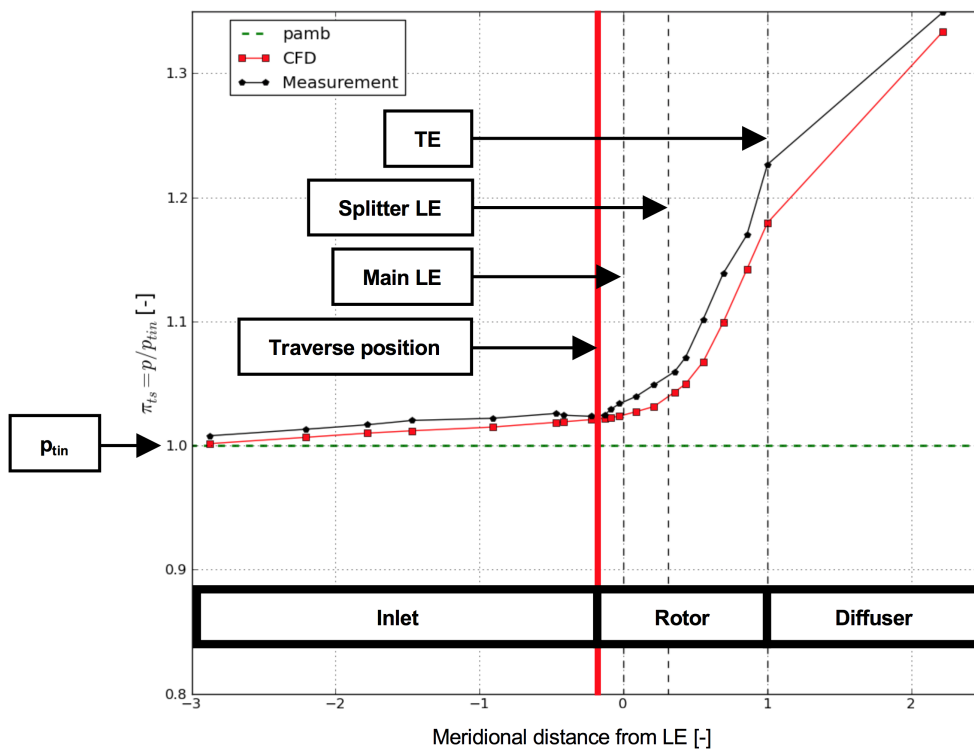


Fig. 3.37 Casing pressure distribution from Experiment and Simulation at $Mu_2 = 0.65$: Low flow

3.5 Summary

This chapter gave an overview of the methods used to obtain results which allowed to investigate the research questions outlined in the previous chapter. The investigations were executed on a turbocharger compressor without bleed channel which was available at the Whittle Laboratory. The geometry of this turbocharger was typical for passenger vehicle applications, more specifically for engines with a capacity between 2.0 and 4.0 litres. The machine was used to build up a test stand as well as a numerical model based on its geometry. The design conditions for the compressor specified by the manufacturer were given, as well as the manufacturer compressor map. The main features of the compressor were introduced and discussed in detail by splitting up the machine into its main components, the inlet, the rotor, the diffuser and the volute.

The inlet of the compressor featured a straight duct with a bellmouth as inlet of a length of 3.8 rotor inlet diameters.

The rotor, which featured a diameter ratio of 1.38, had been scanned with a 3D scanner so that the geometry was known in detail and could be specified in terms of meridional passage geometry, blade turning, blade angle distribution, thickness distribution as well as leading edge angle distribution.

The diffuser featured a pinched design which was described in terms of its key geometry parameters. Based on those parameters, a brief discussion about its operating range and diffuser instability behaviour was presented, which allowed to specify an ideal pressure ratio as well as a critical diffuser inlet angle which, once exceeded, would lead to a stalled diffuser. This value was derived from simple analytical correlations provided in the discussion.

The volute was characterised by its main geometrical dimensions.

In a next step, the experimental setup was presented. The drive system via the turbine side of the turbocharger was explained and the two main control parameters of the test rig were introduced. The first control parameter was the power input via the turbine side which was controlled via turbine inlet guide vanes. The second control parameter was a throttle valve which was placed downstream of the compressor outlet. In order to allow for accurate mass flow measurements, a separate measurement bellmouth was used. This bellmouth was connected to the compressor inlet via a large volume settling chamber to avoid interference of the mass flow measurement and inlet recirculation induced disturbances.

Measurement planes were placed in the machine so that the experiment allowed to investigate the performance of the individual compressor components intake, inlet, rotor, diffuser and volute. Shaft speed was measured via an inductive sensor on the bearing housing of the

turbocharger.

A total pressure traverse was placed upstream of the compressor inlet in order to make sure that undisturbed flow was ingested into the machine. Furthermore, these measurements served to determine the boundary conditions for the numerical model.

A second traverse was placed upstream of the rotor in order to study the total pressure distribution upstream of the rotor and determine the inlet losses.

In order to determine the influence of the non-axisymmetric volute on the circumferential pressure field at the exit of the diffuser, 20 casing pressure tappings were placed in the diffuser around the annulus.

Furthermore, the casing of the machine was equipped with 19 static pressure tappings along the meridional line of the machine. The tappings started about 5.5 meridional rotor lengths upstream of the leading edge and reached to the end of the diffuser.

The measurements have been carried out using simple equipment. Temperatures were measured using T-Type temperature probes. All pressure measurements were carried out with a Cole Parmer high pressure sensor that was specifically calibrated for the measurements. The measurements were set up as time averaged measurements and all values were averaged over 10 seconds which equalled 9305 revolutions at the investigated rotor speed of 50% design speed.

The numerical model of the compressor was put together from two parts. The inlet, rotor and diffuser were modelled three-dimensionally and were calculated using the CFD solver Turbostream. The volute was excluded from this model as it represented the only component of the compressor which was not axisymmetric. The applicability of this method was confirmed with the diffuser exit pressure measurements to determine the volute induced annular pressure variations which were shown to be sufficiently small. This method permitted a simplification of the numerical model. As a result, only one single main passage, which equals a section of 60 degrees, had to be modelled. The numerical compressor model was embedded between a long inlet block to avoid interference with the recirculation phenomenon and a nozzle shaped outlet block which allowed to "throttle" the numerical model by varying the exit crosssection rather than varying the back pressure.

For the volute, a 1D-model was developed by the author which assumed that all radial kinetic energy was lost in the volute and modelled a sudden expansion loss as well as the outlet kinetic energy. Comparisons between this and other models, as well as measurement data from two volutes, found that the present model was an improvement.

In a final step, the 3D numerical model was combined with the 1D Volute model and a disk friction model to represent the whole compressor.

Both experiment and numerical model were validated against the manufacturer performance data. In case of the measurement, the validation was carried out at the 50% speed line and showed very good agreement. In case of the numerical model, the whole compressor map was used to validate the model. Once more, a very good agreement was achieved.

In an error analysis for the numerical model, the individual errors from the 3D model and the 1D model were determined. It was shown that the error of the numerical model roughly scales with the rotor speeds cubed, whereas the error from the 1D model scales linearly with the rotor speed. A comparison of the measurement error with the numerical error was carried out and it was shown that they were small and in the same order of magnitude which was taken to be sufficient as a validation.

Chapter 4

Key features of inlet recirculation

4.1 Introduction

Inlet recirculation is a phenomenon in radial compressors which, despite being present in a broad range of machines, is not well understood. In order to obtain a better understanding of inlet recirculation, a description about the key features of inlet recirculation based on the experimental and numerical results obtained in this work is provided. The description is separated into two parts, the first of which focuses on the onset of the phenomenon. In the second part, the state of the flow with established inlet recirculation is outlined.

In hydraulic turbomachines, inlet recirculation has been known for a long time. One simple idea about the mechanism of inlet recirculation can be found in Guelich's book about centrifugal pumps [20], which has already been introduced in section 2.5.1. There, recirculation is described based on a simplified model as shown in **figure 4.1**. A disk with radial blades is rotating in a closed cavity. Due to the centrifugal forces in the rotor, a radial pressure gradient as defined in **equation 4.1** develops in the rotor. It leads to a parabolic pressure distribution as shown on the left of the figure. As the flow direction is driven by the pressure gradient, the fluid close to the shroud flows out of the rotor and the fluid close to the hub flows into the rotor. A recirculating movement is thus created. This mechanism universally applies to all rotors with a sufficiently small hub to tip radius ratio.

$$\frac{dp}{dr} = \rho \omega^2 r \quad (4.1)$$

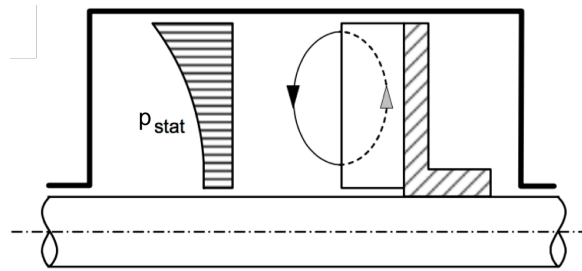


Fig. 4.1 disk with radial blades rotating in a closed housing [20]

In a real machine, however, additional effects due to blade loading, secondary and leakage flows are present and will have an effect on the flow pattern. The resulting fluid behaviour will consequently always be a mix between these mechanisms and is dependent on which of them is the most dominant one. This may vary from machine to machine. Generally the recirculation flow pattern is more localised to the shroud than described above. A more realistic sketch of the recirculation zone in a compressor is given in **figure 4.2 a** which shows a meridional cut through a generic rotor. The red lines show the recirculation zone which extends upstream into the inlet part of the machine. The black lines show the oncoming flow. At the shroud, the recirculation zone forces the oncoming flow to separate around the point marked with a red bar. The flow then enters the rotor and proceeds to the exit so that the machine still remains operational.

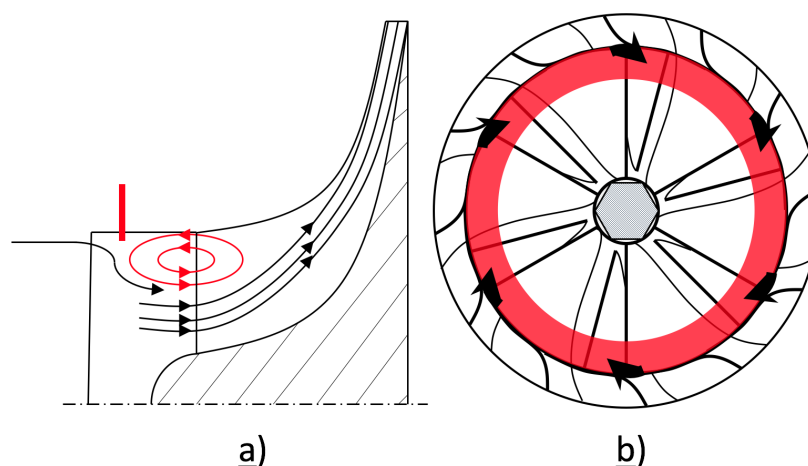


Fig. 4.2 Qualitative pattern of inlet recirculation in a rotor (figure without casing): a: meridional cut b: Cross-sectional cut of the impeller inlet

In that sense, recirculation represents a form of aerodynamic reduction in inlet cross-sectional area by blockage. In the recirculation zone, the flow is pushed out of the rotor into the inlet and, because a rotational velocity component has been acquired, has a strong positive swirl component. Inlet recirculation, unlike rotating stall, is a flow phenomenon which is not periodic but circumferentially symmetric. It builds up a blockage ring around the whole annulus of the machine which appears to be stable in a time averaged sense. A sketch of the recirculation ring around the shroud is given in **figure 4.2 b** where it is shown in red in a cross-sectional plane just upstream of the rotor leading edge. The arrows indicate the strong positive swirl component present in the recirculation zone. The border of the recirculation zone can be defined in different ways. Generally, circumferentially averaged radial profiles are used to do so. The most common approach which was also used by Qiu [35] and Harley [23] is to use a mass flow balance and define the lower limit of the recirculation bubble as that point on the radius, where the mass flow within the recirculation zone sums to zero. An example for their definition of the recirculation zone is provided in **figure 4.3**, which shows a set of such profiles. On the left, the spanwise mass flow is provided in as a non-dimensional value of the mass flow through the machine. The mass flow is summed up from hub to tip so that the point on the span, where it equals the compressor mass flow, marked with a red vertical line and a horizontal black line respectively, can be determined as the border of the recirculation bubble.

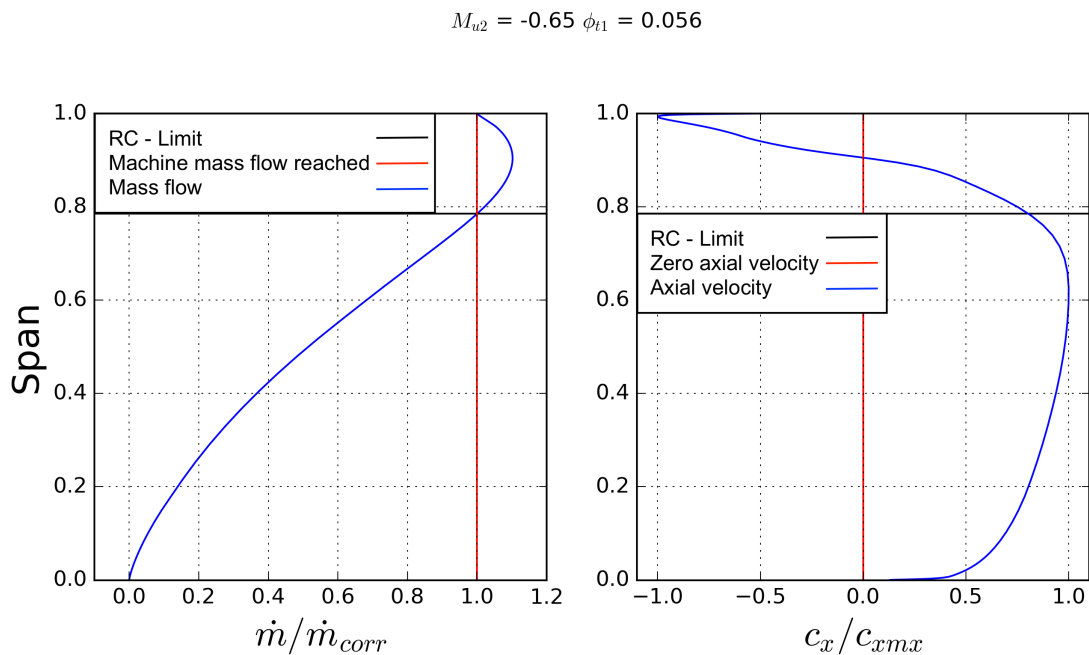
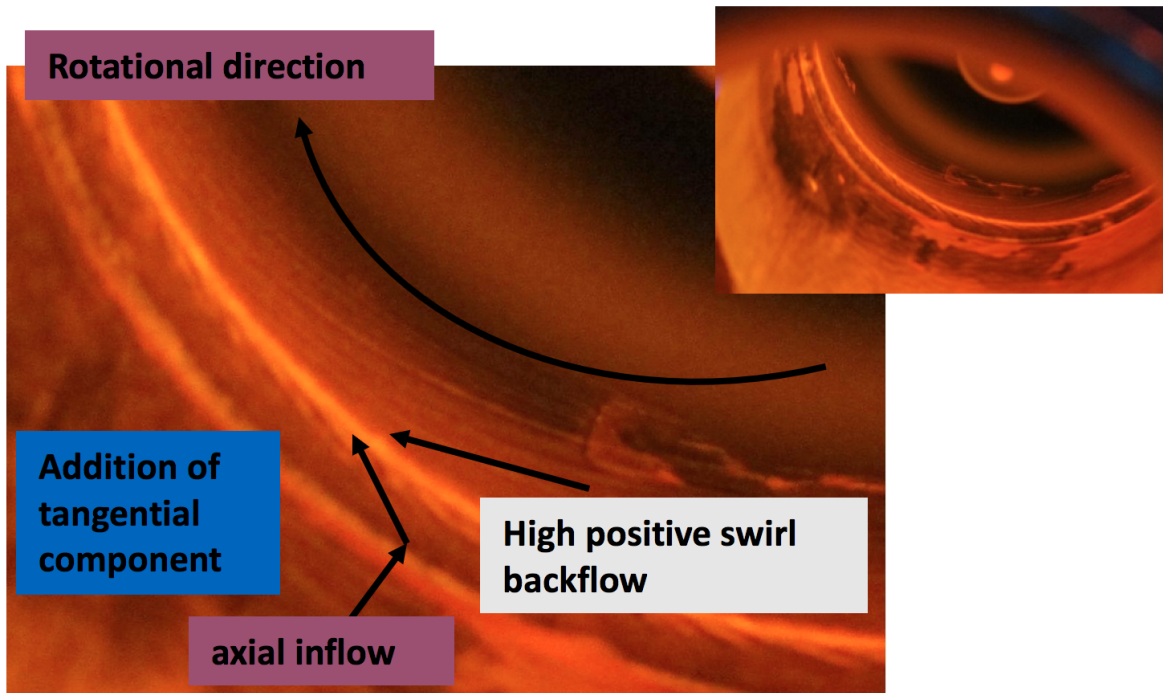


Fig. 4.3 Pitchwise averaged radial profiles in the inlet plane of the research compressor

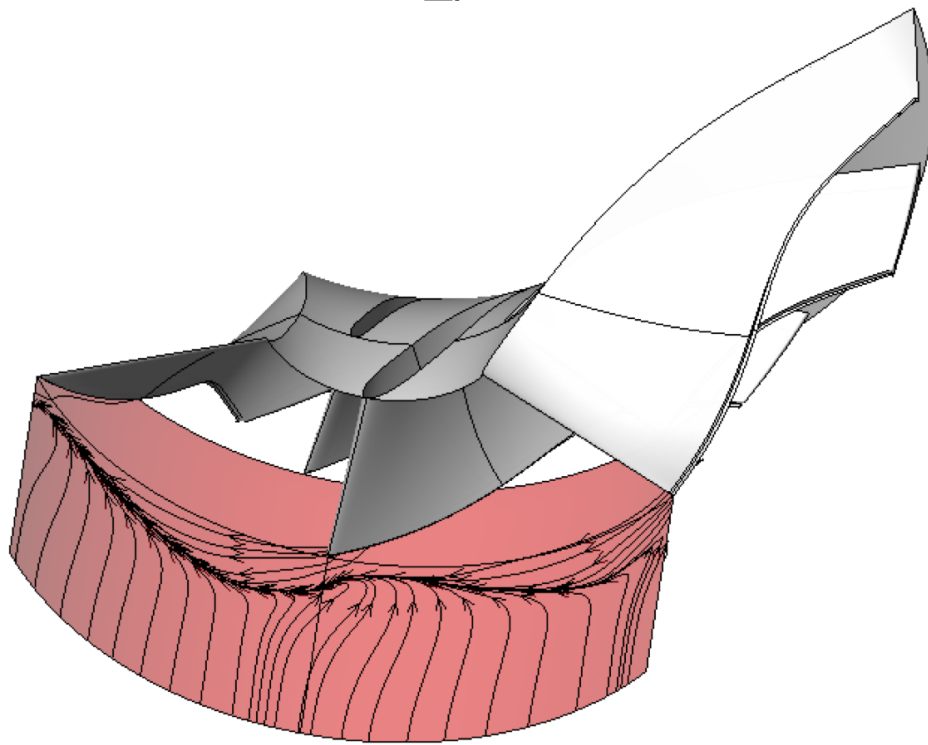
The right graph of figure 4.3 shows the spanwise axial velocity profile which has been nondimensionalised with the maximum axial velocity along the span. It shows the axial velocity distributions in the recirculation zone is composed of a negative as well a positive velocity component, and the zone below, which was named "active flow zone" by Qiu [35].

In order to point out the key features of recirculation however, this thesis uses a different approach. The inlet of the rotor is separated based on the direction of flow, rather than into recirculation and active flow zones. This results in an approach which is clearer in terms of placing a control volume around the rotor and studying the properties of the different mass flows going across the borders. In the following discussion about the key features of inlet recirculation, the distinction will thus be the region where flow is reversed out of the inlet of the rotor, corresponding to the negative axial velocity zone in the right graph of figure 4.3, and the zone where a positive mass flow goes into the rotor inlet.

For better understanding of the phenomenon of inlet recirculation, a simple qualitative test to visualise the casing flow structure at such conditions has been conducted in the machine used for this research. The casing flow structure has been made visible using a mix of silicone oil and fluorescent colour powder. The results are shown in **figure 4.4 a** which shows the inlet casing and the spinning rotor on the top left.



a)



b)

Fig. 4.4 Inlet casing flow visualisation: a) Measurement b) CFD

Figure 4.4 a shows a zoom into the region just upstream of the rotor leading edge. The blurry part of the picture is the rotor. Two bright lines where colour accumulated can be seen. The one further away from the rotor leading edge is the joint of the compressor housing with the inlet bellmouth. The other, brighter line is the point where the recirculation bubble forces the oncoming flow to separate from the casing, also marked in the sketch figure 4.2 a as a red bar. Colour paint is dragged to this line from the oncoming clean flow as well as from the recirculating flow and accumulates there by flow shear stress. The flow visualisation allows a more detailed look into the direction of the flow as it depicts the streak lines of absolute velocity. In the recirculation zone between the separation line and the rotor, the streak lines are strongly inclined to the circumferential direction, indicating a strong positive swirl component as expected from the discussion above. Due to the momentum exchange, a tangential velocity component also is added to the oncoming flow in the vicinity of the recirculation bubble, which will be discussed more clearly in the following section. A similar flow pattern was also found in the numerical simulations and a qualitative example is given in **figure 4.4 b**, again showing streak lines of absolute velocity at the casing. Instead of a straight separation line at the end of the bubble, it is skewed due to the potential field of the rotor. This effect is "smeared out" in the measurement and thus can not be observed. The streaklines cannot be seen in the rotor because they represent the spatial location of points where fluid particles have passed through in the past. As those points move in the relative frame of the rotor, they get "smeared out" and would appear as lines of revolution. Consequently, they are not shown here. Both examples show that recirculation is present in the machine used for this research at the rotor speeds investigated.

In order to discuss the key features of inlet recirculation in more detail, a differentiation between the onset of the phenomenon and the conditions when recirculation is established is useful for a better understanding.

4.2 The onset of inlet recirculation

For the onset point, the flow conditions which lead to inlet recirculation and the location where this onset takes place need to be considered. Qiu [35] describes two factors which contribute to the formation of inlet recirculation and identifies the region close to the leading edge as location for triggering inlet recirculation. In terms of the triggering mechanism, he firstly identifies the formation of a leading edge separation on the suction side of the rotor tip caused by high incidence. Secondly, he points out the radial pressure gradient within the rotor. Both of the mechanisms lead to a low meridional momentum zone in the leading edge tip region. Once the momentum is not strong enough to overcome the adverse pressure gradient in the rotor, the flow is pushed back out of the rotor. In order to determine the onset point, Qiu uses a critical incidence model which assumes that, once this critical incidence is reached, recirculation occurs. As is according to the basic fluid dynamics, and supported, for example by Harley's observations [23], it is clear that this critical incidence can vary significantly, particularly in compressors with a wide operating map like those used in automotive applications. In order to quantify the critical incidence, both authors use the assumption that the inducer part of the rotor acts like a diffuser which has been described in Japinske's Two Elements In Series (TEIS) model [28]. This method allows to quantify incidence with an area ratio as defined in **equation 4.2**. Both authors define a critical area ratio for which inlet recirculation occurs, once it is exceeded.

$$Ar = \frac{\cos\beta_{1b}}{\cos\beta_1} \quad (4.2)$$

Qiu defines it as a constant value of 1.5 whereas Harley describes that the onset of recirculation happens at a critical area ratio of around 1.2 and the area ratio then changes with a parabolic function in the region of the compressor map where inlet recirculation is present. The area ratio for the research compressor has been worked out based on the CFD data and is plotted for different speeds over the global flow coefficient in **figure 4.5**. In addition to the simulation data, Qiu's constant critical area ratio is shown as full horizontal line and Harley's variable critical area ratio is plotted as a dashed line. The graph clearly shows that the compressor investigated in this work, despite being an automotive turbocharger compressor, correlates better with Qiu's constant critical area ratio for the onset point, which is located at the peak point of the area ratio curves around a flow coefficient of 0.071. However, a certain variation with rotor speed can be seen and is not depicted by the models as they do not take into account rotor speed.

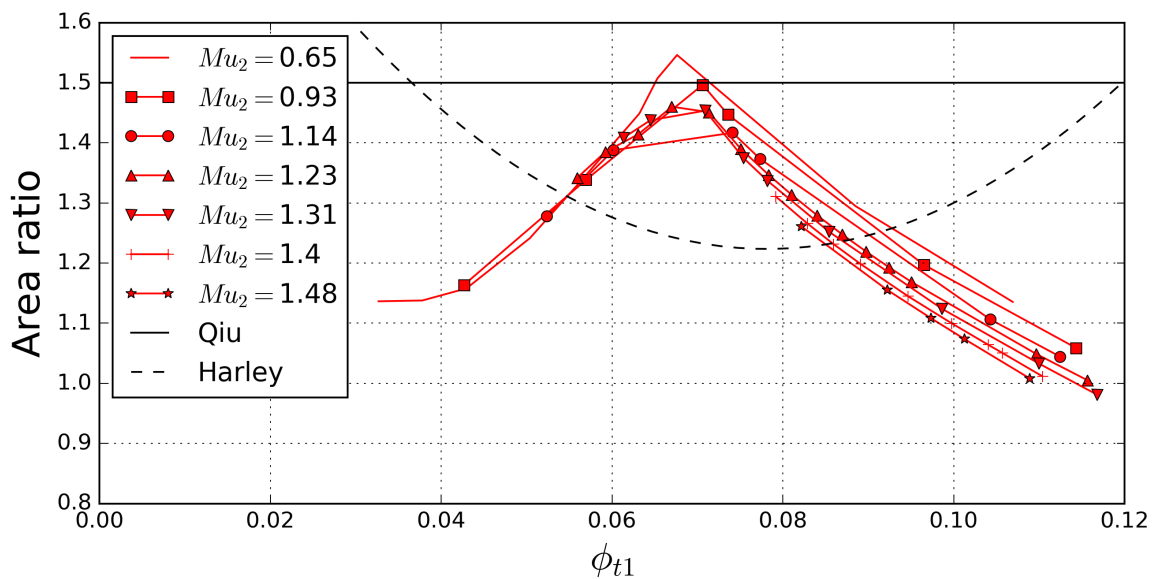


Fig. 4.5 Critical area ratio of the research compressor compared to correlations from literature

These discrepancies could imply that accounting for incidence and the radial pressure gradient does not fully depict the conditions leading to inlet recirculation. When thinking about the conditions which are necessary for the development of inlet recirculation on a more general scale, Qiu described correctly, that the built up of a low momentum zone close to the shroud is necessary and that once this low momentum fluid cannot overcome the adverse pressure gradient, it will inevitably be pushed out of the rotor and lead to inlet recirculation. However, this low momentum region does not necessarily have to be located at the leading edge but can also be located further downstream inside the impeller passage, for example close to the passage throat area as described by Guelich [20]. Following Guelich's argumentation, there are several more potential contributors to this low momentum region than leading edge separation and the radial pressure gradient which can be connected with a shift in triggering location as well. Guelich identifies another two mechanisms.

Firstly the diffusion taking place in the rotor passage, reducing meridional momentum as the flow propagates downstream.

Secondly, the leakage flow across the blade tip which significantly reduces the meridional momentum of the flow close to the casing.

The latter is arguably the most dominant factor on meridional momentum in the tip region.

In conclusion, this means that there is no clear consensus in literature about where and due to which phenomena inlet recirculation occurs.

It is the authors opinion that all four of the described effects, namely leading edge separation,

the radial pressure gradient, passage diffusion and tip leakage flow, all contribute to the built up of a low momentum zone in the casing region of the rotor. Depending on the type of machine, their importance will vary but they will always contribute to a low momentum zone which is the real cause for inlet recirculation. The location where this region of low momentum cannot overcome the adverse pressure gradient in the passage consequently can vary as well. In chapter 7, a study of the effect of tip leakage, is provided.

Following this description, one could imagine that in case of a rotor which is designed with a high level of diffusion in the inducer part, a low momentum zone would built up very early in the passage. In this case a leading edge separation could be sufficient to trigger inlet recirculation by amplifying the low momentum zone which then would not be able to overcome the adverse pressure gradient any more.

In case of automotive turbochargers on the other hand, the inducer part of the rotor is designed to have a low level of diffusion due to the transonic character of the machine and the wide range application achieved by a design more tolerant to high incidence. This would mean that, because these machines allow for a wide incidence variation, no leading edge separation would occur. A low momentum zone large enough to trigger inlet recirculation would consequently take longer to built up and be able to penetrate further into the passage. The point where the adverse pressure gradient could not be overcome any more by this low momentum flow would then be reached in another location of the passage where an additional reduction in meridional momentum would take place. Examples for such a location would be the passage throat or a location of high diffusion in the passage which could be located upstream and downstream of the throat.

In such a case, the contribution of the tip leakage would be much more significant than a leading edge separation because it continuously contributes to the low momentum zone as it propagates downstream along the tip gap.

Similarly, the level of diffusion within the passage as well as the meridional shape of the rotor would gain importance relative to a disturbance caused by leading edge separation the further the flow propagates into the rotor.

Taking into account this shift in importance between mechanisms, the discrepancy in Qiu's and Harley's results regarding the critical area ratio could be understandable as the machines investigated in the two studies featured different design aims. More specifically, Qiu investigated a broad range of machines for different applications which were designed for normal map width. Harley on the other hand investigated automotive turbocharger compressors which were specifically designed for wide range and thus tolerance to high incidence.

The effect of these different designs on the development of inlet recirculation becomes clearer when looking at the critical area ratio criterion which both authors provide. This value is an

indicator for the incidence at the onset point of inlet recirculation. Harley's result of 1.2 is significantly lower than Qiu's outcome of 1.5. The reduction in value could be interpreted as a loss in importance of leading edge separation as a contributor to the low momentum region at the casing.

In return, this could mean that another of the mechanisms mentioned above rises in importance regarding the built up of a low momentum zone so that inlet recirculation takes place at lower area ratios, meaning at higher flow coefficients. The shift of importance of mechanism could also imply a change in triggering location further downstream into the passage in Harley's cases.

Unfortunately both Authors do not provide any information about the triggering location within the rotor of the machine, neither do they show detailed three dimensional results. As the exact geometries in both cases are also unknown, no further evidence to support this theory can be provided.

Due to the complexity of the problem, it is hard to find an universal criterion which can determine the onset point of inlet recirculation.

One clear conclusion is that the onset will take place within the rotor which makes it particularly hard to determine the exact onset point in an experimental setup because this region is simply not accessible with any probing equipment due to the high rotational speeds of the impeller. In order to facilitate the determination of the onset point of inlet recirculation in the machine subject to this investigation, the author has used a more simple approach to determine the presence by using "symptoms" of inlet recirculation, namely the casing pressure just upstream of the rotor as well as the circumferentially averaged spanwise axial velocity profiles in the same location. This procedure can be applied to both, experimental and numerical results and will be explained and applied to the research compressor in chapter 5.

4.3 Established inlet recirculation

In order to characterise inlet recirculation once it has been established in the flow field of the compressor, it is useful to describe the state of the flow separately in terms of mass, momentum and energy conservation.

When looking at the mass conservation of a compressor with inlet recirculation, the observations strongly depend on where the borders of the open control volume to perform the mass flow balance are set. As inlet recirculation is a local phenomenon in the rotor leading edge region, it does not affect the amount of mass going through the compressor from intake to outlet. If the control volume is set around the rotor as shown in **figure 4.6** however, inlet recirculation can be accounted easily. The figure shows the sketch of a rotor with an inlet recirculation bubble at the inlet that is marked with a grey patch. Furthermore, the approximated inlet velocity distribution, as shown in figure 4.5, is shown as a black dashed line. The red arrows mark the mass flows going in and out of the control volume. Under recirculation, a portion of mass is dropped out of the intake of the rotor at the tip and is reingested by it at a lower radius, as shown in the figure.

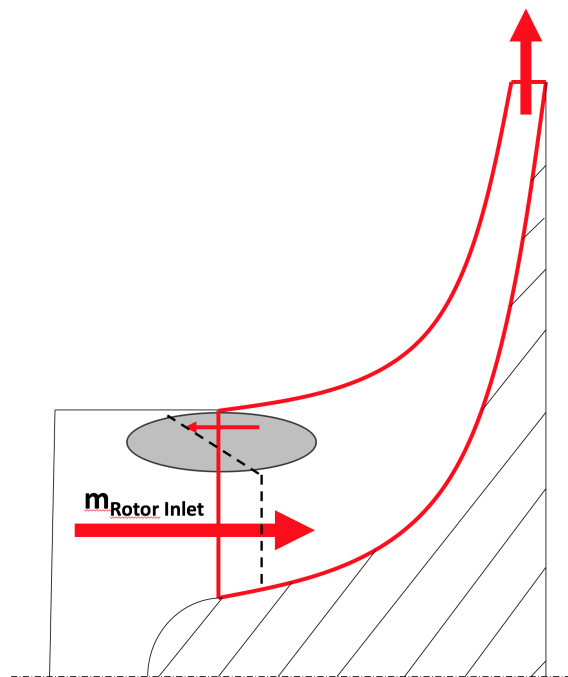


Fig. 4.6 Control volume rotor with mass flows going in and out during inlet recirculation

In order to quantify the effect of the recirculation on the mass flow at the rotor inlet, the CFD results have been processed and the inlet plane was separated into a region of flow into

the rotor and a region of flow out of the rotor. In this way, 1D mean values for the mass flow exiting and entering through the rotor inlet could be determined and correspond to the red arrows at the rotor inlet in figure 4.6. The increased amount of mass flow which is ingested by the rotor under recirculation is shown as $m_{RotorInlet}$ in the mentioned figure and gives the best impression about the situation at the rotor inlet in a conventional sense, meaning regarding the change in inlet velocity triangles and incidence respectively. This value was set in relation to the mass flow going through the overall machine and was plotted over the global flow coefficient for different rotor speeds in **figure 4.7**. Several observations can be made in this plot. Firstly, a significantly larger amount of up to 35% more mass than passing to the machine itself is ingested through the inlet. Secondly, the amount of mass recirculated through the inlet rises almost linearly with a decrease in flow coefficient. Thirdly, the starting point of inlet recirculation shows a small variation of around 4.5% with rotor speed and is located at a global flow coefficient of around 0.071, marked with a dash- dotted line in the figure. Lastly, the maximum amount of additional flow which is recirculated through the inlet decreases with rotor speed and the machine does not show any recirculation for the highest two speed lines.

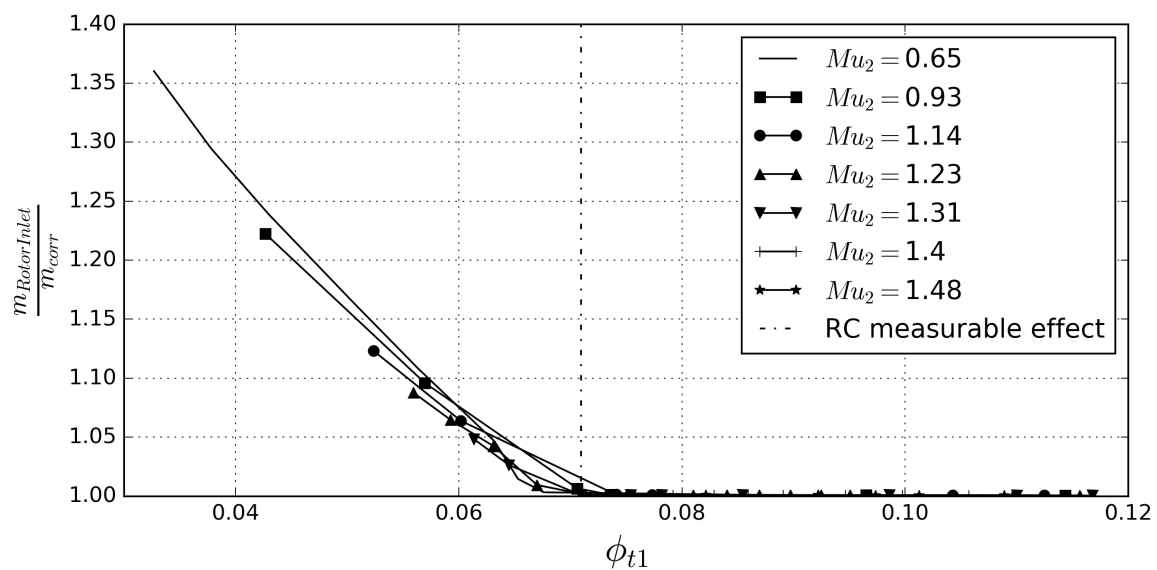


Fig. 4.7 Predicted mass flow into the rotor relative to the mass flow going through the machine over the global flow coefficient at different rotor speeds

Once inlet recirculation is present, the flow exiting the rotor out of the inlet has a certain momentum which is introduced into the inlet of the machine. In order to show the effect of inlet recirculation in terms of momentum, the axial, radial and tangential momentum fluxes in the flow exiting the rotor inlet as well as the flow which enters the rotor inlet under

recirculation, analogue to those shown in figure 4.6, are discussed below.

The momentum is calculated by integrating over the corresponding area of the inlet plane for flow going into and exiting the rotor. Furthermore, the momentum is normalised with the tip speed Mach number squared.

Firstly, the normalised momentum fluxes of the flow exiting from the rotor into the inlet are shown in **figure 4.8** and are plotted over the global flow coefficient.

The top graph shows the axial momentum which is negative, relative to the main flow direction. For all rotor speeds, it increases with a reduction in flow coefficient as the recirculation bubble grows. The gradient of the axial momentum curves remains about constant for all rotor speeds. For the lowest rotor speed, the gradient becomes lower towards small flow coefficient whereas the axial momentum increases almost linearly for higher rotor speeds. This behaviour might be related to the upstream extend of the recirculation bubble.

The second graph shows the radial momentum in the reverse flow region. Generally the radial momentum is low, compared to the axial and tangential values. Just after the onset of inlet recirculation, the radial momentum sharply drops to negative values for all rotor speeds. When throttled to even lower flow coefficients, the radial momentum decreases again and even reaches zero for the lowest rotor speed.

This behaviour can be explained with the meridional shape of the recirculation bubble as shown in figure 4.2a. The flow inside recirculation bubble has an axial and a radial velocity component. In the middle section the axial velocity magnitude will be high, whereas the radial velocity magnitude will be low as the flow in the bubble mainly moves axially. Towards the both ends of the bubble, the flow stagnates in the axial direction and does have a radial component, resulting in a higher radial velocity magnitude.

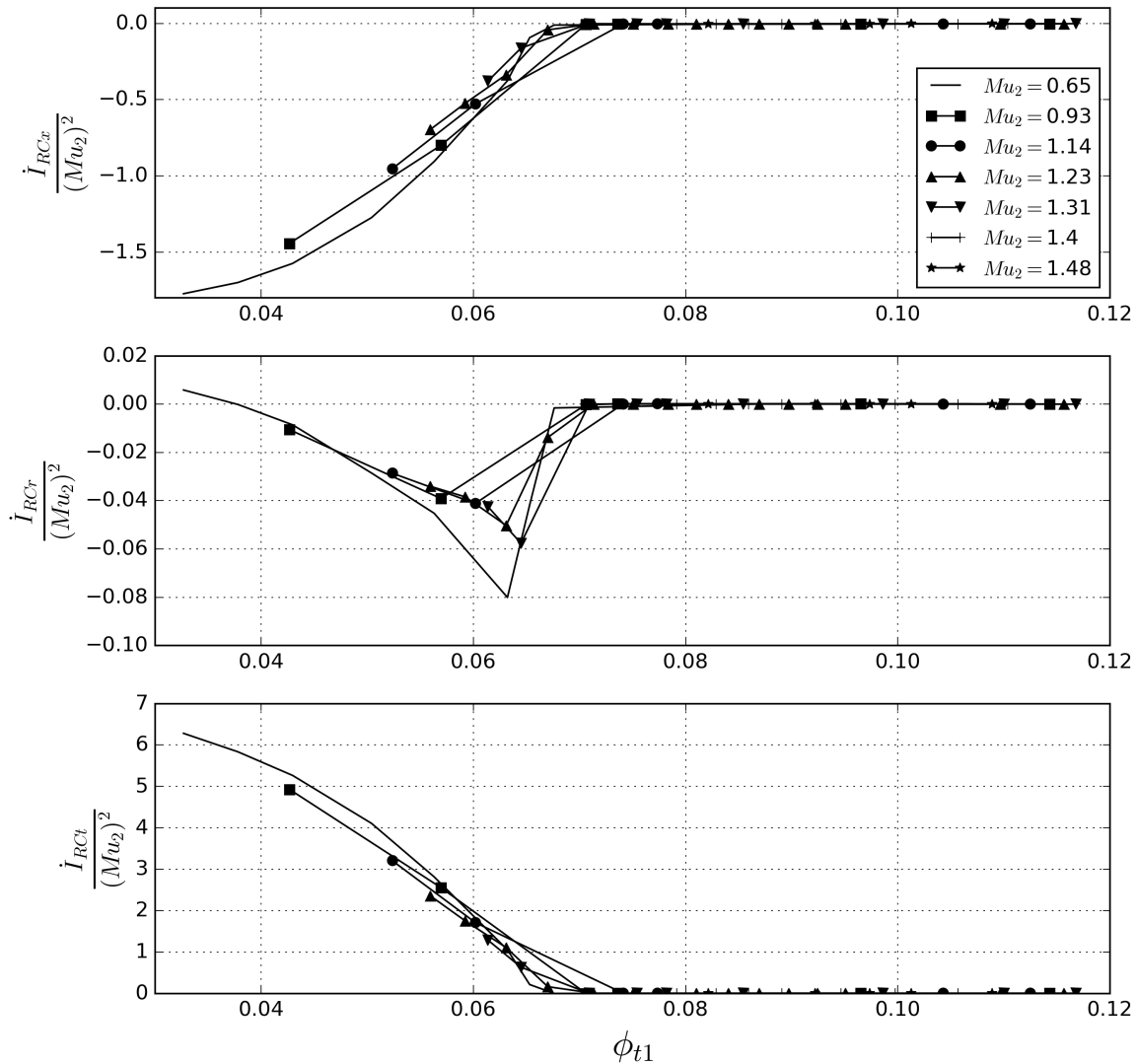


Fig. 4.8 Predicted mean momentum fluxes in the recirculation flow coming out of the rotor inlet

Depending on the size of the bubble, the rotor inlet, where the measurement plane to derive the presented results is located, sees a different cross-section of the bubble. This means that if the bubble is small, the flow in the plane will be in a downward movement, resulting in a high negative radial momentum, as shown in the middle graph of figure 4.8. The larger the bubble becomes, the smaller the radial momentum and the higher the axial momentum. This behaviour becomes clearer when looking at the casing pressure distributions presented in **figures 4.9 to 4.12**. The lines in black show results which were measured and the lines in red show results from the simulations. In this case, the values were taken from the 50% speed line corresponding to a tip speed Mach number of 0.65. Figure 4.9 shows the compressor

characteristic in terms of total to total pressure rise on the top and total to total isentropic efficiency on the bottom. Three operating points are marked in these graphs, where the one at the highest flow coefficient shows no recirculation, the middle one is just after the onset of recirculation and the one at the lowest flow coefficient has strong recirculation. The corresponding casing pressure distributions are shown in the other three graphs. Those are nondimensionalised with the inlet total pressure and plotted over the meridional distance through the machine which was nondimensionalised by the meridional camber length of the rotor. In the casing pressure graphs, the leading and trailing edge of the rotor is marked with vertical dashed lines. Furthermore, the location of the measurement plane for the values presented in figure 4.8 and all other figures in this section is marked with a bold red line. This plane corresponds to Plane 1 in figure 3.12. The qualitative size of the inlet recirculation bubble is marked with thick black lines. Figure 4.10 shows the operating point without recirculation which is visible by all casing pressure taps upstream of the rotor being lower than the inlet total pressure. Figure 4.11 shows a small recirculation bubble which can be seen by the casing pressure values just upstream of the rotor being higher than the inlet total pressure. Consequently, work must have been done to the flow as the static pressure exceeds the inlet total pressure. This case corresponds to the strong gradient region of the radial momentum flux plot in figure 4.8 as the measurement plane observes the "downward" part of the recirculation bubble. Figure 4.12 shows a large recirculation bubble where all casing pressure taps upstream of the rotor leading edge measure a value that exceeds the inlet total pressure. In this case, the bubble is large and the measurement plane only sees the part of axial movement and only a small or no radial movement. This case corresponds to the low radial momentum flux for very small flow coefficients presented in the middle graph of figure 4.8.

As the flow exiting from the rotor inlet already exchanged momentum with the rotor, work has been done to it, which also results in a tangential component of momentum flux in Plane 1 just upstream of the leading edge. The momentum flux for different rotor speeds in the tangential direction is shown in the bottom graph of figure 4.8. Similarly to the axial momentum flux, there is a clear correlation with rotor speed and the tangential momentum flux increases almost linearly with a reduction of global flow coefficient independent of rotor speed. The rate of change remains about constant for different speeds. In case of the lowest speed line, the gradient of the momentum flux curve reduces, whereas it remains almost constant for the other rotor speeds. Again, this behaviour could be related to the extreme axial extend of the bubble in these cases.

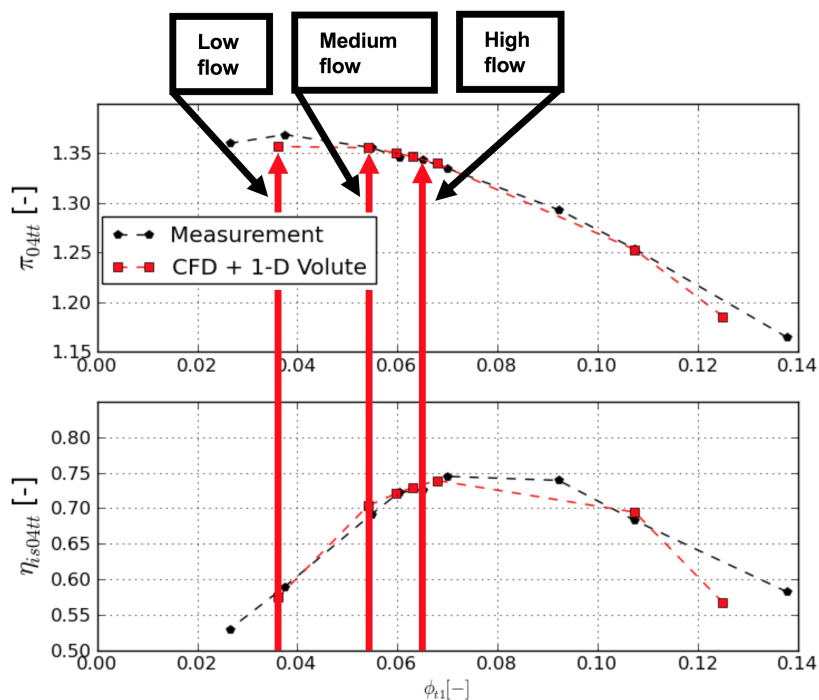


Fig. 4.9 Casing pressure distribution from Experiment and Simulation at $Mu_2 = 0.65$: Compressor characteristic

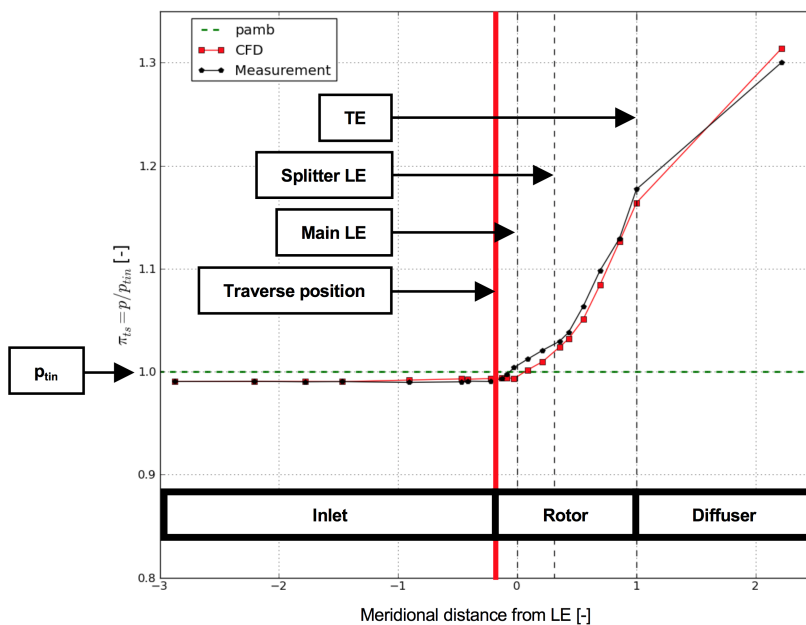


Fig. 4.10 Casing pressure distribution from Experiment and Simulation at $Mu_2 = 0.65$: Clean flow

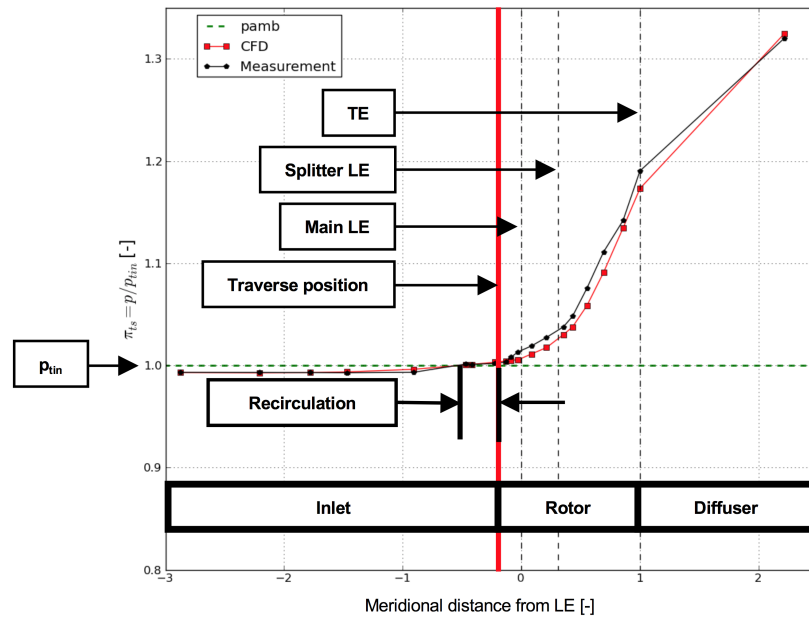


Fig. 4.11 Casing pressure distribution from Experiment and Simulation at $Mu_2 = 0.65$: Established recirculation

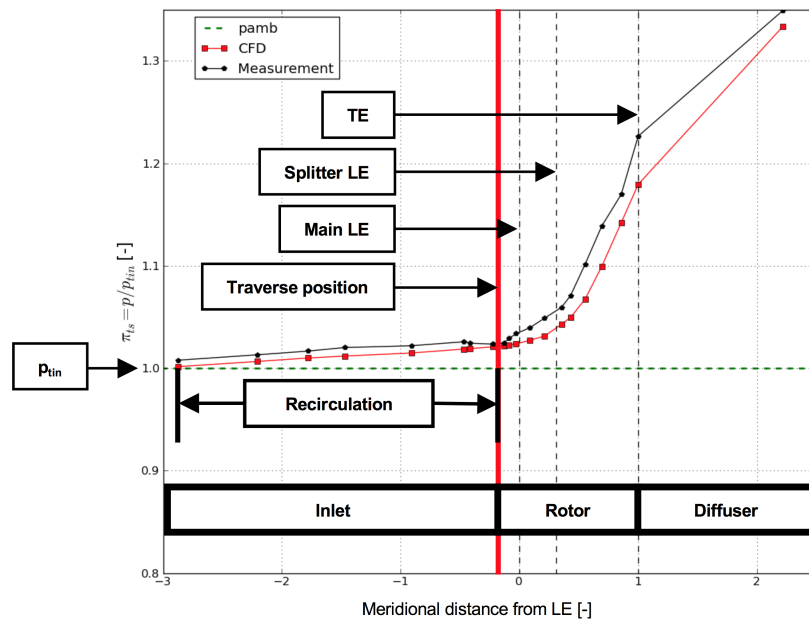


Fig. 4.12 Casing pressure distribution from Experiment and Simulation at $Mu_2 = 0.65$: Strong recirculation

Another way of looking at inlet recirculation in terms of momentum is to focus on the region of the inlet where flow enters the rotor, as shown in figure 4.6. For this region, the normalised momentum fluxes in the axial, radial and tangential direction have been worked

out in the same way as presented for the recirculation flow shown before. The quantities are plotted for different rotor speeds over the global flow coefficient in **figure 4.13**.

The top graph of figure 4.13 shows the normalised axial momentum flux entering the rotor. As the momentum flux scales cubically with speed, it correspondingly increases with rotor speed and flow coefficient. As the graph is normalised with the tip speed Mach number the lines consequently collapse. At flow coefficients which are lower than the onset point of recirculation at ϕ_{r1} of 0.071, as derived from figure 4.7, the rate of change of the axial momentum flux decreases and the gradient in the plot becomes flatter. This behaviour is a result of the reduction of aerodynamic throat area due to the recirculation bubble which, for continuity reasons, requires higher velocities and consequently a higher axial momentum.

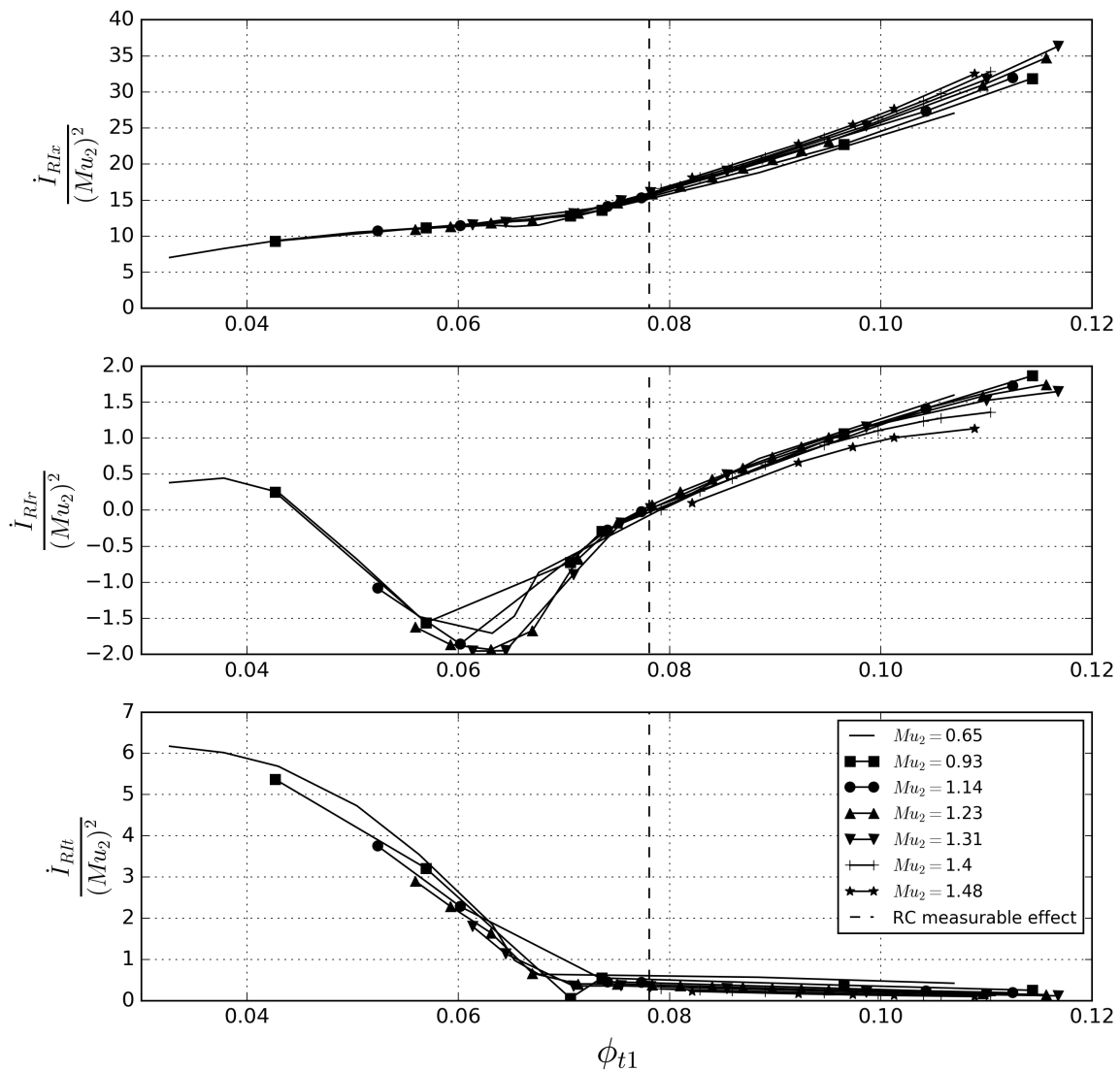


Fig. 4.13 Predicted mean momentum fluxes in the flow going into the rotor inlet

The graph also shows a dashed vertical line at a flow coefficient ϕ_{r1} of 0.078. This value was derived from the middle plot, which shows the radial momentum flux in Plane 1 for different speeds and represents the point of zero radial momentum. This point represents a distinct feature in terms of the onset point of recirculation. It results from the upstream effect of the blockage in the casing region within the rotor passage on the rotor potential field. This blockage might not have developed into an inlet recirculation yet but represents a state prior to inlet recirculation. Further details on the 3D flow field in the casing region will be provided in chapter 7. This means that the point of zero radial momentum could represent a precursor to the onset of inlet recirculation upstream of the rotor. However, it has to be pointed out that the radial momentum is very small compared to the axial and tangential values. Once inlet recirculation is present upstream of the rotor, the swirling component in the flow affects the radial momentum as it induces a radial pressure gradient. Consequently, the radial momentum is reduced.

This observation shows again that it is a matter of definition of where inlet recirculation exactly begins, as has been mentioned in the section about the onset of recirculation before. What can be said in terms of "symptoms" of the phenomenon is that the point of zero radial momentum is reached within a margin of $\pm 1\%$ from the flow coefficient specified above, whereas the mass flow criterion presented before shows a variation of $\pm 4.5\%$. Furthermore, it is reached much earlier than a reverse mass flow is registered, as has been shown in the discussion about the onset of recirculation before. More specifically, the point of zero radial momentum is reached almost 10% earlier in terms of flow coefficient relative to the mass flow criterion. An explanation to why the zero point is reached in almost one single point for all rotor speeds cannot be given yet and requires further investigation into the 3D flow field. Those are provided in chapter 7.

Because the radial momentum cannot be measured in an experiment, it will not be used as a criterion for the onset of inlet recirculation here. However, in a simulation which can predict momentum with sufficient accuracy, this criterion could potentially be used to clearly specify inlet recirculation and should be investigated further and tested on other geometries. Once the recirculation bubble is established, the radial momentum first drops to negative values and then increases again until a value of around zero when throttled to lower flow coefficients. The explanation for this behaviour is the same as for the flow coming out of the rotor.

The bottom graph of figure 4.13 shows the normalised tangential momentum flux in the flow entering the rotor inlet. The tangential momentum gradually increases with a reduction of flow coefficient due to the potential field of the blade being pushed out further into the space in front of the rotor. The influence of the recirculation phenomenon on the tangential momentum takes effect at a flow coefficient of around 0.071, which corresponds to the

starting point determined by the mass flow criterion. In this graph it can clearly be seen that the radial momentum of zero is reached much earlier. After the onset of inlet recirculation, a positive tangential momentum is present in the flow entering the rotor, implying a certain amount of positive pre-swirl which is induced by the recirculation bubble.

This graph clearly shows, that Qiu's assumption that the pre-rotation is confined to the recirculation zone [35] does not apply to this machine. The magnitude of tangential momentum increases with reducing the flow coefficient for all rotor speeds at approximately the same rate. For low speeds, the rate of change decreases with lowering the flow coefficient, whereas it remains almost constant for higher rotor speeds. One explanation for this behaviour is the size of the recirculation bubble. The extend of the recirculation bubble increases with lowering the flow coefficient. This means that more kinetic energy can be dissipated due to transport effects as the area of mixing between the recirculation bubble and the normal flow increases. In return, this reduces the tangential momentum in Plane 1 and contributes to a decreasing rate of change in angular momentum as the flow coefficient reduces.

In order to investigate the conservation of energy during inlet recirculation, the total enthalpy change from the intake of the compressor to Plane 1 has been plotted over the global flow coefficient for different rotor speeds in **figure 4.14**. In order to give a better overview, the total enthalpy values have been nondimensionalised with the total enthalpy change over the compressor wheel. In the figure, the top graph shows the total enthalpy change from the inlet to the region of Plane 1, where the flow exits the rotor into the inlet. It shows that, as soon as inlet recirculation is established, the energy input into the recirculation zone flattens out and maintains a constant value of around 0.7 relative to the total enthalpy change over the wheel.

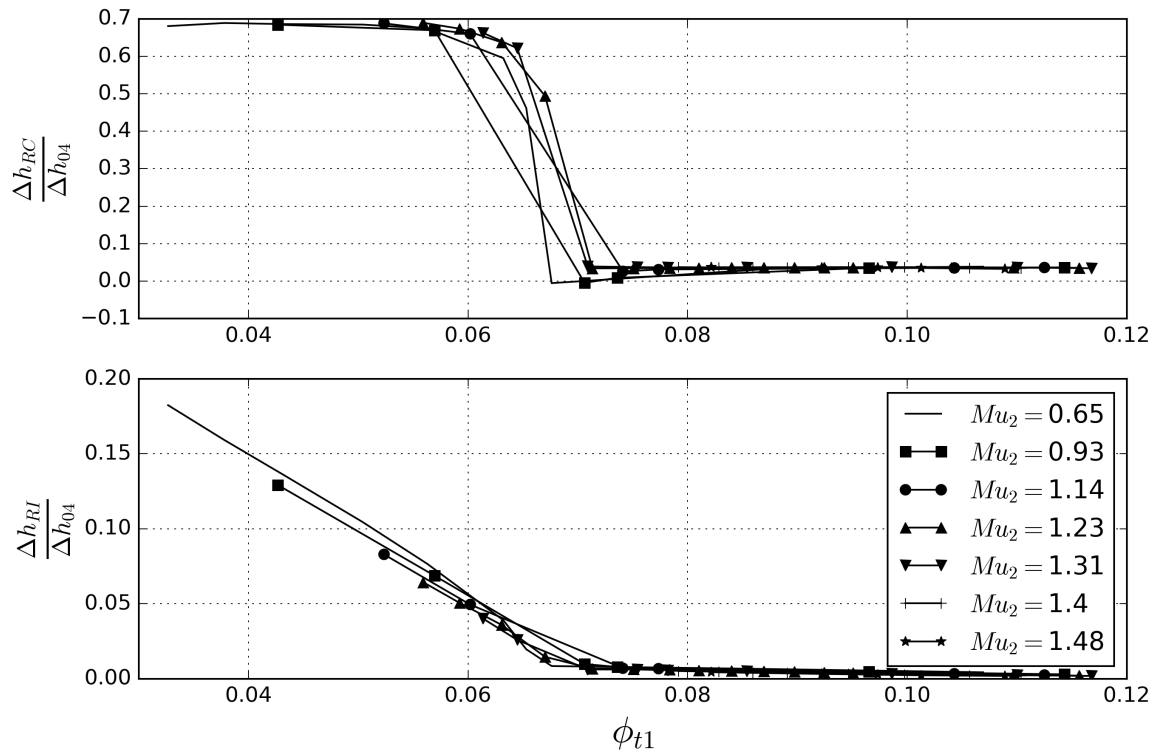


Fig. 4.14 **Top:** Predicted enthalpy in the recirculated mass flow exiting the rotor for different speeds ; **Bottom:** Predicted enthalpy in the mass flow entering the rotor for different speeds

The bottom graph of figure 4.14 shows the total enthalpy change from the intake to the part of Plane 1 where the flow enters the rotor. It shows that the amount of energy in the flow entering the rotor increases as soon as inlet recirculation is present. Furthermore, the energy increases almost linearly with a decreasing flow coefficient. This behaviour can be well understood when looking at the top graph of the same figure which shows the amount of energy in the recirculated flow. It shows that the energy in the recirculated flow stays almost constant for varying flow rates. As the amount of energy brought into the inlet flow due to recirculation is a product of the specific enthalpy and the mass flow, the latter has to be considered as well. Figure 4.7 shows that the mass flow recirculated into the inlet increases almost linearly with a reduction in flow coefficient. As a result, the rate of increase in total energy at the inlet Plane with a reduction in flow coefficient is also almost linear as it is almost entirely a function of the increased recirculated mass flow. Further assessment of the amount of energy in the recirculation bubble and the losses related to it are provided in chapter 6.

4.4 Conclusions

In order to characterise inlet recirculation, key features of the phenomenon have been investigated and described in this section. The location and general shape have been described and it was shown that inlet recirculation is a phenomenon which takes place in the tip region of the rotor inlet of a radial compressor wheel. The bubble can extend far downstream into the rotor and far upstream into the inlet. Furthermore, the flow within the recirculation bubble features a strong positive swirl component. The phenomenon is non periodic in a time averaged sense. Furthermore, it can extend into the passage radially up to 20% of the span.

An approach from literature to characterise inlet recirculation based on a distinction between a recirculation zone and an active zone area was introduced and it was shown that an alternative approach based on a distinction between the mass flow direction allows to make a characterisation of the recirculating flow pattern based on mass, momentum and energy.

An overview of approaches to define the onset point of inlet recirculation has been provided and it was shown that the common technique of using an incidence based criterion might not be sufficient to fully depict the situation. Instead, it was argued that the portions of flow in the shroud area featuring low meridional momentum could be the proximate cause for triggering inlet recirculation. It was furthermore described that this low momentum region could originate from four mechanisms, namely leading edge separation, the radial pressure gradient, passage diffusion and tip leakage flow. It was argued that, depending on the design of the machine, the importance of these contributors could vary. This argument was supported by a comparison of two results from the public domain where one described a general radial compressor and the other described an automotive compressor with low passage diffusion in the inducer due to its transonic nature and wide range design. For the latter type of machine, it was shown that recirculation occurred at much lower incidence values than in the other case, implying that other phenomena than incidence induced suction side separation could have contributed more to a built up of low momentum fluid at the rotor shroud.

For the established recirculation bubble in the flow field, a characterisation based on mass, momentum and energy was provided. It showed that the mass flow feeding out of the rotor into the inlet and the recirculation zone increases almost linearly with a reduction in flow coefficient and that it can reach values of up to 35% of the main mass flow. Furthermore it was shown that the phenomenon only occurs at low and medium rotor speeds whereas it does not occur prior to surge at high speeds.

A momentum analysis in the flow entering the rotor through the inlet showed that the radial

momentum summed to zero prior to the presence of inlet recirculation upstream of the rotor for all rotor speeds. This was related to the potential effects of the blockage region at the casing within the passage which is present prior to inlet recirculation. Further investigations on alternative geometries could provide information whether this behaviour applies to other machines as well.

The investigation of the energy in the recirculation showed that in the flow exiting the rotor through the inlet during recirculation, the amount of energy reaches values of around 70% of the total enthalpy change from inlet to exit of the rotor and remains about constant. It was furthermore shown that the energy in the flow entering the rotor during recirculation rises almost linearly with a reduction in flow coefficient for all rotor speeds.

Inlet recirculation is understood to be the result of a subtle balance between the meridional momentum inside the impeller inducer passage and the local static pressure field. Consequently several major design geometry parameters can have an effect on the onset and maintenance of inlet recirculation. Those parameters are identified as:

- The rotor main blade leading edge loading
- The casing meridional curvature, particularly in the inducer part
- The impeller inlet to exit area ratio, which determines the part speed flow coefficient
- The relative tip clearance gap size which influences the blockage and loss in the tip region

Because of the importance of the tip clearance effects which particularly play a role in small sized turbocharger compressors due to the large relative tip gap size, this factor has been studied in more detail. The results are presented in chapter 7.

Chapter 5

Compressor low flow operation analysis

5.1 Introduction

In order to get a clearer picture about the conditions at which inlet recirculation occurs, the research compressor is investigated to identify the regions in the operating map with presence of inlet recirculation. An analysis of the stability limits of the different components of the machine is provided to ensure no other flow phenomena are present in the onset region of inlet recirculation. This ensures that the altered behaviour can clearly be related to inlet recirculation. As a criterion to track the onset of inlet recirculation, the casing pressure values as well as the radial distribution of the axial velocity at the inlet of the rotor are used. The results are then plotted into the compressor map of the research compressor to provide information for all rotor speeds and allow a separation of the region with normal flow and the region with inlet recirculation. Furthermore, the effect of the passage shock on the recirculation region is discussed.

5.2 Compressor low flow operation analysis

In order to study the effect of inlet recirculation, it is important to gain further understanding about the operating points where the phenomenon occurs in the compressor. Furthermore it is important to take into account the stability limits of all components in order to make sure that no other disturbances are present. To achieve this aim, a stability analysis has been carried out on the research compressor. For the analysis, the performance and operational limitations of the four main parts Inlet, Rotor, Diffuser and Volute, as introduced in chapter 3 were investigated. For the part speed region, experimental data from the test rig and simulation data can be used. An analysis of the full compressor map can be obtained via the CFD calculations. The aerodynamic behaviour of the different parts of the machine are discussed separately below and a compressor map which outlines the region where recirculation occurs is provided. Furthermore, the influence of rotor speed on the recirculation region is assessed.

The inlet plays a negligible role as a source for flow disturbances which can lead to instability of the compressor. Assuming a clean inflow, this part of the machine inherently cannot cause problems as it only consists of a bellmouth followed by a straight duct. As a result, it will not be dealt with further in the following analysis.

The volute is designed to produce no static pressure at design conditions despite the amount of pressure rise which results from the radius change from inlet to outlet. At off design, however it acts as a diffusion device. At very low flow conditions, large scale separations can occur at the tongue. These large scale separations can destabilise upstream components in the machine. In case of the compressor subject to this work, the matching of its components leads to flow conditions where either the diffuser or the rotor fail earlier than the volute so that volute instabilities do not play a major role and consequently will not be further discussed here. A more detailed description of the volute performance has been given in section 3.4.3 in the Methods chapter 3.

Due to its rotational asymmetry, the volute does have an effect on the performance of the upstream parts of the machine as soon as it is not operated at design flow conditions. The asymmetry of the pressure field leads to pressure fluctuations in the rotating parts of the machine and locally higher back-pressures in the static parts, making it more likely for flow separations to appear at these circumferential positions. The circumferential non-uniformity caused by the volute could be determined by the static pressure variation measurements introduced in section 3.4.2, where a $\pm 1.2\%$ circumferential casing pressure variation at the diffuser inlet was determined at the onset point of recirculation. Although the flow at the diffuser and volute inlet is compressible in reality, the assumption of a constant total pressure

and density is made. This simplification allows the volute induced pressure fluctuation to be interpreted as a change in dynamic head and consequently be converted into a change in flow angle in the diffuser after **equation 5.1**. For the onset point of recirculation at 50% rotor speed, this adds an uncertainty of 4 degrees to the volute as well as the diffuser inlet angle. The uncertainty is accounted for in the discussion about diffuser instabilities below.

$$\alpha = \sin^{-1} \left(\frac{c_t}{\sqrt{\frac{2}{\rho}(p_t - p)}} \right) \quad (5.1)$$

The rotor is the most complex part of the compressor in terms of geometry and flow structure. In order to obtain an overview of the phenomena in the rotor, two distinct points on its characteristics were determined. The first one was the absolute instability limit where surge occurred. For the measurement it was defined as that point where strong pressure fluctuations indicating a surge hysteresis started to occur. Numerically, surge was not determined directly. Instead, the calculations were stopped at operating points where numerical convergence could not be achieved any more.

The second distinct point was the onset of inlet recirculation. For this point, a criterion based on the casing pressure measured right upstream of the rotor leading edge was defined. The local pressure was measured and compared to the inlet total pressure. For a normal flow pattern, the static pressure upstream of the leading edge inherently has to be lower than the upstream total pressure in the intake Plane 0 due to the losses present in the intake duct. A value higher than the inlet total pressure implies that a certain amount of work must have been done to the flow which could only have happened inside the rotor. Consequently, the flow at the casing must have been recirculated from inside of the rotor. This feature of an abnormally high static pressure can be used as a criterion to define the onset of inlet recirculation. More specifically, the criterion indicates that high pressure flow from inside of the rotor is recirculated back upstream of the rotor leading edge and into the inlet. In a first step, the criterion was applied to the 50% design speed case.

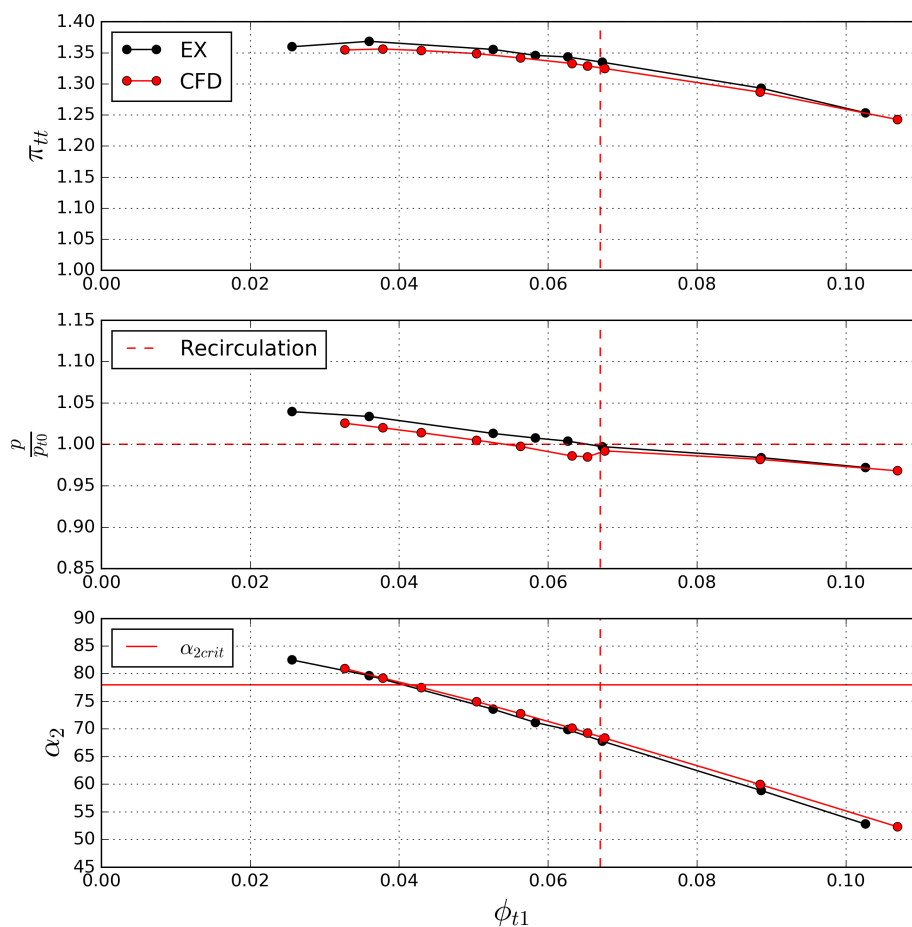


Fig. 5.1 Rotor and diffuser stability [$M_{u2}=0.65$]

The results are shown in **figure 5.1**, where the black curves show the experimental results and the red curves show the CFD results. The top graph shows the total to total pressure rise of the compressor over the global flow coefficient. The results derived from the simulation and those from the experiment, agree very well. The instability limit was defined as described above and is given by the operating point with the smallest flow coefficient where operation, respectively convergence of the simulation was still possible.

The onset of recirculation is marked with a vertical red dashed line. Its position was determined based on the recirculation criterion shown in the middle graph of the figure. There, the ratio of local casing pressure just upstream of the leading edge in Plane 1 to the inlet total pressure is plotted over the global flow coefficient. At a flow coefficient of $\phi_{t1} \cong 0.0675$, the casing pressure exceeds the inlet total pressure and recirculation is present upstream of the rotor leading edge. For the CFD data, the curve looks slightly different with a "dip" in local static pressure rather than a continuous rise. This "dip" can also be observed

in the casing pressure distribution in figures 4.10 to 4.12 where it can clearly be seen that the casing pressure is slightly under-predicted in the simulation compared to the experiment. Nevertheless, the trend for the casing pressure is picked up in the right way. This clear marker at the same flow coefficient indicates the onset of recirculation which is defined as flow being expelled from the rotor leading edge. It has to be noted that this criterion defines the onset of recirculation at lower flow coefficients than the mass flow criterion and the radial pressure gradient criterion introduced in the last section, which determined the onset point at global flow coefficients of 0.071 and 0.078 respectively.

The diffuser is a part of the machine where instabilities can occur in form of VDRS or AIRS, as discussed in **section 3.2.3**. Based on empirical and analytical correlations given in that section, a critical diffuser inlet angle α_{2crit} of 78 degrees was determined. The diffuser inlet angle is plotted over the global flow coefficient in the bottom graph of figure 5.1. In the same graph, the instability limit of the diffuser is shown as a horizontal red line. As can be seen, the diffuser operates at inlet angles around 67 degrees at the flow coefficient where recirculation occurs. Even when taking into account the additional penalty of 4 degrees from the volute induced circumferential angle variation, the diffuser operates well below the critical inlet angle. This means that during the onset of recirculation, the diffuser is operating stably. The graph also shows that the numerically determined diffuser inlet angle agrees very well with the measured one. Small deviations can be explained by an inaccurate prediction of secondary flows in terms of magnitude and thus blockage in the numerical rotor. These prediction uncertainties in secondary flows can lead to a large error in the prediction of the slip velocity at the exit of a radial machine. The error in return adds to the difference in exit flow angle as well. An overview of the diffuser performance predicted by CFD at different rotor speeds is given in **figure 5.2**, which shows the diffuser inlet angle over the flow coefficient at the rotor outlet ϕ_2 . To give an orientation, the analytically determined critical diffuser inlet angle is plotted as a horizontal red line. The graph shows that the diffuser operates well below the critical diffuser inlet angle for the majority of operating points. For the two lowest rotor speeds, the critical angle gets exceeded for the lowest flow coefficients. For the lowest speed case, it has been shown in figure 5.1 that the onset of recirculation happens well before the critical angle gets exceeded. For the rotor speed of M_{u2} of 0.91, where the critical diffuser angle also gets exceeded for the lowest flow coefficients, the onset point of recirculation is reached at much higher a flow coefficient than diffuser instability, as can be seen in figure 5.5. For the remaining rotor speeds, the critical diffuser angle never gets exceeded so that stable diffuser operation can be assumed. As the distance from the critical flow angle where the diffuser gets unstable is so big, it can safely be said that at the

onset point of recirculation, the diffuser operates stably at all times, even when accounting for eventual deviations in the diffuser inlet angle due to numerical errors.

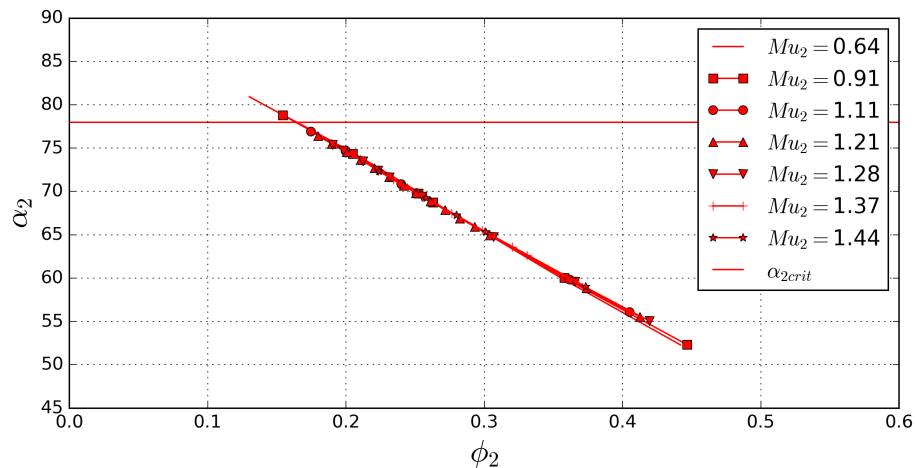


Fig. 5.2 Numerically obtained diffuser inlet angle for all rotor speeds

In order to distinguish the region with and without recirculation at different rotor speeds and obtain information about the whole operating map, the numerical results were used. In order to further clarify the onset point of inlet recirculation, a vertical cut through the numerical domain at the same position as the casing pressure tap which provided the data for the middle graph in figure 5.1 was taken and the pitchwise averaged axial velocity was plotted over the span. The results for the 50% speed line are shown in **figure 5.3** where the black line represents the operating point with a normal flow pattern and the red line represents the first operating point where recirculation is present. In the latter case, the reverse flow region occupies about 5% of the rotor span at the tip. In figure 5.1, these operating points can be seen as the closest ones to the vertical dashed line indicating the onset of recirculation. Regarding the change in flow rate in order to change the flow pattern, the difference between the two operating points is 3.4% relative to the normal operating point and as such very small. This means that the change between the two flow patterns occurs within a very small bandwidth of operating points and almost spontaneously.

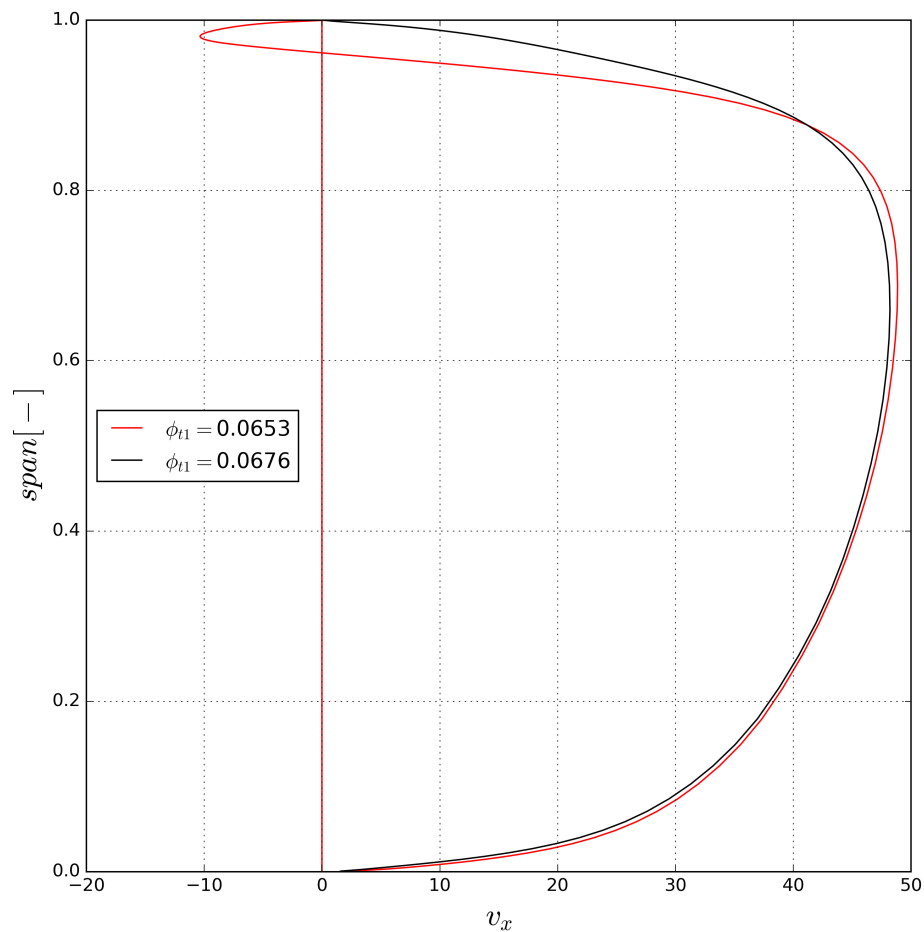


Fig. 5.3 Numerically obtained inlet pitchwise averaged axial velocity distribution [$M_{t2}=0.65$]

The described procedure was carried out for all rotor speeds of the research compressor. The results are shown in **figure 5.4**. The right graph shows the pitchwise averaged axial velocity over the span for the operating points with the lowest flow rate at which a normal flow pattern was detected, meaning no presence of reversed flow. The left graph shows the same values for the operating point with the highest flow rate at which a recirculating flow pattern was found. In order to provide a better overview, the individual flow coefficients are not given but the corresponding operating points can be seen in figure 5.5 as those points closest to the line separating the normal flow region from the recirculating flow region.

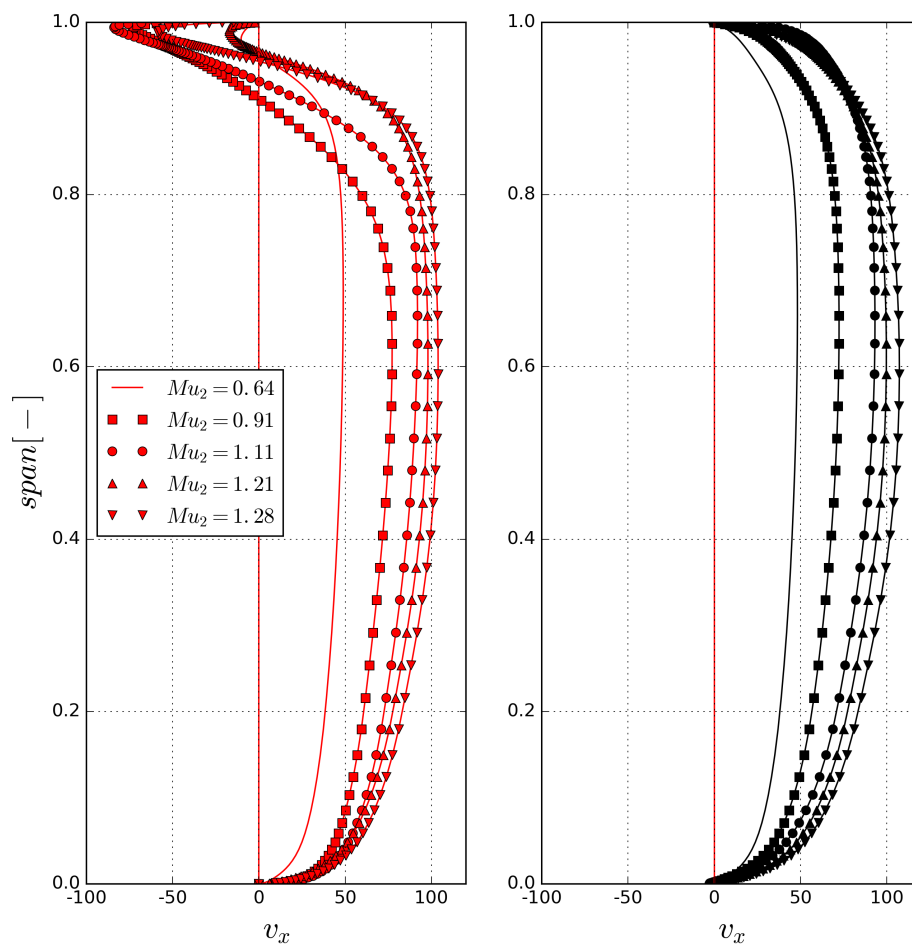


Fig. 5.4 Numerically obtained inlet pitchwise averaged axial velocity distribution for all rotor speeds

Figure 5.5 shows the compressor map of the research compressor and provides an overview of the operating points featuring recirculation. The part of the operating map where normal flow upstream of the rotor was found is coloured in green, the part where recirculation was present is coloured in red. For the low speed region, about 40% of the compressor map width are affected by recirculation. For the subsonic region of the compressor map, this value remains about constant. For transonic operation, the percentage of map width showing recirculation reduces. For the highest speeds, the compressor does not show any inlet recirculation but goes into surge directly. This behaviour is discussed in more detail below.

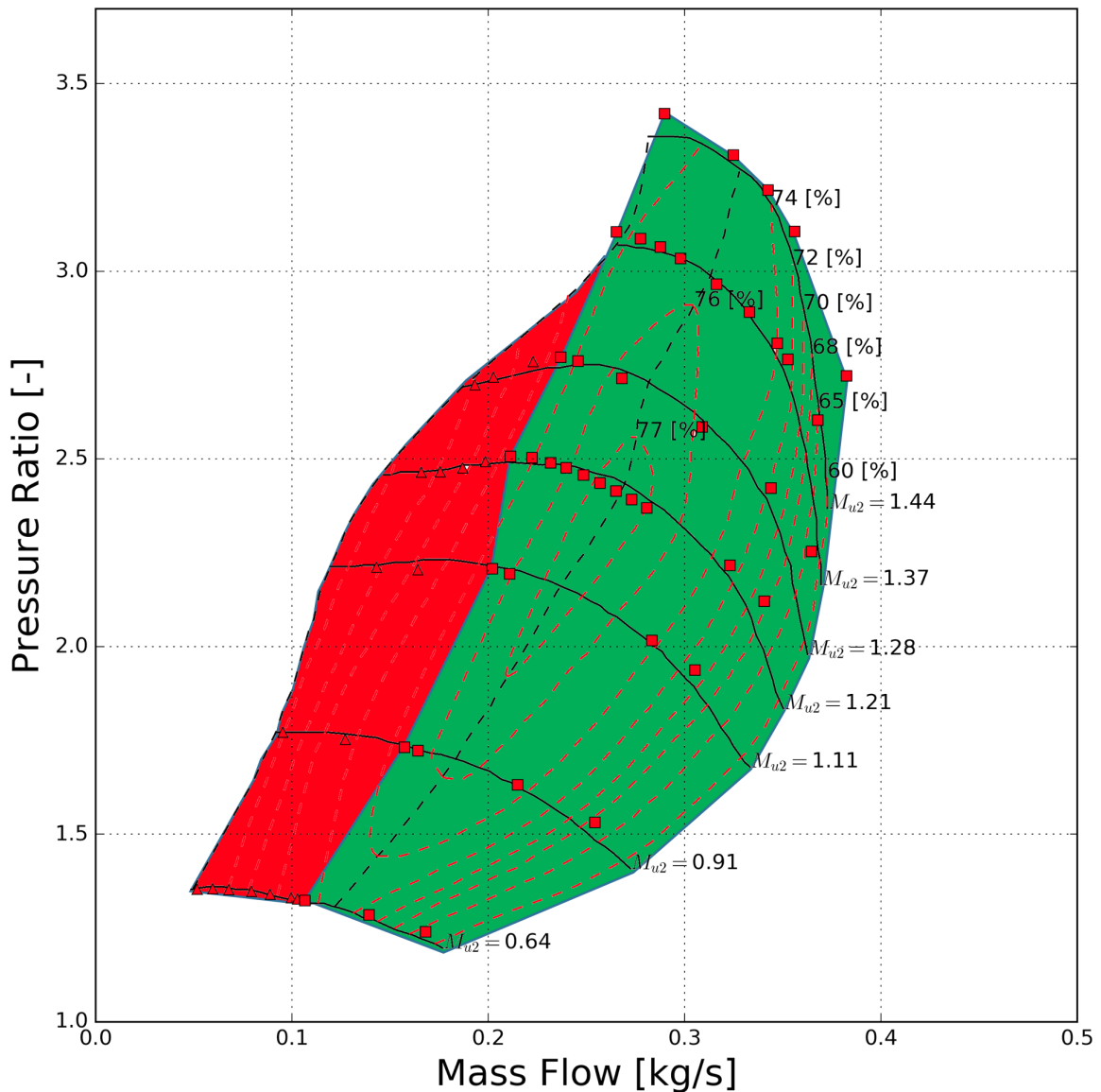


Fig. 5.5 Compressor map with normal flow region in green and recirculation region in red

A clearer analysis about the size of the region in which recirculation is present relative to the overall map size can be provided by defining a map width criterion W_{rc} as shown in **equation 5.2**. The criterion represents a relation of the width of the recirculation region to the map width at the corresponding speed, as shown in red in figure 5.5. The recirculation region is bordered by the mass flow at which recirculation was observed in the inlet spanwise axial velocity profile and the minimum mass flow. The overall map width is bordered by the maximum and the minimum mass flow of the corresponding constant speed line.

$$W_{rc} = \frac{\dot{m}_{rc} - \dot{m}_{min}}{\dot{m}_{max} - \dot{m}_{min}} \quad (5.2)$$

The map width criterion was used to investigate whether there is a correlation between the size of the recirculation region and the flow velocity, respectively rotor speed. In order to do so, the Mach number of the relative flow at the tip was calculated, which represents firstly a criterion for the rotor speed and secondly a criterion for the flow speed in the inducer tip region. **Figure 5.6** shows the map width criterion over the inlet tip Mach number. Several observations can be made from this graph. Firstly, the recirculation region continuously decreases with an increasing tip Mach number and consequently with rotor speed. Secondly, there is a jump in the size of the recirculation region from around 37% to around 26% map width in the speed range where the flow in the rotor inlet gets transonic around a tip Mach number of 0.9. It has to be noted that this is the mean tip Mach number. In the region of the blade suction side, higher speeds are to expect locally due to the streamline curvature, which explains why the jump in recirculation region size happens at tip Mach numbers lower than one.

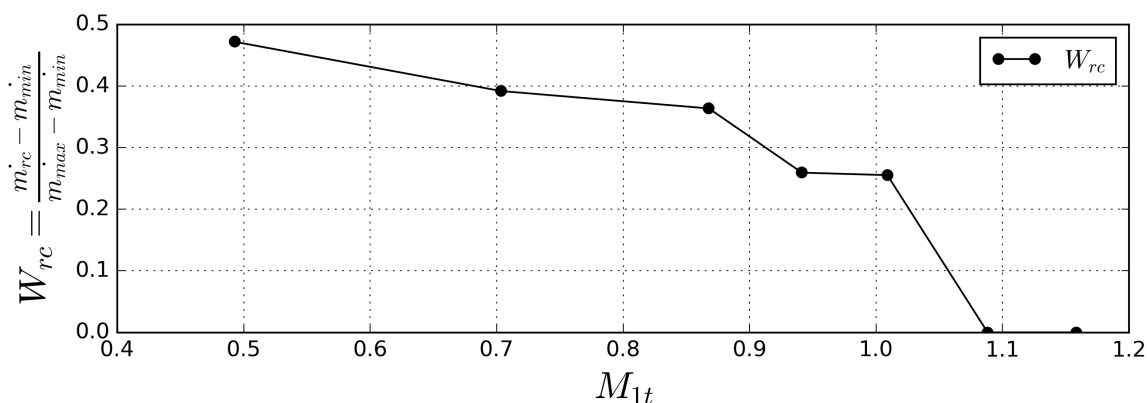


Fig. 5.6 Measure for the part of the map which is occupied by recirculation in terms of map width W_{rc} over the tip speed Mach number

This can be seen in more detail in **figure 5.7**, which shows the inducer part of the single passage numerical model. In the graph, the x-axis corresponds to the rotational axis and the inflow is from the left side of the picture into the machine. Two iso surfaces of a Mach number of unity are plotted into the geometry. The green iso surface is for a tip Mach number of 0.87, which corresponds to the point just before the jump in figure 5.6. The red iso surface corresponds to the next higher rotor speed at a tip Mach number of 0.94 just after the jump. Figure 5.7 shows that the size of the shock wave is significantly increased for the higher

rotor speed. The green iso surface shows only a localised shock region indicating a small passage shock which is localised to the suction side of the blade. For the higher rotor speed, the passage shock is much larger and extends further into the passage itself.

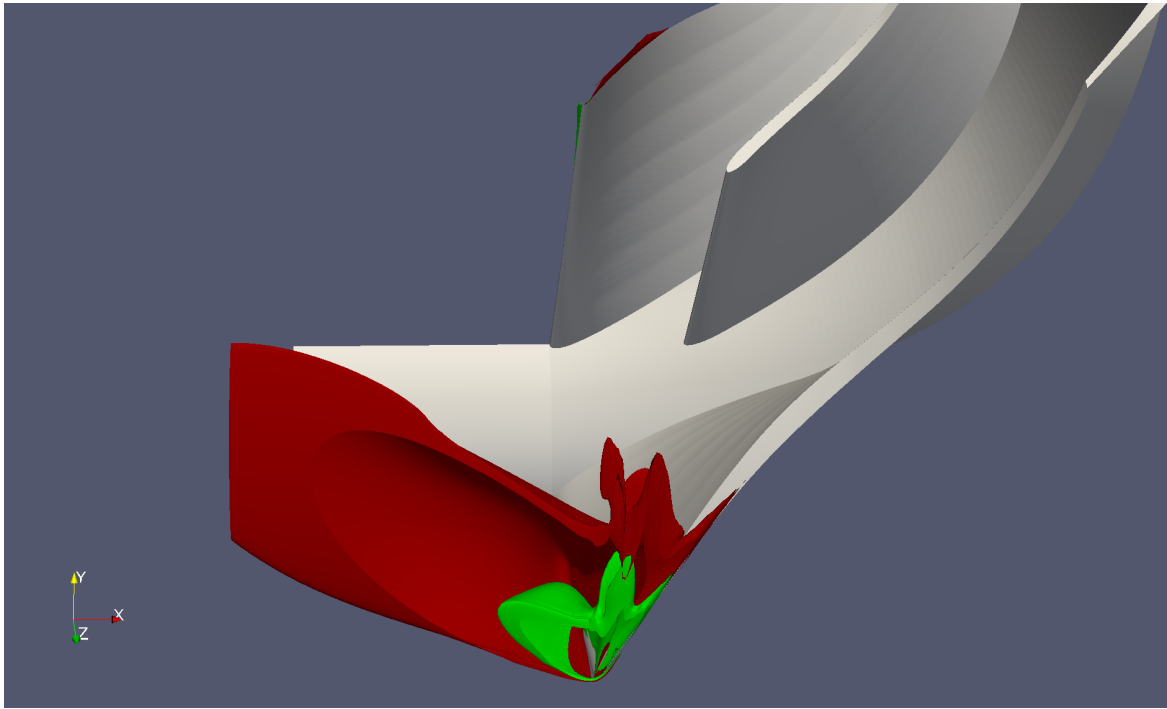


Fig. 5.7 View into the inducer part of the compressor wheel rotating around the x-axis showing contours of constant absolute Mach number of unity just prior to inlet recirculation for a inlet tip Mach number of 0.87 in green and 0.94 in red

Because the passage shock and inlet recirculation take place in the same location of the machine, the two phenomena will inevitably interact. Although inlet recirculation appears to be circumferentially symmetric in a time averaged sense, it still incorporates a disruption in the flow field. Combined with the amplification effect of a shock on disturbances, those disruptions will lead to a more unstable flow field more quickly. As a result, at high speeds, the minimum achievable mass flow before the flow becomes unstable is reached at higher mass flows where inlet recirculation cannot fully develop. These observations do not imply that the shock is responsible for the compressor to surge and no connections between the shock and the fact that the compressor surges directly without developing inlet recirculation at high rotor speeds can be made.

However, a shock has two general effects:

Firstly, a shock always goes along with a compression, meaning that kinetic energy is converted into pressure. This in return means that a shock will reduce the momentum available in the flow. As explained in the previous section that low meridional momentum is

one key feature for the development of inlet recirculation. Consequently, a shock contributes to the reduction of meridional momentum so that inlet recirculation could be triggered earlier. Secondly, a shock itself represents a disturbance in the flow and can furthermore amplify disturbances which pass through. An already deteriorated flow field like the one under recirculation could become destabilised quicker, thus the part of the compressor map which shows the effect of recirculation on a constant speed line is reduced.

5.3 Conclusions

This section provided information about which parts of the compressor map features inlet recirculation. Therefore, the performance of the four different parts of the compressor, inlet, rotor, diffuser and volute was discussed in order to assess whether they could suffer from disturbances in the region where recirculation occurs. It was found that no flow instabilities sourcing from the inlet, the volute and the diffuser were present in the region of onset of recirculation. Instead the rotor developed inlet recirculation and eventually caused the system to fail at low flows for low speed.

In order to assess the behaviour of the rotor, two distinct points on a constant speed line were determined. The data was acquired from the numerical model and the experiment. Firstly the instability limit where surge occurred was defined by the presence of strong pressure fluctuations in case of the experiment and by not achieving sufficient convergence with the simulation. Secondly the onset point of inlet recirculation was determined via a static pressure criterion and a reverse flow criterion upstream of the rotor. Concurrence between the casing pressure data of the experiment and the simulation was found for the 50% speed case. Recirculation could be tracked via the casing pressure just upstream of the rotor leading edge as the phenomenon caused this value to rise above the inlet total pressure, implying that work must have been done to the flow which could only have happened inside the rotor.

It was shown that inlet recirculation occurs way before the compressor goes into surge. Furthermore, it was found that the change between a normal flow pattern and inlet recirculation in the inlet Plane 1 occurred within a very small change of flow coefficient. This implies an almost spontaneous initiation of inlet recirculation, meaning within a few rotations of the impeller. In order to determine the region where recirculation is present at different rotor speeds, the numerically obtained data was used. Radial velocity profiles were used as a criterion to mark this region in the compressor map, as the reverse flow in the recirculation zone could be tracked easily. Once more, it was shown that the onset point of recirculation strongly depends on its definition. For example, the pressure and velocity criterion used in this section defined the onset at different flow coefficients than the mass flow criterion and the radial momentum criterion which were introduced in the last section. In order to use an approach which can be applied to both, the experiment and the numerical model, the definition based on pressure together with the matching velocity profiles was used.

It was found that inlet recirculation was present not only in the subsonic region of the rotor but also in parts of the transonic part of the compressor map. In terms of range, recirculation

was present over about 40% of the compressor map at low rotor speeds. This value decreased with increasing rotor speed and the compressor surged directly in the high speed region. In order to further assess the changing size of the recirculation region at different rotor speeds, a map width criterion was defined. This map width criterion was plotted over the inlet tip Mach number, which represented a measure for rotor speed and flow velocity in the inlet tip region. It was found that the width of the recirculation region reduced significantly, once sufficiently large shocks were present in the inducer tip region. The size and location of the shocks at the critical operating points were assessed and it was found that there was a significant difference. The effect of reducing the width for the recirculation region can be explained via two effects due to the presence of the shock. Firstly, a shock is a compression mechanism and as a result it converts a certain amount of kinetic energy into potential energy, reducing meridional momentum. As discussed in the section before, low meridional momentum is the key quantity in the triggering process of inlet recirculation so that a shock could cause the phenomenon to start earlier. Secondly, a shock itself is a strong disturbance in the flow field. In addition, any disturbances which are passed through the shock, are being amplified. This means that a shock has an overall destabilising effect.

A deteriorated flow field such as that during the presence of inlet recirculation could become destabilised quicker at higher mass flows, so that the part of the compressor map which shows the effect of recirculation on a constant speed line is reduced. However, no connections between the shock and the fact that the compressor surges directly without developing inlet recirculation at high rotor speeds could be made. The stability analysis showed that a wide part of the low speed region up to the transonic region of the compressor map was affected by inlet recirculation. The size of that region rises the question about how much energy is dissipated by the phenomenon. This question will be discussed in the next section.

Chapter 6

The energetic cost of inlet recirculation and accounting for it during preliminary design

6.1 Introduction

This chapter provides insight into the energetic costs of inlet recirculation. This was accomplished by splitting up the machine into its different components. Those components were analysed separately regarding their performance. Furthermore, disk friction was taken into account. The energetic cost of inlet recirculation was determined in two ways. Firstly, it was accounted via a simple model based on the work input into the machine. In addition, the losses occurring in the recirculation region were worked out from the combined mode, represented by the numerical model for the inlet, the rotor and the volute as well as the low order volute model.

6.2 Compressor performance analysis

In order to assess the overall performance as well as the individual part performance of the compression system, an analysis based on the combined model was carried out. In addition, the calculations have been validated with measurement data. Following the annotation introduced in chapter 3, the compressor has been split up into inlet, rotor, diffuser and volute. An overview of the measurement planes, is given in the sketch **figure 6.1**. The thermodynamic properties obtained in the experiment at these locations are listed in **table 6.1**.

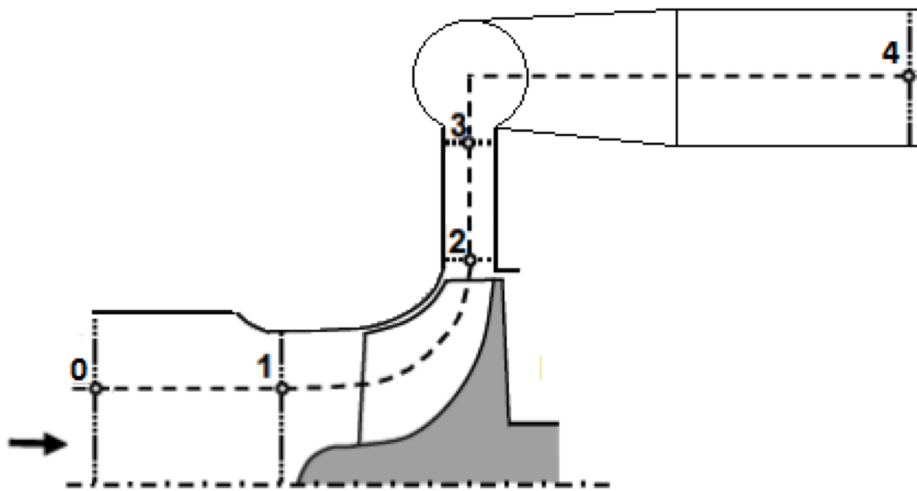


Fig. 6.1 1-D Measurement planes

Table 6.1 measured thermodynamic properties

property	0	1	2	3	4
p_t	X	X			X
T_t	X	X			X
p	X	X	X	X	X

The experimental data of the compression system has been analysed in a similar way as described in the author's diploma thesis [39]. There, the Author developed a model to predict radial compressor characteristics based on the 1D theory of turbomachinery and with the help of empirical correlations. The work was verified with a set of measurements which provided the rotor speed, mass flow, total conditions at the inlet and outlet of the machine as well as the static pressures at the rotor inlet, the diffuser inlet and the volute inlet. Together

with the geometry data which was known for the machine, it was possible to work out the performance of the different parts of the machine individually. Using an iterative method based on the 1D theory of turbomachinery, all quantities which were necessary to describe the thermodynamic and fluid dynamic state of the fluid in the control planes between the parts of the machine could be calculated. Based on this data, the individual parts of the machine could be described in terms of efficiency and pressure recovery. In a second step, models for the individual parts were developed and tested. The inlet was not modelled in the diploma thesis and it was assumed to be loss free. Heat transfer from the turbine side, disk friction, recirculation in the ported shroud and slip were accounted for in the rotor model. For the efficiency model, an approach for whole compressor stages developed by Casey and Robinson [6] was applied to the compressor wheel for the first time. It agreed well with the measurement data. The diffuser performance was modelled using a linear approach which was derived from the measurement. The spiral was modelled using a simple parabolic correlation. When compared to the performance data of the overall machine, the combined models for the individual parts of the machine resulted in good agreement with an average error of 2.4% in terms of pressure rise and 1.45% in terms of efficiency.

In the work presented here, the same methodology of splitting up the compressor into its components has been applied. For the individual parts, several improvements have been made on the individual component models. Opposed to the diploma thesis, the reduced order compressor model was not used in design, but in analysis mode to derive information from the experimental dataset. Corresponding to the components, the following methods have been applied:

For the inlet, a loss model, which allowed to account for all losses which were not related to inlet recirculation was developed, so that inlet recirculation could be accounted for separately. The model is presented in the corresponding section below.

For the rotor, the model was run in analysis mode in order to derive the thermodynamic and fluid dynamic values at the rotor inlet and outlet. No heat transfer was implemented as the test rig had been run as a cold gas stand. A loss model for disk friction and slip was included. The recirculation model for the ported shroud was modified and used to depict inlet recirculation. Further explanation to the model is provided in the following section about the rotor.

The diffuser performance was taken directly from the numerical results.

The volute was also run in analysis mode to obtain the performance from the experiment and was compared to the volute model developed in this work which was introduced in section 3.4.3.

In general, this section is aimed to develop a method to analyse the numerical data. In

addition, the experimental data was used to validate and support.

The overall compressor performance in terms of total to total polytropic efficiency derived from the combined model, which comprises the numerical model for the inlet, the rotor and the diffuser and the low order volute model, is thus compared to the manufacturer data for different rotor speeds in **figure 6.2**. In addition to the data from the combined model, the lowest constant speed performance plot on the top left of figure 6.2 also shows performance data from the experiment. The manufacturer data was marked as dashed black lines with data points shown as dots labelled "GT". The combined model data was marked as full red lines with data points shown as squares labelled "SIM". The experimental data was marked as full black line with data points as triangles labelled "EX". The data from the simulation was corrected using a model for disk friction as the mechanism was not included in the combined model. The comparison shows a good qualitative agreement, particularly for best efficiency and operating points at lower flow rates. For higher flow conditions, the simulations significantly under-predict the choking losses so that it has to be assumed that the incidence related more complex flow field under these conditions quantitatively deviates from the experiment. Furthermore, the low order volute model contributed to this offset as had been shown in section 3.4.3.

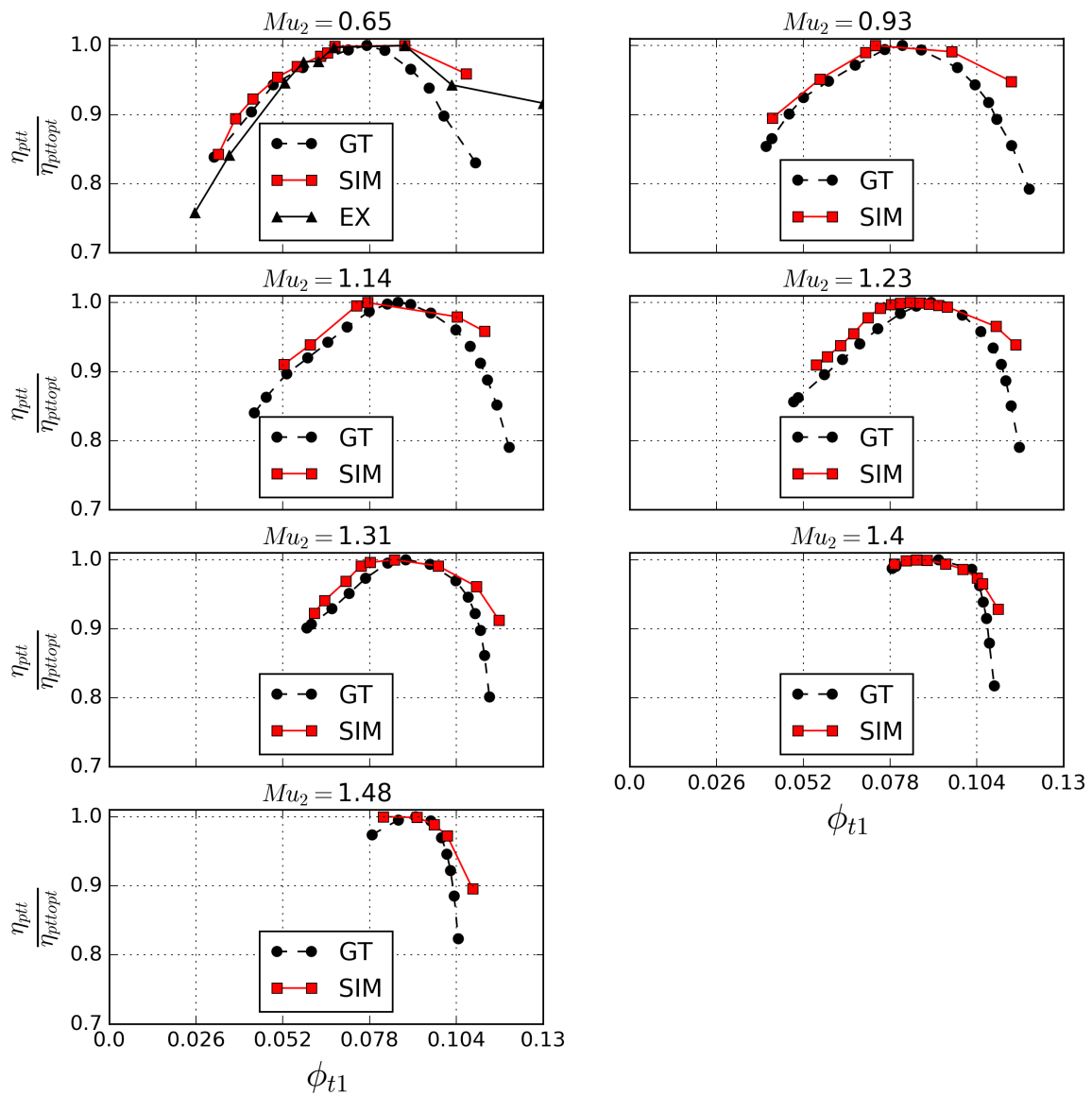


Fig. 6.2 Comparison of the compressor performance in terms of total to total polytropic efficiency at different speeds from: **GT** - Manufacturer; **SIM** - Combined Model; **EX** - Experiment

6.2.1 Intake box and Inlet

The loss occurring in the intake of the compressor was determined experimentally via two sets of measurements. These allowed to separate the loss in the intake box and the inlet bellmouth independent of inlet recirculation. A sketch of the inlet and intake section of the machine is given in **figure 6.3**. The intake box is defined by the planes 0 and 1' and the inlet bell mouth is located between 1' and 1.

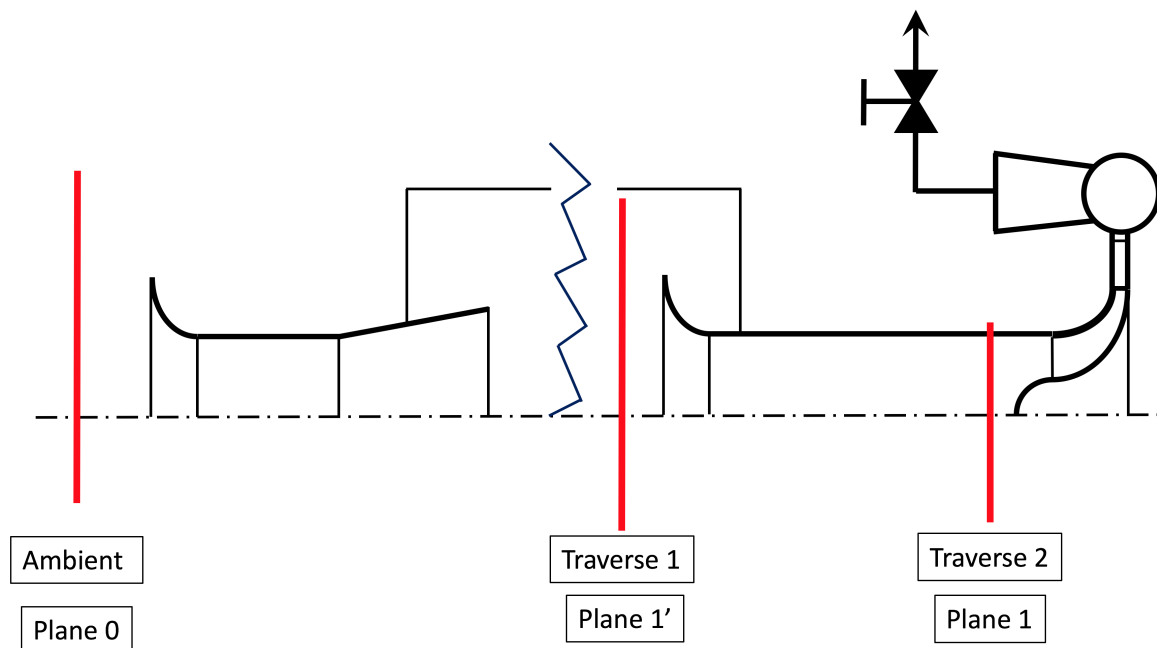


Fig. 6.3 Sketch of intake duct

The Intake duct consists of two bell-mouths and a connector tube. In terms of loss sources, several mechanisms can be identified. The flow through the intake system experiences a total pressure loss due to friction in both bell mouths as well as on the side walls of the intake box. Furthermore, wall corner vortices contribute to the loss. The most dominant loss source is the mixing loss occurring when the jet from the first bell mouth exits into the settling chamber and mixes with the air there. The cumulated loss can be expressed as a total pressure loss as defined in **equation 6.1**, where an arbitrary process from state 0 to state 1 is considered. The mechanisms are a function of velocity and thus can be modelled as a fraction of the inlet dynamic head via a constant K_{loss} .

$$\zeta_{01} = \frac{p_{t0} - p_{t1}}{p_{t0}} = K_{loss} \frac{p_{t0} - p_0}{p_{t0}} \quad (6.1)$$

The compression system subject to this investigation was located between station 1' at the inlet of the second bellmouth and station 4, which corresponds to the volute outlet.

This means that the intake box was not of interest and thus had to be calculated out. In order to separate the loss occurring in the intake box and the inlet bell mouth, two total pressure traverses were carried out. The results of the first one in plane 1', just upstream of the inlet bell mouth, have been shown in detail in section 3.4.1. The results of the second traverse in plane 1, upstream of the rotor, are not shown in detail but it should be mentioned that no results could be obtained from this traverse at low flow coefficients, where inlet recirculation was present as the phenomenon extended further upstream than the traverse location, deteriorating the measurement as the pitot probe could not cope with the high flow angles inside the recirculation bubble. For this analysis, the area averaged mean values of these traverses, which were obtained experimentally were used. In **figure 6.5**, the experimentally obtained total pressure loss is shown over the corrected mass flow in form of data points. Best fit curves were calculated to the measurement points in order to determine the corresponding loss coefficient defined in equation 6.1. Those are shown as full lines with the same colours as the corresponding data points in the figure. The loss in the intake between station 0 and 1' is shown in black with squares for the experimentally obtained data points. The cumulated loss occurring in the intake and inlet bellmouth between station 0 and station 1 is shown in red with dots for the experimentally obtained data points. As mentioned before, no experimental values were available for mass flows smaller than 0.11 Kg/s in this set of data points as measurement Plane 1 was deteriorated by the presence of recirculation. In order to determine the losses occurring in the inlet bellmouth between station 1' and station 1 only, the two loss coefficients which were derived from the experimental data as described above were subtracted from each other.

In addition to the experimentally obtained loss coefficients, the inlet loss was determined from the numerically obtained data. In order to do so, a virtual traverse plane at the same distance to the leading edge of the rotor as in the experiment was defined and a mean total pressure was calculated. The best fit curve for the numerical data is shown as full green line in figure 6.4 and the fitted data points are shown as green triangles. From this analysis, a total of four loss coefficients was obtained. Those are listed in **table 6.2**. From the two experimentally obtained loss coefficients for the intake and for the intake plus the inlet, the loss coefficient for the inlet bellmouth of 0.19 was derived. The numerically obtained loss coefficient for the inlet bellmouth corresponds exactly to this value.

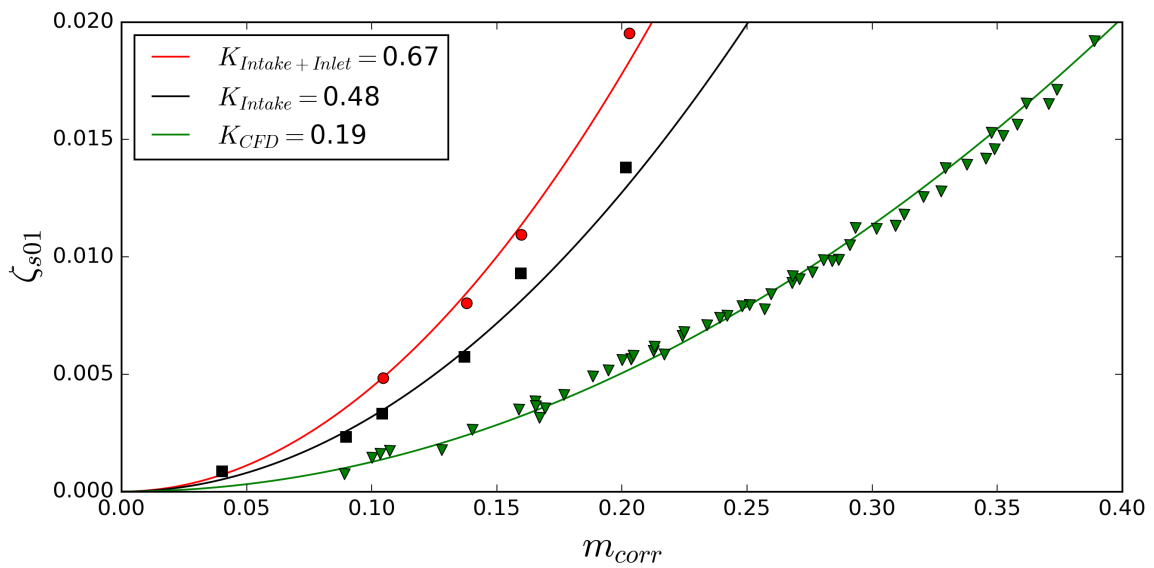


Fig. 6.4 Loss coefficient in the intake duct and inlet bellmouth

Table 6.2 Intake and Inlet bellmouth loss coefficients

Intake box	K_{Intake}	0.48	[-]
Intake box + Inlet bellmouth	$K_{Intake+Inlet}$	0.67	[-]
Derived inlet bellmouth	$K_{Bellmouth} = K_{Intake+Inlet} - K_{Intake}$	0.19	[-]
Numerical Inlet bellmouth	K_{CFD}	0.19	[-]

6.2.2 Rotor

In order to determine the rotor performance, simulation data was used and combined with experimental results for the model validation. In a first step, the work input coefficient was analysed and the additional work feeding into the recirculation bubble was derived.

In order to do so, the work input was plotted over the rotor outlet flow coefficient in the top graph of **figure 6.5**. Several quantities are shown in the graph.

Firstly, the theoretically possible Euler work which derives from the geometry and accounts for slip at the rotor exit with a constant factor from the Wiesner correlation is shown as a dashed line. The slip velocity derived from the Wiesner correlation, which is entirely geometry based is shown as a dashed horizontal line.

Secondly, the two full red lines show the work input and the slip velocity derived from the CFD calculations at 50% rotor speed. Besides the Euler work, an additional component which causes the work input coefficient from CFD to be higher than the Euler work can be seen. This difference represents the additional work due to inlet recirculation. The slip velocity derived from CFD drops off for low flow coefficients. As the change of slip velocity with mass flow and rotor speed is commonly known, it will not be discussed in more detail here. The Wiesner correlation is used in this work because of its simplicity and good approximation.

Finally, the results obtained from the experiment are plotted into the graph. The dashed line with black dots represents the total enthalpy rise over the compressor wheel. The blue line with dots corresponds to the work input into the flow and results from subtracting the disk friction loss from the total enthalpy rise. As the numerical model does not include disk friction, the work input should correspond to the experimental values shown in blue. As shown in figure 6.5, this is the case where the combined model and the experiment show good agreement. The green lines show the Euler work and the slip velocity derived from the experiment when accounting for inlet recirculation with a simple model. The graph shows that the corrected curves from the experiment line up very well with the theoretical values for the Euler work derived from the geometry and the Wiesner estimate for slip velocity. A more detailed explanation for the different models used to obtain these results is provided below.

From the measurements in the experiment, the total enthalpy rise plotted as black dashed line in figure 6.5 was obtained. In order to compare it to the work input in the simulation, the disk friction model given in **equation 6.2** [5] was used. The disk friction factor k_{DF} of 0.004 was estimated by fitting the slope of the experimental working line to the one determined via CFD. The resulting curve is shown as blue line in the top graph.

$$\frac{\Delta h_t}{u^2} = \left(1 + \frac{k_{DF}}{\phi_{t1}} \right) \lambda \quad (6.2)$$

A comparison between the work input curves from CFD and experiment with the theoretical curve for the Euler work shows that a significant amount of additional work is put into the system at low flow coefficients. This observation corresponds to the findings of Stepanoff [43] and can be explained with the phenomenon of inlet recirculation. One indicator therefore is the presence of this additional work from the onset point of recirculation at a rotor outlet flow coefficient of around 0.3, which corresponds to a global flow coefficient of 0.0675 as determined as the onset point of recirculation in section 4. A simple model presented has been used to account for this additional work and to calculate the actual Euler work. It is based on the assumption that a certain percentage of the total energy input into the rotor is dissipated in the recirculation bubble. The energy can be expressed in terms of power. Consequently a ratio of the power input into the recirculation zone and the total power input as shown in **equation 6.3** can be defined. The power can be expressed as a product of mass flow and total enthalpy change. This means that the power ratio can be expressed as the product of a mass flow ratio and a total enthalpy ratio.

$$\frac{P_{RC}}{P_{04}} = \frac{\dot{m}_{RC}}{\dot{m}_{04}} * \frac{\Delta h_{RC}}{\Delta h_{04}} \quad (6.3)$$

In section 4.3, both of these two ratios were discussed. Based on the mass flow analysis shown in figure 4.7, it was found that there is a linear correlation between the recirculation mass flow and the mass flow going through the rotor. Based on an energy analysis shown in figure 4.14, it was shown that the ratio between the energy input into the recirculation zone and the overall energy input into the machine reaches a constant value, except for a steep gradient phase around the onset point. All these findings were independent of rotor speed. Taking these simple correlations, a the loss model shown in **equation 6.4** which is based on the work coefficient can be defined. Here, the lost work due to recirculation gets subtracted to obtain the Euler work.

$$\lambda_{Euler} = \lambda - \lambda_{RC} \quad (6.4)$$

In order to determine the work input into the inlet recirculation zone λ_{RC} , the model presented in **equation 6.5** was used. It is only applied if the rotor exit flow coefficient drops below a critical value ϕ_{2RC} of 0.3 which corresponds to the onset point of recirculation.

As discussed above, the ratio between the energy input into the recirculation zone and the overall machine was determined to be at a constant value which has been implemented into the model via the loss coefficient k_{RC} . The coefficient was determined to be 0.7 by curve fitting the experimental values to the Euler working line. As the correlation between the recirculation and the main flow was determined to be linear, the exponent exp_{RC} of the model was set to 1. The resulting working line is shown in green for the experiment in figure 6.5. As the Numerical working line is virtually identical to the experimental one, it is not shown in the figure. Regarding the determination of the onset point of recirculation for the model, the static pressure criterion presented in section 4 was used here. For the compressor used in this work, it could also have been possible to use Qiu's critical area ratio [35] criterion. This can be seen in figure 4.5. However the criterion was shown not to be universal by Harley [23].

$$if : \phi_2 < \phi_{2RC} : \lambda_{RC} = k_{RC} (\phi_{2RC} - \phi_2)^{exp_{RC}} \quad (6.5)$$

An indication about the exit flow conditions is given via the slip velocity, also drawn in the top graph of figure 6.5. Here, the numerically obtained slip velocity is shown in red, the experimental one is shown in green and for comparison, the Wiesner correlation is given as a dashed line. The Wiesner correlation is given in **equation 6.6** and results to a value of 0.161 for this machine.

$$\frac{c_s}{u_2} = \frac{\sqrt{\cos\beta_{2b}}}{Z^{0.7}} \quad (6.6)$$

The slip factors from the simulation and the experiment were obtained via a simple average over the varying values over the flow coefficient under the assumption of a constant, single slip factor for all operating conditions, like Wiesner. The experimental value of 0.149 was taken as a datum case, which means that the value from the Wiesner correlation is 8.3% higher. The numerical slip factor averages at 0.167 and is 11.9% higher than the experimental value. The difference in slip indicates that the secondary flows in the rotor are over-predicted in the numerical case, allowing the rotor to do less turning. However, the experimental data, having been worked out with a 1-D method, is subject to errors itself, particularly as no total pressure values were available at the rotor and diffuser outlet.

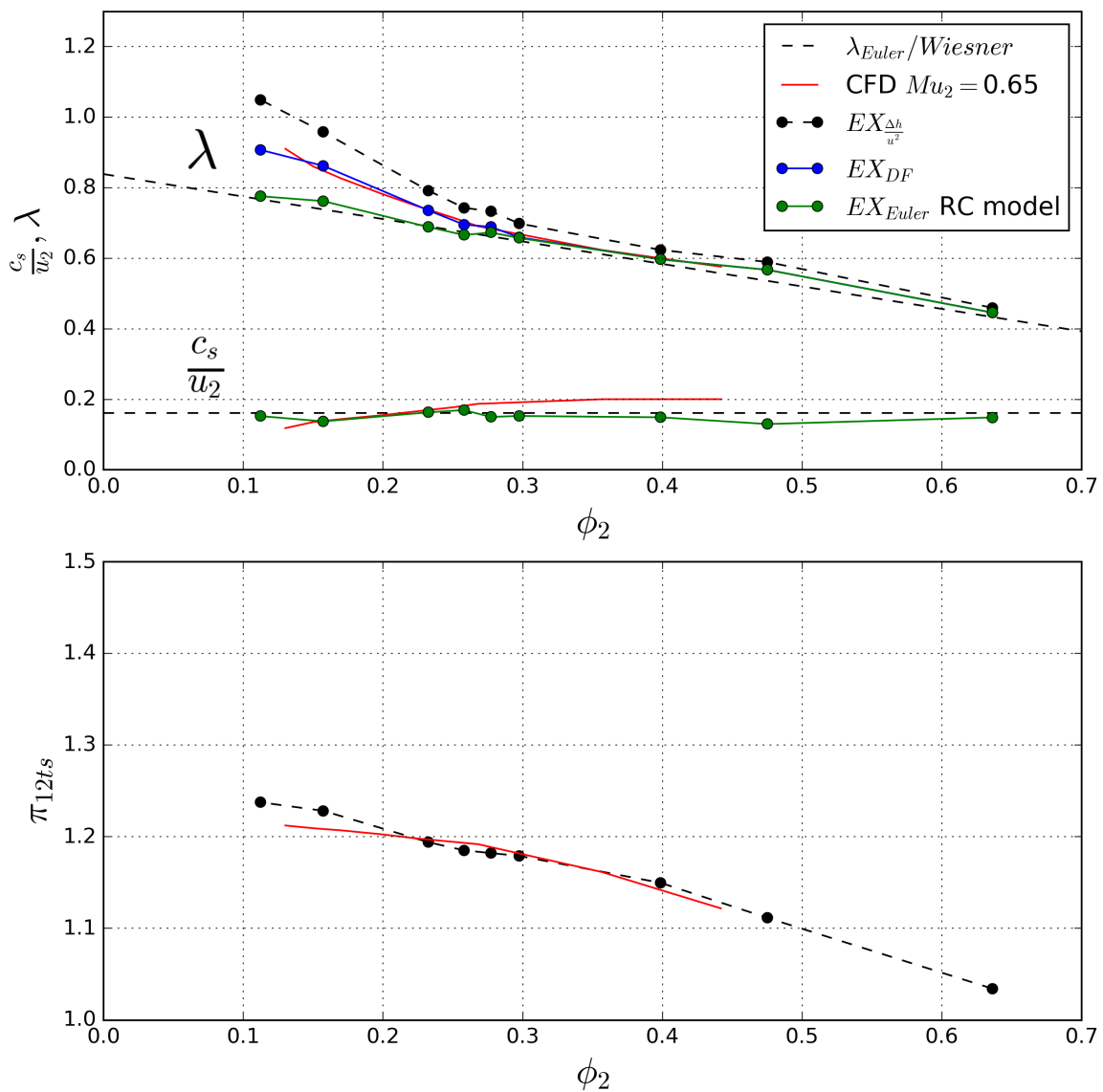


Fig. 6.5 work coefficient and pressure rise over the rotor

To gain more confidence in the numerical data, the directly measured static pressure values from the experiment were compared. The resulting total to static pressure rise curve for the rotor is shown in the bottom part of figure 6.5. As before, the numerical result is shown as a red line and the measured values in dashed black. The graph shows very good agreement between measurement and numerical simulation. The rotor performance then was calculated from the numerically obtained values for total pressure and temperature. **Figure 6.6** shows the total to total polytropic efficiency curve for the rotor which shows a continuous decrease towards low global flow coefficients. No signs of an abrupt change due to the onset of inlet recirculation can be seen.

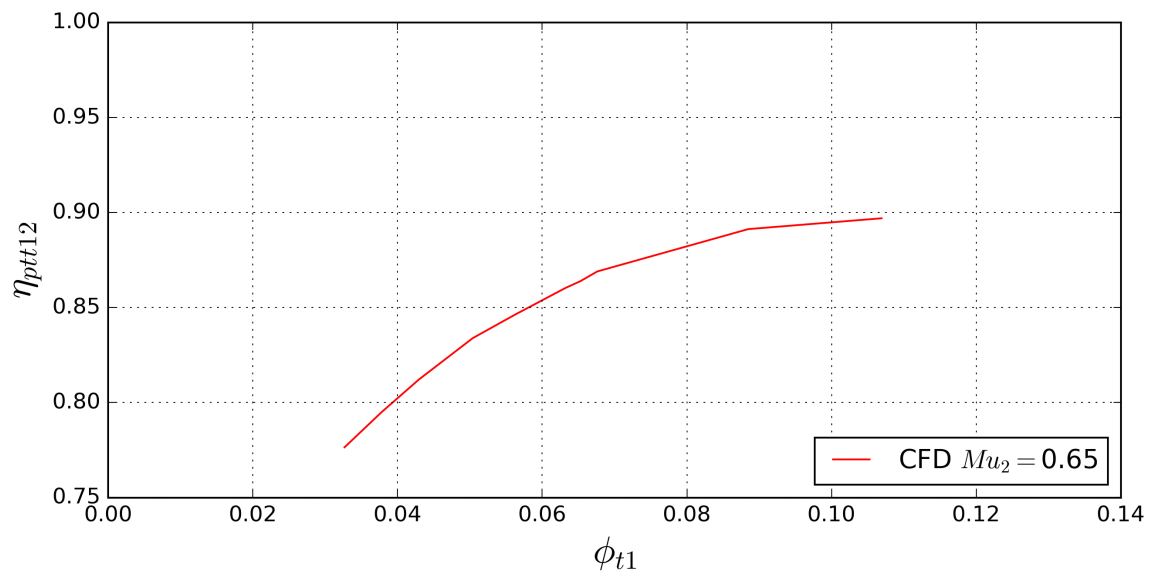


Fig. 6.6 polytropic total to total efficiency of the rotor

6.2.3 Diffuser

The diffuser performance was derived from the numerical model data. The pressure recovery coefficient is plotted over the diffuser inlet angle and is shown in **figure 6.7**. In order to give an orientation, two dashed lines are plotted into the graph. The horizontal line marks the ideal pressure recovery coefficient for an incompressible case with the same geometry. The vertical line marks the instability limit of the diffuser determined in section 3.2.3.

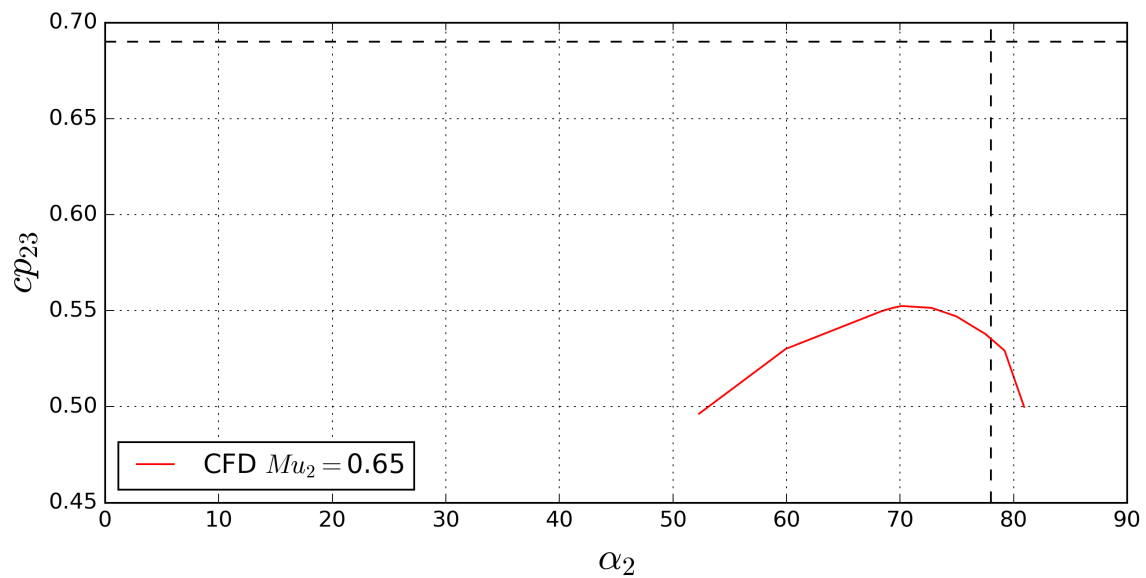


Fig. 6.7 diffuser pressure recovery coefficient derived from the numerical model

6.2.4 Volute

The volute performance was determined using the low order volute model introduced in 3.4.3 which showed good agreement with the measurement data. The pressure recovery coefficient obtained from the low order model with input data from the numerical calculations is shown over the volute inlet angle in **figure 6.8**. In addition, the experimentally obtained pressure recovery coefficient is shown. They agree only partially. The reason is the difference in slip velocity between experiment and CFD. Because the slip in the numerical model is 11.9% smaller, the tangential velocity exiting from the rotor is correspondingly larger, making not only the rotor more efficient than in the measurement but also resulting in a different diffuser and low order volute model behaviour as the inlet angles are different. Consequently, the low order volute model predicts a different performance from the experiment. However, the obtained performance values are good enough to estimate a qualitative split up of the losses occurring in the different parts of the machine to give an orientation and estimate the relative impact of recirculation.

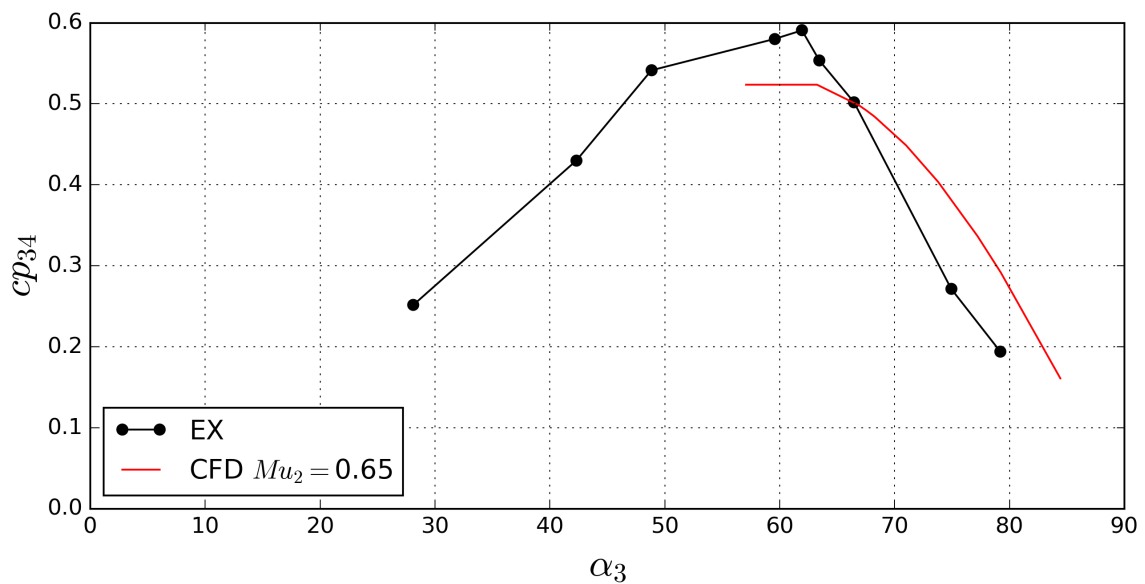


Fig. 6.8 Volute pressure recovery coefficient

6.2.5 Loss breakdown

The above mentioned analyses of the individual components of the compression system were used to carry out loss breakdown according to the individual components inlet, rotor, diffuser and volute. Furthermore the disk friction loss was taken into account and treated as a separate loss mechanism which is not directly related to a component and was derived from the experiment. In the rotor, the loss due to inlet recirculation was separated from other aerodynamic losses using a technique which is described further below. The resulting loss breakdown graph is presented in **figure 6.10** which shows the loss relative to the total enthalpy rise in the machine over the global flow coefficient as defined in section 3.3.2. The losses shown are calculated after **equation 6.7**.

$$\zeta = \frac{\Delta s T_2}{\Delta h_{t12}} \quad (6.7)$$

In order to calculate the losses associated with inlet recirculation, the inlet plane of the numerical model was split up in two different sections in the same way as shown in figure 4.6. It shows one section where recirculating mass flow would come out of the rotor into the inlet and one section where the flow goes into the rotor. A detailed principle schematic of the split inlet plane is given in **figure 6.9** which shows a meridional cut through the rotor and the inlet. The recirculation zone is marked with a bold red line. Black arrows represent flow paths of particles which enter the machine from outside through the inlet bellmouth. The bottom streamlines go through the machine and leave it through the rotor outlet. The top streamline labelled A enters the rotor but then gets caught in the recirculation zone. This behaviour will be further explained later. The two parts of the inlet plane are marked with thick boxes and arrows in the flow direction. The grey box with the rotor inward facing arrow labelled normal is the region where the flow enters the rotor. The red box with the outward facing arrow labelled RC is the part of the inlet plane with recirculated mass flow. In order to determine the direction of the mass flow, the mass flux in every cell of the numerical plane was calculated and added to the corresponding sub plane 1-D mean value. With this procedure, the thermodynamic and fluid dynamic properties of the flow upstream of the rotor under recirculation could be determined. In order to calculate the loss associated with the recirculation zone, the entropy rise between the upstream inlet plane 0 and the new rotor inlet plane was calculated. As the loss coefficient for the inlet under normal flow conditions without recirculation was known, the additional inlet recirculation loss could be calculated as the difference, see **equation 6.8**

$$\zeta_{RC} = \zeta_{01normal} - \zeta_{inlet} \quad (6.8)$$

Recirculation loss calculated in this way represents a lumped value of all losses which occur in the region of the recirculation zone within the rotor and outside. As a result, other loss mechanisms, which occur in the region where the recirculation zone is present, accumulate in this value. Examples include the tip leakage loss, blade and shroud end-wall losses within the recirculation zone as well as the mixing loss between the recirculating flow and the normal flow going from the intake into the rotor.

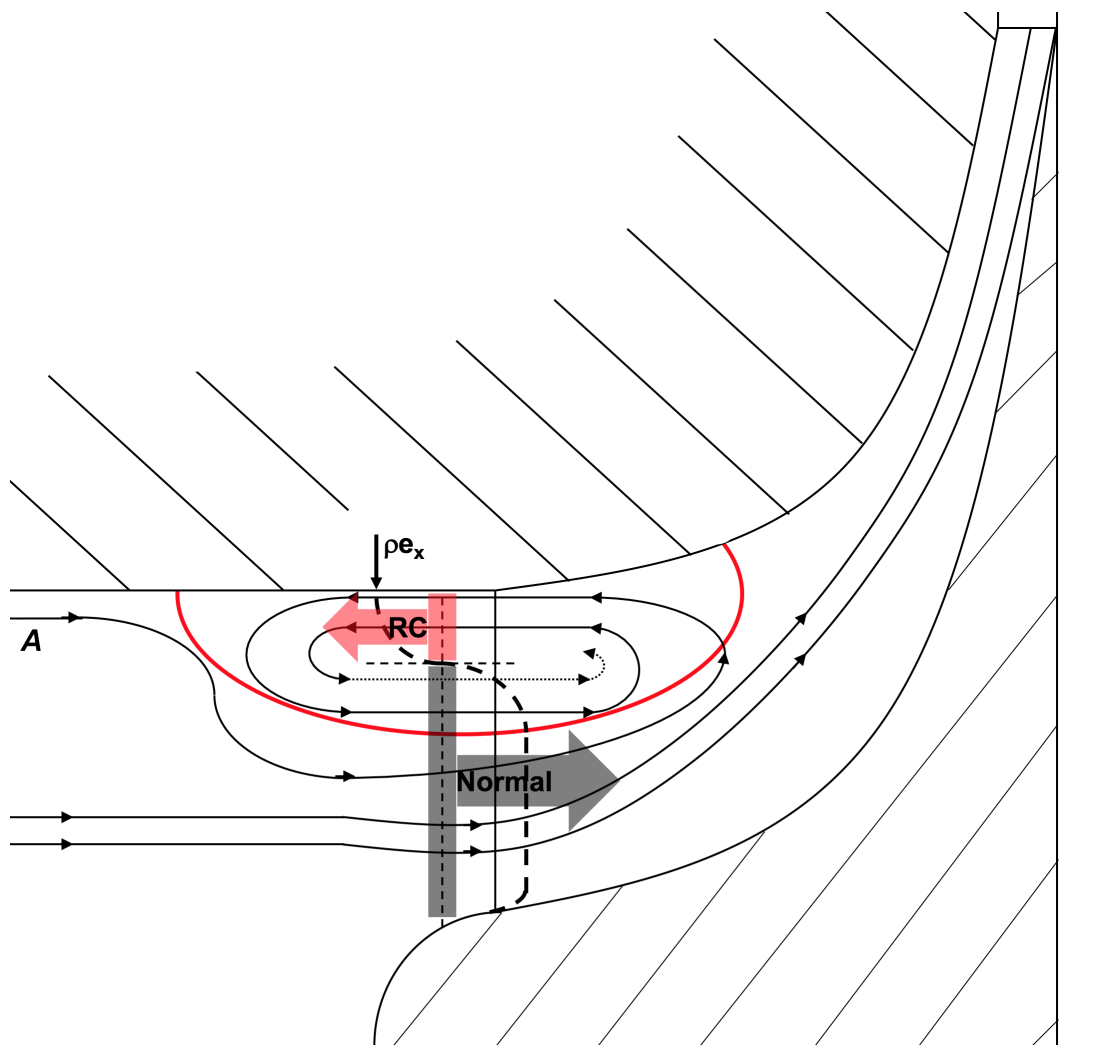


Fig. 6.9 Meridional cut through the rotor and inlet: Inlet plane with recirculation and normal sub planes, recirculation bubble and streamline

This accumulation becomes more obvious when following a fluid particle as it travels on the streamline labelled A in figure 6.9 over time. The particle starts in the normal oncoming flow and passes under the recirculation bubble. Here, it goes through a mixing process with the recirculating flow and a positive swirl component is added to it. The particle then enters the rotor and gets caught in the recirculation bubble. Here, it can be exposed to the reduced but still present tip gap flow or the end-wall boundary layers. Once caught in the recirculation bubble the particle may stay within the recirculation zone and swirl around several times, accumulating the losses occurring on the way.

Figure 6.10 shows the resulting loss breakdown, where the losses are added on top of one other in the order given in the legend. The data points are marked as dots for the Intake loss, as inverted triangles for inlet recirculation, as squares for the rotor loss, as triangles for the diffuser loss, as octagon for the volute loss and as stars for the disk friction loss. The intake loss is represented by the small black area at the bottom of the graph. There on top is the rotor loss shown in green. The recirculation loss is shown separately as the red patch on the bottom left corner of the graph. The recirculation occurs at about 60% maximum flow coefficient, occupying roughly 40% of the map width. The pink area represents the diffuser loss which roughly stays constant over the whole map width. The blue area shows the loss occurring in the volute which, compared to the overall loss varies only slightly. The yellow area shows the disk friction loss which varies with the flow rate of the machine and reduces towards high flow rates. In addition to the losses in the different components, the work input associated with recirculation determined in **section 6.2.1** is plotted as a dashed line and will be discussed below.

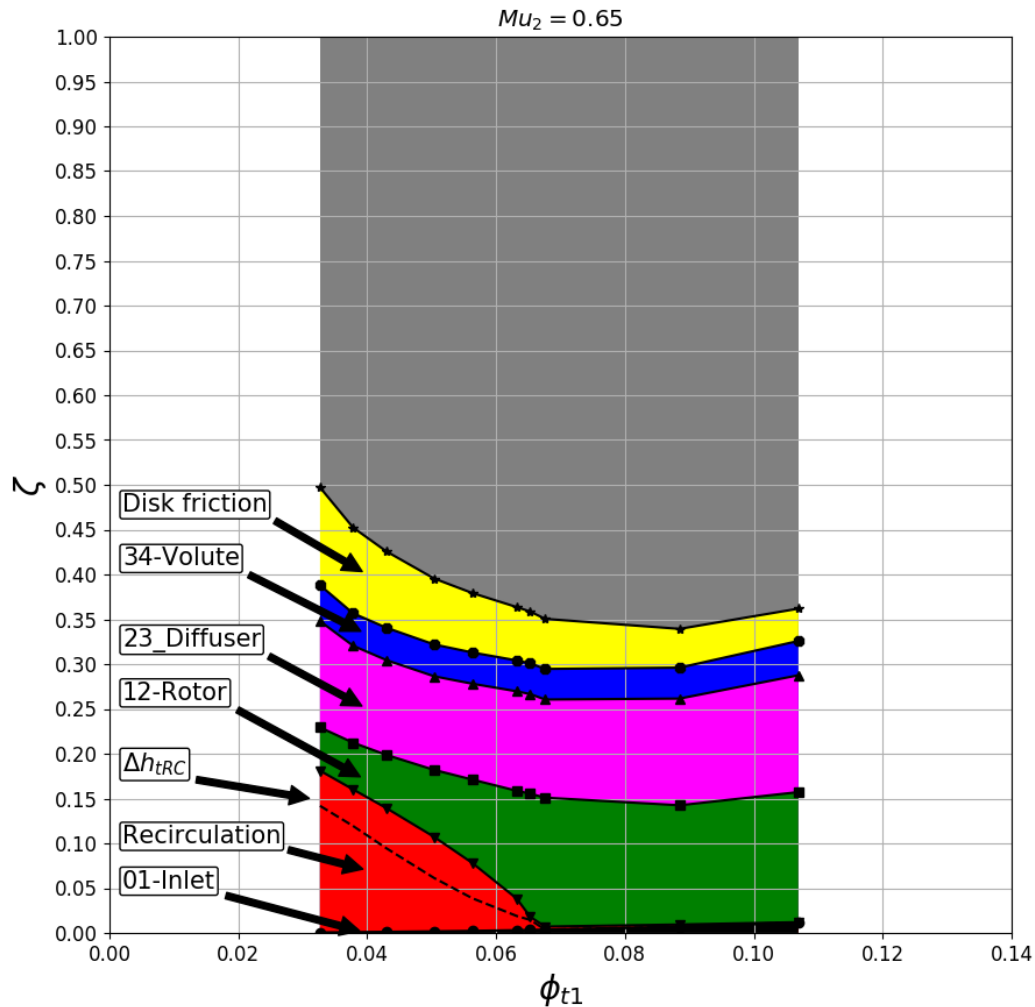


Fig. 6.10 Loss breakdown of the compression system at low speed of $Mu_2=0.65$; Losses stacked in the order of the legend from bottom to top

In order to examine the losses in more detail, those were plotted relative to the total loss in **figure 6.11** so that a comparison between the components is easier. The data points are marked as dots for the Intake loss, as inverted triangles for inlet recirculation, as squares for the rotor loss, as triangles for the diffuser loss, as octagon for the volute loss and as stars for the disk friction loss. Firstly, the relative magnitude is compared to the degree of reaction of the machine which was calculated to be 0.65 indicating that 65% of the enthalpy rise happens in the rotor. When not accounting for disk friction, this split can roughly be found in the loss split between the rotor and the static components diffuser and volute. When compared to

similar work found in literature, namely Stepanoff [43], who described a loss he could not explain in his experiment and assumed it could be related to inlet recirculation, the magnitude of the recirculation loss relative to the total rotor loss is similar to the values obtained in this work.

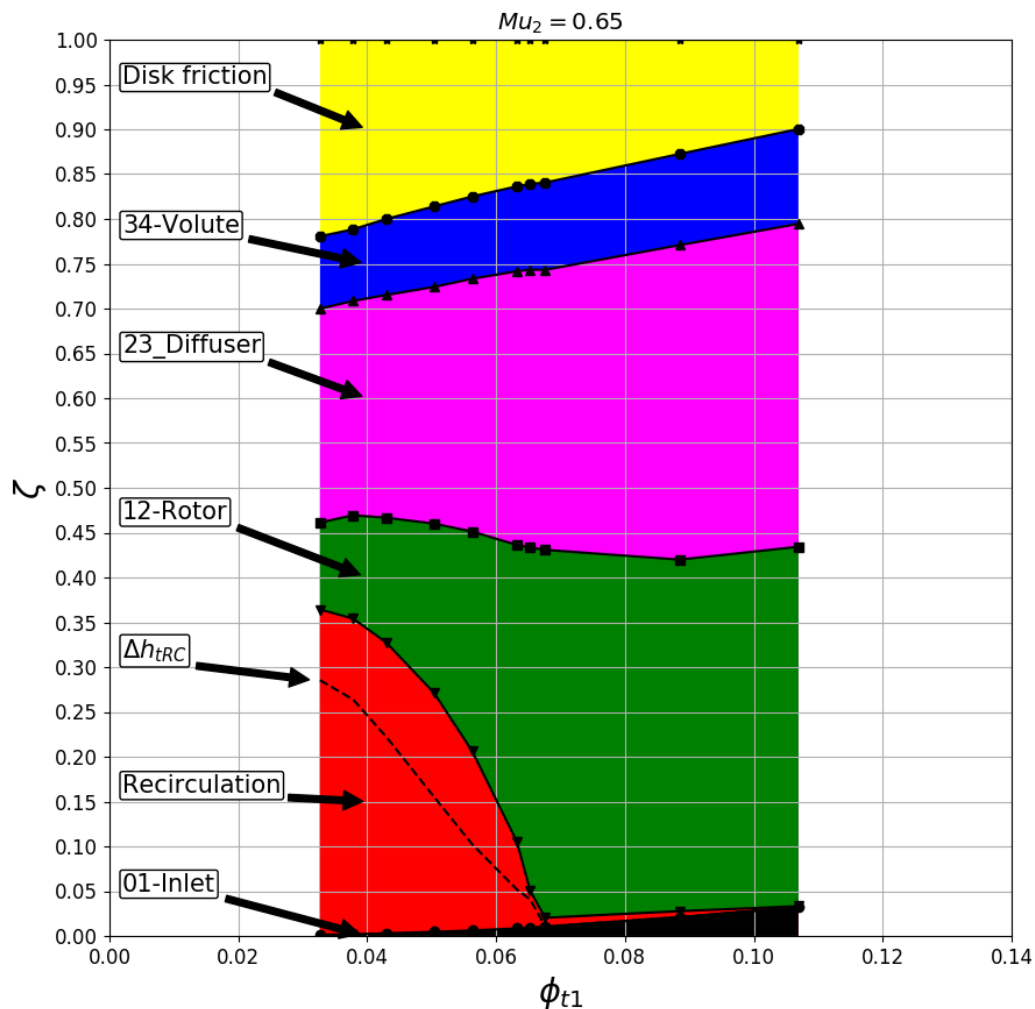


Fig. 6.11 Loss breakdown of the compression system at low speed of $Mu_2=0.65$; Losses stacked in the order of the legend from bottom to top

A comparison between the work loss determined in section 6.2.1, which applied to both, the experiment and the simulation equally as the work coefficients were almost identical and the recirculation loss calculated from the simulation, a significant difference of up to 6% is found. In order to understand this difference, the two loss parameters have to be

discussed further. The work loss represents the additional amount of work which is necessary to sustain the inlet recirculation bubble, not taking into account any aerodynamic losses which derive from the presence of the phenomenon. The numerically obtained loss value described above also accounts for secondary losses which occur due to the interaction of the recirculation bubble with the normal flow which comes from the intake and passes through into the rotor inlet. At the interface, free shear layer mixing takes place and causes additional losses. Loss sources which are present in the tip region under normal flow conditions without inlet recirculation are counted into the recirculation loss with this method, which is why the loss was described as "lumped" loss for the recirculation above. The tip leakage vortex does not occur under recirculation due to the small blade loading in the tip leading edge region. The leakage losses occurring in the part of the blade where the recirculation bubble is present now are accounted in the recirculation loss, so do the blade end-wall losses and the shroud end-wall losses as those get carried out of the rotor with the recirculating flow. The leakage losses are significantly reduced due to the small blade loading in the tip region under recirculation. Furthermore, additional losses due to the mixing of the recirculation zone with the flow passing through the machine normally occur. Those are at least partly accounted for in the recirculation loss whereas another part is passed on downstream. As a result, the loss count from the cut planes in the numerical model is higher than the lost work estimated from the Euler work.

6.2.6 Conclusions

This section assessed the energetic costs of inlet recirculation using CFD data which is supported by experimental data. Towards this objective, the compressor was split up into four components, the inlet, the rotor, the diffuser and the volute. For each of these components, the performance at 50% rotor speed was determined over the full flow range. The experimental data was processed using an iterative method to calculate the thermodynamic and fluid dynamic properties in the measurement planes between the compressor components which were suitable to validate and support the numerical results. This method used analytical and empirical correlations based on the 1D theory of turbomachinery.

The inlet of the machine needed to be split up in zones of negative and positive mass flow to account for the losses associated with inlet recirculation separately as the phenomenon partly takes place in this component of the machine. This was accomplished by determining the loss coefficient for the inlet at operating points where clean flow was given. The loss coefficient was validated using results from both, measurement and simulation.

The rotor was analysed in two ways. In a first step, the work input into the flow was investigated and it was found that additional work had to be put into the flow once inlet recirculation was present. This additional work could be accounted for with a simple model which used the findings of section 4 that showed a linear increase of the recirculated mass flow with a reduction in flow coefficient and a constant energy input into the recirculated flow for varying flow conditions. In the analysis of the work coefficient, the disk friction and slip were further accounted for in the model. No heat transfer model had to be used to process the experimental data as the measurements were taken on a cold gas stand. However, a reduced order heat transfer model could be included for cases in turbocharger applications where heat transfer effects are important and the system is not adiabatic.

The numerical model was run as adiabatic without disk friction. In a second step, the lost work within the rotor was determined using data from the numerical model that was extracted in 1D measurement planes corresponding to those in the experiment.

The diffuser performance was derived from the numerical model by extracting 1-d values from cut planes in the positions corresponding to those in the experiment.

The volute performance was determined using performance data from the experiment and the volute model which was introduced in section 3.4.3.

The results were summarised in a loss break down analysis for the whole compressor where

the energetic costs of inlet recirculation were determined using two approaches. First, the additional work necessary during the presence of inlet recirculation was determined using the work input coefficient. In a second step, the CFD results were used to determine the increase in entropy in the recirculation zone and consequently the loss associated with it. Both quantities were then compared to the losses in the components of the machine and the disk friction loss. It was found that in the research compressor which features a degree of reaction typical for radial compressors of 0.65 at the nominal design flow rate, up to 35% of the total loss occurring in the compressor were associated with the recirculation region. It was furthermore found that the loss of efficiency can be traced back to two sources. First, up to 29% of the total loss of efficiency is caused by the additional work necessary to sustain the inlet recirculation bubble. The second source, which makes out up to 6% of the total loss of efficiency is related to the mixing of the secondary flow phenomena associated with inlet recirculation. Examples for these secondary flow phenomena include free shear layer mixing, blade tip clearance flow, casing end-wall friction and blade end-wall friction inside the recirculation region.

Chapter 7

The effect of tip clearance on inlet recirculation and its onset point

7.1 Introduction

During the analysis of the key features of inlet recirculation in section 4, the low momentum fluid in the tip region of the rotor has been identified to be the main driver for the onset of inlet recirculation. The blade tip gap is one of the main sources for low momentum flow. Consequently, a variation of the tip gap size offers the opportunity to vary the size of the low momentum region. This study investigates the sensitivity of the low momentum region at the casing and the onset point of inlet recirculation as defined in chapter 4 to the size of the tip clearance gap. This was accomplished by reducing the tip gap from its datum size in two steps to almost zero. In a second step, the three dimensional casing flow structure is discussed for different tip gap sizes with the aim of gaining further understanding about the onset point of recirculation and the recirculation related performance penalties.

7.2 The effect of tip clearance on inlet recirculation and its onset point

The research compressor features a constant tip gap along the whole chord of the rotor in its datum configuration, as can be seen in **figure 7.1**, which shows the meridional shape of the tip gap. The full black line represents the casing and the dotted lines represent the tip of the rotor for the different cases of the study. The largest tip gap represents the datum case which features a tip gap of 0.5mm or 2.76% relative to the leading edge span and is shown as the black dotted line. The second case with a tip gap of 1.27% is shown in red and the third case which features a tip gap of 0.22% is shown in green.

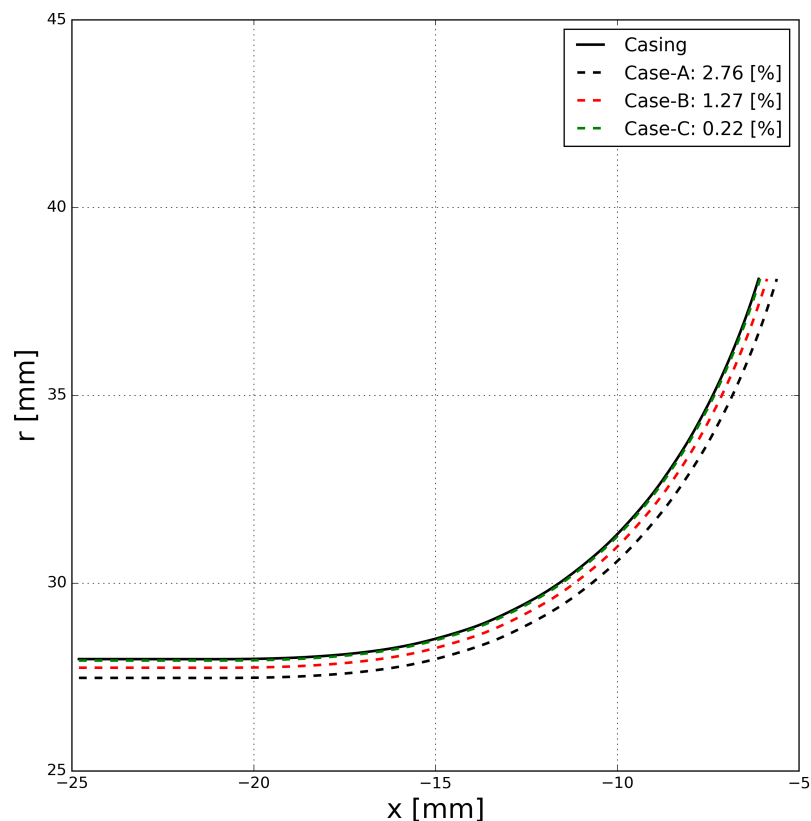


Fig. 7.1 Meridional cut through the tip gap of the research compressor with tip gap variations as dashed lines

For this study, the tip gap size has been reduced in two steps, resulting in a total of three cases with tip gap sizes between 2.76% and 0.22% relative to the leading edge span. The three cases are named A for the datum case, B for the medium size case and C the smallest

tip gap size. The absolute and relative tip gap sizes are listed in **table 7.1**. Furthermore, the absolute tip gap size is shown visually in **figure 7.2** for all three cases.

Table 7.1 Tip gap size in absolute terms and relative to the leading edge span

Case	Absolute [mm]	Relative to LE span [%]
A	0.5	2.76
B	0.23	1.27
C	0.04	0.22

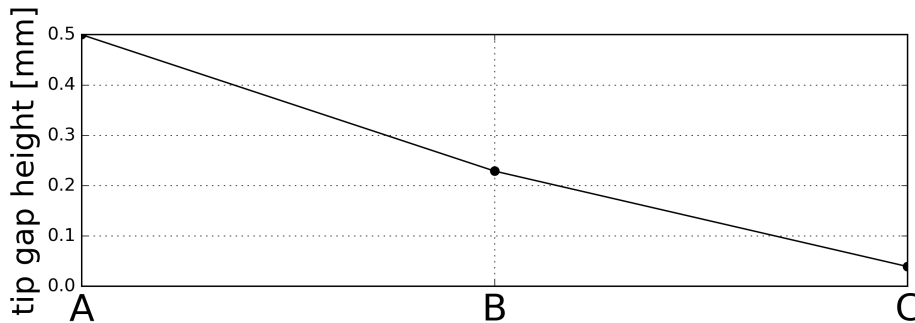


Fig. 7.2 Absolute size of the tip gap for the case study

In order to investigate the influence of the tip gap size on the performance and the onset point of inlet recirculation, calculations at 50% design speed have been carried out for the three models.

All modelling parameters like the blocking structure and boundary conditions were maintained the same as those of the datum case. More specific information about the modelling was provided in section 3.4. The 3D CFD models were combined with the 1D Volute model introduced in section 3.4.3 in order to obtain a full compressor performance characteristic. The results are shown in **figure 7.3**, which shows the overall compressor characteristics in two graphs. The top graph shows the total to total pressure rise over the global flow coefficient. The bottom graph represents the total to total polytropic efficiency of the compressor over the global flow coefficient. The datum case A with the largest tip gap is shown in black lines with dots, case B is shown with red lines and squares and case C with the smallest tip gap is shown as green lines with triangles. In terms of the total to total pressure rise, the reduction in tip gap results in an increased head rise capability over the whole compressor range, as can be seen in the top graph of figure 7.3. For the cases B and C, the tip gap was reduced in steps of approximately 50% relative to the datum case A. Correspondingly, the

head rise capability increased equally between the cases. Furthermore, the presence of inlet recirculation changed the slope of the pressure rise curve of the compressor.

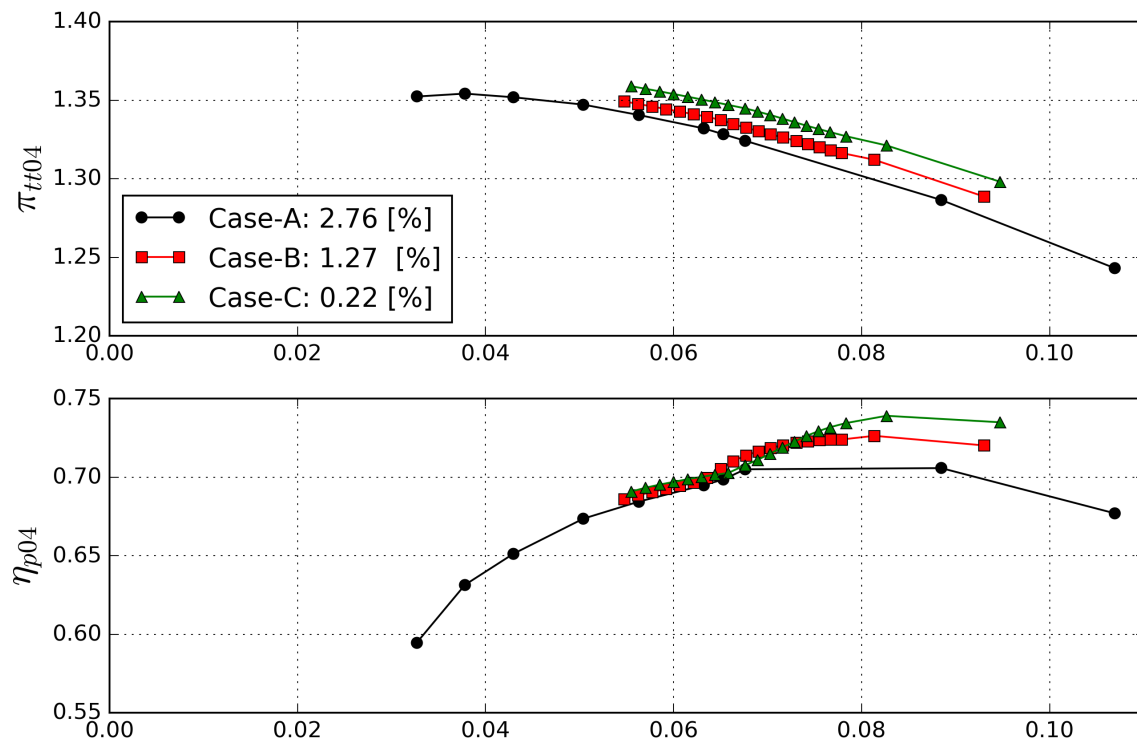


Fig. 7.3 Compressor performance

Regarding the overall compressor polytropic efficiency, the cases differ significantly. For high flow coefficients, a reduction in tip gap size results in an increased overall efficiency of the machine. In absolute terms, case C performs around 3.5% better than the datum case A which features a peak efficiency of around 70%. Case B results in a 2.5% better peak efficiency than the datum case.

When throttled towards lower flow coefficients, the cases A and B show similar trends with a progressive decrease in efficiency up to a kink at a flow coefficient of around 0.0676. This kink could be identified as the onset point of inlet recirculation and will be further explained later.

At flow coefficients lower than the kink, the efficiency continues to drop but with a lower gradient. In this region, case B performs slightly better than case A, as to expect with a lower tip gap. Case C shows different performance characteristics with a steeper decrease in efficiency from the peak performance point to the kink. The kink itself is located at the same flow coefficient as in the cases with larger tip gap. Again, the efficiency continues to drop after the onset point of recirculation but with a smaller gradient. Case C gives slightly better

efficiencies than the other two cases in this region.

Overall, the performance gains due to a reduced tip gap are significant at high flow coefficients. However, the performance gains are minimal as soon as the inlet recirculation has extended upstream of the rotor leading edge.

The effect causing this increase in efficiency can best be shown by looking at the leakage mass flow over the rotor blades which is provided in **figure 7.4**. The graph shows the tip leakage mass flow as a percentage of the compressor corrected mass flow over the global flow coefficient for the three different tip gap heights. The top graph shows the main blade leakage flow, the bottom graph shows the splitter blade leakage flow. Case A is shown as black full line with dots, case B is shown as red line with squares and case C is shown as green line with triangles. As can be seen, the leakage flow reduces almost linearly with the reduction in tip gap height. In general, the leakage over the main blade is two to three times higher than over the splitter blade which is mainly due to the 30% reduced chord length of the splitter blade. Furthermore, the tip leakage flow increases with a reduction in flow coefficient due to the increased blade loading when throttled to operating points with higher incidence. However, the tip leakage mass flow curves show a discontinuity around the onset point of inlet recirculation at a flow coefficient of 0.676, particularly in case of the main blade. This is taken as a clear indicator of a change in blade loading around the main blade leading edge as the pressure difference over the blade is the driver for the leakage flow.

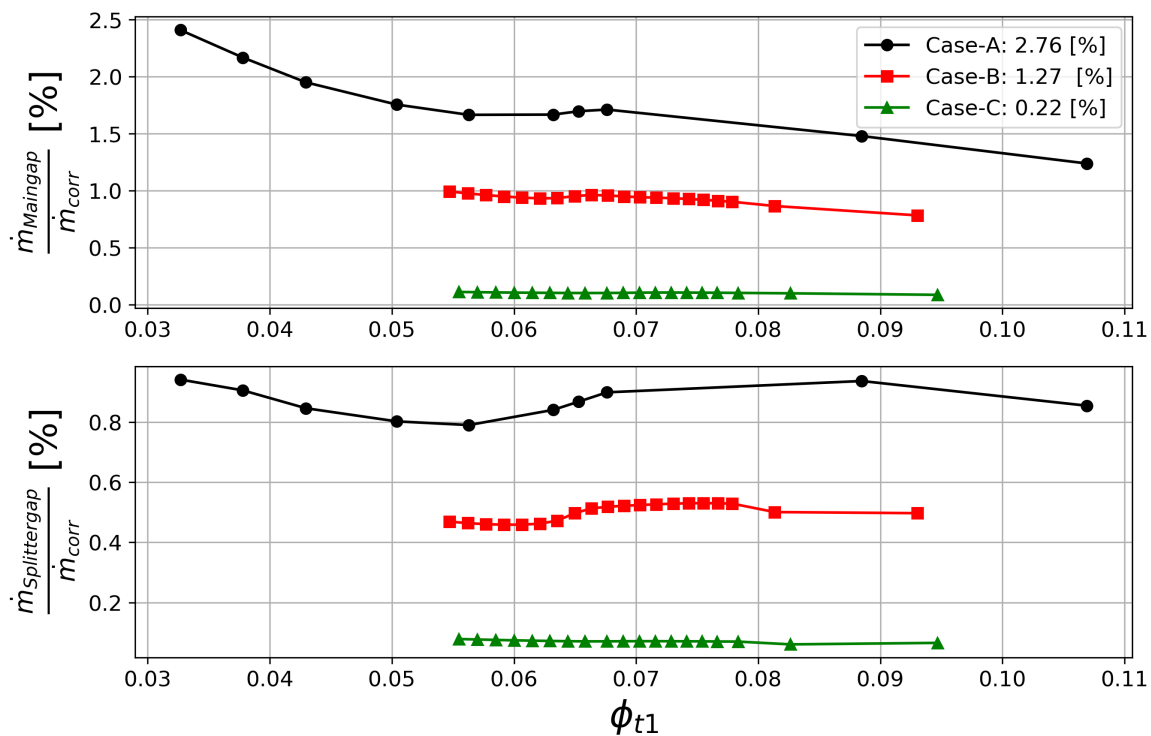


Fig. 7.4 tip leakage mass flow as percentage of overall mass flow for different tip gap heights

In order to gain further insight into the effects of the tip gap reduction, the rotor performance characteristics has been investigated and is shown in **figure 7.5**. Only the data at flow coefficients in the region of interest are presented and discussed. Figure 7.5 shows three graphs. The top graph shows the total to static pressure rise of the rotor over the global flow coefficient. The middle graph represents the total to total polytropic efficiency of the rotor over the global flow coefficient. The bottom graph shows the static casing pressure relative to the inlet total pressure in the rotor inlet plane as defined in section 3.3. This value is used to determine the onset point of inlet recirculation in the same way as shown in chapter 5. The three cases are displayed with the consistent colours and symbols as in the previous graph. Regarding the total to static pressure rise curves in the top graph of the figure, the increased head rise capability due to the reduced tip gap can be seen. All three cases show a change in slope with a "saddle point" like region around a flow coefficient of 0.0676. For flow coefficients that are smaller than the value at operating point Z, the gradient of the static pressure rise curves is increased relative to the slope at flow coefficients which are higher than operating point X.

The total to total polytropic efficiency plot in the middle graph of figure 7.5 shows performance gains for high flow coefficients due to the reduction in tip gap size and consequently reduced tip leakage losses. When throttled to low flow coefficients, the same behaviour as in

the previous graph which displayed the overall compressor performance can be seen. The performance gains due to a reduced tip gap are minimal as soon as the recirculation bubble is present. The rotor performance graph clearly identifies the rotor as the source for this behaviour.

In order to clearly associate the slope of efficiency with inlet recirculation, the inlet casing pressure criterion which has been used in chapter 5, has been plotted in the bottom graph of figure 7.5. Regarding the datum case A and the first reduction step of case B, a similar slope of the casing pressure at the inlet can be observed. Around the onset point of inlet recirculation, both cases show a significant drop in casing pressure which, once recirculation has been established rises again once the compressor is throttled to lower flow coefficients. The smallest tip gap case C however shows a different behaviour. Here, the casing pressure probe does not show a dip and the value keeps increasing steadily instead. The only sign of an occurrence of reverse flow upstream of the leading edge is a slight change of gradient on the pressure rise characteristic of the pressure probe.

One significant observation is the fact that the tip gap variation did not have an effect on the location of the onset point of inlet recirculation. In all three cases, the onset point happened around the same global flow coefficient of 0.0676.

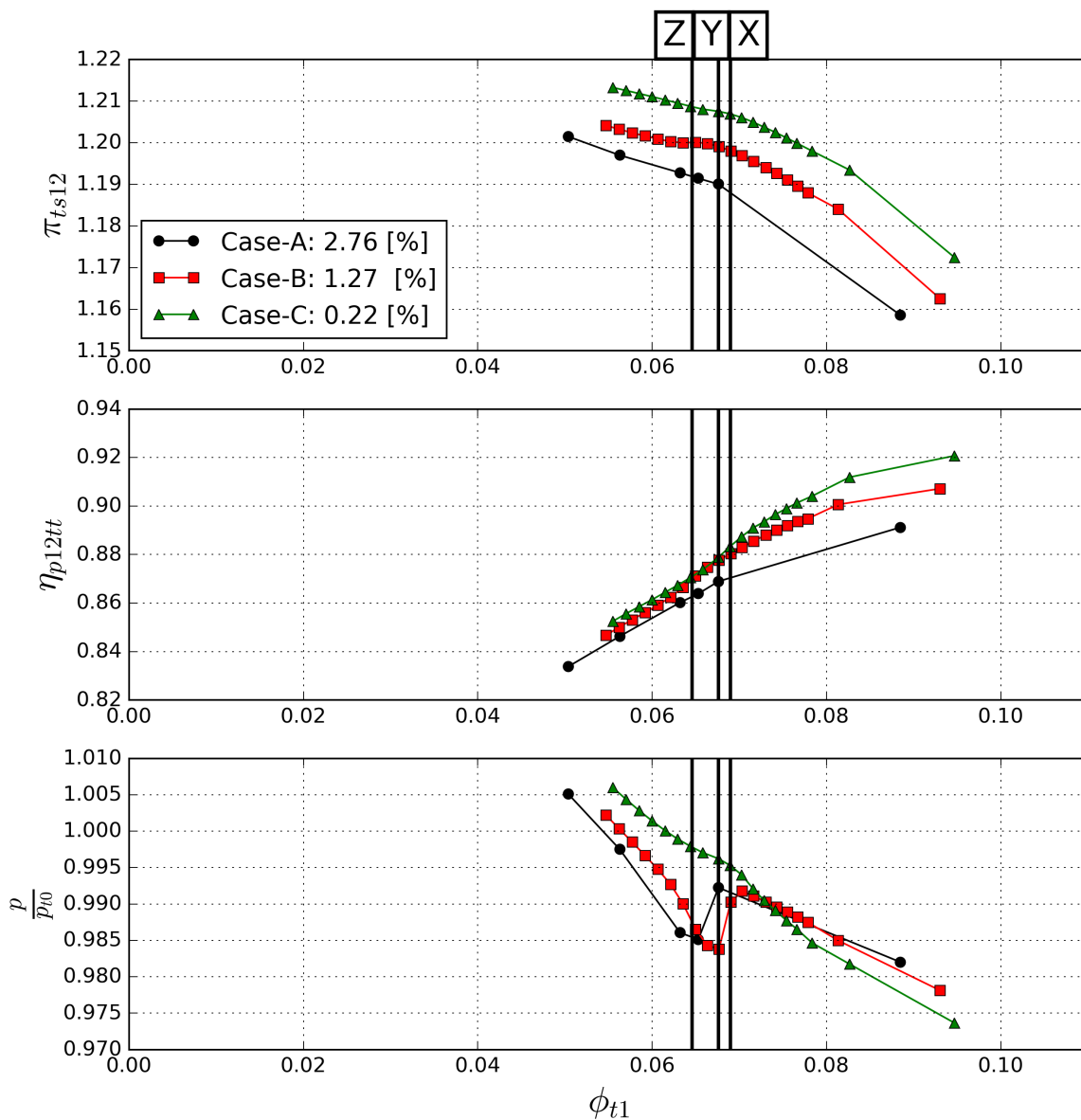


Fig. 7.5 Rotor performance and inlet casing pressure over the global flow coefficient

In order to further assess this behaviour as well as the altered slope of the inlet casing pressure in case C, three distinct operating points have been chosen and were marked with bold black vertical lines in figure 7.5. Operating point X represents the last operating point prior to the onset of recirculation and is located at a global flow coefficient of 0.069. Operating point Y is located at a global flow coefficient of 0.0676 and represents an operating point approximately at the onset point of inlet recirculation and will be supported with further evidence below. Operating point Z is located at a global flow coefficient of 0.0646 and represents the flow conditions with recirculation. In order to facilitate observations, only

cases B and C will be analysed further as case A and B showed a similar behaviour.

At the operating points X,Y and Z, the pitchwise averaged inlet axial velocity distributions at the location of the inlet plane have been calculated and are plotted in **figure 7.6** . In addition, the vertical red line marks zero axial velocity so that regions of negative axial velocity can be identified easily. This procedure is the same as has been used to define the region where recirculation occurs in chapter 5.

The left graph shows the spanwise axial velocity distributions in plane 1 which is located just upstream of the rotor main blade leading edge for the three operating points of case B. The right graph shows the velocity distributions for case C. For both cases, operating point X shows a normal velocity distribution with no negative axial velocities. At operating point Y, case B does not show any negative axial velocity but a slight depression in the velocity distribution in the upper 5% of the span. In case C, a small amount of negative axial velocity is present at the casing, indicating recirculation. For operating point Z, both cases show a negative velocity region at the casing, indicating the presence of inlet recirculation. In case C, the negative axial velocity region extends down to 96% span, whereas it only reaches to 94% in case B. Overall, the velocity distributions show great similarity for both cases. The onset point of inlet recirculation has been defined in chapter 4 as that point, at which negative axial velocity is present upstream of the rotor.

For both cases, the onset point of inlet recirculation is reached at the same flow coefficient, implying that the tip gap size does not have an effect on the onset point of recirculation.

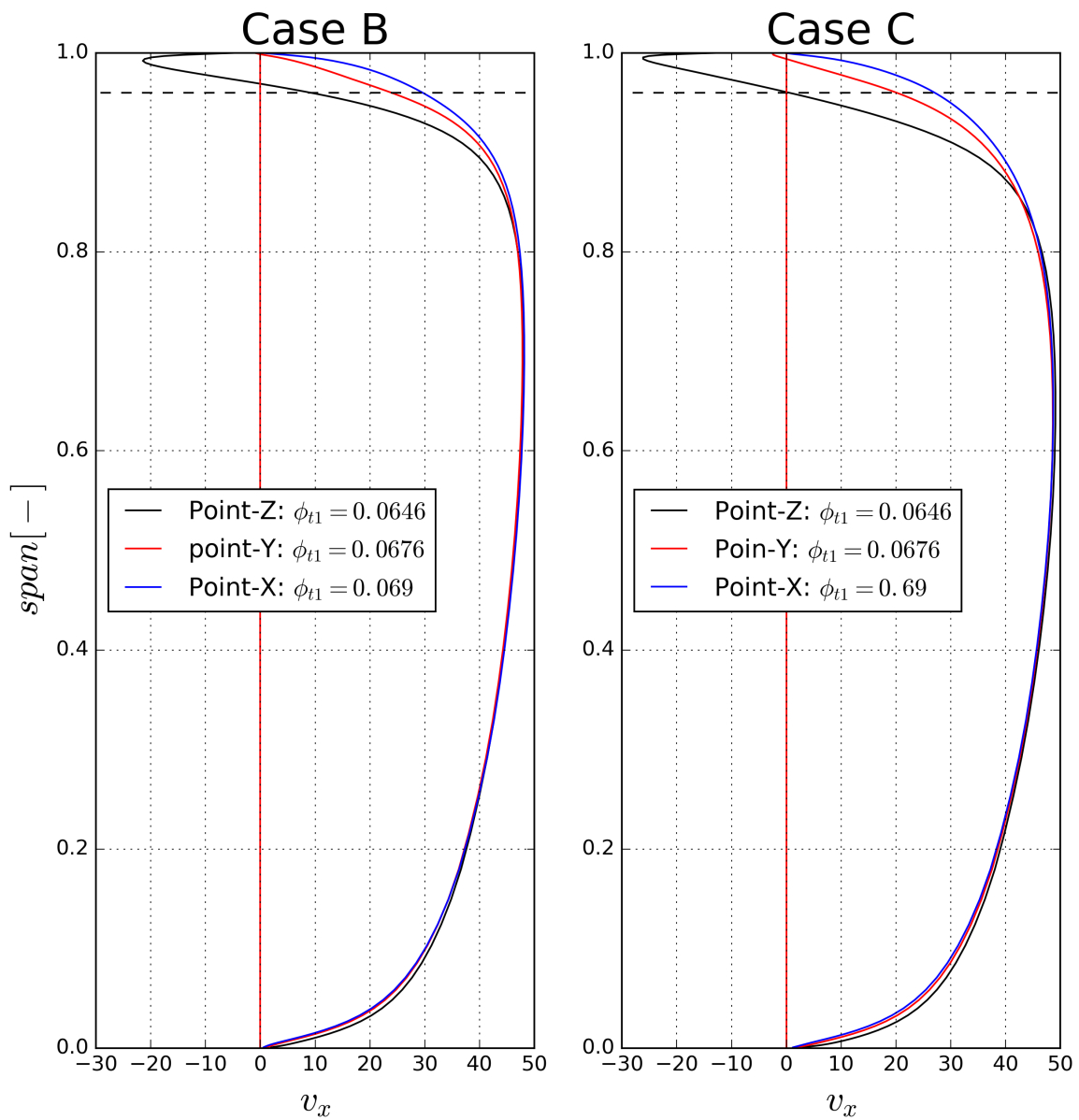


Fig. 7.6 Spanwise axial velocity distributions upstream of the rotor leading edge at a rotor speed of $Mu_2=0.65$

7.3 Analysis of the 3D flow field

Up to this point, the tip gap study provided several results and characteristic features which were related to the reduced tip leakage flow over a smaller tip gap.

Firstly, the total to total pressure rise capabilities of the compressor as well as the total to static pressure rise capabilities of the rotor were enhanced with a reduced tip gap size. This gain in pressure rise capabilities was maintained over the whole width of the characteristics, even when inlet recirculation was present.

Secondly, the efficiencies of both the overall compressor and the rotor were increased for high flow conditions because of reduced tip leakage losses. Regarding the shape of the efficiency curves, the larger tip gap cases A and B showed a lower peak efficiency which gradually dropped up to the onset point of inlet recirculation. The small tip gap case C featured the highest peak efficiency which dropped off much quicker towards low flow coefficients. It reached approximately the same efficiency at the onset point of inlet recirculation, giving it a more "pointed" shape. One important observation was that for flow conditions where inlet recirculation was present, the efficiency gains due to the reduced tip gap size, which were significant at high flow rates, were marginalised to a small amount.

Regarding the objective of this study the effect of a reduced tip gap on the onset point of inlet recirculation, it could be shown that the tip gap had no effect on the onset point of inlet recirculation. The onset point was defined as the point where negative axial velocity regions were present upstream of the rotor. In order to specify the operating point where inlet recirculation would happen, the casing pressure just upstream of the rotor leading edge and pitchwise averaged radial velocity profiles in the inlet plane were investigated. The recirculation onset point was found at almost exactly the same flow rate for all three tip gap sizes making the effect of the reduced tip gap flow due to a smaller gap on the onset point negligible.

However, a difference between the medium tip gap case B and the low tip gap case C could be found in the casing pressure values where case C did not show a "dip" at the onset point of inlet recirculation. This behaviour could be explained with the significantly reduced intensity of the tip leakage vortex for small tip gaps. Large tip gaps lead to a strong leakage flow which results in a higher mixing loss as well as higher kinetic energy at the casing. In return, this means that the static pressure is reduced. The described behaviour is much weaker without the tip leakage flow. The "dip" which was registered by the casing pressure tap in case B represented the point where the high swirl flow of the tip leakage vortex hit the adjacent leading edge and caused the static pressure upstream of the leading edge to drop. In case C, this effect was reduced so much that it did not have an effect on the static pressure tap.

The observation that the tip gap size had no effect on the onset point of inlet recirculation rises the question about how it can be associated with the theory that the low momentum flow in the casing region is responsible for triggering inlet recirculation.

Furthermore, the presence of inlet recirculation marginalised the efficiency gain due to the smaller tip gap and resulted in an almost identical efficiency curve for all tip gap cases, as shown in figure 7.5. A more detailed investigation of this behaviour was possible using the technique to work out the loss due to inlet recirculation introduced in chapter 6. The results are shown in **figure 7.7**, which displays the inlet recirculation loss over the global flow coefficient. As can be seen, the behaviour does not change with a variation in tip gap size.

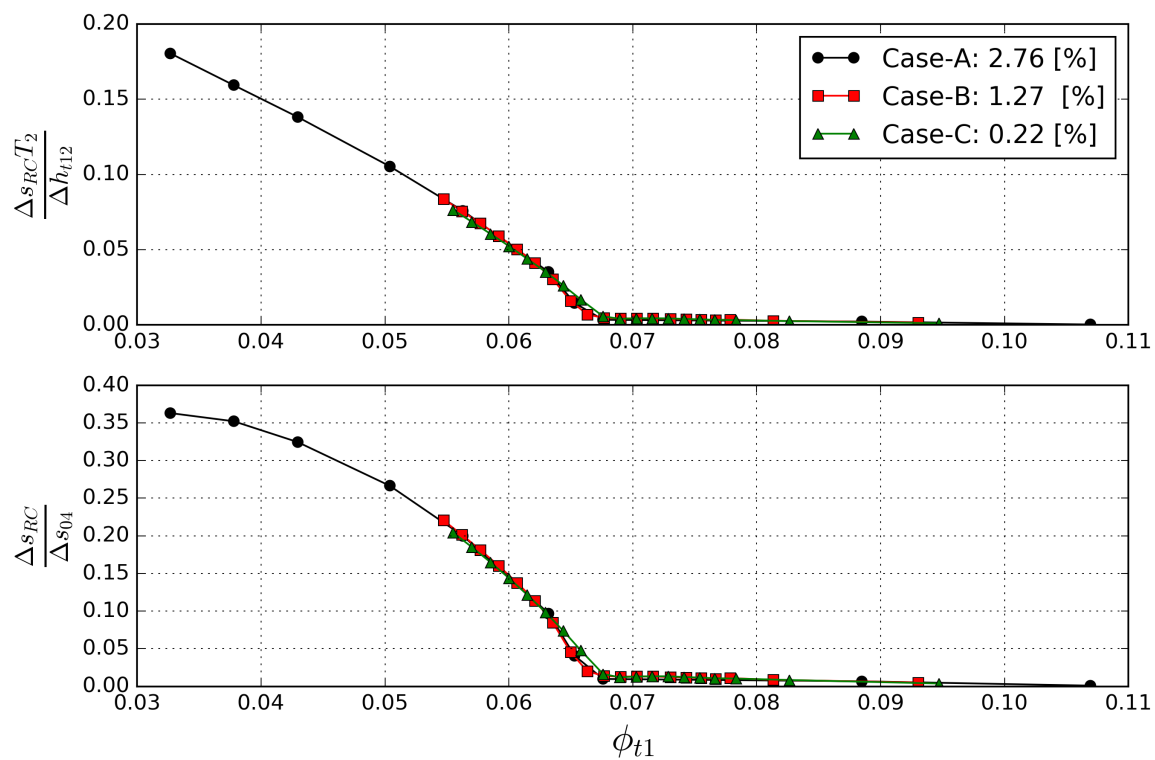


Fig. 7.7 "lumped" inlet recirculation loss for different tip gap heights

To increase understanding, for the similarity in onset point and lost work, a 3D flow analysis which compares the medium tip gap case B and the low tip gap case C has been executed.

To investigate the casing flow structure, the tip leakage flow over the first 5% of the blade has been tracked for the three operating points X, Y and Z for cases B and C. This was realised by tracking the streamlines of relative velocity. In order to visualise the forward shift in tip leakage vortex, a 2D projection from the top into the rotor passage of a surface at 98% span

is shown in **figure 7.8**. The left projection shows Case B and the right projection shows case C. In both cases, surface streamlines of relative velocity for operating point X are shown in black, those for operating point Y are shown in blue and those for operating point Z are shown in red. For case B, the streamlines clearly show how the passage vortex moves forward with a reduction in flow coefficient. For case C, a tracking of the tip leakage vortex turned out to be difficult as it does not extend into the passage and the flow remains attached to the blade in the inducer part, as can be seen in figure 7.8 on the right. Instead, the tip leakage flow is merged with the flow of the shroud boundary layer as can be seen in **figure 7.9**, which shows the iso surfaces at 100%span.

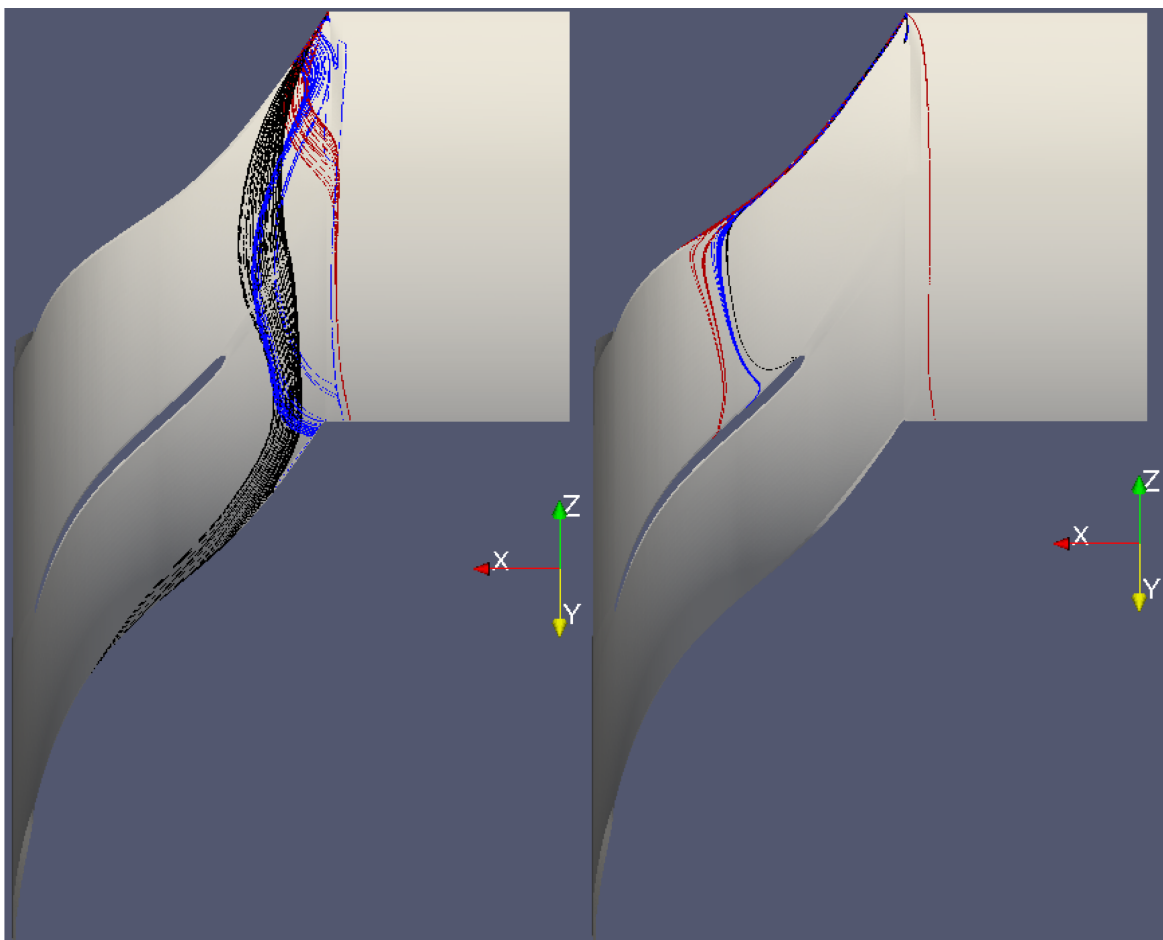


Fig. 7.8 Surface stream lines on surface of constant radius 98% passage height; **Left:** Case B = 98.6% span ; **Right:** Case C = 97.5% span; **Black:** Point-X ; **Blue:** Point-Y; **Red:** Point-Z

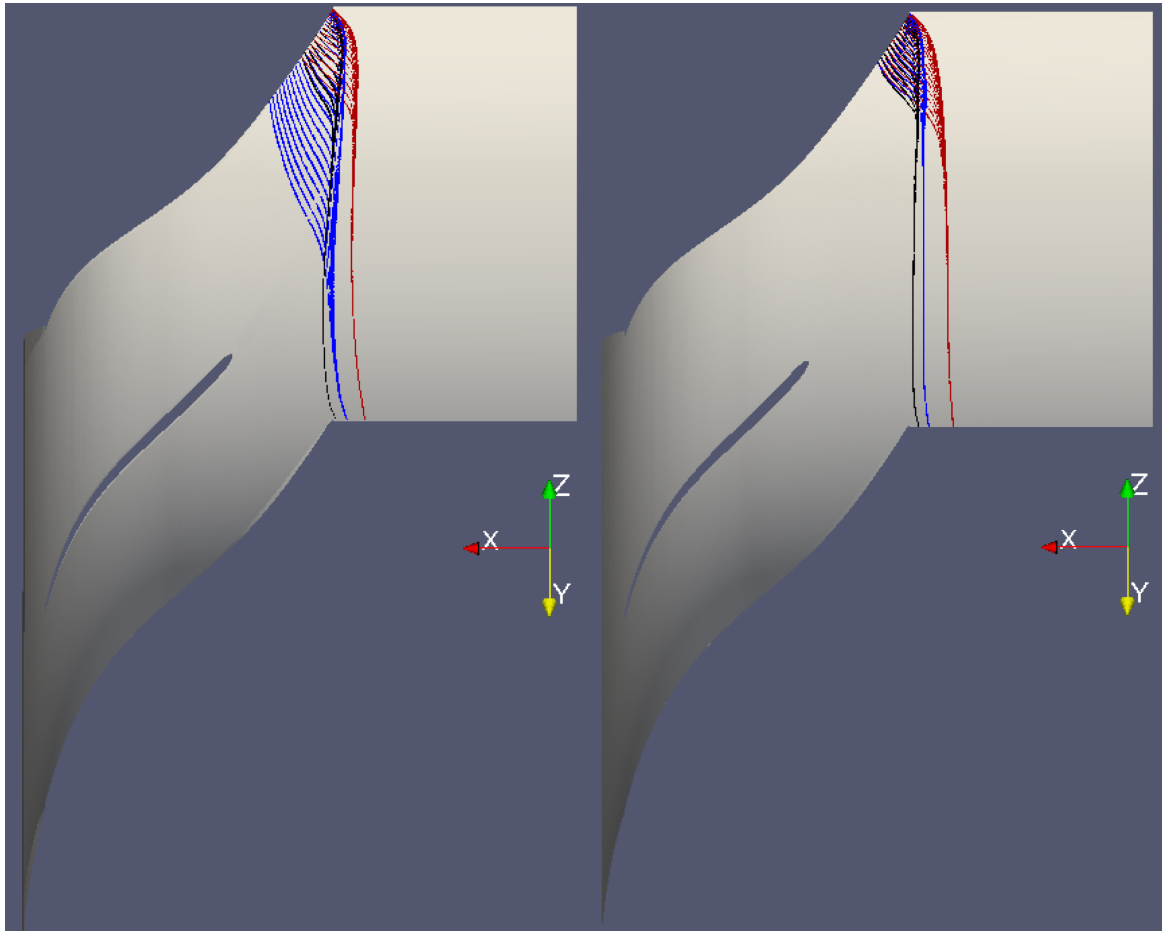


Fig. 7.9 Surface stream lines on ISO surface at 100% span; **Left:** Case B = 98.73% passage height; **Right:** Case C = 99.78% passage height; ; **Black:** Point-X ; **Blue:** Point-Y; **Red:** Point-Z

A tracking of the tip leakage flow and its propagation into the passage is presented in **figure 7.10** which shows the numerical geometry of the rotor and the diffuser with the casing removed so that the passage can be seen. Case B is shown on the left and case C is shown on the right. The streamlines are shown in black. Operating point X, which features the highest global flow coefficient of 0.069 is shown on the top. Operating point Y, which was identified as the point where inlet recirculation starts causing a negative axial velocity upstream of the rotor at a global flow coefficient of 0.0676 is in the middle. Operating point Z where about 4% of the span on the casing showed negative axial velocity upstream of the rotor at a global flow coefficient of 0.0646 is shown at the bottom.

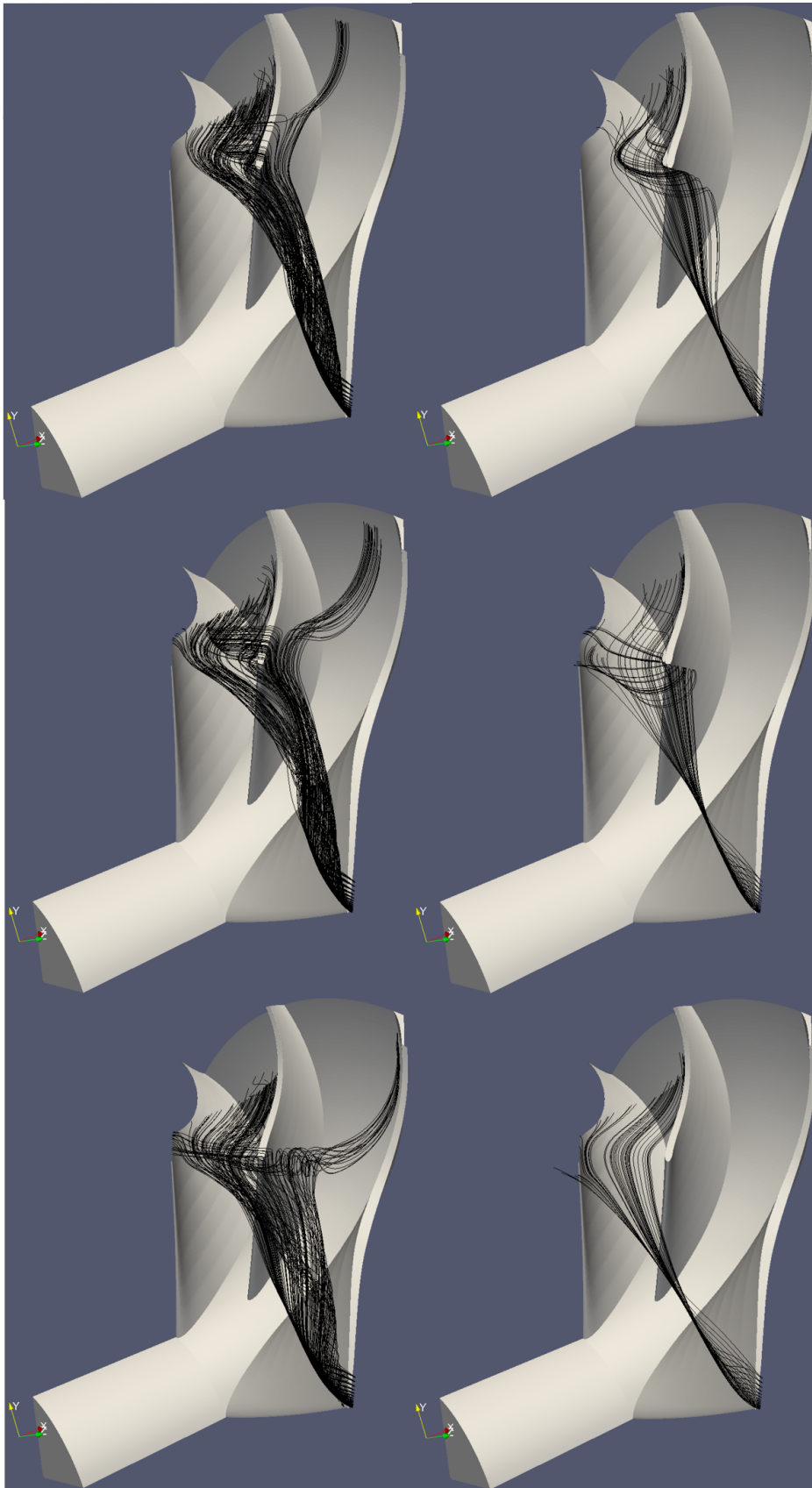


Fig. 7.10 Streamlines of relative velocity for operating points X(top),Y(middle) and Z(bottom). **left:** Case B; **right:** Case C

The stream lines which originate from the main blade leading edge tip gap allow to track the direction of the tip leakage vortex in both cases which makes out a major part of the low momentum region at the casing. For both cases, it is visible how the trajectory of the tip leakage vortex increases in angle as the machine is throttled towards lower flow coefficients. Here, the direction of the leakage vortex can be tracked in both cases and appears to be similar. However, the vortex in case B which features the larger tip gap shows a much stronger swirling motion as the tip leakage flow across the blade is stronger and feeds in more tangential momentum. The major difference of the two flow fields is located around the splitter blade leading edge and the exducer part of the suction side splitter passage. Here, the two flow fields are completely different. In case B, the flow originating from the main blade leading edge tip hits the splitter blade leading edge and divides into both splitter passages. It propagates downstream in the pressure side splitter passage on the left. In the suction side splitter passage on the right, the streamlines propagate towards the rotor exit and are pushed towards the middle of the splitter passage due to the high pressure region on the pressure side of the splitter blade. This effect is amplified when the machine is throttled towards lower flows so that the streamlines are pushed further towards the main blade suction side for operating points Y and Z. For operating point Z, the streamlines show that the flow approaching the suction side splitter passage stagnates around the splitter blade leading edge. One part is pushed towards the main blade suction side and propagates downstream towards the rotor exit. Another part is pushed towards the main blade leading edge along the casing. This behaviour of the flow being pushed back upstream towards the main blade leading edge coincides with the establishment of inlet recirculation. Furthermore, the observations imply that the point where the low momentum casing flow cannot overcome the adverse pressure gradient any more is reached far downstream in the passage around the splitter blade leading edge. More specifically, it is the high pressure region along the pressure side of the splitter blade which provides a resistance big enough for the casing flow to stagnate and reverse. This effect is even more pronounced in case C with the smaller tip gap. Here, the low momentum flow originating from the main blade leading edge tip gap is unable to penetrate into the suction side splitter passage for all three operating points. Instead, it propagates towards the exit entirely through the pressure side splitter passage. The part of the flow which heads towards the suction side splitter blade stagnates around the splitter blade leading edge and reverses along the casing. For operating point X, it is then washed down the pressure side splitter passage. For operating points Y and Z, it is pushed towards the pressure side of the main blade leading edge, again going along with the onset of inlet recirculation. The comparison of the casing flow structure of case B and C shows that the tip leakage flow does have a strong effect on the casing flow structure. However, it does not affect the onset

point of inlet recirculation. For the onset of inlet recirculation, the point of stagnation and reversal of the flow is important as this represents the location where the momentum of the casing flow cannot overcome the adverse pressure gradient in the passage any more. In both cases this happens around the splitter blade leading edge tip on its pressure side. This means that the pressure field in the splitter passage plays a crucial role in the onset of inlet recirculation. More precisely, it is the adverse pressure gradient in the splitter passage, which is the strongest on the pressure side on the splitter blade which provides enough adverse pressure to reverse the casing flow. This means that inlet recirculation does not develop in the inducer directly but is a result of the strong adverse pressure gradient in the middle part of the rotor.

This behaviour becomes more clear when looking at a the total to static pressure rise in the casing region as shown in **figure 7.11**. Here, the total to static pressure rise from inlet to the corresponding location on a meridional cut plane is shown. The cut plane is positioned at the tip of the blade. The figure shows all 6 different cases in the same way as the previous figure. On the pressure side of the splitter blade, a high pressure region can be seen whereas there pressure on the splitter blade suction side is expectedly lower. This difference in static pressure appears to be the reason for the low momentum flow to be diverted towards the suction side of the splitter blade and propagate downstream in the corresponding splitter passage. Comparing the same operating point for case B and C, the figure shows that the static pressure rise on the splitter blade suction side is stronger in case C. This could be an explanation why the inlet recirculation occurred slightly earlier in case C, as shown in figure 7.6.

The figure also shows a low pressure region on the main blade leading edge suction side which is much more pronounced in case B, which is a result of the stronger leakage across the blade due to an increased tip gap size. Furthermore, the stronger leakage leads to a larger amount of kinetic energy and loss in the leading edge region. This in return leads to a lower static pressure in the leading edge region. The low pressure due to increased kinetic energy and loss is one reason for the "dip" In the static pressure probe measurement of case B, shown in figure 7.5. In the small clearance case C on the other hand, the "dip" is not visible because the leakage is smaller and consequently, a not as strong leakage vortex is formed.

A more clear visualisation of the fact that the inlet recirculation region starts in the suction side splitter passage is provided in **figure 7.15** . The figure shows the 3D geometry of the rotor with the inlet planes of the main passage and the splitter passage. On those planes, the axial velocity has been plotted in such a way that the region with positive axial velocity is shown in red and regions with negative axial velocity are marked in blue. On the left of the

figure, the results of case B are presented, and on the left, case C is shown. From top to bottom, the operating points Z,Y and Z are displayed.

For operating point X, it is only case C which shows a negative axial velocity region at the entry of the suction side splitter passage. The main passage as well as the other splitter passage show positive velocities. This implies that the casing flow in the suction side splitter passage has been reversed for case C at operating point X because the low momentum flow could not overcome the adverse pressure gradient at the casing.

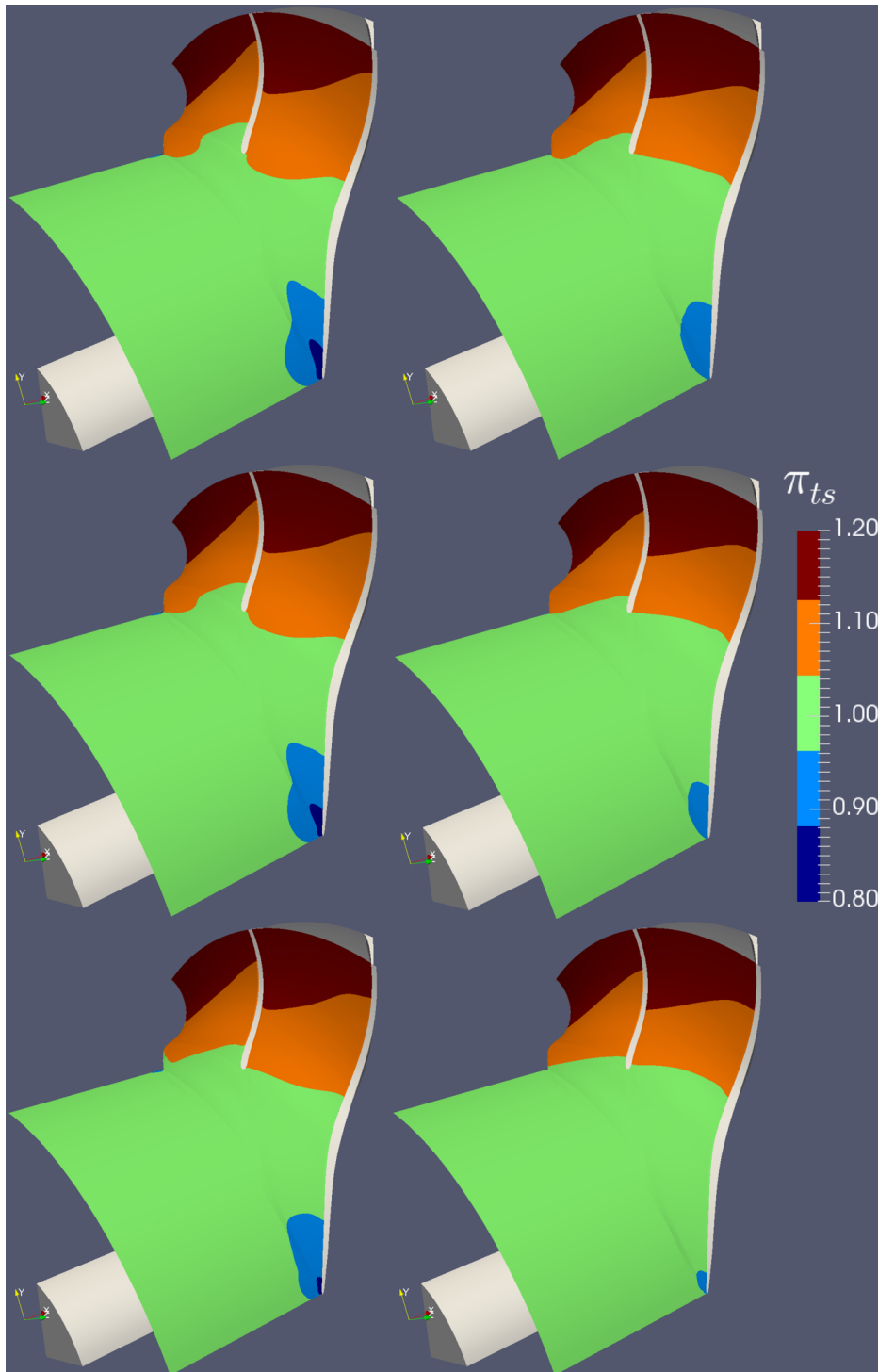


Fig. 7.11 Meridional cut through the machine at the rip radius showing the total to static pressure rise for **Operating points: X (top), Y (middle) and Z (bottom)**. **Positive velocity: red; Negative velocity: blue** **Left: Case B; Right: Case C**

Furthermore, the negative velocity region indicates that the source of inlet recirculation originates from this splitter passage and that the onset location is further downstream in this passage than the leading edge.

For operating point Y, which represents the "onset point" of recirculation as defined before based on the negative velocity plot of the rotor inlet plane, both cases show a negative velocity region in the suction side splitter passage. Furthermore, the main blade inlet starts to be affected in both cases as it shows a small negative velocity region around the main blade leading edge. It has to be noted that for the larger tip clearance case B, both splitter passages show a negative velocity region whereas it is confined to the suction side splitter passage in the small tip clearance case C. This behaviour can be explained with the increased tangential momentum in the casing flow in case B which forces the low momentum region at the casing further towards the main blade pressure side and into the pressure side splitter passage.

Operating point Z represents the case with inlet recirculation present in the main passage inlet. The size of the negative axial velocity region at the rotor inlet is approximately the same for both cases, which could also be seen in the radial velocity profiles in figure 7.6. In the splitter passages however, the picture is different for both cases. In case B, the negative velocity region is confined to the surrounding area of the splitter leading edge and is present in both splitter passages. In case C, the pressure side splitter passage is much less affected and a significant part of the suction side splitter passage shows negative axial velocity. This implies that in case of a small tip gap, only the splitter passage on the suction side of the main blade is affected by inlet recirculation whereas the pressure side passage remains unaffected. Again this can be explained with the significantly reduced amount of leakage flow, as shown in figure 7.4, which does not push the low momentum flow towards the pressure side of the main blade.

More detailed insight can be gained by studying the tip gap mass flux along the blade chord. A visualisation is provided in **figure 7.12** which shows the tip gap mass flux nondimensionalised with the compressor mass flux over the non dimensional chord for the six cases presented above. The leakage flux over the main blade is shown as black lines and the leakage flux over the splitter blade is given as red lines. The leakage flux over the main blade and splitter blade will be discussed separately.

Comparing the main blade leakage of case B and C the leakage distribution is much more uniform in case C. In case B, a large amount of leakage is located around the leading edge in the first 10% of the chord. This explains the more pronounced leakage vortex in case B and the fact that the low momentum casing flow gets pushed more towards the suction side splitter passage. Around 50% span, the main blade leakage has its minimum which is due to the presence of the splitter blade which takes over part of the load. In the last third of the

chord, the leakage increases again. Furthermore the leakage flux fluctuates in both cases because the upstream leakage flow hits the main blade gap.

In case of the splitter blade, the tip leakage is much stronger in case C. For case B, the tip leakage over the splitter blade features about the same distribution as the main blade in the last 40% of the chord. In Case C, the leakage over the splitter blade exceeds the one of the main blade by approximately 10% indicating a higher loading of the splitter blade in the exducer. This can be explained with the behaviour observed in figure 7.10, which showed that the tip leakage flow in case C only propagated into the suction side splitter passage. Consequently the loading around the tip of the splitter blade is less affected.

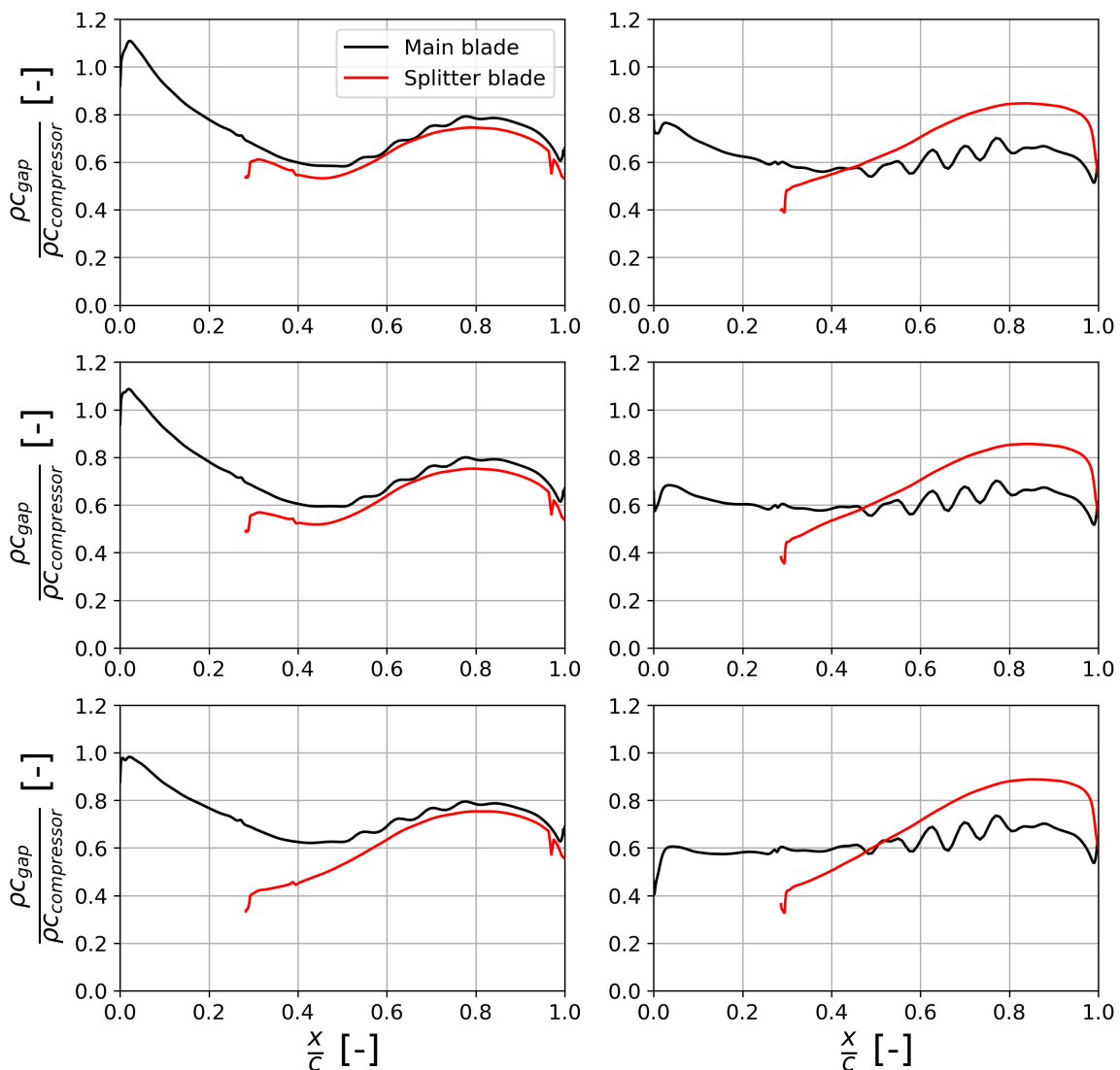


Fig. 7.12 Non dimensional tip gap mass flux over non dimensional chord for the main and splitter blade for operating points X(top),Y(middle) and Z(bottom). **left:** Case B; **right:** Case C

As the tip gap flow is driven by the blade loading around the tip, the blade loading in the tip region is examined in **figures 7.13 and 7.14**. The figures show the blade loading in terms of surface pressure nondimensionalised with the intake total pressure for the three operating points described above. Figure 7.13 shows the loading distribution over the chord at 98% span whereas figure 7.14 shows the loading at 95.5% span. The latter figure is provided to show the location where the altered tip clearance has no effect on the loading any more. Figure 7.14 will not be discussed in more detail but shows the same features as figure 7.13. Figure 7.13 shows the blade loading distribution of the main blade on the left and the splitter

blade on the right. Case B is shown as full lines and case C is shown as dashed lines. The Pressure side is shown in red and the suction side is shown in blue. The main and splitter blade will be discussed separately. Between case B and C, the loading of the main blade suction side is different in the first 20% of the chord. Case B has a higher loading, which causes the stronger tip leakage vortex. Over the remaining chord length the slope and loading magnitude are approximately the same for both cases. The pressure side loading shows the major difference between case B and C for the main blade. Here, the loading in case B is around 10% lower in case B compared to case C over the whole chord for all three operating points. This agrees with the reduced tip leakage flow shown in figure 7.12. Case C has an almost uniform loading over the whole chord.

The splitter blade loading shows again a different behaviour. The pressure side and suction side will be discussed separately. The splitter blade suction side shows an almost identical behaviour to the main blade. Case C however features a higher suction side pressure around the tip for the highest flow case implying less loading in case C compared to case B. The splitter blade pressure side has an about 10% decreased loading for case B compared to case C, similar to the main blade. Case C shows an increase in loading towards the rotor exit. When throttled to low flow coefficients, the blade loading decreases around the splitter blade tip for both cases, indicating the onset of recirculation. This goes along with the flow reversal around the splitter blade tip shown in figure 7.10.

Overall the blade loading in the reduced tip gap case does not show such a strong loading in the front section of the main blade due to the low pressure region developing on the suction side. Furthermore it is able to maintain constant loading along the whole chord for the main blade. In case of the splitter blade, loading is maintained in the exducer when throttled to low mass flows whereas the loading collapses at the splitter blade tip for both cases due to the onset of recirculation.

Regarding the question about the identical "lumped" inlet recirculation loss independent of tip gap size, as shown in figure 7.7, the comparison shown in figure 7.15 should be considered. As outlined above, the figure shows that for both cases, the inlet recirculation occupies approximately the same radial space in the passage. This could also be seen in the axial velocity plot in figure 7.6. This means that the inlet recirculation loss accounts approximately for the same region and all individual loss sources occurring within it as well. Because inlet recirculation accompanies an unloading of the tip region of the blade, the tip leakage and consequently the losses associated with it diminish significantly. This behaviour goes some way to explain why the "lumped" inlet recirculation loss is independent from the tip gap size.

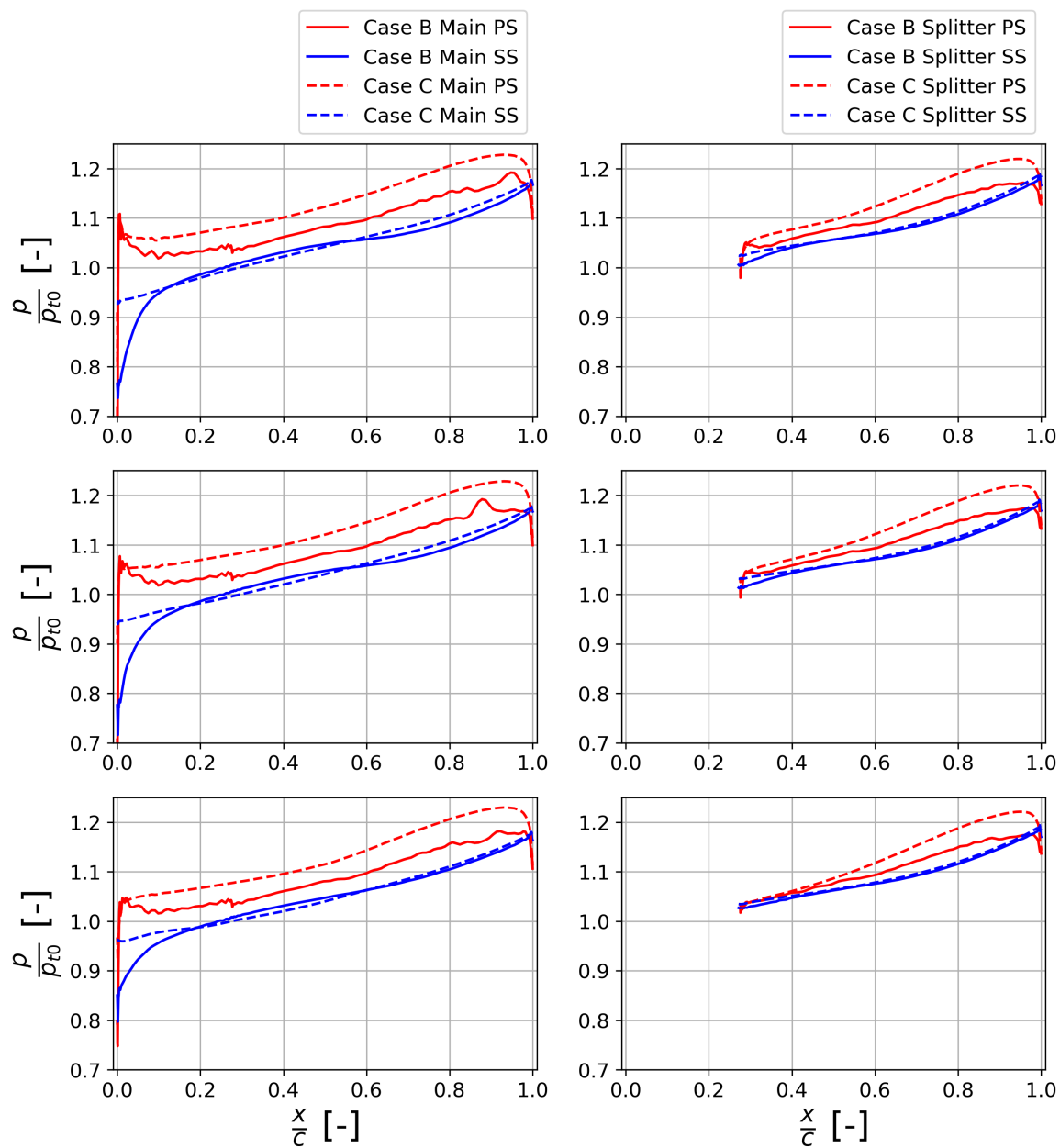


Fig. 7.13 Blade loading in terms of non dimensional pressure at 98% passage height for Case B (=98.6% span) as full lines and for Case C (=97.5% span) as dashed lines; **Left:** Main blade **Right:** Splitter blade; **Top:** Point-X ; **Middle:** Point-Y; **Bottom:** Point-Z

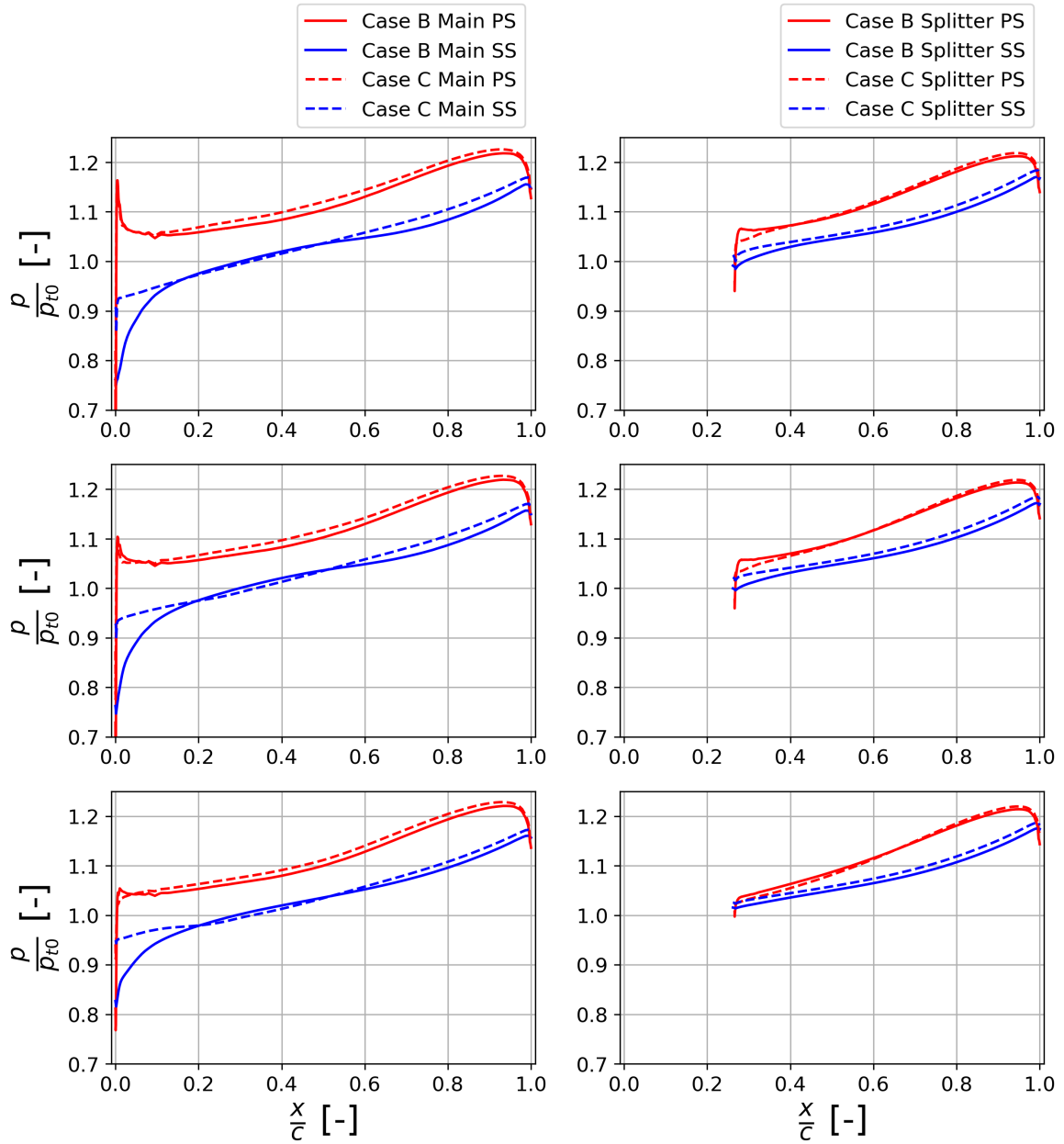


Fig. 7.14 Blade loading in terms of non dimensional pressure at 96% passage height for Case B (=96.6% span) as full lines and for Case C (=95.5% span) as dashed lines; **Left:** Main blade **Right:** Splitter blade; **Top:** Point-X ; **Middle:** Point-Y; **Bottom:** Point-Z

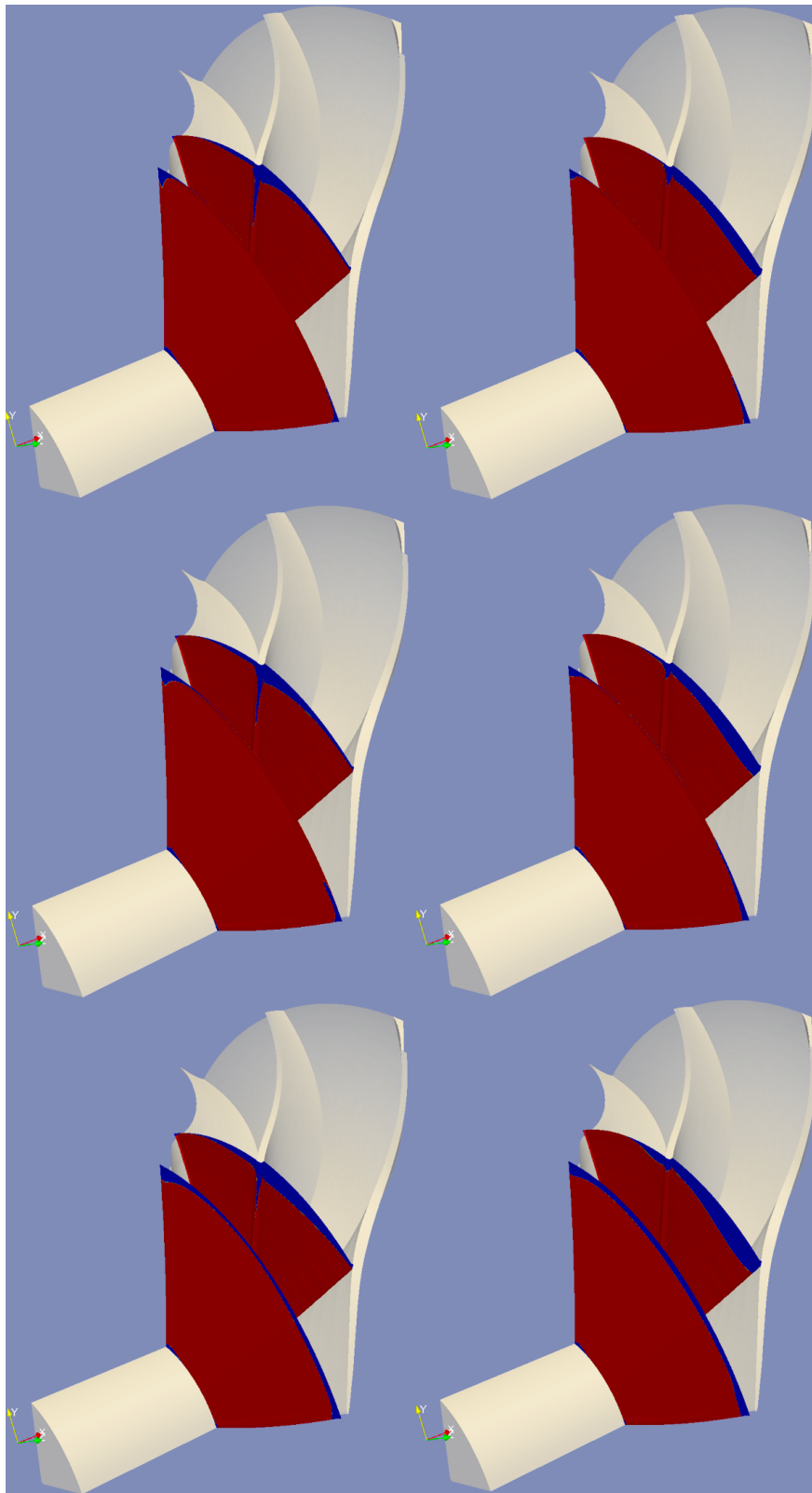


Fig. 7.15 Axial velocity field at the main and splitter passage entries for **Operating points:** X (top), Y (middle) and Z (bottom). **Positive velocity:** red; **Negative velocity:** blue **Left:** Case B; **Right:** Case C

7.4 Conclusions

The tip gap study compared three cases of different tip gap height in order to determine the effect of tip leakage on the onset point of inlet recirculation. This was based on the fact that the tip leakage flow is a significant contributor to the low momentum flow in the casing region of the rotor passage.

In an initial step, the study compared the different cases in terms of their performance. It was shown that the pressure rise capabilities increased significantly with a reduction in tip gap height over the whole flow range. This was the case for operating points with and without inlet recirculation.

Regarding the efficiency of the machine and more specifically the rotor, a different result was observed. For operating points without inlet recirculation, a significant rise in efficiency was observed as the tip gap size was reduced. This could be explained with a significant reduction of the tip leakage losses as the tip gap got reduced. Particularly the peak efficiency was improved with a decreased tip gap. A smaller tip gap led to a more "peaked" efficiency curve meaning that the gradient at which efficiency decreased with a reduction of mass flow was higher for a smaller tip gap. At flow coefficients where inlet recirculation was present, the efficiency gains due to a reduced tip gap were lost. At the onset point of inlet recirculation, approximately the same efficiency was reached for all tip gap sizes.

A more detailed study based on the "lumped" inlet recirculation loss as defined in the previous chapter revealed that the inlet recirculation loss was not affected by a change in tip gap size and the performance penalty due to inlet recirculation was the same for all cases.

This observation was explained with the three dimensional extent of the recirculation zone within the rotor which occupied a similar area independent of the tip gap size. The similarity in extent could represent the first part for an explanation of the independence of loss from the tip gap size. The second part was the unloading of the blade in the region where recirculation was present, which involved the tip gap as well. Because there was no driving force for the leakage flow, this loss source resulted in being diminished off.

In order to define the onset point of inlet recirculation, the technique presented in chapter 5 was used, which was based on the casing pressure at the rotor inlet as well as the spanwise axial velocity profiles at the inlet of the rotor. The onset point of inlet recirculation was then defined as that point, at which a negative velocity was present upstream of the rotor inlet. Regarding the inlet casing pressure, it was shown that for the large tip gap cases, a "dip" was present at the onset point of inlet recirculation. This "dip" could not be observed for the

smallest tip gap case. Instead, the inlet casing pressure rose continuously. However, reverse flow could be observed in both cases in the spanwise axial velocity plots.

Based on these observations, it was found that inlet recirculation started at almost exactly the same flow coefficient for all tip gap cases. As a result, a tip gap variation had no effect on the onset point of inlet recirculation. Furthermore, the size of the recirculation zone was not affected.

This left the question about how this observation could be associated with the theory that the low momentum flow in the casing region was responsible for triggering inlet recirculation. Further insight into the behaviour of the machine was gained with a 3D flow analysis that compared the medium tip gap case B and the small tip gap case C. The study revealed that, despite an almost identical onset point of inlet recirculation upstream of the rotor, the casing flow structure within the rotor was very different. The casing flow structure was visualised with streamlines of relative velocity which were used to track the flow originating from the first 5% of the rotor main blade tip gap. It was shown that the trajectories of the tip leakage vortex were similar in both cases and that the casing flow hit the leading edge of the splitter blade. In the medium tip gap case B, the low momentum flow then propagated into both splitter passages. The adverse pressure gradient in the splitter passage close to the suction side of the main blade forced the low momentum flow on the casing towards the main blade suction side as it propagated towards the exit of the rotor. This effect was amplified when the machine was throttled to lower flow coefficients. For the operating point Z, which featured the lowest flow coefficient, a part of this flow reversed and propagated towards the leading edge of the main blade from pressure side. This was also the point when recirculation was registered in the rotor inlet plane.

For case C with the smallest tip gap, the flow structure was different. Here, the low momentum flow could not enter into the suction side splitter passage but stagnated and reversed close to the splitter blade leading edge. In the pressure side splitter passage, it could propagate downstream towards the rotor exit. At the operating point Z with the lowest flow coefficient, the low momentum flow was pushed towards the leading edge of the main blade from the pressure side and went along with the onset of recirculation in the inlet plane.

The investigation of the 3D flow structure showed that the flow reversal leading to inlet recirculation occurred much further downstream than previous theories would suggest. Furthermore it occurred in only one of the splitter passages, namely the one close to the main blade suction side initially. In terms of mechanism, this showed that the low momentum flow on the casing stagnated and reversed when it reached the high pressure region on the pressure side of the splitter blade.

An analysis of the tip leakage along the blade chord revealed an altered distribution between case B and case C. The larger tip clearance case showed a strong variation in tip leakage with a peak in the inducer part of the main blade. At high flow coefficients, the leakage distribution over the splitter blade showed a similar trend as for the main blade. Around the onset point of recirculation, the leakage around the splitter blade leading edge reduced, indicating a loading breakdown in this area. The small tip gap case featured a much more uniform leakage distribution for the main blade with a less pronounced peak in the inducer part. The splitter blade showed a different behaviour with an increasing leakage along the chord that exceeded that of the main blade by a maximum of 10%. In case C, the splitter blade featured a small amount of leakage for all operating points around the leading edge. The low leading edge loading could be linked with the redistribution of the oncoming main blade tip leakage vortex by the splitter blade potential field observed in figure 7.10.

The loading distribution as the driving mechanism for the tip leakage flow was examined in the top 4% of the blade span. It was shown that a reduction in tip gap had only a small effect on the blade loading for blade heights lower than 96%, identifying the top 4% as the region of interaction between the blade and the clearance. Within this region, a reduction in tip gap resulted in a more uniform loading distribution along the chord of the main blade. The main changes could be observed in the inducer part where the suction side low pressure region due to the blade end wall - clearance flow interaction was reduced. The splitter blade loading featured a more uniform loading distribution at reduced clearances as well. The splitter blade leading edge region however showed a reduction in loading for both tip clearances. For the lowest flow coefficient, representing the onset of recirculation, the blade loading of the splitter blade was almost identical for the different clearances. The match in loading distribution under recirculation could be taken as an indicator for the similar performance of the machine with altered tip clearance.

Regarding the region which was occupied by inlet recirculation within the rotor, the 3D flow analyses showed that only the suction side splitter passage was affected in the low tip gap case C, whereas both passages were equally affected for the medium tip gap case B. One explanation for this behaviour was the significantly weaker tip leakage flow across the main blade which induced less tangential momentum into the casing flow. Consequently, the low momentum flow remained closer to the main blade suction side instead of being pushed into the passage.

Regarding measures to influence the onset and development of inlet recirculation, this study confirmed that a reduction of the tip gap is ineffective. Furthermore, the study showed that

the location of the onset of recirculation cannot be found in the inducer part of the rotor but further downstream in the region of high meridional curvature. The assumption of a zone of low meridional momentum causing the onset of inlet recirculation still remains valid. However, other measures should be investigated in order to alter the onset point. Options to do so include a modification of the meridional shape of the passage, most importantly on the casing. Furthermore alterations to the location of the splitter blade could help controlling the onset point of inlet recirculation. Furthermore, an alteration of the blade shape to control diffusion could lead to success. Particularly a smaller amount of diffusion on the splitter blade pressure side close to the casing could help as this is the region where the low momentum flow stagnates and reverses during the onset process.

Regarding the reduced order modelling of inlet recirculation, the question arises whether it is possible to accurately and universally predict the onset point of inlet recirculation with a simple inducer diffusion model as suggested by Qiu [35] as this study showed that the onset point of inlet recirculation is located far downstream in the passage.

Chapter 8

Conclusions and future work

8.1 Introduction and scope of work

In the automotive industry, the demand for high fuel efficiency cars together with increasingly challenging emission regulations has created the demand for more efficient engines with an improved power to weight ratio. This has led to the trend of downsizing internal combustion (IC) engines. The most economical way to realise such a motor is to turbocharge the IC engine. A petrol driven combustion engine features a very wide engine speed band which requires turbochargers that can cope with a broad range of different mass flows. For the compressor side of the turbocharger this represents a particularly difficult task as its operating range is limited. Regarding the different operating conditions in every day usage of cars with turbocharged engines, the deficient performance of the compressor limits the behaviour of the drive train particularly during transient conditions such as the drive-away process or acceleration from low engine speeds. This behaviour is commonly known as the turbo lag.

This situation has led to altered design requirements for turbocharger compressors so that in the modern design process, peak efficiency at nominal speed is not the main focus any more. Instead, the performance at part speed and low flow conditions which is directly related to the turbo lag has gained significant attention. The character of the flow at these operating points is much more complex than under design conditions.

The most dominant flow feature at low flow conditions is the phenomenon of inlet recirculation, a flow condition where a large portion of the flow which has been ingested into the rotor of the machine is expelled again through the inlet, creating a blockage ring on the casing. Whilst inlet recirculation represents the main loss source at low speed and low flow in a centrifugal compressor, it also seems to play a role in keeping the compressor functional

instead of stalling or dropping into a surge hysteresis loop

Whilst the phenomenon of inlet recirculation has been known for a long time, particularly in hydraulic pumping devices, it is not very well understood. Investigations up to now have revealed the general flow structure of the phenomenon [37] and a significant amount of loss has been related to it [43]. Furthermore attempts to depict inlet recirculation in reduced order models have been made, for example by Qiu [35]. However, the method leaves margin for improvement, particularly when applied to turbocharger compressors, as can be seen in the results by Harley [23]. Detailed investigations into the three dimensional flow structure of inlet recirculation have not been carried out up to now. Studies about design parameters are very scarce and limited to the use of inlet guide vanes.

With the scope on improving the part speed low flow performance of automotive turbocharger compressors, more specifically the range and transient behaviour, this work intended to increase the understanding of inlet recirculation as a dominant feature in this region.

The research necessary to approach the problem has been carried out on an automotive turbocharger compressor which was available at the Whittle Laboratory. An experimental test stand was built to obtain insight with measurements and a numerical model based on the compressor geometry was used to carry out time averaged numerical simulations.

The following research questions were addressed:

8.1.1 Under which conditions does inlet recirculation occur?

Many descriptions and explanations of inlet recirculation and its key features have been published. However, these theories are mutually contradictory, especially regarding the causes of inlet recirculation. Furthermore, no information which outlined the regions in a compressor map that were affected by inlet recirculation could be found.

Both points were considered vital for the present research for two reasons. Firstly, a tool to determine the presence of inlet recirculation was needed. Secondly the importance of inlet recirculation based on its occurrence in the compressor map had to be estimated in order to find out whether it played an important enough role regarding compressor low flow low speed performance.

To find out the conditions at which inlet recirculation occurs, a study on its key features was conducted. Furthermore a compressor low flow operation analysis was carried out in order to identify the areas affected by inlet recirculation in a compressor map.

8.1.2 What are its effects on compressor performance in terms of energetic cost?

In addition to knowledge about the operating regions which are affected by inlet recirculation, it is crucial to obtain information about the performance penalty resulting from the presence of the phenomenon. Although reduced order models have been presented in open literature to account for inlet recirculation during preliminary design, no information which set the losses due to inlet recirculation in relation to other losses in a compressor have been found. In this work, a study on the energetic costs of inlet recirculation and its impact relative to the losses from the different components of a compressor has been carried out.

8.1.3 How can inlet recirculation be accounted for in preliminary design?

One of the most important tools for a designer is the availability of accurate low order models to account for the complex phenomena of a real machine as early as possible during the design process. In this work, an approach which was based on a control volume analysis for conservations of mass, momentum and energy was used and a low order model was derived to provide such a tool.

8.1.4 How can a designer influence the mechanisms sustaining recirculation?

Inlet recirculation represents the dominant flow phenomenon at part speed and low flow conditions in a compressor. It is thus desirable to find out about how the phenomenon can be controlled. The low meridional momentum flow at the casing of the rotor has been identified to play a key role for the onset of inlet recirculation. As the tip leakage flow is a strong contributor to the low momentum flow, a tip gap study has been conducted to investigate the effect on the onset of recirculation.

8.2 Experimental and numerical methods and validation

The investigations during this work have been executed on a turbocharger compressor without bleed channel which was available at the Whittle Laboratory. The geometry of this turbocharger was typical for passenger vehicle applications, more specifically for engines with a capacity between 2.0 and 4.0 litres. The geometry was used to build up a test stand as well as a numerical model.

The experimental setup consisted of the compressor side of this turbocharger which was combined with a downstream throttle valve to control back pressure. The turbine in combination with a vacuum pump was used as a propulsion system. Variable turbine inlet guide vanes allowed control over the power input into the compressor.

In order to allow accurate mass flow measurements during the presence of inlet recirculation, a separate bellmouth was used which was placed far upstream of the compressor inlet and connected via a high volume settling chamber.

The compressor was equipped with probes that allowed to investigate the performance of the components inlet, the rotor, the diffuser and the volute separately.

The casing of the machine was equipped with static pressure tapings along the meridional line of the machine. Their positions were located between 5.5 meridional rotor lengths upstream of the rotor to the diffuser exit.

A total pressure traverse upstream of the rotor inlet was set up to determine the flow conditions there. Those were then used as inlet boundary conditions for the numerical model.

In order to determine the influence of the non-axisymmetric volute on the circumferential pressure field at the exit of the diffuser, casing pressure tapings were placed in the diffuser around the annulus. Those were used to determine the exit boundary conditions of the numerical model.

The numerical model of the compressor was put together from two parts. The inlet, rotor and diffuser were modelled three-dimensionally and were calculated using the CFD solver Turbostream. The volute was excluded from this model as it represented the only component of the compressor which was not axisymmetric. This applicability of this method was confirmed using the results of the measurements for the circumferential pressure field in the diffuser which showed that the annular pressure variations were sufficiently small. This allowed to simplify the numerical model to one single main passage. The numerical compressor model was embedded between a long inlet block to avoid interference with the recirculation phenomenon and a nozzle shaped outlet block which allowed to "throttle" the numerical model by varying the exit crosssection rather than varying the back pressure and gave more stability for near stall calculations.

For the volute, a 1D- model was developed by the author which assumed that all radial kinetic energy was lost in the volute and modelled a sudden expansion loss as well as the outlet kinetic energy. The model was compared to other models from the public domain as well as measurement data of two volutes and it was found to be an improvement compared to other models.

The 3D numerical model was combined with the 1D Volute model and a disk friction model to represent the whole compressor.

Both experiment and numerical model were validated against the manufacturer performance data. In case of the measurement, the validation was carried out at the 50% speed line and showed very good agreement. In case of the numerical model, the whole compressor map was used to validate the model and again, a very good agreement was achieved.

In an error analysis for the numerical model the individual errors from the 3D model and the 1D model were determined. It was shown that the error of the numerical model roughly scales with the rotor speeds cubed, whereas the error from the 1D model scales linearly with the rotor speed. Because it was impossible to determine whether deviations came from the measurement or the calculations, a comparison of the measurement error with the numerical error was carried out and it was shown that they were small and in the same order of magnitude which was taken to be sufficient as a validation.

8.3 Key features of inlet recirculation

In order to characterise inlet recirculation, key features of the phenomenon have been investigated and described with results from the experiment and the numerical model.

It was shown that inlet recirculation is a phenomenon which takes place in the tip region of the rotor inlet of a radial compressor wheel. The recirculation bubble can extend far downstream into the rotor and far upstream into the inlet. Furthermore, the flow within the recirculation bubble features a strong positive swirl component. The phenomenon is non periodic in a time averaged sense. Furthermore, it can extend into the passage radially up to 20% of the span.

A more detailed description of the phenomenon was carried out using an approach based on a control volume around the rotor. This meant that the inlet of the rotor was split up into a zone with mass flow which was expelled into the inlet and mass flow which entered the rotor. The approach allowed to make a characterisation of the recirculating flow pattern based on mass, momentum and energy and was considered to be more physical than the approaches found in literature. Those treated the recirculation bubble as a separate system in the shroud

where a recirculating mass flow was circulated in and out of the rotor. A second "active" flow zone was then defined based on the overall mass flow going through the machine.

Using the control volume approach, the onset of inlet recirculation and established recirculation were discussed separately.

Regarding the onset point of inlet recirculation, techniques described in the public domain are based on a criterion which is based on the main blade incidence to define a critical incidence angle. Examples where the criterion was used have shown that the critical incidence value is not universal. As the research in this work investigated the rotor flow field with regard to inlet recirculation for the first time, it was found that the real starting point of inlet recirculation is located far downstream in the rotor passage close to the splitter blade pressure side in the machine subject to this investigation. There, the low momentum flow close to the casing cannot overcome the adverse pressure gradient any more. As the splitter blade induces its own potential field, the adverse pressure is particularly high on its pressure side. The low momentum region in the casing is a result of four mechanisms, namely leading edge separation, the radial pressure gradient, passage diffusion and tip leakage flow. Depending on the specific design of a compressor, the importance of these mechanisms as a contributor to the low momentum zone will vary. As a result, the onset of inlet recirculation could happen at different incidences for different types of machine.

The established recirculation zone can be characterised based on the input of mass, momentum and energy. The mass flow being expelled from the rotor inlet increases almost linearly with a reduction in global flow coefficient and can reach values of up to 35% of the main mass flow. Prior to the point where inlet recirculation causes negative flow in the rotor inlet, the radial momentum upstream of the rotor reaches zero, which could be a result of the potential effects of the blockage present in the casing region. Once the inlet recirculation is present in the inlet, it induces a positive tangential velocity component into the flow. The induced tangential momentum increases almost linearly with lowering the global flow coefficient. In terms of energy, the flow exiting the rotor carries around 70% of the total enthalpy rise of the machine. This value remains constant and is independent of flow coefficient and rotor speed.

8.4 When does inlet recirculation occur?

The starting point of inlet recirculation is located in the rotor passage close to the pressure side leading edge. In order to make it possible to determine the presence of inlet recirculation in both the experiment and the numerical calculation, a "symptom" of inlet recirculation

which can be measured upstream of the rotor is much more feasible as the rotating frame is not accessible with probing equipment. One option to do so is the casing pressure just upstream of the rotor leading edge. It rises to values which exceed the inlet total pressure as soon as inlet recirculation is present, indicating that work has been done to the flow. In case of numerical calculations, it is possible to use the radial distribution of the axial velocity upstream of the rotor which becomes negative at the shroud as soon as inlet recirculation is present.

A clear identification of inlet recirculation can be deteriorated by flow phenomena sourcing from other components of the machine. For the compressor subject to this research, the matching of the components is so that the diffuser and the volute operate disturbance free in the region of onset of recirculation. As a result, all changes in the values which are used to determine inlet recirculation can clearly be related to the phenomenon.

In the compressor map, a large region at flow rates lower than design conditions is affected by inlet recirculation and the phenomenon occurs well before the compressor goes into surge. In terms of flow range, inlet recirculation is present over about 40% of the map width at low rotational speeds. This value decreases as the rotor speed is increased. It is present beyond the point where the inlet flow becomes transonic. As soon as shocks are present, the recirculation region diminishes significantly. This behaviour could be a result of the destabilising effect of the shock as it represents a disturbance. Furthermore it reduces meridional momentum due to the shock compression. For high speeds, the compressor surges directly.

8.5 Reduced order modelling of inlet recirculation

Inlet recirculation is a highly complex three dimensional flow phenomenon which extends far into the rotor and can extend far upstream into the inlet of the compressor.

However, its behaviour seems to be predictable up to a certain extent. The amount of mass flow being expelled from the rotor into the inlet shows a linear correlation with the global flow coefficient of the machine.

The transported specific energy is about constant once the inlet recirculation has been expelled out of the rotor. For the machine subject to this research the energy remained constant at 70% of the rotor total enthalpy rise.

The total energy in the recirculation zone thus is proportional to the recirculation mass flow. Furthermore, the size of the bubble scales with the amount of mass expelled from the rotor inlet. This in return means that there is a clear correlation between the amount of energy lost due to inlet recirculation and the size of the recirculation bubble.

The correlations for the recirculation mass flow and the specific energy allow to depict inlet recirculation with a simple model provided in **equations 8.1 and 8.2**. The work needed to sustain inlet recirculation is added to the Euler work in form of an additional work coefficient λ_{RC} , as shown in the first equation. The additional work λ_{RC} can be estimated using the second equation, where the exponent has to be set to 1 due to the linear correlation between the mass flow through the machine and the mass flow into the inlet recirculation zone. It is recommended to estimate the onset point of inlet recirculation, and thus the parameter ϕ_{2RC} based on the critical area ratio by Qiu [35]. Although this correlation does not seem to apply to all cases and showed to be problematic for automotive turbocharger applications, it still remains the best estimate available.

$$\lambda = \lambda_{Euler} + \lambda_{RC} \quad (8.1)$$

$$if : \phi_2 < \phi_{2RC} : \lambda_{RC} = k_{RC} (\phi_{2RC} - \phi_2)^{exp_{RC}} \quad (8.2)$$

8.6 The energetic costs of inlet recirculation

Inlet recirculation requires a significant amount of additional work input into the compressor. One way of accounting for it is to determine the entropy rise from the intake of the compressor to the inlet of the machine. At the inlet of the machine, only the part of the inlet area where flow enters the inlet is taken into account. This value represents the "lumped" loss which includes all secondary losses occurring in the part of the annulus height in the rotor and the inlet which is occupied by the recirculation. This means that mixing losses as well as end-wall, profile and tip leakage losses in the recirculation zone are all lumped together as one single loss parameter. The "lumped" recirculation loss can make out up to 35% of the total loss occurring in a compressor at low speed. This makes it the the largest contributor compared to the inlet, the rest of the rotor, the diffuser, the volute and the disk friction loss. The "lumped" loss can be split up into two parts. Around 80% of the "lumped" loss source from the additional energy which is necessary to sustain the inlet recirculation bubble. The remaining 20% represent secondary losses occurring in the region of the bubble which include the loss sources mentioned above. In addition to the secondary loss within the rotor, the mixing between the clean inflow and the recirculation bubble in the inlet add to the rise in entropy at the rotor inlet.

8.7 The effect of tip clearance on inlet recirculation

The tip clearance flow in a compressor represents one of the major contributors to the low momentum region in the casing. Furthermore tip leakage is a significant source of loss. In turbocharger compressors, the tip leakage plays a more significant role due to the large relative tip gap size. The tip leakage flow has a significant effect on the flow structure in the casing of the rotor. The smaller the leakage flow, the less the low momentum region gets pushed towards the pressure side of the main blade. As a result, the low momentum region is more confined to the splitter passage close to the main blade suction side where the flow stagnates due to the adverse pressure gradient. Consequently this passage is affected much stronger by blockage from a recirculation region for small tip gaps, whereas the other splitter passage remains mostly free.

The size of the tip gap does however not have an effect on the onset point of inlet recirculation. Instead, the low momentum flow at the casing stagnates once it reaches the pressure side of the splitter blade around its leading edge. The operating point at which this point is reached is not shifted by the size of the tip gap. When throttled to lower flow rates, the reverse flow region starts to expel out of the rotor inlet. The size and intensity is independent of the tip gap size. Furthermore the "lumped" inlet recirculation loss is unaffected by the tip gap as well and remains the same. In terms of rotor efficiency, this means that the gains due to a reduced tip gap are only present for flow conditions without inlet recirculation. Under recirculation, the efficiency gain due to the smaller tip gap is marginalised. This behaviour is most likely related to the fact that, independent of the tip gap, the blockage region within the rotor maintains the same size. Furthermore, the blockage region at the shroud leads to an unloading of the rotor tip which diminishes the tip leakage due to a small pressure difference between the suction and pressure side of the blade.

However, the rotor still benefits from enhanced pressure rise capabilities for reduced tip gap sizes, even when inlet recirculation is present.

8.8 Future work

The present work showed that the energy loss associated with the recirculation is directly proportional to the size of the blockage created by it. This in return means that a reduction in size of the recirculation bubble would have a direct impact on the efficiency of the compressor in the low-speed and low-flow area of the compressor map, a region crucially important for engine startup performance. In order to achieve this aim, further understanding about design parameters which affect inlet recirculation is necessary.

Inlet recirculation is understood to be the result of a subtle balance between the meridional momentum inside the impeller passage and the local static pressure field. Consequently several major design geometry parameters can have an effect on the onset and maintenance of inlet recirculation. Those parameters are identified as:

- The rotor main blade leading edge loading
- The casing meridional curvature, particularly in the inducer part
- The impeller inlet to exit area ratio, which determines the part speed flow coefficient
- The relative tip clearance gap size which influences the blockage and loss in the tip region

Further insight about the behaviour of inlet recirculation and how to control it could be gained by varying the geometry of a centrifugal compressor according to these geometry parameters.

In addition, a repositioning or loading redistribution of the splitter blade could have an effect on the onset of inlet recirculation as the pressure side of the splitter blade was identified to be the location of high adverse pressure gradient where the casing low momentum flow stagnates.

The insights from such geometrical studies could also help to improve reduced order modelling for the starting point of inlet recirculation as the state of the art techniques are not universally applicable.

Regarding the inception of inlet recirculation, several questions remain to be clarified.

The correlation between inlet recirculation and stall for example has not been understood up to now. In a radial machine, it seems to be unlikely for spike type stall inception to develop at low speeds because of the presence of inlet recirculation. The question whether the phenomena replace each other remains unclear. Furthermore the failure mechanism of a rotor with inlet recirculation which starts to surge is unknown. One idea could be that such

a machine would develop a disturbance with the length scale of one rotor circumference similar to modal stall inception due to the presence of a loading asymmetry sourcing from the volute.

More insight into these questions could be gained via a time resolved investigation of a centrifugal compressor that could be carried out with Kulite measurements experimentally or via time resolved calculations on a full annulus model.

A convenient method for map width enhancement in automotive turbocharger compressors is the usage of a bleed channel. The device bleeds off a certain portion of the casing flow and recirculates it back into the inlet via a separate channel. In a compressor with such a more complex geometry, it could be that inlet recirculation does occur under certain flow conditions. One possible study could investigate the presence of inlet recirculation in such a case.

References

- [1] Bammert, K. and Rautenberg, M. (1975). Radialverdichter, messungen an beschauelten diffusoren, abschlussbericht. *FVV-Forschungsber. 184, Frankfurt.*
- [2] based on John Denton (2016). *Turbostream GPU based solver.* www.turbostream-cfd.com.
- [3] Camp, T. R. and Day, I. J. (1998). A study of spike and modal stall phenomena in a low-speed axial compressor. *J. Turbomach 120(3), 393-401 (Jul 01, 1998) (9 pages)* doi:10.1115/1.2841730.
- [4] Casey, M. V. (2010). Turbochargers. *Lecture notes, Institute of Thermal Turbomachinery and Machinery Laboratory (ITSM), University of Stuttgart, Germany.*
- [5] Casey M. V., R. C. J. (2006). A guide to turbocharger compressor characteristics. *Dieselmotorentechnik, 10. Symposium TAE Esslingen ISBN 3-924813-65-5.*
- [6] Casey M. V., R. C. J. (2011). A method to estimate the performance map of a centrifugal compressor stage. *ASME GT2011-45502.*
- [7] Daily and Neece (1960). Chamber dimension effects on induced flow and frictional resistance of enclosed rotating disks. *J. Basic Engineering, Vol 86, No 3, pp 607-619. Basic Eng 82(1), 217-230 doi:10.1115/1.3662532.*
- [8] Daugherty, R. L. (1915). *Centrifugal pumps.* McGraw-Hill Book Company Inc., New York.
- [9] Day, I. and Young, A. (2012). Stall and surge. *Cambridge Turbomachinery course.*
- [10] Day, I. J. (1993). Stall inception in axial flow compressors. *Journal of Turbomachinery 115(1), 1-9, Jan01, 1993 (9 pages).*
- [11] Eck, D. I. B. (1972). *Ventilatoren.* Springer.
- [12] Eckardt, D. (1980). Flow field analysis of radial and backswept centrifugal compressor impellers. *25th Intl Gas Turbine Conf ASME, New Orleans, 1980, 77-86.*
- [13] Emmons, H. W., Pearson, C. E., and Grant, H. P. (1955). Compressor surge and stall propagation. *TRANS. ASME, Vol. 77, Apr. 1955, pp. 455- 469.*
- [14] Enyon, P. A. and Whitfield, A. (2000). Pressure recovery in a turbocharger compressor volute. *Proceedings of the Institution of Mechanical Engineers, Part A Journal of Power and Energy-2000-Eynon-599-610.*

- [15] Federal Motor Transportation Authority, K. B. A. (2011). Number of passenger cars in germany on 01.01.2012, split after fuels. *Homepage kba.de*.
- [16] Fringe, P. and Van den Braembusche, R. A. (1985). A theoretical model for rotating stall in the vaneless diffuser of centrifugal compressors. *ASME J. of Engineerign for Gas Turbines & Power, Vol. 107, No 2, pp 468-474*.
- [17] Gancedo, M. et al. (2013). Experimental investigation of flow instability in a turbocharger ported shroud compressor. *Proceedings of ASME Turbo Expo 2013, GT2013-95134*.
- [18] Greitzer, E. M. (1978). Surge and rotating stall in axial flow compressors. *Parts I and II, ASME, J. of Engineering dor Power, 98, p190-217*.
- [19] Greitzer, E. M. (1980). The stapility of pumping systems - the 1980 freeman scholar lecture. *ASME, J. Fluids Engineering Vol. 103, pp 193-243*.
- [20] Guelich, J. F. (2010). *Centrifugal Pumps, ISBN 9783642128240 and 9783642128233*. Springer.
- [21] Hah, C. and Rabe, D. C. (2004). Role of tip-leakage vortices and passage shock in stall inception in a swept transonic compressor rotor. *Proceedings of ASME Turbo Expo 2004, GT2004-53867*.
- [22] Harley, P. et al. (2014a). Inlet recirculation in automotive turbocharger centrifugal compressors. *IMEchE 11th International Conference on Turbochargers and Turbocharging, London, UK, 0045*.
- [23] Harley, P. et al. (2014b). Meanline modelling of inlet recirculation in automotive turbocharger centrifugal compressors. *ASME GT2014-25853*.
- [24] Harley, P., Starke, A., Bamba, T., and Filsinger, D. (2016). Axial groove casing treatment in an automotive turbocharger centrifugal compressor. *IMEchE 12th International Conference on Turbochargers and Turbocharging, London*.
- [25] Jansen, W. (1964a). Rotating stall in radial vaneless diffusers. *J. Basic Engineering, Vol.86, No 4, pp 750-758*.
- [26] Jansen, W. (1964b). Steady flow in a radial vaneless diffuser. *J. Basic Engineering, Vol 86, No 3, pp 607-619*.
- [27] Japikse, D. (2000). *Diffuser Design Technology*. Concepts ETI, ISBN-10: 0933283083.
- [28] Japikse, D., W.Marscher, and Furst, R. B. (2006). *Centrifugal Pump Design and Performance*. Concepts NREC, White River Junction, Vermont.
- [29] Japinske, D. (1996). Centrifugal compressor design and performance. *Concepts NREC, ISBN 0-933283-03-2, Vermont, USA*.
- [30] Kaemmerer, N. and Rautenberg, M. (1986). A distinction between different types of stall in a centrifugal compressor stage. *Journal of Engineering for Gas Turbines and Power Vol.108 / 83*.

- [31] MarketsandMarkets (2012). Turbocharger market by vehicle type, fuel type, technology and region - industry trends and forecast to 2019. *Marketsandmarkets.com*.
- [32] Moore, F. and Greitzer, E. (1986). A theory of post stall transients in axial compression systems: Part i - development of equations and part ii application. *Journal of Engineering for gas Turbines and Power*, 108, p68- 76 and p231- 239.
- [33] Muggli, F. A. et al. (2001). Cfd calculation of a mixed flow pump characteristic from shut- off to maximum flow. *Proceedings of ASME FEDSM'01, FEDSM2001-18072*.
- [34] Pfleiderer, C. and Petermann, H. (1952). *Stroemungsmaschinen*. Springer.
- [35] Qiu, X., Japikse, D., and Anderson, M. (2008). A meanline model for impeller flow recirculation. *Proceedings of ASME Turbo Expo 2008: Power for Land, Sea and Air*.
- [36] Ribaud, Y. (1987). Experimental aerodynamic analysis relative to three high pressure ratio centrifugal compressors. *The american society of mechanical engineers*, 87-GT-153.
- [37] Ribi (1996). *Flow in Radial Turbomachines*. VKI Lecture series.
- [38] Schleer, M. and Abhari, R. S. (2011). Clearance effects on the onset of instability in a centrifugal compressor. *ASME GT2011-90084*.
- [39] Schreiber, C. (2011). Prediction of radial compressor characteristics for turbochargers. *Diploma thesis, ITSM University of Stuttgart*.
- [40] Senoo, Y., Kinoshita, Y., and Ishida, M. (1977). Asymmetric flow in vaneless diffusers of centrifugal blowers. *Trans ASME Journ. Fluids Eng.* 99: 104-114.
- [41] Sideris, M. (1988). Circumferential distortion of the flow in centrifugal compressors due to outlet volutes. *PhD- Thesis, RUG-VKI*.
- [42] Spakovszky, Z. S. (2002). Backward traveling rotating stall waves in centrifugal compressors. *Paper No. GT2002-30379, pp. 529-543; 15 pages doi:10.1115/GT2002-30379; ASME Turbo Expo 2002: Power for Land, Sea, and Air Volume 5: Turbo Expo 2002, Parts A and B Amsterdam, The Netherlands, June 3–6, 2002 Conference Sponsors: International Gas Turbine Institute ISBN: 0-7918-3610-X | eISBN: 0-7918-3601-0 Copyright © 2002 by ASME*.
- [43] Stepanoff, A. J. (1967). *Centrifugal and Axial Flow Pumps*. John Wiley & Sons, New York.
- [44] Tamaki, H. (2011). Effect of recirculation device with counter swirl vane on performance of high pressure ratio centrifugal compressor. *Proceedings of ASME Turbo Expo 2011, GT2011-45360*.
- [45] Tamaki, H. et al. (2015). Enhancement of centrifugal compressor operating range by control of inlet recirculation with inlet fins. *Proceedings of ASME Turbo Expo 2015, GT2015-42154*.
- [46] Tanaka, T. (1980). An experimental study of backflow phenomena in a high specific speed propeller pump. *ASME 80-FE-6*.

-
- [47] Traupel, W. (1965). *Thermische Turbomaschinen, Band 1, 3rd edition, Springer, ISBN 3-540-67374-8, 2001*. Springer.
- [48] Tsujimoto, Y., Yoshida, Y., and Mori, Y. (1996). Study of vaneless diffuser rotating stall based on two-dimensional inviscid flow analysis. *J. Fluids Eng* 118(1), 123-127.
- [49] Van den Braembusche, R. A. (2013). Centrifugal compressors analysis & design. *von Karman Institute Lecture series Course Note 192, p316*.
- [50] Weber, C. R. and Koronowski, M. E. (1986). Mean line performance prediction of volutes in centrifugal compressors. *International Gas Turbine Conference and Exhibit Düsseldorf, West Germany; 86-GT-216*.
- [51] Y. Senoo, Y. K. (1978). Limits of rotating stall and stall in vaneless diffuser of centrifugal compressors. *ASME P 78 GT 19*.

Appendix A

Measurement equipment specifications

A.1 Temperature probes

Temperature probes:

- T- Type
- Comark tempscan c8600 12 channel thermometer
- Thermocouple characterising accuracy to EN 60584-1 : 1995 ; also ITS-90: T-Type
Range C -200 +400 Maximum error +- C <0.03

Pressure probes:

- One Sensor

Table A.1 Cole Parmer Model EW-68848-28

specifications:

Media compatibility	gases or liquids compatible with 17-4PH stainless steel
Accuracy	+/-1% full scale
Output	1 to 5 V
Range	0 to 30 psig
Process connection	1/4" NPT(M)
Electrical connections	3-ft cable
Power	8 to 30 VDC
Brand	Ashcroft
Model	V230PSI
Make	VSeries
